UNIVERSITY OF CALIFORNIA SAN DIEGO

Inspection of Structures by Passive Extraction of Acoustic Transfer Functions and Ultrasonic Imaging

A dissertation submitted in partial satisfaction of the requirements for the degree

Doctor of Philosophy

in

Structural Engineering

by

Simone Sternini

Committee in Charge:

Professor Francesco Lanza di Scalea, Chair
Professor William S. Hodgkiss
Professor Hyonny Kim
Professor William A. Kuperman
Professor Kenneth J. Loh

2018

The dissertation of Simone Sternini is approved, and it is acceptable in quality and form for publication on microfilm and electronically:

_____

_____

_____

_____

_____

Chair

University of California San Diego

2018

DEDICATION

To my Family

TABLE OF CONTENTS

LIST OF FIGURES

LIST OF TABLES

ACKNOWLEDGEMENTS

There won't be enough words to acknowledge all the people that have played an important role during my PhD experience, but I'll try my best. First of all, I would like to thank my advisor Prof. Francesco Lanza di Scalea who gave me the possibility to start this amazing experience here at UC San Diego that definitely changed my life. He has always been an exceptional mentor and a strong reference point throughout these years, constantly supporting me both on the academic and the personal level.

A special acknowledgement goes to my family, that always believed in me during my academic career, constantly supporting me and making me feel close to them even when we were half a world away. Their love was the driving force that helped me go forward even in the most difficult times.

This journey would not have been the same without my amazing colleagues, that made my PhD experience unforgettable. A special mention goes to Margherita Capriotti and Albert Liang, whom I had the honor to work with most of time and that made even the hardest moments really fun (especially in Pueblo, CO, when we were freezing in the middle of the desert). A big acknowledgement goes also to Xuan "Peter" Zhu, Stefano Mariani, Thompson Nguyen, Ranting Cui, Diptojit Datta, and Yichao Yang for being great colleagues and friends.

Special thanks go to all my friends that represented a fundamental part of my life during these PhD years. They all mean something special to me and they made me live unforgettable experiences that I will always carry in my heart. In particular, I would like to thank Iacopo, Matteo, Marco, Ernesto, Frank, the usual suspects (Marcello, Jonathan, and Dario), Roberto, Filippo, Ana, Elisabetta, Sara, Giacomo, Orsola, Roberta, Le Fripon, Gianmarco, Manuela, Cinzia, Carla, Simone, Lorenzo, Macarena, Yvonne and Julie (for not killing me after all the time that I bothered

them with questions), Ivana, Dario, Valeria, Enrico, i due Antonino, and many others! You all have been my family here and because of every one of you this experience has been the best I could have asked for!

A special mention goes to Nathalí for two years and a half that I will never forget and for being a special person to me.

This dissertation is a collection of papers that have been accepted or submitted.

Chapter 2 is, in full, a reprint of material published in F. Lanza di Scalea, X. Zhu, M. Capriotti, A. Y. Liang, S. Mariani, S. Sternini, "Passive Extraction of Dynamic Transfer Function From Arbitrary Ambient Excitations: Application to High-Speed Rail Inspection From Wheel-Generated Waves," *ASME Journal of Nondestructive Evaluation, Diagnostics, and Prognostics of Engineering Systems*, vol. 1, no. 1, pp. 011005-011005-12, 2017. The dissertation author was the primary investigator and author of this paper.

Chapter 3 is, in full, a reprint of material published in F. Lanza di Scalea, S. Sternini, A. Y. Liang, "Robust passive reconstruction of dynamic transfer function in dual-output systems," *Journal of the Acoustical Society of America*, vol. 143, no. 2, pp. 1019-1028, 2018. The dissertation author was the primary investigator and author of this paper.

Chapter 4 is, in full, a reprint of S. Sternini, A. Y. Liang, F. Lanza di Scalea, "Rail Flaw Imaging by Improved Synthetic Aperture Focus Techniques," submitted to *Materials Evaluation*. The dissertation author was the primary investigator and author of this paper.

Chapter 5 is, in full, a reprint of material published in S. Sternini, A. Y. Liang, F. Lanza di Scalea, "Ultrasonic Synthetic Aperture Imaging with Interposed Transducer-Medium Coupling Path," *Structural Health Monitoring*, 2018, https://doi.org/10.1177/1475921718805514. The dissertation author was the primary investigator and author of this paper.

Chapter 6 is, in full, a reprint of material published in F. Lanza di Scalea, S. Sternini, T. V. Nguyen, "Ultrasonic Imaging in Solids Using Wave Mode Beamforming," *IEEE Transactions on Ultrasonics, Ferroelectrics, and Frequency Control*, vol. 64, no. 3, pp. 602-616, 2017. The dissertation author was the primary investigator and author of this paper.

Chapter 7 is, in full, a reprint of S. Sternini, A. Pau, F. Lanza di Scalea, "Minimum Variance Imaging in Plates Using Guided Wave Mode Beamforming," submitted to *IEEE Transactions on Ultrasonics, Ferroelectrics, and Frequency Control*. The dissertation author was the primary investigator and author of this paper.

VITA

2010 Bachelor of Science in Building Engineering, University of Bologna, Italy

2013 Master of Science in Civil Engineering, University of Bologna, Italy

2018 Doctor of Philosophy in Structural Engineering,
University of California, San Diego

PUBLICATIONS

JOURNAL ARTICLES

1. **S. Sternini**, A. Pau, F. Lanza di Scalea, "Minimum Variance Imaging in Plates Using Guided Wave Mode Beamforming," *IEEE Transactions on Ultrasonics, Ferroelectrics, and Frequency Control*, in review.

2. A. Y. Liang, **S. Sternini**, M. Capriotti, F. Lanza di Scalea, "High Speed Ultrasonic Rail Inspection by Passive Non-contact Technique," *Materials Evaluation*, in review.

3. **S. Sternini**, A. Y. Liang, F. Lanza di Scalea, "Rail Flaw Imaging by Improved Synthetic Aperture Focus Techniques," *Materials Evaluation*, in review.

4. **S. Sternini**, A. Y. Liang, F. Lanza di Scalea, "Ultrasonic Synthetic Aperture Imaging with Interposed Transducer-Medium Coupling Path," *Structural Health Monitoring*, 2018, https://doi.org/10.1177/1475921718805514.

5. H. Hu, X. Zhu, C. Wang, L. Zhang, X. Li, S. Lee, Z. Huang, R. Chen, Z. Chen, C. Wang, Y. Gu, Y. Chen, Y. Lei, T. Zhang, N. Kim, Y. Guo, Y. Teng, W. Zhou, Y. Li, A. Nomoto, **S. Sternini**, Q. Zhou, M. Pharr, F. Lanza di Scalea, S. Xu, "Stretchable ultrasonic transducer arrays for three-dimensional imaging on complex surfaces," *Science Advances*, vol. 4, no. 3, pp. 1-11, 2018.

6. F. Lanza di Scalea, **S. Sternini**, A. Y. Liang, "Robust passive reconstruction of dynamic transfer function in dual-output systems," *Journal of the Acoustical Society of America*, vol. 143, no. 2, pp. 1019-1028, 2018.

7. **S. Sternini**, A. Quattrocchi, R. Montanini, A. Pau, F. Lanza di Scalea, "A match coefficient approach for damage imaging in structural components by ultrasonic synthetic aperture focus," *Procedia Engineering*, vol. 199, pp. 1544-1549, 2017.

8. F. Lanza di Scalea, X. Zhu, M. Capriotti, A. Y. Liang, S. Mariani, **S. Sternini**, "Passive Extraction of Dynamic Transfer Function From Arbitrary Ambient Excitations: Application to High-Speed Rail Inspection From Wheel-Generated Waves," *ASME Journal of Nondestructive Evaluation, Diagnostics, and Prognostics of Engineering Systems,* vol. 1, no. 1, pp. 011005-011005-12, 2017.

9. F. Lanza di Scalea, **S. Sternini**, T. V. Nguyen, "Ultrasonic Imaging in Solids Using Wave Mode Beamforming," *IEEE Transactions on Ultrasonics, Ferroelectrics, and Frequency Control,* vol. 64, no. 3, pp. 602-616, 2017.

CONFERENCE PROCEEDINGS

1. F. Lanza di Scalea, X. Zhu, M. Capriotti, A. Y. Liang, S. Mariani, **S. Sternini**, R. Wilson, "High-speed Non-contact Ultrasound System for Rail Track Integrity Evaluation," SPIE Conference on Smart Structures and NDE, Denver, CO, 2018.

2. F. Lanza di Scalea, X. Zhu, M. Capriotti, A. Y. Liang, S. Mariani, **S. Sternini**, R. Wilson, G. Carr, "High-speed Rail Inspection by Passive Acoustic Technique," Transportation Research Board Annual Meeting, Washington, DC, 2018.

3. **S. Sternini**, A. Y. Liang, F. Lanza di Scalea, R. Wilson, "Pushing the Limits of Ultrasonic Imaging of Solids by Wave Mode Beamforming and GPU Processing," 11th International Workshop on Structural Health Monitoring, Stanford University, 2017.

4. M. Capriotti, **S. Sternini**, F. Lanza di Scalea, "Passive Defect Detection and Imaging in Structures by Cross-correlations of Infrared Thermography Measurements," 11th International Workshop on Structural Health Monitoring, Stanford University, 2017.

5. **S. Sternini**, A. Quattrocchi, R. Montanini, F. Lanza di Scalea, "Ultrasonic Damage Imaging of Structural Components with Bulk and Guided Waves using Match Coefficients," SPIE Conference on Smart Structures and NDE, Portland, OR, USA, 2017.

6. **S. Sternini**, T. V. Nguyen, F. Lanza di Scalea, "Ultrasonic Imaging Using Global Matched Coefficients," 8th European Workshop on Structural Health Monitoring, Bilbao, Spain, 2016.

7. T. V. Nguyen, **S. Sternini**, F. Lanza di Scalea, "3D Ultrasonic Imaging Applications on Rails," ASME Joint Rail Conference, Coulmbia, SC, 2016.

8. S. Mariani, T. V. Nguyen, X. Zhu, **S. Sternini**, F. Lanza di Scalea, M. Fateh, R. Wilson, "Non-contact Ultrasonic Guided Wave Inspection of Rails: Next Generation Approach," ASME Joint Rail Conference, Coulmbia, SC, 2016.

9. **S. Sternini**, T. V. Nguyen, F. Lanza di Scalea, "Ultrasonic Imaging using Wave Structure-based Weights and Global Matched Coefficients," SPIE Conference on Smart Structures and NDE, Las Vegas, USA, 2016.

10. M. Capriotti, **S. Sternini**, F. Lanza di Scalea, S. Mariani, "Extraction of Thermal Green's Function Using Diffuse Fields: A Passive Approach Applied to Thermography," SPIE Conference on Smart Structures and NDE, Las Vegas, USA, 2016.

11. S. Mariani, T. V. Nguyen, **S. Sternini**, F. Lanza di Scalea, M. Fateh, R. Wilson, "Defect detection performance of the UCSD non-contact air-coupled ultrasonic guided wave inspection of rails prototype," SPIE Conference on Smart Structures and NDE, Las Vegas, USA, 2016.

12. T. V. Nguyen, **S. Sternini**, F. Lanza di Scalea, "Advances in Ultrasonic Imaging for Internal Flaws in Structures," Annual Conference of the Prognostics and Health Management Society, Coronado, CA, USA, 2015.

13. **S. Sternini**, T. V. Nguyen, F. Lanza di Scalea, "Tomographic Imaging of Structural Flaws with New Adaptive Weights on Array," 10th International Workshop on Structural Health Monitoring, Stanford University, 2015.

14. T. V. Nguyen, **S. Sternini**, F. Lanza di Scalea, "On Defect Imaging Using Ultrasonics for Structural Health Monitoring," The 22nd International Congress on Sound and Vibration, Florence, Italy, 2015.

ABSTRACT OF THE DISSERTATION

Inspection of Structures by Passive Extraction of Acoustic Transfer Functions and Ultrasonic Imaging

by

Simone Sternini

Doctor of Philosophy in Structural Engineering

University of California San Diego 2018

Professor Francesco Lanza di Scalea, Chair

Inspection of structures is a critical task that needs to be performed in order to guarantee the safety of structural components during their service life. Different Non-Destructive Evaluation (NDE) techniques can be used to inspect aerospace, civil, and biological systems to ensure their structural integrity and to identify the presence of damages and defects, which could impair the correct functioning of the overall structure.

The focus of this dissertation is the inspection of structures through the passive extraction of the acoustic transfer function of the medium under consideration, and the 2D and 3D characterization of defects by means of ultrasonic imaging. The first part of the dissertation addresses the issue of defect detection in railroad tracks by extracting the acoustic transfer function

of rails through a normalized cross-correlation operator, which exploits the random acoustic vibrations generated by the train wheels. A technique to remove uncorrelated noise from the recorded signals is also introduced to make the transfer function reconstruction more robust. A statistical outlier analysis is used to detect any variation in the transfer function of the rail as the train moves along the track, in order to identify locations where discontinuities (joints, welds, defects) might be present. A prototype with multiple pairs of capacitive sensors was developed to perform the inspection in a non-contact, passive-only, high-speed manner. Results from fields tests performed at the Transportation Technology Center (TTC) in Pueblo, CO, have demonstrated the potential of the system for the reliable inspection of railroad tracks at speeds up to 80mph.

The second part of the dissertation is focused on the characterization of defects using ultrasonic imaging to create 2D and 3D images of the inspected medium. Imaging in bulk solids and plates is performed using sensor arrays and an improved beamforming algorithm that uses information about the structure of the propagating acoustic wave modes to improve the defect characterization process. Furthermore, the experimental application to railroad tracks and the implementation on a Graphics Processing Unit (GPU) shows the potential for the accurate real-time imaging of rail flaws.

Chapter 1

Introduction

Non-Destructive Evaluation (NDE) techniques have been widely used to ensure structural safety and reliability by providing reliable solutions for the maintenance of aerospace, civil, and infrastructure systems. While active approaches have been the focus of several studies, a passive framework is often desirable since it removes the requirement for active source control and reduces the complexity of the signal conditioning and data acquisition system. Since passive NDE techniques exploit the acoustic noise introduced by environmental or mechanical excitations into the system of interest, common applications of this passive approach are structures such as bridges, wind turbines and railroad tracks.

In recent years, it has been shown that the impulse response function (Green's function in the acoustics community) can be reconstructed from ambient noise fields by using pairs of sensors. Lobkis et al. [1] demonstrated the reconstruction of the direct signal between two transducers both theoretically and experimentally by cross-correlation of their recorded responses to a diffuse acoustic field. It was also shown that the quality of the reconstruction could be improved by increasing the spatiotemporal randomness of the noise sources. Similarly, Weaver et al. [2] demonstrated the emergence of the Green's function from cross-correlation of diffuse fields in

open systems. Roux et al. [3] provided a model for the emergence of the Green's function between receiver pairs from the ensemble average of cross-correlation in a 3D homogeneous free space, and demonstrated that the derivative of the noise correlation function converges to the Green's function.

In the NDE and Structural Health Monitoring (SHM) fields, various applications of transfer function reconstruction from ambient noise can be found. Farrar et al. [4] estimated the impulse response function of a bridge between two receivers and used this estimation to extract modal parameters of the structure. Snieder et al. [5] extracted time-arrival structures containing the propagation of waves in a building by deconvolution of signals recorded at different building levels. Sabra et al. [6] performed the extraction of Lamb wave Green's functions from correlation of random Lamb fields.

In the first part of this dissertation, the application of interest is high-speed rail track integrity evaluation. The most common rail inspection technique uses a fluid-filled wheel probe with piezoelectric transducers that ultrasonically inspect the rail track. The main drawback of this system is the limited inspection speed, normally up to 25mph, which causes traffic disruption along the inspected sections. The railroad industry needs a reliable system which is able to monitor the railway tracks in an efficient manner, in order to avoid catastrophic and costly accidents. The proposed study demonstrates the possibility of inspecting railroad tracks through the passive reconstruction of the rail transfer function from wheel-generated excitations, and the ability of detecting rail discontinuities such as joints, welds, and defects at speeds up to 80mph. Chapter 2 will show the steps that have been performed to extract the acoustic transfer function of the rail and the defect detection prototype that has been used for the field tests. Results will be shown for speeds going from 25mph to 80mph in order to show the feasibility of the system for accurate

defect detection. Chapter 3 will explain an improvement to the algorithm used for the transfer function extraction, in which a robust reconstruction in a dual-output system is performed in order to eliminate any uncorrelated noise that may be present in the recorded signals.

The second part of the dissertation will show some results obtained using ultrasonic imaging techniques for defect characterization. In particular, the Synthetic Aperture Focus (SAF) technique [7, 8] was applied to rail specimens in order to create 2D and 3D images of simulated and natural rail flaws. The imaging algorithm was implemented on a Graphics Processing Unit (GPU) framework [9] in order to achieve pseudo real-time imaging. Chapter 4 will illustrate all the steps that have been performed to obtain accurate images of rail flaws, thus allowing for the correct identification of their location, size, and orientation.

Chapter 5 will show the implementation of the imaging algorithm when an interposed coupling path, such as a transducer wedge, is placed between the ultrasonic array and the medium of interest. A ray tracing formulation has been introduced to account for the different propagation paths of multiple wave modes that refract at the wedge/medium interface. Moreover, compounding images obtained from different wave modes improves the imaging results in terms of dynamic range and spatial resolution. Experimental results will be shown for simulated defects on an aluminum block.

Chapter 6 will discuss some improvements to conventional beamforming techniques, such as Delay-and-Sum (DAS) and Minimum Variance Distortionless Response (MVDR) processor, for damage imaging in bulk solids using longitudinal and shear waves. A set of weights, which depend on the wave mode structure of the propagating ultrasonic waves, is introduced in a Matched Field Processing (MFP) approach in order to improve the focus of the array on the defect location.

Wave mode compounding is also performed to show the additional improvement that can be achieved by combining multiple wave mode combinations that coexist in the material.

Finally, Chapter 7 extends the concepts introduced in Chapter 6 to the case of damage imaging in plates using ultrasonic guided (Lamb) waves. Different sets of weights based on the wave mode structure of the propagating Lamb modes (S0, A0, and SH0 for the case considered) are introduced and their effectiveness in improving the reconstructed images is demonstrated for damage imaging on an aluminum plate using the MVDR beamformer.

References

[1] Lokbis, O.I., and Weaver, R.L., 2001, "On the Emergence of the Green's Function in the Correlations of a Diffuse Field," J. Acoust. Soc. Am., 110(6), pp. 3011-3017.

[2] Weaver, R.L., and Lokbis, O.I., 2004, "Diffuse Fields in Open Systems and the Emergence of the Green's Function (L)," J. Acoust. Soc. Am., 116(5), pp. 2731-2734.

[3] Roux, P., Sabra, K.G., Kuperman, W., and Roux, A., 2005, "Ambient noise cross correlation in free space: theoretical approach," J. Acoust. Soc. Am., 117(1), pp. 79–84.

[4] Farrar, C. and James, G., 1997, "System identification from ambient vibration measurements on a bridge," J. Sound Vib., 205(1), pp. 1-18.

[5] Snieder, R., 2004, "Extracting the Green's function from the correlation of coda waves: a derivation based on stationary phase," Phys. Rev. Lett. E, 69, pp. 0466101-0466108.

[6] Sabra, K., Srivastava, A., Lanza di Scalea, F., Bartoli, I., Rizzo, P., and Conti, S., 2008, "Structural health monitoring by extraction of coherent guided waves from diffuse fields," J. Acoust. Soc. Am., 123(1), pp. EL8-EL13.

[7] Flaherty, J. J., Erikson, K. R., and Lund, V. M., 1967, "Synthetic Aperture Ultrasonic Imaging Systems," U.S. Patent 3,548,642.

[8] Jensen, J. A., Nikolov, S. I., Gammelmark, K. L., and Pedersen, M. H., 2006, "Synthetic aperture ultrasound imaging," Ultrasonics, 44(1), pp. e5-e15.

[9] Martin-Arguedas, C. J., Romero-Laorden, D., Martinez-Graullera, O., Perez-Lopez, M., and Gomez-Ullate, L., 2012, "An ultrasonic imaging system based on a new SAFT approach and a GPU beamformer," IEEE Transactions on Ultrasonics, Ferroelectrics, and Frequency Control, 59(7), pp. 1402-1412.

Chapter 2

Passive Extraction of Dynamic Transfer Function from Arbitrary Ambient Excitations: Application to High-speed Rail Inspection from Wheel-generated Waves

Abstract

The general topic of this paper is the passive reconstruction of an acoustic transfer function from an unknown, generally nonstationary excitation. As recently shown in a study of building response to ground shaking, the paper demonstrates that, for a linear system subjected to an unknown excitation, the deconvolution operation between two receptions leads to the Green's function between the two reception points that is independent of the excitation. This is in contrast to the commonly used cross-correlation operation for passive reconstruction of the Green's function, where the result is always filtered by the source energy spectrum (unless it is opportunely normalized in a manner that makes it equivalent to a deconvolution).

This concept is then applied to high-speed ultrasonic inspection of rails by passively reconstructing the rail's transfer function from the excitations naturally caused by the rolling wheels of a moving train. A first-generation prototype based on this idea was engineered using non-contact air-coupled sensors, mounted underneath a test railcar, and field tested at speeds up to 80 mph at the Transportation Technology Center in Pueblo, CO. This is the first demonstration of passive inspection of rails from train wheel excitations and, to the authors' knowledge, the first attempt ever made to ultrasonically inspect the rail at speeds above ~ 30 mph (that is the maximum speed of common rail ultrasonic inspection vehicles). Once fully developed, this novel concept could enable regular trains to perform the inspections without any traffic disruption and with great redundancy.

2.1 Introduction

The passive reconstruction of the Green's function (or, generally, a transfer function) between two points of a medium without an active controlled excitation has been of interest in many scientific fields. The most commonly used operation for this purpose is a cross-correlation between two receivers that has been shown theoretically to lead, for example, to the coherent Green's function of a medium subjected to diffuse random fields. The time-averaged cross-correlation essentially builds up the coherent portion of the travelling waves between the two receivers by a constructive averaging process. This process has been shown to work in both closed and open systems [1-7]. Applications of passive reconstruction of the Green's function by cross-correlations of random fields has been demonstrated in ultrasonics including guided waves [1, 8-16], seismology [17-21], underwater acoustics [7, 22, 23], dynamic characterization of highway

bridges excited by street traffic [24, 25], of hydrofoils excited by flow-induced vibrations [26], and of buildings excited by ground shaking [27].

It is also known that the cross-correlation operator filters the reconstructed impulse response between the two receiving points by the source energy spectrum [4]. Snieder [5] explicitly remarks how the cross-correlation operator may not give the correct frequency dependence of the Green's function without correction for the energy spectrum. This problem was circumvented by Snieder and Safak [27] by replacing the cross-correlation operation with a deconvolution operation in a wave reverberant system (the Millikan Library in Pasadena, CA) with wave radiation losses into the ground, and subjected to ground shaking as the excitation. By deconvolving the acceleration responses between different floors of the building, the authors were able to reconstruct the inter-story transfer function without the effects of the ground excitation and without the effects of the building's coupling to the ground.

The elimination of the excitation source in passive transfer function reconstruction is clearly necessary in those cases where the excitation source is unknown and generally unstable, e.g. non-stationary and/or random. This is the case, for example, of the acoustic excitation of a rail track by the rolling wheels of a moving train. Structural inspection of rails for internal defect detection is a task that is typically carried out by ultrasonic tests performed by piezoelectric transducers hosted in fluid-filled wheels [28], known by the rail inspection community as Rolling Search Units (RSUs). The typical inspection is performed today by specialized vehicles (hi-railers) that travel at relatively low speeds (~30 mph maximum) compared to regular train traffic (~ 60 mph and above).

For several years, the authors have conducted research to improve the RSU approach for ultrasonic rail inspections by introducing non-contact excitation and sensing of the ultrasonic

waves in the rail steel [29-34]. The various systems developed previously, however, still relied on the traditional active-passive approach requiring the controlled excitation source. The present paper introduces a radically new approach of ultrasonic rail inspection. This new approach consists of passively reconstructing the impulse response of the rail at two points by deconvolving the responses of non-contact air-coupled receivers under excitations naturally caused in the rail by the rolling wheels of a moving train. Therefore the train wheels replace the controlled ultrasonic excitation of the rail by a transducer or the like. Passive reconstruction of the rail transfer function from acoustic noise was recently discussed using the cross-correlation operation in laboratory tests involving contact piezoelectric transducers [35]. For the present objective of enabling the passive rail inspection by using the wheel excitations (that are nonstationary and random), the need to eliminate the effect of the source leads to the use of the deconvolution operation instead. A first-generation prototype based on this passive inspection idea was field tested at the Transportation Technology Center (TTC) in Pueblo, CO at speeds of up to 80 mph, therefore at much higher speeds than what possible with conventional RSU inspection units.

The paper first presents a theoretical treatment of cross-correlation versus deconvolution as it applies to an open dynamic system excited by an unknown source. It then describes the passive-only, non-contact inspection prototype that was designed and built around this idea. It finally reports representative results from the first passive-only rail inspection tests conducted at TTC at speeds between 25 mph and 80 mph.

2.2 Theoretical Considerations: Cross-correlation versus Deconvolution

Let us consider the schematic of Fig. 2.1, showing a rail track dynamically excited by a rolling wheel *W,* and whose acoustic response is measured by two receivers at locations *A* and *B*.

Let us also assume that both receivers are only sensitive to waves propagating uni-directionally from left to right in Fig. 2.1 (this is the case of air-coupled acoustic sensors oriented at a specific Snell's law angle). The primary objective of this exercise is to isolate the transfer function of the test structure (the rail in the present application) between location A and location B, $G_{AB}(\omega)$, without the effect of the source excitation (the rolling wheel in the present application). If $G_{AB}(\omega)$ can be isolated, discontinuities in the rail (such as defects) can be detected as a change in the transfer function, similarly to a pitch-catch active-passive ultrasonic guided-wave approach [30-34].

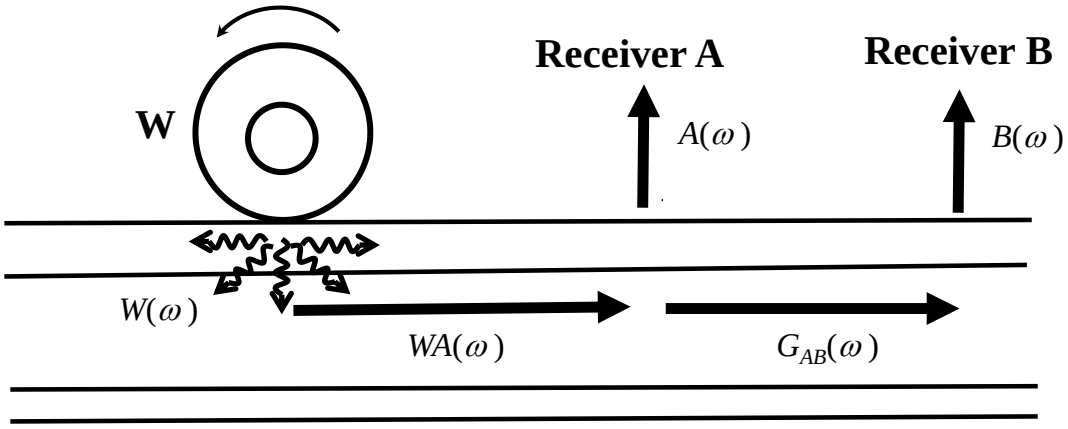

Figure 2.1: Schematic of passive reconstruction of transfer function

The problem is more easily formulated in the frequency domain. Assuming linearity, the response measured at *A* from the random wheel excitation, $V_A(\omega)$, is given by the convolution (product in the frequency domain) between the wheel excitation spectrum $W(\omega)$, the transfer function (Green's function) of the rail between the wheel and location A, $WA(\omega)$, and the frequency response of the receiving sensor, $A(\omega)$:

$$V_A(\omega) = W(\omega) \cdot WA(\omega) \cdot A(\omega) \qquad \textit{Response at A} \qquad (2.1)$$

where the symbol $\cdot$ means product.

The response measured at *B* will be similar to the above expression, with the addition of the transfer function (Green's function) of the rail between location *A* and location *B*, $G_{AB}(\omega)$, and considering (in general) a different frequency response for the receiving sensor, $B(\omega)$:

$$V_B(\omega) = W(\omega) \cdot WA(\omega) \cdot G_{AB}(\omega) \cdot B(\omega) \qquad \textit{Response at B} \tag{2.2}$$

Option 1- Cross-correlation operation

The frequency-domain cross-correlation between the responses at *A* and at *B*, $Xcorr_{AB}(\omega)$, yields the following result:

$$Xcorr_{AB}(\omega) = V_A^*(\omega) \cdot V_B(\omega) = W^*(\omega) \cdot WA^*(\omega) \cdot A^*(\omega) \cdot W(\omega) \cdot WA(\omega) \cdot G_{AB}(\omega) \cdot B(\omega) = \left|W(\omega)\right|^2 \cdot \left|WA(\omega)\right|^2 \cdot A^*(\omega) \cdot B(\omega) \cdot G_{AB}(\omega) \tag{2.3}$$

where the asterisk (*) means complex conjugate, and $|\ |$ indicates modulus. The terms $|\ |^2$ are auto-correlations, since $Autocorr(\omega) = F^*(\omega) \cdot F(\omega) = \left|F(\omega)\right|^2$, which physically correspond to the energy spectrum of the function.

If the two receivers have the same response $A(\omega) = B(\omega) = R(\omega)$, that is a reasonable assumption if the same receiver types are used, Eq. (2.3) simplifies to:

$$Xcorr_{AB}(\omega) = \left|W(\omega)\right|^2 \cdot \left|WA(\omega)\right|^2 \cdot \left|R(\omega)\right|^2 \cdot G_{AB}(\omega) \tag{2.4}$$

The above Eqs. (2.3) and (2.4) contain the desired impulse response of the rail between A and B, $G_{AB}(\omega)$, but "scaled" or "colored" by the energy spectra of (a) the wheel excitation, (b) the transfer function of the rail between the wheel excitation and receiver *A*, and (c) the receiver responses. In a test configuration where the inspection probe is moved along the rail, spectra (a) and (b) are generally expected to change, whereas spectra (c) are invariant. Since the inspection relies on

tracking changes to the rail transfer function alone, $G_{AB}(\omega)$, the effects of (a) and (b) need to be eliminated. That is why the cross-correlation operator is not a good metric for a passive inspection approach that relies on a varying excitation.

Option 2- Normalized Cross-correlation operation

Here we show that the autocorrelation of the responses from either A or B can be used as a suitable normalization factor to isolate the desired impulse response $G_{AB}(\omega)$. For example, normalizing the cross-correlation of Eq. (2.3) by the autocorrelation of receiver *A* yields:

$$NormXcorr_{AB}(\omega) = \frac{Xcorr_{AB}(\omega)}{Autocorr_{A}(\omega)} = \frac{|W(\omega)|^2 \cdot |WA(\omega)|^2 \cdot A^*(\omega) \cdot B(\omega) \cdot G_{AB}(\omega)}{|W(\omega)|^2 \cdot |WA(\omega)|^2 \cdot |A(\omega)|^2} = \frac{B(\omega)}{A(\omega)} G_{AB}(\omega) \tag{2.5}$$

resulting in the desired transfer function $G_{AB}(\omega)$, only scaled by the receivers' responses $A(\omega)$ and $B(\omega)$. Since the receivers do not change during the inspection, the ratio $B(\omega)/A(\omega)$ is just a constant scale factor that cannot cause false positive detections. If needed, $B(\omega)/A(\omega)$ could also be calibrated once for the particular receivers used and eliminated altogether from the test output. If the two receivers have the same response $A(\omega) = B(\omega) = R(\omega)$, Eq. (2.5) further simplifies to:

$$NormXcorr_{AB}(\omega) = \frac{Xcorr_{AB}(\omega)}{Autocorr_{A}(\omega)} = G_{AB}(\omega) \tag{2.6}$$

which is the perfect reconstruction of the impulse response of the test object. The cross-correlation of Eq. (2.3) can be also normalized by the autocorrelation of receiver B. In this case,

$$NormXcorr_{AB}(\omega) = \frac{Xcorr_{AB}(\omega)}{Autocorr_{B}(\omega)} = \frac{|W(\omega)|^2 \cdot |WA(\omega)|^2 \cdot A^*(\omega) \cdot B(\omega) \cdot G_{AB}(\omega)}{|W(\omega)|^2 \cdot |WA(\omega)|^2 \cdot |G_{AB}(\omega)|^2 \cdot |B(\omega)|^2} = \frac{A^*(\omega)}{B^*(\omega)} \frac{G_{AB}(\omega)}{|G_{AB}(\omega)|^2} \tag{2.7}$$

resulting in the impulse response, $G_{AB}(\omega)$, only scaled by its own energy spectrum $|G_{AB}(\omega)|^2$ and by the receivers' (conjugate) responses $A^*(\omega)$ and $B^*(\omega)$. Therefore, Eq. (2.7) is also a suitable metric for a passive inspection.

In summary, the cross-correlation between receiver *A* and receiver *B*, once normalized by the autocorrelation of either receiver (but not both simultaneously), provides a metric that is able to isolate changes in the test object's impulse response $G_{AB}(\omega)$ in a passive-only manner and without the influence of the variable excitation. Changes in $G_{AB}(\omega)$ can be then directly related to the presence of an internal flaw between *A* and *B* without any spurious effects that may cause false detections.

Option 3- Deconvolution operation

It is here demonstrated that the deconvolution operation yields results that are formally equivalent to the normalized cross-correlation discussed above. Deconvolving receiver *A* from receiver *B* yields:

$$Deconv_{BA}(\omega) = \frac{V_B(\omega)}{V_A(\omega)} = \frac{W(\omega)\cdot WA(\omega)\cdot G_{AB}(\omega)\cdot B(\omega)}{W(\omega)\cdot WA(\omega)\cdot A(\omega)} = \frac{B(\omega)}{A(\omega)} G_{AB}(\omega) \tag{2.8}$$

that is the test object's impulse response only scaled by the receiver responses (that do not change during a test). This result is identical to the normalized cross-correlation of Eq. (2.5). If the receivers have the same response, Eq. (2.8) further simplifies to:

$$Deconv_{BA}(\omega) = \frac{V_B(\omega)}{V_A(\omega)} = G_{AB}(\omega) \tag{2.9}$$

i.e. the "ideal" impulse response reconstruction.

Similarly, deconvolving receiver *B* from receiver *A* yields:

$$Deconv_{AB}(\omega) = \frac{V_A(\omega)}{V_B(\omega)} = \frac{W(\omega)\cdot WA(\omega)\cdot A(\omega)}{W(\omega)\cdot WA(\omega)\cdot G_{AB}(\omega)\cdot B(\omega)} = \frac{A(\omega)}{B(\omega)}\frac{1}{G_{AB}(\omega)} = \frac{A(\omega)}{B(\omega)}\frac{G^*_{AB}(\omega)}{\left|G_{AB}(\omega)\right|^2} \quad (2.10)$$

that is exactly the conjugate version of the normalized cross-correlation of Eq. (2.7), i.e. its time-reversed version. If the receivers have the same response, Eq. (2.10) simplifies to:

$$Deconv_{AB}(\omega) = \frac{V_A(\omega)}{V_B(\omega)} = \frac{G^*_{AB}(\omega)}{\left|G_{AB}(\omega)\right|^2} \quad (2.11)$$

i.e. the desired impulse response, only time-reversed and scaled by its own energy spectrum.

In summary, the deconvolution is a suitable operation for the inspection because it is able to isolate changes in the test object's impulse response $G_{AB}(\omega)$ in a passive-only manner without the influence of changing excitation spectrum and other spurious factors.

The time-domain impulse response function can be then retrieved from the frequency domain through an inverse Fourier Transform:

$$G_{AB}(t) = {}^{1}\!/_{2\pi} \int_{-\infty}^{\infty} G_{AB}(\omega)\, e^{i\omega t}\, d\omega \quad (2.12)$$

Physically, the ideal $G_{AB}(t)$ corresponds to the response of the test object (rail) at location B from an impulse excitation at A. It will therefore contain both standing waves (at low frequency values) and travelling waves (at high frequency values). In practice, however, the passively-reconstructed version of this Green's function will retrieve usable data only within the frequency spectrum of the excitation and that of the receivers' response. As long as this transfer function is stable along a test run, it will enable robust defect detection. In other words, only the reconstruction of a *stable* transfer function between two points of the structure (not necessarily the retrieval of the ideal Green's function) is the sufficient condition for successful passive structural inspection. A similar

argument of passive reconstruction of an "imperfect" Green's function has been, for example, presented in studies of structural monitoring of a highway bridge by cross-correlation of directional traffic-induced acoustic sources [25].

2.3 Averaging to Increase the Signal-to-Noise Ratio of the Passive Reconstruction

The impulse response G_{AB} emerges from the constructive interference of wave modes continuously excited by the random (wheel) excitation and propagating in the rail along the line connecting the two receivers. Furthermore, the rail structure at hand is practically a one-dimensional waveguide, where the random wave fields travel along one direction that is also the direction of alignment of the receiver pairs. This is a desirable feature, since studies of cross-correlations of multi-directional diffuse acoustic fields [5, 22, 36] have demonstrated that the transfer function is mostly reconstructed by wave fields aligned with the receivers.

The constructive interference process under continuous excitation clearly benefits from signal averaging in time. Following a known result in cross-correlation of diffuse fields [5, 22, 25, 36], the rate of convergence (Signal-to-Noise Ratio - SNR) of this kind of process can be written as:

$$SNR \propto \sqrt{T\,\Delta f}\, e^{-\alpha D} \tag{2.13}$$

where T is the length of the recording time window, Δf is the source bandwidth, α is the linear attenuation coefficient in the test material (in dB/m), and D is the distance between the two receivers.

Experimentally, the SNR can be determined by the peak amplitude of the reconstructed impulse response in the time domain, $G_{AB}(t)$, divided by the standard deviation of the total reconstructed signal taken away from the expected arrival time ("noise"):

$$SNR = \frac{Max(G_{AB}(t))}{Std(G_{AB}(t))} \tag{2.14}$$

The directivity beam consideration of Refs. [22, 36] do not apply to the rate of convergence in the case at hand since all sources are in the "end-fire" direction of the receiving array. Similarly, geometrical spreading effects included in Ref. [22] can be neglected in a unidirectional waveguide. Of primary importance from Eq. (2.13) is the fact that long recording time windows (besides large bandwidths) help with the emergence of the passively-reconstructed transfer function.

An additional requirement in the application at hand, where both excitation and reception are moving along the test piece (in-motion scanning test), is the stationarity of the reconstructed transfer function that can only be ideally guaranteed for a fixed position of the test object (rail). Therefore, a compromise must be found between the long recording times required by the averaging process and the stationarity (or spatial localization) of the transfer function reconstruction. The test speed clearly affects this compromise, since higher speeds will have to result in shorter recording times to maintain sufficient spatial localization. The topic of the recording time window will be further discussed with the experimental results presented in Section 2.4.3.

2.4 Application to High-Speed Inspection of Rails

The next sections describe a system developed on the idea of passive reconstruction of the impulse response from deconvolution operations applied to high-speed inspection of rails. When a train is in motion, the rotating wheels produce continuous dynamic excitations of the rail, in a

way that is sometimes treated as an array of point sources at the rail/wheel interface [37]. Such excitation is also randomized and made generally nonstationary by the unevenness and irregularities of the wheel and rail surfaces [38], as well as acceleration and braking actions. The challenge is therefore to extract a transfer function of the rail that is not affected by the variability of this type of excitation.

2.4.1 Passive-only Rail Inspection Prototype

A prototype based on these ideas was designed, constructed and field tested at TTC in Pueblo, CO, the largest facility for railroad transportation research testing in the US. The US Federal Railroad Administration (FRA) DOTX-216 test car was used to host the prototype (Fig. 2.2a). The sensing head was mounted on a beam that was rigidly connected to the front axle of the car (Fig. 2.2b and 2.2c). The sensing head consisted of two arrays of capacitive air-coupled receivers positioned at a minimum lift-off of 3-in from the rail's top surface. This lift-off guaranteed true non-contact probing of the rail. The receivers were narrowband devices centered at three different frequency bands. All results shown in this paper were obtained from receivers centered at 120 kHz. This was a reasonable frequency to examine for inspection purposes, since ultrasonic guided waves in rails are known to offer good sensitivity to defects in the range of 20 kHz - 500 kHz [31- 34, 39-44]. The separation between two sensors in a pair was ~ 18 in (~ 45 cm). As shown in Fig. 2.2b, the receivers were opportunely inclined from the rail surface to best capture the leaky surface waves propagating in the railhead according to Snell's law, in a similar manner utilized by the authors in previous air-coupled rail inspection systems with active excitation [30-34]. The receivers' orientation also effectively provided a directional sensing of the waves excited by wheels located to only one side of the arrays (front end), with virtually no sensitivity to waves propagating in the opposite direction (as from reflections or excited from

wheels located to the other side of the arrays – back end). The array lay-out was such that up to four independent pairs of 120 kHz sensors could be utilized concurrently to increase the rate of convergence of the passively extracted transfer function G_{AB}.

The signal acquisition from the air-coupled receivers was accomplished by a National Instruments (NI) PXI unit running LabVIEW Real-time to guarantee deterministic processing. The data unit also recorded a tachometer TTL pulse, that marked the spatial position of the test car with a resolution as small as 1" (2.54 cm), and a high-speed camera (SONY ICX-424 with a 6mm C-mount lens) with appropriate illumination (30k Lumens LED flood light) that recorded videos of the rail during each run. The purpose of the camera was to verify the presence of visible discontinuities in the rail, i.e. joints and welds, when the prototype detected an anomaly.

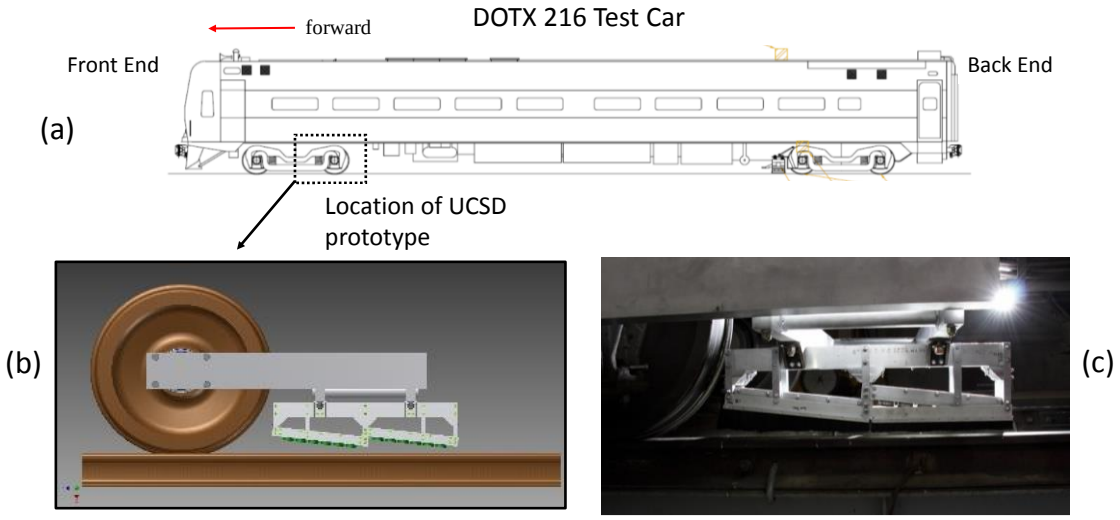

Figure 2.2: The passive inspection prototype for the first field tests at the Transportation Technology Center. (a) The FRA DOTX-216 test car. (b) and (c) The prototype's sensing head with non-contact air-coupled receivers

2.4.2 Test Lay-out and Procedure

Test runs were made at both TTC's Railroad Test Track (RTT) that allowed maximum test speeds of 80 mph, and at TTC's Rail Defect Test Facility (RDTF) that allowed maximum test speeds of 25 mph. A locomotive was used to tow the DOTX-216 car instrumented with the passive-

only prototype. The tested lengths depended on test speed and were about 18,000 ft for the RTT and about 2,000 ft for the RDTF at the highest speeds.

The runs at the RTT were conducted between markers R42 and R25 (see Fig. 2.3a). As shown in the figure, this test zone featured a tangent track in the middle, with curved tracks at the beginning and at the end. As many as three joints and seven welds were identified in the RTT test zone through visual survey and the high-speed camera (a snapshot of a joint from the camera is shown in Fig. 2.3a). Runs at the RTT test track were conducted at the speeds of 10 mph to 80 mph (max speed allowed) in 10 mph increments. This was the first time, to the authors' knowledge, that an ultrasonic inspection system was tested in motion on a rail at speeds larger than ~ 30 mph.

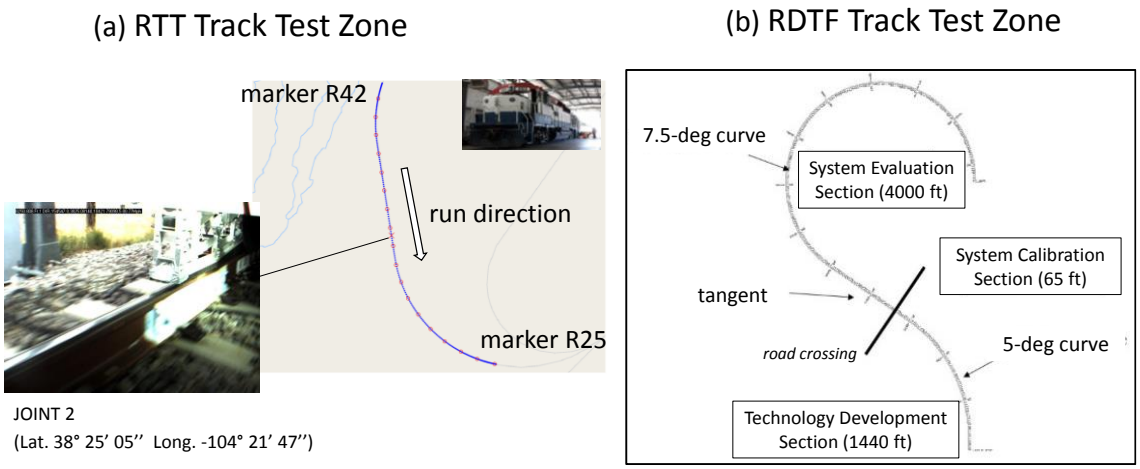

Figure 2.3: Rail tracks used for the field test at TTC. (a) The Railroad Test Track (RTT). (b) The Rail Defect Test Facility (RDTF)

In addition to the high-speed tests at the RTT, some test runs were conducted at the RDTF at speeds of 25 mph (max speed allowed). Specifically, these runs were conducted at the Technology Development Section of the RDTF facility (Fig. 2.3b), a mostly curved track with several known defects. The authors were quite familiar with the RDTF facility, since it was the test site for the earlier active-passive research prototypes [30-34]. This was the first time that ultrasonic defect detection in the RDTF track was attempted in a passive-only manner.

2.4.3 Data Processing and Proof-of-Concept Transfer Function Reconstruction

The data processing steps implemented in the prototype are schematized in Fig. 2.4.

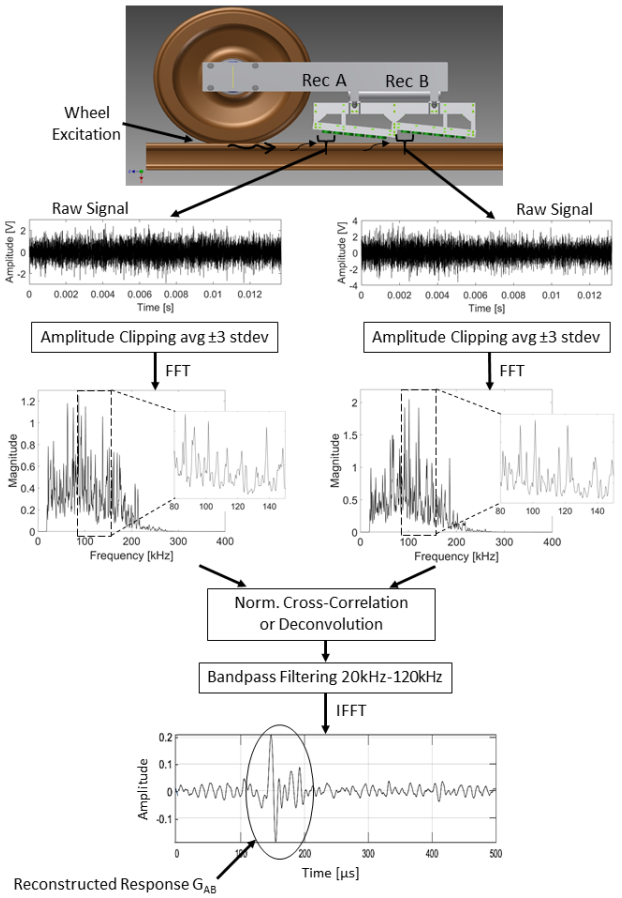

Figure 2.4: Signal processing steps for the passive reconstruction of the transfer function

For each run, recordings from the pairs of air-coupled receivers at locations *A* and *B* under the continuous wheel excitation were first amplitude clipped to within the average +/- 3 standard deviations. This is a common step also taken in cross-correlation of diffuse fields to prevent isolated spikes to contribute disproportionally to the passive reconstruction of the impulse response. The signals were then processed by the deconvolution operation of Eqs. (2.8) and (2.9). The time-domain transfer function between *A* and *B*, $G_{AB}(t)$, was finally obtained by averaging

over four sensor pairs the frequency-domain $G_{AB}(\omega)$ after bandpass filtering and inverse Fourier Transform of Eq. (2.12).

Figure 2.5(a) shows a representative recording from one of the receivers in the RTT track at 60 mph. This trace shows a high signal strength variability which is expected from the random wheel/rail contact conditions (surface unevenness, acceleration, braking, etc..). The result of the deconvolution between two receivers is shown in Fig. 2.5(b) for two different snapshots of the raw recording that correspond, respectively, to a "quiet" zone and to a "loud" zone. The loud zone is caused by rail unevenness, flanging of the wheels, or other conditions that exacerbate the wheel-rail contact. The deconvolved signal of Fig. 2.5(b) shows the clear arrival of a wave mode at about 140 μsec, that is the expected travel time of the leaky surface wave in the rail between the two receiver locations. As discussed in Section 2.2, the emergence of this wave arrival results from the constructive interference of the multiple wheel-generated waves that creates the coherent wavefront. The two plots in Fig. 2.5(b) also show that the reconstructed wavefront arrival at 140 μsec is very similar for both the "quiet" zone and the "loud" zone. This confirms the ability to reconstruct a stable coherent arrival independently of the instantaneous strength of the wheel excitation source.

Fig. 2.5(c) compares the wave arrival reconstructed in a pristine section of the rail to one reconstructed near a joint location in the same RTT track. The 140 μsec arrival for the joint location shows a substantial drop in amplitude as a result of the wave scattering from the discontinuity.

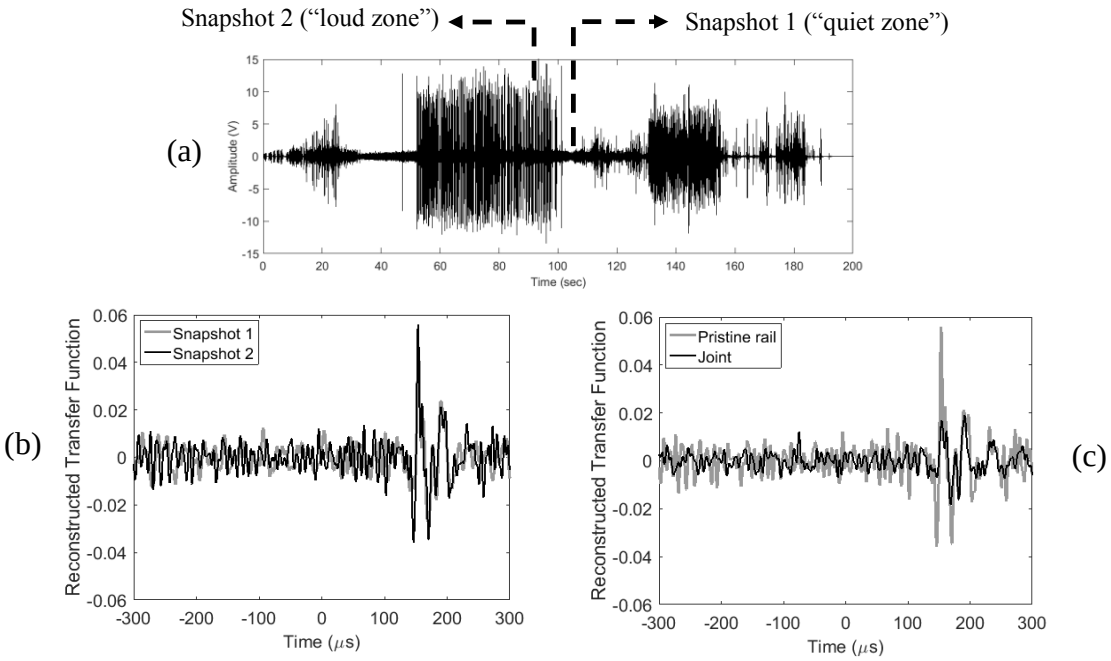

Figure 2.5: (a) Representative recording (raw data) of wheel-generated acoustics in the RTT track at 60 mph. (b) Passively reconstructed signals from a "loud zone" (snapshot 2) and from a "quite zone" (snapshot 1). (c) Passively reconstructed signals from a pristine rail location and near a joint

Since internal rail flaws also act as wave scatterers, the potential exists for this passive-only approach to be used for rail flaw detection.

It was discussed in Section 2.3 how the rate of convergence of the passively reconstructed transfer function (or equivalently its SNR) is expected to increase with increasing recording time lengths according to Eq. (2.13). It was also discussed how, for the application at hand involving a scanning inspection, an additional constraint is the spatial localization of the transfer function that is being reconstructed. This second constraint imposes an upper limit to the length of the recording time window that also depends on test speed, with higher speeds requiring shorter time windows for spatial localization. Accordingly, a study was conducted to determine the time window length that resulted in a good compromise between SNR of the prototype's reconstructed transfer function and spatial localization in the rail. Fig. 2.6 plots the SNR of the reconstructed transfer function at the 140 μsec arrival, calculated from Eq. (2.14), for various recording time

lengths and for three runs on the RTT track at the speeds of 30 mph, 50 mph and 80 mph. The three curves end at different times since shorter time windows are required for higher speeds as discussed above. The first observation from the plots in Fig. 2.6 is the confirmation that the SNR generally increases with increasing recording time. However, the rate of increase is seen to drop for the longest recording times considered, due to the loss of spatial localization in the rail and consequent non-stationarity of the reconstructed transfer function. The figure also shows that the SNR generally decreases with increasing test speed, as a result of the increased standard deviation of the incoherent portion of the wheel-generated excitation. The time window durations that correspond to a spatial localization in the rail to within 8 in (20.3 cm) are marked by stars for each of the three speeds. These points correspond to a SNR of ~12 at 30 mph, ~9 at 50 mph and ~4.5 at 80 mph. These values were chosen as the final recording time windows to provide an acceptable compromise between achievable SNR and spatial localization. This choice also effectively meant that the prototype "averaged" the transfer function of the rail over an 8 in (20.3 cm) "gage length".

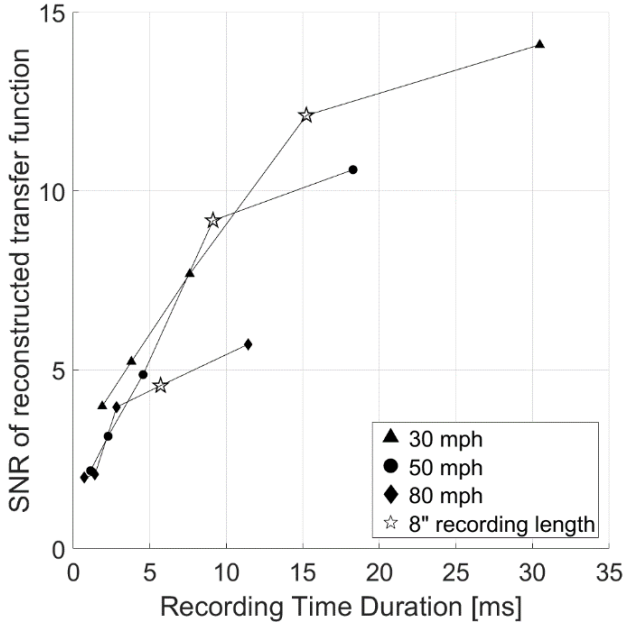

Figure 2.6: Signal-to-Noise Ratio of passively-reconstructed transfer function for increasing recording times from runs on the RTT track at 30 mph, 50 mph and 80 mph. Star symbols correspond to an 8 in (20.3 cm) spatial gage length

The final signal processing step that was implemented in the prototype was an outlier analysis to compute a statistically robust metric (herein referred to as "Damage Index") related to the strength of the reconstructed transfer function. A similar statistical analysis was implemented in the previous active-passive versions of the rail inspection systems developed by the authors [30-34], and it does not need to be described here in detail. In summary, the Damage Index (*D.I.*) was calculated as the Mahalanobis Squared Distance [45, 46] defined in a multivariate sense:

$$D.I. = (x - \bar{x})^T \cdot Cov^{-1} \cdot (x - \bar{x}) \tag{2.15}$$

where x is the feature vector extracted from the passively-reconstructed transfer function, $\bar{x}$ is the mean vector of the baseline distribution, Cov is the covariance matrix of the baseline distribution, and *T* represents transposed. The feature vector contained the following three metrics: maximum amplitude, root mean square and variance of the reconstructed transfer function. The statistical computation of the *D.I.* normalizes the data by the normal (baseline) data variability that occurs during a run. As such, compared to a simple deterministic metric, the *D.I.* of Eq. (2.15) dramatically increases the probability of detection and decreases the probability of false alarms of this kind of inspection, as amply shown in the aforementioned prior works. Moreover, the baseline distribution of the reconstructed signal features in the prototype was collected adaptively at each position along the rail and considering the preceding 350 ft (107 m) of rail. Finally, an "exclusive" [45] version of the baseline was adopted, whereby extreme values of the *D.I.* (i.e. values larger than mean + twice the standard deviation) were removed from the baseline computation. This removal ensured that only pristine portions of rail were considered in the baseline computation.

2.4.4 Results from TTC's Railroad Test Track (RTT)

The runs at the RTT were conducted between markers R42 and R25 at the speeds of 10 mph to 80 mph in 10 mph increments. Figures 2.7 and 2.8 show representative results of the D.I. computed from the multivariate outlier analysis of the passively-reconstructed transfer function for five runs at different test speeds, according to the process described in Section 2.4.3. The distance covered by each run depended on the intended target speed, with longer distances needed to reach the higher speeds at "steady state." The distances covered for each of the runs are schematized in the top drawings of Figs. 2.7 and 2.8. The peaks in the *D.I.* traces labeled as "Joint #" and "Weld #" were confirmed by either information provided by TTC staff or by images collected by the video camera at those specific locations.

Figure 2.7 reports the results from a 30-mph run and from a 50-mph run. At 30 mph, Fig. 2.7a, the plot shows a remarkably clear detection of two joints (Joint 2 and Joint 3) and two welds (Weld 4 and Weld 5), with flat noise floor with low risk of false positive detections in the clean part of the rail. It can also be noticed that the trace does not appear degraded when moving from the tangent portion of the track to the curved portion (after position ~4500 ft in Fig. 2.7a). The result for 50 mph, Fig. 2.7b, shows a similarly clear trace, confirming the detection of Joint 2 and Weld 4 of the 30-mph run, and showing additional true detections (Weld 1, Weld 2 and Weld 3) in the additional distance covered. The fact that Weld 3 was detected at 50 mph but not at 30 mph suggests that the lower speeds may be less desirable than the higher speed. This is an interesting result possibly associated to the fact that slower rotational speeds of the wheels have difficulty generating higher acoustic frequencies that were monitored by the first version of the prototype. Additional discussion on the role of test speed is provided in Section 2.5 - Discussion and Conclusions. The few small peaks that are also visible, but not marked by a label (e.g. the peak at position ~4,400 ft in Fig. 2.7b) could be caused by an unknown discontinuity in the track (e.g. a

weld or internal defect) or by a false positive detection. Further investigations (e.g. an independently conducted detailed survey of the track such as a conventional ultrasonic inspection with RSU rolling probes) would be needed to determine the true nature of these "unaccounted" peaks. Overall, Fig. 2.7 shows good promise for the possibility to (a) extract a stable transfer function of the rail in a passive-only manner by exploiting the natural wheel excitations, and (b) process the passively-reconstructed transfer function to detect rail discontinuities in a statistically robust manner. This is especially interesting since no previous attempt exists, to the authors' knowledge, to ultrasonically inspect a rail at speeds higher than ~30 mph.

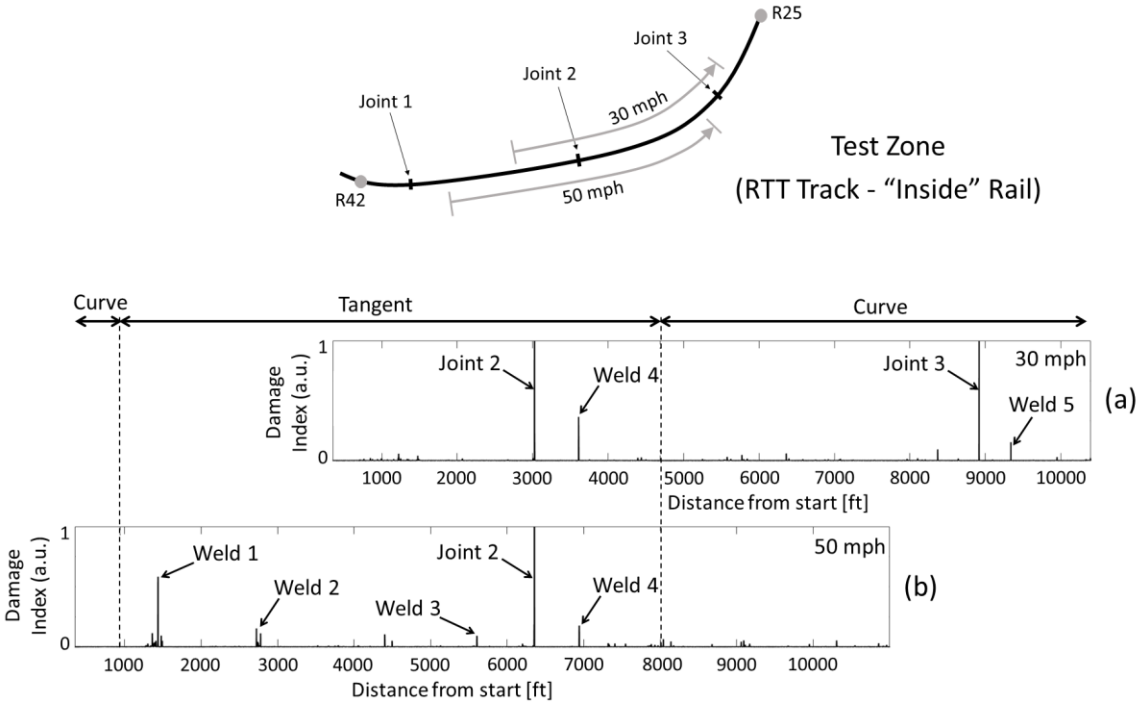

Figure 2.7: Representative results from the passive inspection of the RTT track at (a) 30 mph and (b) 50 mph

Figure 2.8 reports the results of a 60-mph run, a 70-mph run, and an 80-mph run. The 60-mph run, Fig. 2.8a, continues to show a very clear detection of true discontinuities (Joint 2, Joint 3, Weld 2 and Weld 3). The clean portions of the rail continue to show a nearly flat noise floor and, therefore, small risk of false positive detections. As discussed above, the few peaks seen beyond the labeled

discontinuities could be due to undetected true discontinuities or to false detections, with further investigations needed to clarify this question. The 70-mph trace in Fig. 2.8b confirms all true detections of the 60-mph run, with additional true detections seen in the additional portion of rail covered (Joint 1, Weld 7). The noise floor at 70 mph is slightly raised compared to the lower speeds, likely a result of the increased mechanical vibrations (e.g. sensor misalignment) caused by the very high speed. For example, railroad contractors assisting with the field tests indicated that the accelerations expected at the car axle or below the car primary suspension at high speeds can be as high as 30 g (rms) in the vertical direction (during sustained operation) and 100 g (rms) in all directions (during shocks). Clearly, these operational conditions should be considered extremely severe for a "typical" operation of an air-coupled ultrasonic receiver. Nevertheless, remarkably, all of the three confirmed Joints and the seven confirmed Welds in the test track are actually detected at the 70-mph speed. A similar result is provided by the 80-mph trace in Fig. 2.8c, where all of the confirmed discontinuities remain detected with the exception of Weld 5. This is a quite remarkable result considering, again, the potential difficulties associated with attempting to operate an inspection system mounted to the axle of a train car running at 80 mph.

2.4.5 Results from TTC's Rail Defect Test Facility (RDTF)

While the main focus of the TTC field tests was to test the stability of the transfer function's passive reconstruction at sustained speeds, the instrumented DOTX-216 car was moved to the Technology Development Zone of the RDTF track for a preliminary test on defect detection potential. The RDTF contains various known rail flaws.

Figure 2.9 shows traces from a run conducted at the maximum allowed speed of 25 mph, zoomed-in for three different zones of the track, and all consisting of a curved lay-out. Zone 1 in Fig. 2.9a, from left to right, shows the clear detections of a Joint, a "Crushed Head" defect and a

Weld. Zone 2 in Fig. 2.9b shows the detections of a “Shelling” defect, a “Transverse Defect” simulated by a saw cut and extending for 20% of the rail Head Area (H.A.), a Joint, a “Detail Fracture” defect extending for 7% of the rail H.A., and a second Joint. The peak at position ~5,116 ft prior to the first Joint could be due to an unmapped rail condition, or it could be a false positive. Zone 3 in Fig. 2.9c shows the detection of a “Detailed Fracture” defect extending for 20% of the rail H.A., a Joint, a 20% H.A. “Transverse Fissure” defect, and another Joint. The peak at position ~5,242 ft is not accounted for.

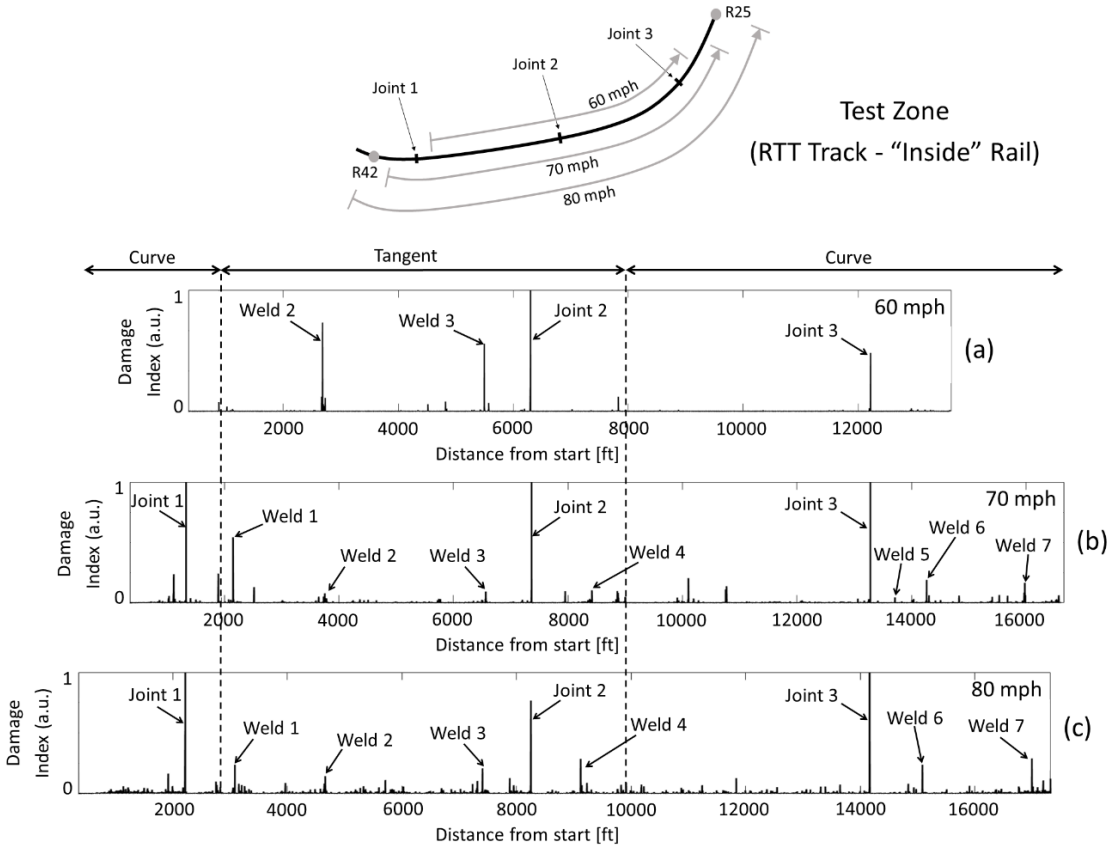

Figure 2.8: Representative results from the passive inspection of the RTT track at (a) 60 mph, (b) 70 mph, and (c) 80 mph

Overall, the results in Fig. 2.9 show the potential for detecting relevant rail flaws by the passive approach. The fact that 25 mph was the maximum speed permitted on the RDTF track did not allow study of the defect detection performance at sustained speeds. Since the approach relies

on wheel generated noise as the acoustic excitation of the rail, both signal strength and signal frequency bandwidth are expected to increase with increasing wheel rotational speed. Therefore, it is possible that the speed of 25 mph will require the monitoring of lower frequencies for optimum rail inspection performance, and additional field tests are being planned to confirm this hypothesis.

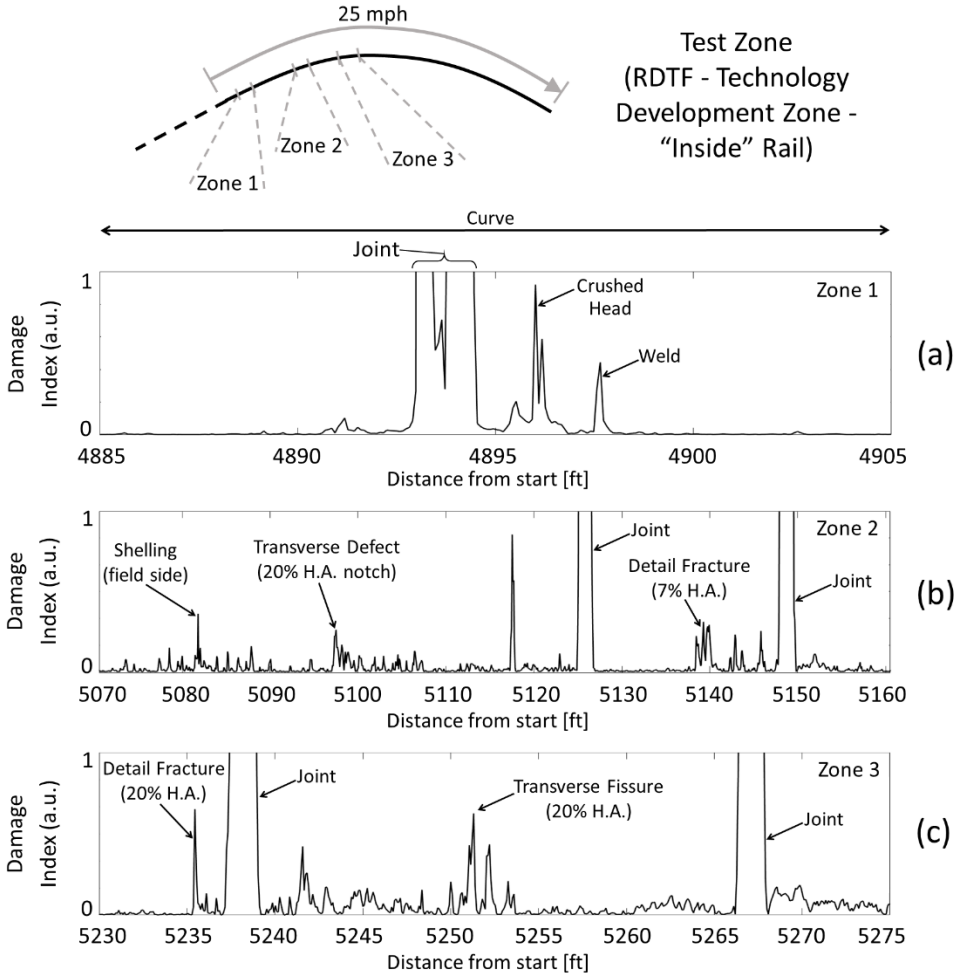

Figure 2.9: Representative results from the passive inspection of the RDTF Defect Farm at 25 mph in three different test zones

2.5 Discussion and Conclusions

The general research topic addressed in this paper is the passive-only extraction of an acoustic transfer function between two receiving points of a linear system subjected to a continuous dynamic excitation that is arbitrary and generally non-stationary. The specific

application of this topic considered here is the ultrasonic inspection of railroad tracks by exploiting the natural excitations provided by the rotating wheels of a running train. This implementation would enable to perform rail inspections at speeds that are unthinkable by current RSU ultrasonic search units that can conventionally test rails at a maximum speed of ~ 30 mph. Moreover, the ability to inspect the rail at regular traffic speed would enable individual trains to perform the testing without any traffic disruptions while guarantying an unprecedented level of inspection redundancy (since multiple trains run several times on the same track). This increased redundancy would lead to increased probability of defect detection and reduced probability of false alarms.

Several researchers have established the passive reconstruction of a transfer function (Green's function) of a system subjected to random acoustic fields from time-averaged cross-correlations of measurements at two receiving points. However, cross-correlation (or a normalized version of it where the autocorrelations of both receivers are used as the normalization factor) results in a Green's function that is affected by the energy spectrum of the excitation. This problem would make it impossible to inspect a system subjected to a highly variable excitation (such as the nonstationary wheel excitation of a rail). Utilizing the convolution theorem, the paper shows that a deconvolution operator (or, equivalently, a cross-correlation operator normalized by only one of the receivers but not both) is theoretically able to isolate the Green's function passively without the influence of the excitation source spectrum. While the theoretical development provided in the paper examines an open system with directional receivers (which applies to the case study of wheel excitations of a rail probed by air-coupled ultrasonic receivers), the deconvolution operation was previously shown to provide this important result also in reverberating systems with reflecting boundaries [27]. It is also important to highlight that a sufficient condition for an effective structural inspection is not to reconstruct the "ideal" Green's function of the test object, but rather

to reconstruct a *stable* transfer function of the object, i.e. one that is invariant during the scanning of a defect-free region of the object.

The length of the recording time window for the deconvolution operation is an important factor in the application at hand. Since the receivers are moving relative to the test object (rail), a compromise must be identified between the long recording times necessary for the emergence of the transfer function by the constructive interference of the random excitations, and the short times required for the spatial localization of the reconstructed transfer function. The paper identifies a suitable time duration that is able to provide a satisfactory signal-to-noise ratio of the reconstructed transfer function at varying test speeds.

A first-generation prototype for the passive-only inspection of rails was designed, constructed and mounted on the DOTX-216 test car for field tests at the Transportation Technology Center in Pueblo, CO. The prototype utilizes pairs of capacitive air-coupled ultrasonic receivers for truly non-contact probing of the rail. An outlier analysis statistical processing applied to the reconstructed transfer function helped to increase the detection of true rail discontinuities and decrease the detection of false alarms. The prototype was tested on the RTT track of TTC at speeds as high as 80 mph, where no ultrasonic inspection system for rails has ever been tested – to the authors' knowledge. The results show that the potential indeed exists to reconstruct stable transfer functions of the rail at these speeds, despite the variability of the wheel excitations, and consequently detect rail discontinuities such as joints and welds. For example, the run at 70 mph detected all of the three known joints and the seven known welds. The run at 80 mph also successfully detected most of the known discontinuities with the exception of one missed weld.

Limited tests were also conducted on the RDTF defect farm of TTC, where much lower speeds were allowed. Preliminary analysis of a run at 25 mph on the RDTF indicated the potential

for the system to detect rail defects such as Crushed Heads, Detail Fractures and Transverse Fissures. Clearly, for a true assessment of defect detection performance, the trade-off between probability of detection and probability of false alarms will have to be quantitatively determined. One way to do this is to generate Receiver Operating Characteristic (ROC) curves on a well mapped rail track. This step will be part of a second field test that is being planned for the second-generation prototype with a focus on defect detection performance.

The important role of test speed on the inspection performance of the passive system has not been fully characterized. Since the technique proposed relies on wheel generated excitations, both strength and bandwidth of the reconstructed transfer function are expected to increase with increasing wheel rotational speed. This consideration would suggest that different frequency bands may have to be optimally tracked in a way that is adaptive to the current test speed. Several design options to implement this bandwidth adaptability are being considered for the second-generation prototype.

Another relevant factor is the lay-out of the track, specifically a tangent track versus a curved track. For example, on a curved track the wheels will flange differently for different speeds depending on whether the train is above or below the "balance" speed for that curve. Different wheel flanging conditions will clearly change the strength and bandwidth of the excitation source. While the proposed signal processing is theoretically able to eliminate the source from the transfer function reconstruction, its signal-to-noise ratio (or rate of emergence) will likely be affected by the source bandwidth. The second-generation prototype is being designed to further increase the opportunities for signal averaging by exploiting multiple time snapshots for the same receiver pair. Increasing the averaged samples will improve the rate of convergence of the reconstructed signal and thereby further stabilize the performance in curves regardless of train speed.

An additional aspect that is being improved in the second-generation prototype is the "co-location" of the separate receiver pairs that are averaged together. The physical dimensions of the receivers utilized in the first–generation system resulted in a spatial offset that was not optimal to ensure spatial localization of the transfer function.

A final open question is the role of rail lubrication on the passive inspection idea. The tests reported in the paper did not provide an opportunity to examine this factor (no lubrication was applied in addition to the lubrication that may have been already present on the rail at the time of the tests). Clearly, different lubrication conditions will change the wheel-rail contact. Additional studies will be needed to shine light on this question.

Acknowledgements

Team members at UCSD Albert Liang, Margherita Capriotti, and Xuan "Peter" Zhu collaborated with this research. Several individuals and organizations were instrumental for the preparation and the conduction of the field test at the Transportation Technology Center. They include: FRA Program Manager Dr. Robert Wilson and Chief of the Track Research Division in the FRA Office of Research, Development and Technology Gary Carr for technical advice and project oversight; Eric Sherrock and Jeff Meunier of ENSCO for field test support; FRA on-site representatives Jay Baillargeon and Luis Maal for field test observation; TTCI Program Manager Dr. Dingqing Li for field test logistics and support.

This project was funded by the U.S. Federal Railroad Administration under grant FR-RRD-0027-11-01, with former Program Manager Mr. Mahmood Fateh and current Program Manager Dr. Robert Wilson.

Chapter 2 is, in full, a reprint of material published in F. Lanza di Scalea, X. Zhu, M. Capriotti, A. Y. Liang, S. Mariani, S. Sternini, "Passive Extraction of Dynamic Transfer Function

From Arbitrary Ambient Excitations: Application to High-Speed Rail Inspection From Wheel-Generated Waves," *ASME Journal of Nondestructive Evaluation, Diagnostics, and Prognostics of Engineering Systems*, vol. 1, no. 1, pp. 011005-011005-12, 2017. The dissertation author was the primary investigator and author of this paper.

References

[1] Lokbis, O.I., and Weaver, R.L., 2001, "On the Emergence of the Green's Function in the Correlations of a Diffuse Field," J. Acoust. Soc. Am., 110(6), pp. 3011-3017. DOI: http://dx.doi.org/10.1121/1.1417528

[2] Roux, P., and Fink, M., 2003, "Green's function estimation using secondary sources in a shallow water environment," J. Acoust. Soc. Am., 113(3), pp. 1406-1416. DOI: http://dx.doi.org/10.1121/1.1542645

[3] Derode, A., Larose, E., Tanter, M., de Rosny, J., Tourin, A., Campillo, M., and Fink, M., 2003, "Recovering the Green's function from field-field correlations in an open scattering medium," J. Acoust. Soc. Am., 113(6), pp. 2973-2976. DOI: http://dx.doi.org/10.1121/1.1570436

[4] Weaver, R.L., and Lokbis, O.I., 2004, "Diffuse Fields in Open Systems and the Emergence of the Green's Function (L)," J. Acoust. Soc. Am., 116(5), pp. 2731-2734. DOI: http://dx.doi.org/10.1121/1.1810232

[5] Snieder, R., 2004, "Extracting the Green's function from the correlation of coda waves: a derivation based on stationary phase," Phys. Rev. Lett. E, 69, pp. 0466101-0466108. DOI: https://doi.org/10.1103/PhysRevE.69.046610

[6] Roux, P., Sabra, K.G., Kuperman, W., and Roux, A., 2005, "Ambient noise cross correlation in free space: theoretical approach," J. Acoust. Soc. Am., 117(1), pp. 79–84. DOI: 10.1121/1.1830673

[7] Sabra, K.G., Roux, P. and Kuperman, W.A., 2005, "Emergence rate of the time domain Green's function from the ambient noise cross correlation," J. Acoust. Soc. Am., 118(6), pp. 3524-3531. DOI: http://dx.doi.org/10.1121/1.2109059

[8] Michaels, J.E., and Michaels, T.E., 2005, "Detection of structural damage from the local temporal coherence of diffuse ultrasonic signals," IEEE Trans. Ultras. Ferr. Freq. Contr., 52(10), pp. 1769-1782. DOI: 10.1109/TUFFC.2005.1561631

[9] Larose, E., Lobkis, O.I., and Weaver, R.L., 2006, "Passive correlation imaging of a buried scatterer," J. Acoust. Soc. Am. 119(6), pp. 3549-3552. DOI: http://dx.doi.org/10.1121/1.2200049

[10] Van Wijk, K., 2006, "On estimating the impulse response between receivers in a controlled ultrasonic model," Geophysics, 71(4), pp. SI79-SI84. DOI: 10.1190/1.2215360

[11] Sabra, K., Srivastava, A., Lanza di Scalea, F., Bartoli, I., Rizzo, P., and Conti, S., 2008, "Structural health monitoring by extraction of coherent guided waves from diffuse fields," J. Acoust. Soc. Am., 123(1), pp. EL8-EL13. DOI: http://dx.doi.org/10.1121/1.2820800

[12] Tippmann, J. D., and Lanza di Scalea, F., 2016, "Passive-Only Defect Detection and Imaging in Composites Using Diffuse Fields," Mechanics of Composite and Multi-Functional Materials, Vol. 7, Springer International Publishing, Cham, Switzerland, pp. 67–72.

[13] Tippmann, J. and Lanza di Scalea, F., 2015, "Passive-only damage detection by reciprocity of Green's functions reconstructed from diffuse acoustic fields with application to wind turbine blades," J. Intell. Mater. Syst. Struct., 26(10), pp. 1251-1258. DOI: 10.1177/1045389X14538539

[14] Tippmann, J., Zhu, X., and Lanza di Scalea, F., 2015, "Application of damage detection methods using passive reconstruction of impulse response functions," Phil. Trans. R. Soc. A., 373(2035), pp. 1-17. DOI: 10.1098/rsta.2014.0070

[15] Duroux, A., Sabra, K. G., Ayers, J., Ruzzene, M., 2010, "Extracting guided waves from cross-correlations of elastic diffuse fields: applications to remote structural health monitoring," J. Acoust. Soc. Am., 127(1), pp. 204-215. DOI: 10.1121/1.3257602

[16] Chehami, L., De Rosny, J., Prada, C., Moulin, E., and Assaad, J., 2015, "Experimental study of passive defect localization in plates using ambient noise," IEEE Trans. Ultras. Ferr. Freq. Contr., 62(8), pp.1544-1553. DOI: 10.1109/TUFFC.2014.006935

[17] Campillo, M., and Paul, A., 2003, "Long-range correlations in the diffuse seismic coda," Science, 299(5606), pp. 547-549. DOI: 10.1126/science.1078551

[18] Roux, P., Sabra, K.G., Gerstoft, P., Kuperman, W.A., and Fehler, M.C., 2005, "P-waves from cross-correlation of seismic noise," Geoph. Res. Lett., 32(19), pp. L193031- L193034. DOI: 10.1029/2005GL023803

[19] Shapiro, N.M., Campillo, M., Stehly L., and Ritzwoller, M., 2005, "High resolution surface-wave tomography from ambient seismic noise," Science, 307(5715), pp. 1615–1617. DOI: 10.1126/science.1108339

[20] Sabra, K.G., Gerstoft, P., Roux, P., Kuperman, W.A., and Fehler, M.C., 2005, "Extracting time-domain Green's function estimates from ambient noise," Geophys. Res. Lett., 32(3), pp. L033101- L033106. DOI: 10.1029/2004GL021862

[21] Sabra, K.G., Gerstoft, P., Roux, P., Kuperman, W.A. and Fehler, M.C., 2005, "Surface wave tomography from microseisms in Southern California," Geophys. Res. Lett., 32(14), pp. L14311. DOI: 10.1029/2005GL023155

[22] Roux, P., Kuperman, W.A. and the NPAL Group, 2004, "Extracting coherent wave fronts from acoustic ambient noise in the ocean," J. Acoust. Soc. Am., 116(4), pp. 1995-2003. DOI: http://dx.doi.org/10.1121/1.1797754

[23] Sabra, K.G., Roux, P. and Kuperman, W.A., 2005, "Arrival-time structure of the time-averaged ambient noise cross-correlation function in an oceanic waveguide," J. Acoust. Soc. of Am., 117(1), pp. 164-174. DOI: http://dx.doi.org/10.1121/1.1835507

[24] Farrar, C. and James, G., 1997, "System identification from ambient vibration measurements on a bridge," J. Sound Vib., 205(1), pp. 1-18. DOI: https://doi.org/10.1006/jsvi.1997.0977

[25] Salvermoser, J., and Hadziioannou, C., 2015, "Structural monitoring of a highway bridge using passive noise recordings from street traffic," J. Acoust. Soc. of Am., 138(6), pp. 3864-3872. DOI: http://dx.doi.org/10.1121/1.4937765

[26] Sabra, K.G., Winkel, E.S., Bourgoyne, D.A., Elbing, B.R., Ceccio, S.L., Perlin, M., and Dowling, D.R., 2007, "Using cross-correlation of turbulent flow-induced ambient vibrations to estimate the structural impulse response. application to structural health monitoring," J. Acoust. Soc. of Am., 121(4), pp. 1987-1995. DOI: http://dx.doi.org/10.1121/1.2710463

[27] Snieder, R., and Safak, E., 2006, "Extracting the building response using seismic interferometry: theory and application to the Millikan Library in Pasadena, California," Bull. Seis. Soc. Am., 96(2), pp. 586-598. DOI: 10.1785/0120050109

[28] Lanza di Scalea, F., 2007, "Ultrasonic Testing Applications in the Railroad Industry," Non-destructive Testing Handbook, 3rd edition, P.O. Moore, ed., American Society for Nondestructive Testing, Columbus, OH, pp. 535-552.

[29] McNamara, J. and Lanza di Scalea, F., 2002, "Air-coupled ultrasonic testing of railroad rails," Materials Evaluation, 60(12), pp. 1431-1437.

[30] Coccia, S., Phillips, R., Bartoli, I., Salamone, S., Lanza di Scalea, F., Fateh, M., and Carr, G., 2011 "UCSD/FRA non-contact ultrasonic guided wave system for rail inspection: an update," Journal of the Transportation Research Board, Transportation Research Record, 2261, pp. 143-147.

[31] Coccia, S., Bartoli, I., Marzani, A., Lanza di Scalea, F., Salamone, S. and Fateh, M., 2011, "Numerical and experimental study of guided waves for detection of rail head defects," NDT&E Int. 44(1), pp. 93-100. DOI: https://doi.org/10.1016/j.ndteint.2010.09.011

[32] Mariani, S., Nguyen, T., Phillips, R., Kijanka, P., Lanza di Scalea, F., Staszewski, W., Fateh, M. and Carr, G., 2013, "Non-contact air-coupled ultrasonic guided wave inspection of rails,"

Structural Health Monitoring International Journal, Special Issue on Noncontact Measurement Technologies, 12(5-6), pp. 539-548. DOI: 10.1177/1475921713498533

[33] Mariani, S. and Lanza di Scalea, F., 2018, "Predictions of defect detection performance of air-coupled ultrasonic rail inspection system," Structural Health Monitoring International Journal, 17(3), pp. 684–705.

[34] Mariani, S., Nguyen, T., Zhu, X. and Lanza di Scalea, F., 2016, "Field test performance of non-contact ultrasonic rail inspection system," ASCE Journal of Transportation Engineering, Part A: Systems, 143(5), pp. 040170071-0401700714. DOI: http://dx.doi.org/10.1061/JTEPBS.0000026

[35] Sadoudi, L., Moulin, E., Assaad, J., Benmeddour, F., Bocquet, M., and El Hillali, Y., 2016, "Experimental study of acoustic noise correlation technique for passive monitoring of rails," Mat. Sci. Appl., 7(12), pp. 848-862. DOI: 10.4236/msa.2016.712065

[36] Woolfe, K.F., and Sabra, K.G., 2015, "Variability of the coherent arrivals extracted from low-frequency deep-ocean ambient noise correlations," J. Acoust. Soc. Am., 138(2), pp. 521-532. DOI: http://dx.doi.org/10.1121/1.4923447

[37] Thompson, D. J. 1993. "Wheel-rail noise generation, Part I: Introduction and interaction model," J. Sound Vib., 161(3), pp. 387-400. DOI: https://doi.org/10.1006/jsvi.1993.1082

[38] Thompson, D.J., and Jones, C.J.C., 2000, "A review of the modelling of wheel/rail noise generation," J. Sound Vib., 231(3), pp. 519-536. DOI: https://doi.org/10.1006/jsvi.1999.2542

[39] Wilcox, P., Evans, M., Pavlakovic, B., Alleyne, D., Vine, K., Cawley, P., and Lowe, M., 2003, "Guided wave testing of rail," Insight, 45(6), pp. 413–420. DOI: https://doi.org/10.1784/insi.45.6.413.52892

[40] Cawley, P., Lowe, M. J. S., Alleyne, D. N., Pavlakovic, B., and P. Wilcox, 2003, "Practical long range guided wave testing: applications to pipes and rail," Materials Evaluation, 61(1), pp. 66–74.

[41] Hesse, D., and Cawley, P., 2006, "Surface wave modes in rails," J. Acoust. Soc. Am., 120(2), pp. 733–740. DOI: http://dx.doi.org/10.1121/1.2211587

[42] Rose, J. L., Avioli, M. J., Mudge, P. and Sanderson, R., 2004, "Guided wave inspection potential of defects in rail," NDT&E Int., 37(2), pp. 153–161. DOI: https://doi.org/10.1016/j.ndteint.2003.04.001

[43] Rose, J. L., Avioli, M. J. and Song, W.J., 2002, "Application and potential of guided wave rail inspection," Insight, 44(6), pp. 353–358.

[44] Bartoli, I., Lanza di Scalea, F. Fateh, M., and Viola, E., 2005, "Modeling guided wave propagation with application to the long-range defect detection in railroad tracks," NDT&E Int., 38(5), pp. 325–334. DOI: https://doi.org/10.1016/j.ndteint.2004.10.008

[45] Worden, K., Manson, G., Fieller, N.R.J., 2000, "Damage detection using outlier analysis," J. Sound Vib., 229(3), pp. 647–667. DOI: https://doi.org/10.1006/jsvi.1999.2514

[46] Worden, K., Sohn, H., Farrar, C.R., 2002, "Novelty detection in a changing environment: regression and interpolation approaches," J. Sound Vib., 258(4), pp. 741–761. DOI: https://doi.org/10.1006/jsvi.2002.5148

Chapter 3

Robust passive reconstruction of dynamic transfer function in dual-output systems

Abstract

The focus of this paper is the estimation of the dynamic transfer function between two outputs of a linear system subjected to an uncontrolled, and generally unknown excitation, and accounting for possible uncorrelated noise present at both outputs. Several applications of this case exist in the passive identification of dynamic systems including the health monitoring and/or non-destructive evaluation of structures subjected to natural "ambient" excitations. It is well known that noise-robust transfer function estimation of a single-input-single-output system can be achieved by a normalized cross-power spectrum operation. The paper shows that, for the subject case of a dual-output system, particular caution must be placed in the choice of the normalization factor to apply to the cross-power spectrum of the two outputs. In particular, an "inter-segment" averaging method is proposed for the normalization factor in combination with the classical "intra-segment" averaging of the cross-power spectrum in order to estimate the transfer function between the two outputs without the influence of the excitation spectrum and of the uncorrelated noise at

the two receivers. Validating results are presented for synthetic signals and for experimental signals from an application to high-speed ultrasonic rail inspection exploiting the train wheels as the "ambient" excitation.

3.1 Introduction

The reconstruction of the dynamic transfer function, $H(f)$, of a system that is excited by a source input and monitored at one or more outputs is of great interest for several applications, including signal channel characterization, dynamic characterization of various media, structural modal analysis, structural monitoring and structural inspections. A realistic scenario is that of added noise at the output(s) that is uncorrelated with itself and with the source input. In the case of a linear Single-Input-Single-Output (SISO) system, Roth [1] showed that a simple deconvolution of the excitation input from the output does not isolate the system's $H(f)$ because it retains the noise power spectrum that is added to the output. He circumvented this problem based on the fact that the cross-power spectrum of zero-mean uncorrelated signals tends to zero in an ensemble average sense. Accordingly, noise cancellation for transfer function estimation in a SISO system can be achieved by an averaged cross-power spectrum between the source excitation and the output, normalized by an averaged auto-power spectrum of the source. Roth [1] and other authors [2, 3] also showed that an analogous operation can be performed to minimize noise in the estimation of the magnitude-squared coherence function of dynamic SISO systems. The averaging is most often performed in the time domain by segmenting the signals' time histories. The time domain averaging is exactly equivalent to the ensemble averaging if the process is ergodic [3]. A classical window (e.g. Hamming) is usually applied to the time segments prior to performing Fourier Transforms for the computation of the cross-power and the auto-power spectra. The time averaging process to eliminate uncorrelated noise has been formalized by well-known algorithms

such as the Weighted Overlapped-Segment Averaging (WOSA) technique also known as Welch's method [4]. Welch's method utilizes overlapped segments to retain the information in the tails that are cut out by the windowing application. A 50% segment overlap is generally considered effective [3]. Regardless of the specific averaging process, this method of transfer function estimation in SISO systems requires the knowledge of the excitation source spectrum.

In many recent applications of dynamic testing and structural health monitoring, however, the interest is to extract the transfer function in a completely passive manner, exploiting excitations that are uncontrolled, non-stationary and generally unknown. This is the case of ambient excitations that are natural to the structure during operations (e.g. traffic excitation of a bridge [5, 6], seismic ground shaking of a building [7], aerodynamic fluctuations in aircraft and wind turbine blades [8, 9] and acoustic excitation of a rail track from train wheels [10]). A related research field, very popular in underwater acoustics [11-13], seismology [14-19], as well as ultrasonic structural inspections [20-28], is the passive extraction of the system's time-domain Green's function $G_{AB}(t)$ in the presence of random "diffuse" acoustic or ultrasonic fields. In all of these cases, the typical scenario is to utilize at least two receivers that can measure the output at two points of the structure, A and B, with the goal to reconstruct the $H_{AB}(f)$ (or, equivalently, the $G_{AB}(t)$ in the time domain). This is a case, therefore, of a dual-output system. The most popular operation to achieve passive transfer function reconstruction in these dual-output systems is a time-averaged cross-correlation of the outputs at the two receivers. The cross-correlation operation, however, retains the source excitation spectrum, that of course can cause problems if the source is nonstationary or random. Snieder and Safak [7] and Snieder [19] showed that a deconvolution operation between the two receivers can successfully eliminate the source spectrum and isolate the "pure" transfer function of the structure. The deconvolution operation was recently applied to the passive-only ultrasonic

structural inspection of rails from natural train wheel excitations with the goal of achieving high-speed test capabilities (80 mph and beyond) that are not permitted by conventional rail inspection methods (limited to ~25- 30 mph max) [10].

However, these previous studies on the dual-output methods for passive transfer function reconstruction did not consider the presence of uncorrelated noise that may be added to the two outputs. This paper addresses this situation and proposes a way to minimize the noise in the estimation of the transfer function. In particular, it is shown that the simple analogy to the SISO system (i.e. the normalized averaged cross-power spectrum [1]) does not lead to a robust estimation in a dual-output counterpart because it does not eliminate the noise power spectrum at one of the receivers. The problem is that the normalization factor used for SISO is an auto-power spectrum computed *on the same averaging segments* of the signal (herein referred to as "*intra-segment*" averaging). The paper shows that noise minimization can be obtained by utilizing a normalization factor that computes the cross-power spectrum between *pairs of different segments* (herein referred to as *"inter-segment"* averaging). Besides increasing the total number of averages using n segments to $n!/(2(n-2)!)$ averages (against $(2n-1)$ averages with a 50% overlap for the classical "intra-segment" averaging), the inter-segment operation effectively eliminates the uncorrelated noise at the output, in addition to eliminating the excitation power spectrum from the final transfer function estimation. The proposed method also assumes that the excitation and the transfer function are stationary during the observation time window (piecewise-stationary). In many practical applications, the observation time windows can be made sufficiently short such that this requirement is easily satisfied. The paper explores these concepts analytically, and it presents validation results from both simulated signals and experimental signals.

It was discussed how one potential application of this study is high-speed ultrasonic rail inspection. Current rail inspections are conducted at a maximum speed of ~ 25-30 mph by specialized vehicles operating ultrasonic transducers hosted in fluid-filled wheels that roll over the rail top surface (Rolling Search Units – RSUs) [29]. UCSD is working under sponsorship by the US Federal Railroad Administration (FRA) to develop a new inspection approach for rails that can be carried out at regular train speeds (~80 mph and possibly beyond). An ability to test rails at high speed would radically change rail inspection practices because it would allow individual trains to perform the tests with minimal traffic disruption and great opportunity for redundancy given the multiple train passes on the same rail track. Dual-output ultrasonic monitoring of wheel-generated excitations offers the potential to achieve such high tests speeds. Local changes in the passively-extracted transfer function of the rail can be related to the presence of a discontinuity (joint, weld or internal flaw) similarly to what already established in active ultrasonic rail testing [29-33]. The final experimental case study presented here demonstrates the effectiveness of the "inter-segment" averaging operation over other operations in the passive rail inspection approach under realistic test conditions at 60 mph.

3.2 Robust Transfer Function Reconstruction in Single Output System

A SISO system is schematized in the block diagram of Fig. 3.1, with excitation spectrum $E(f)$, transfer function $H(f)$, and output spectrum $O(f)$. Let us also assume that the system is linear and piecewise-stationary, meaning that the statistics of the excitation $E(f)$ do not change during the observation time window of $O(f)$. The excitation spectrum is also assumed to be known. Let us also assume that a noise component with spectrum $N(f)$ is being added to the observation. This noise is uncorrelated with the excitation and can come from a variety of sources in practical transfer

function estimation tests. The goal is to estimate the system's transfer function $H(f)$ with minimum effect from the noise $N(f)$.

A simple deconvolution of the excitation from the output will of course retain the noise contribution in the estimation of $H(f)$:

$$Deconv = \frac{O(f)}{E(f)} = \frac{E(f)\cdot H(f) + N(f)}{E(f)} = H(f) + \frac{N(f)}{E(f)} \tag{3.1}$$

Hence this operation is not ideal if the noise content is substantial. The solution in this case is to compute an "averaged" cross-power spectrum between the output and the excitation (cross-correlation in the time domain), normalized by an "averaged" auto-power spectrum of the excitation (autocorrelation in the time domain) [1]. This is based on the fact that the cross-power spectrum of two uncorrelated signals $S_1(f)$ and $S_2(f)$, each with zero DC component, tends to zero as an ensemble average. Hence:

$$\left\langle S_1^*(f)\cdot S_2(f)\right\rangle = 0 \quad \text{if } \left\langle S_1(t)\right\rangle = \left\langle S_2(t)\right\rangle = 0 \tag{3.2}$$

where * means complex conjugate and $\langle\ \rangle$ is ensemble average. The requirement for zero DC components is necessary for the ensemble to vanish from the destructive interference of the positive and negative uncorrelated realizations.

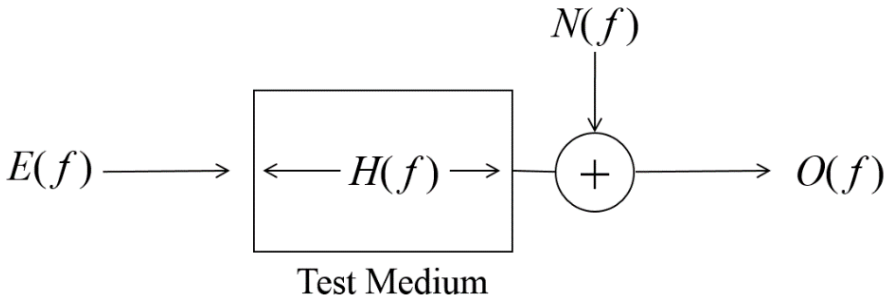

Figure 3.1: Schematic of SISO system for the estimation of H(f)

The ensemble averaged cross-power spectrum between the output and the excitation is:

$$\langle Cross\_Power \rangle = \langle E^*(f) \cdot O(f) \rangle = \langle E^*(f) \cdot E(f) \cdot H(f) \rangle + \langle E^*(f) \cdot N(f) \rangle = |E(f)|^2 \cdot H(f) \tag{3.3}$$

since the term $\langle E^*(f) \cdot N(f) \rangle$ vanishes for uncorrelated noise. The noise term is therefore eliminated from the estimation of the transfer function $H(f)$. The term $|E(f)|^2$ is the auto-power spectrum of the excitation that "scales" or "colors" the transfer function estimation.

Therefore, normalizing the averaged cross-power spectrum of (3.3) by the auto-power spectrum of the excitation isolates the system's transfer function $H(f)$ without the noise term:

$$\frac{\langle Cross\_Power \rangle}{\langle Auto\_Power \rangle} = \frac{\langle E^*(f) \cdot O(f) \rangle}{\langle E^*(f) \cdot E(f) \rangle} = \frac{|E(f)|^2 \cdot H(f)}{|E(f)|^2} = H(f) \tag{3.4}$$

Experimentally, is it impractical to record ensemble averages. *Time* averages are instead performed in practice, representing identical behavior if the random process is ergodic [3]. A practical way to perform time averages is to divide the time signals into multiple segments, compute the spectra for each segment, and then average over the various segments. If the signals are divided into n time segments, the normalized cross-power spectrum operation therefore becomes

$$\frac{\langle Cross\_Power \rangle}{\langle Auto\_Power \rangle} = \frac{\frac{1}{n} \sum_{i=1}^{n} E_i^*(f) \cdot O_i(f)}{\frac{1}{n} \sum_{i=1}^{n} E_i^*(f) \cdot E_i(f)} = H(f) \tag{3.5}$$

where the spectra are computed separately for each segment i. Common practice is to apply a window (e.g. Hamming) to each time segment before computing the spectra via Fourier Transforms. In order to avoid the loss of information at the edges of the segment, a 50% overlap can be used in analogy with coherence function estimations [2]. A 50% overlap with n segments

increases the total number of averages to (2*n*-1) terms.

It should be remarked that computation of (3.4) or (3.5) requires knowledge of the excitation signal $E(f)$.

Since each of the summation terms in the numerator and the denominator of (3.5) is computed *for the same segment i*, we will refer to this method as "*intra-segment averaging*." The reason for this specification will be clear in the next section.

3.3 Robust Transfer Function Reconstruction in Dual-Output System

The dual-output case is schematized in the diagram of Fig. 3.2. Of interest here is the passive estimation of the transfer function of the system between *A* and *B*, $H_{AB}(f)$. In structural monitoring applications, for example, knowledge of $H_{AB}(f)$ allows for the dynamic identification of the structure and/or the detection of potential damage between the two monitored locations *A* and *B*. The excitation $E(f)$ is not controlled or known, and it is assumed piecewise-stationary, meaning that its statistics do not change during the observation time windows of $O_A(f)$ and $O_B(f)$. Uncorrelated noise components $N_A(f)$ and $N_B(f)$ are also assumed to be present at each of the two outputs.

Assuming linearity, the two outputs can be expressed as:

$$O_A(f) = E(f) \cdot EA(f) + N_A(f) \quad receiver\ A \tag{3.6}$$

$$O_B(f) = E(f) \cdot EA(f) \cdot H_{AB}(f) + N_B(f) \quad receiver\ B \tag{3.7}$$

where $EA(f)$ is the transfer function of the system from the excitation to output *A*.

3.3.1 Normalized Cross-Power Spectrum with Intra-Segment Averaging

Let us consider what happens if one follows the same procedure outlined in the previous

section consisting of the cross-power spectrum normalized by the auto-power spectrum in an ensemble average sense. Using expressions (3.6) and (3.7), the ensemble averaged cross-power spectrum between the two outputs is:

$$\begin{aligned}\langle Cross\_Power\rangle &= \left\langle O_A^*(f)\cdot O_B(f)\right\rangle = \left\langle \left|E(f)\right|^2\cdot\left|EA(f)\right|^2\cdot H_{AB}(f)\right\rangle + \\ &\left\langle E^*(f)\cdot EA^*(f)\cdot N_B(f)\right\rangle + \left\langle E(f)\cdot EA(f)\cdot H_{AB}(f)\cdot N_A^*(f)\right\rangle + \\ &\left\langle N_A^*(f)\cdot N_B(f)\right\rangle = \left|E(f)\right|^2\cdot\left|EA(f)\right|^2\cdot H_{AB}(f)\end{aligned} \tag{3.8}$$

In (3.8), we use the fact that averaged cross-power spectra of uncorrelated signals (assumed with zero DC component) are zero. Consequently: $\left\langle E^*(f)\cdot EA^*(f)\cdot N_B(f)\right\rangle = 0$ because noise N_B is uncorrelated with either E or EA; $\left\langle E(f)\cdot EA(f)\cdot H_{AB}(f)\cdot N_A^*(f)\right\rangle = 0$ because noise N_A is uncorrelated with either E, EA or H_{AB}; and $\left\langle N_A^*(f)\cdot N_B(f)\right\rangle = 0$ because noise N_A is uncorrelated with noise N_B. In summary, the averaged cross-power spectrum of the two receiver outputs yields the desired transfer function $H_{AB}(f)$ but "scaled" or "colored" by the power spectrum of the excitation $\left|E(f)\right|^2$ and that of the transfer function between excitation and receiver A $\left|EA(f)\right|^2$. Importantly, this operation also eliminates the noise components in both output A and output B (N_A and N_B).

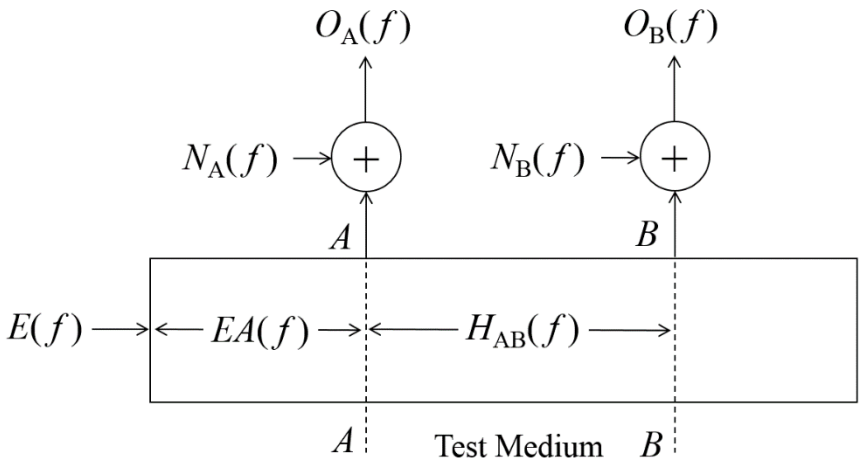

Figure 3.2: Schematic of dual-output system for the passive estimation of HAB(f)

Assuming ergodic processes, as discussed in the previous section, the ensemble average $\langle O_A^*(f)\cdot O_B(f)\rangle$ can be replaced by the more convenient time average. Using the classical "intra-segment averaging" of the previous section, time averaging for *n* segments yields:

$$\langle Cross\_Power\rangle = \frac{1}{n}\sum_{i=1}^{n} O_{A,i}^*(f)\cdot O_{B,i}(f) = |E(f)|^2\cdot|EA(f)|^2\cdot H_{AB}(f) \tag{3.9}$$

where the same segment *i* is used for each cross-power spectrum term in the summation. If a 50% overlap between segments is utilized, the summation is carried out for (2*n*-1) terms.

It is still quite necessary, however, to eliminate in (3.9) the effect of the excitation power spectrum $|E(f)|^2$, since it is here assumed uncontrolled and unknown. Using the auto-power spectrum of output *A* as the normalization factor in analogy with the previous section, yields:

$$\begin{aligned}\langle Auto\_Power\rangle &= \langle O_A^*(f)\cdot O_A(f)\rangle = \langle |E(f)|^2\cdot|EA(f)|^2\rangle + \\ &\langle E^*(f)\cdot EA^*(f)\cdot N_A(f)\rangle + \langle E(f)\cdot EA(f)\cdot N_A^*(f)\rangle + \\ &\langle N_A^*(f)\cdot N_A(f)\rangle = |E(f)|^2\cdot|EA(f)|^2 + |N_A(f)|^2\end{aligned} \tag{3.10}$$

This result shows that the auto-power spectrum, if computed by the classical "intra-segment averaging," still contains the power spectrum of the noise $|N_A(f)|^2$ because the auto-power spectrum of an uncorrelated signal does not vanish if it is taken in the same time segment. For example, for Gaussian white noise, $|N_A(f)|^2=\sigma^2$ i.e. the power spectrum is flat and assumes a value equal to the noise variance. Hence the intra-segment averaged normalized cross-power spectrum for the dual output case yields:

$$\frac{\langle Cross\_Power\rangle}{\langle Auto\_Power\rangle} = \frac{\frac{1}{n}\sum_{i=1}^{n} O_{A,i}^{*}(f)\cdot O_{B,i}(f)}{\frac{1}{n}\sum_{i=1}^{n} O_{A,i}^{*}(f)\cdot O_{A,i}(f)} = \frac{|E(f)|^2\cdot|EA(f)|^2\cdot H_{AB}(f)}{|E(f)|^2\cdot|EA(f)|^2+|N_A(f)|^2} \tag{3.11}$$

and the transfer function $H_{AB}(f)$ cannot be properly isolated because of the noise term $|N_A(f)|^2$.

3.3.2 Normalized Cross-Power Spectrum with Inter-Segment Averaging

A solution to this problem is to realize the fact that the noise $N_A(f)$ is assumed to be *uncorrelated* in time, and therefore the cross-power spectrum of the same signal *between different time segments* tends to zero in the ensemble average sense.

Therefore an *inter-segment* averaged auto-power spectrum can be formulated as the averaged cross-power spectrum of output *A* between two different time segments:

$$\begin{aligned}\langle Auto\_Power\rangle_{inter-segment} &= \frac{1}{\bar{n}}\sum_{i=1}^{n-1}\sum_{j=i+1}^{n} O_{A,i}^{*}(f)\cdot O_{A,j}(f) = \\ |E(f)|^2\cdot|EA(f)|^2 &+ \frac{1}{\bar{n}}\sum_{i,j} N_{A,i}^{*}(f)\cdot N_{A,j}(f) = |E(f)|^2\cdot|EA(f)|^2\end{aligned} \tag{3.12}$$

where $\bar{n} = {}^{n!}\!/_{2(n-2)!}$ is the number of the possible combinations of two different segments for a total of *n* segments. Segment overlapping may not be as beneficial in the inter-segment averaging since the same portions of the noise from different time realizations could be cross-correlated. The noise term N_A is thus eliminated because the cross-power spectrum of the uncorrelated signal performed between different segments *i* and *j*, $N_{A,i}^{*}(f)\cdot N_{A,j}(f)$, tends to zero on average. Strictly speaking, the above expression (3.12) is exact if the signals $E(f)$ and $EA(f)$ are correlated in both amplitude and phase among the different segments. In general, this is not the case, since the segmentation cannot take into account specific phase relations. Hence, a much more reasonable assumption is that $E(f)$ and $EA(f)$ between different segments are correlated in amplitude but not in phase. This

is true, for example, if the total observation window is small compared to the expected variation time of the excitation. In order to properly deal with this case, let us reformulate output *A* from (3.6) as:

$$O_A(f) = E(f) \cdot EA(f) + N_A(f) = S_A(f) + N_A(f) \tag{3.13}$$

where S_A contains the correlated signals recorded at *A* and N_A is the uncorrelated noise. Signal S_A is assumed to be time invariant during the observation window. Each inter-segment cross-power spectrum $S^*_{A,i}(f) \cdot S_{A,j}(f)$ will therefore have an amplitude that is consistent and a phase that is, instead, random. Analytically:

$$\begin{aligned} &\left\langle S^*_A(f) \cdot S_A(f) \right\rangle_{inter-segment} = \frac{1}{\bar{n}} \sum_{i=1}^{n-1} \sum_{j=i+1}^{n} S^*_{A,i}(f) \cdot S_{A,j}(f) = \\ &\frac{1}{\bar{n}} \sum_{i,j} \left| S_{A,i}(f) \right| e^{-i\phi_{A,i}} \left| S_{A,j}(f) \right| e^{i\phi_{A,j}} = \frac{1}{\bar{n}} \sum_{i,j} \left| S_{A,i}(f) \right| \left| S_{A,j}(f) \right| e^{i\Delta\phi_{A,ij}} \end{aligned} \tag{3.14}$$

One option that could be considered to minimize noise $N_A(f)$ in light of the randomness of the inter-segment phase differences $\Delta\phi_{A,ij}$ is taking the modulus of the cross-power spectra terms. Hence:

$$\left\langle \left| O^*_A(f) \cdot O_A(f) \right| \right\rangle_{inter-segment} = \frac{1}{\bar{n}} \sum_{i=1}^{n-1} \sum_{j=i+1}^{n} \left| O^*_{A,i}(f) \cdot O_{A,j}(f) \right| \tag{3.15}$$

However, expression (3.15) will still contain the noise term since taking the modulus produces a non-zero DC bias that prevents the inter-segment auto-power spectrum of uncorrelated noise to tend to zero after averaging.

The best option to minimize the uncorrelated noise terms by inter-segment averaging properly accounting for the phase decorrelation of the signal among the different segments is to

appropriately "shift" the signals in each segment so that they are forced to be in phase. This step is somewhat analogous to the "delay-and-sum" procedure of synthetic aperture focus in radar and ultrasonic imaging. If the signals in each segment are shifted in time such that their phases are aligned in all segments, phase correlation is enforced in addition to amplitude correlation. Since only the signal $S(t)$ is correlated within the observation window, while the noise $N(t)$ is uncorrelated, the appropriate time lag for each segment pair can be determined by the peak of the cross-correlation function between the two segments. Hence:

$$\tau_{ij} = \arg\max\left(\int_{-\infty}^{+\infty} O_{A,i}^{*}(t)\, O_{A,j}(t+\tau)\, dt\right) \tag{3.16}$$

The shifted version of the inter-segment auto-power spectrum then becomes:

$$\begin{aligned} \left\langle Auto-power \right\rangle_{\substack{inter-segment \\ shifted}} &= \frac{1}{\bar{n}} \sum_{i=1}^{n-1} \sum_{j=i+1}^{n} O_{A,i}^{*}(f) \cdot O_{A,j}(f)\, e^{-i2\pi f \tau_{ij}} \\ &= \left|S_A(f)\right|^2 + \frac{1}{\bar{n}} \sum_{i,\,j} N_{A,i}^{*}(f) \cdot N_{A,j}(f) = \\ &= \left|S_A(f)\right|^2 = \left|E(f)\right|^2 \left|EA(f)\right|^2 \end{aligned} \tag{3.17}$$

This procedure successfully eliminates the noise term since $\frac{1}{\bar{n}} \sum_{i,\,j} N_{A,i}^{*}(f) \cdot N_{A,j}(f) = 0$ for uncorrelated noise. Therefore, expression (3.17) is the final normalization term that needs to be applied to the averaged cross-power spectrum of (3.9) in the dual-output transfer function estimation problem:

$$\begin{aligned} \frac{\left\langle Cross\_Power \right\rangle_{intra-segment}}{\left\langle Auto\_Power \right\rangle_{\substack{inter-segment \\ shifted}}} &= \frac{\frac{1}{n} \sum_{i=1}^{n} O_{A,i}^{*}(f) \cdot O_{B,i}(f)}{\frac{1}{\bar{n}} \sum_{i=1}^{n-1} \sum_{j=i+1}^{n} O_{A,i}^{*}(f) \cdot O_{A,j}(f)\, e^{-i2\pi f \tau_{ij}}} = \\ \frac{\left|E(f)\right|^2 \cdot \left|EA(f)\right|^2 \cdot H_{AB}(f)}{\left|E(f)\right|^2 \cdot \left|EA(f)\right|^2} &= H_{AB}(f) \end{aligned} \tag{3.18}$$

In summary, the normalized cross-correlation spectrum computed according to (3.18) estimates passively the transfer function between two receivers *A* and *B* without influence/control of the excitation and without uncorrelated noise that may be added to either one of the two receivers. It is worth noting that that the quantities to be averaged in (3.18) are calculated for the same segments in the numerator (intra-segment cross-power spectrum), and for different segments in the denominator (inter-segment auto-power spectrum).

3.4 Validation

The primary conclusions derived in the previous section for the reconstruction of the transfer function in a dual-output system were validated by numerical and experimental results. Let us consider, again, a signal at receiver *A* composed of a correlated portion $S_A(f)$ and uncorrelated noise $N_A(f)$, i.e. $O_A(f) = S_A(f)+N_A(f)$. The following three options were derived in Section 3.3 for the normalization factor of the transfer function estimation.

Option 1- Intra-segment averaging:

$$\left\langle Auto\_Power \right\rangle_{\text{int}ra-segment} = \frac{1}{n}\sum_{i=1}^{n} O_{A,i}^{*}(f)\cdot O_{A,i}(f) = \left|S_A(f)\right|^2 + \left|N_A(f)\right|^2 \tag{3.19}$$

It was discussed how (3.19) is not an optimum normalization factor because it contains the power spectrum of the noise.

Option 2- Inter-segment averaging with modulus:

$$\left\langle Auto\_Power \right\rangle_{\substack{\text{int}er-segment \\ \text{mod}ulus}} = \frac{1}{\bar{n}}\sum_{i=1}^{n-1}\sum_{j=i+1}^{n}\left|O_{A,i}^{*}(f)\cdot O_{A,\text{j}}(f)\right| = \left|S_A(f)\right|^2 + k\left|N_A(f)\right|^2 \tag{3.20}$$

where $0 \le k \le 1$ is a factor that depends on how much of a specific noise signal is retained once the modulus negates the zero-DC requirement necessary for complete destructive interference. It

was discussed how (3.20) is also not an optimum normalization factor because it still contains a portion of the noise.

Option 3- Inter-segment averaging with shifting:

$$\left\langle Auto-power\right\rangle_{\substack{inter-segment\\shifted}} = \frac{1}{\bar{n}} \sum_{i=1}^{n-1} \sum_{j=i+1}^{n} O_{A,i}^{*}(f) \cdot O_{A,j}(f) e^{-i2\pi f \tau_{ij}} = \left|S_A(f)\right|^2 \tag{3.21}$$

where the time lag τ_{ij} is given from (3.16). It was discussed how (3.21) is a suitable operator in practical cases because it can isolate the signal power spectrum without the uncorrelated noise. The following case studies were performed to validate these conclusions. Most of these studies involve an SISO system because they are only concerned with testing the normalization factor proposed for the dual-output problem.

3.4.1 Synthetic Signals

The first case study was that of a 100 kHz synthetic sinusoid signal $S_A(t)$ embedded in white Gaussian noise $N_A(t)$ with power equal to 20 times that of the pure sinusoid (Fig. 3.3). The goal was to extract the power spectrum of the sinusoid signal at 100 kHz. For segmenting, the option of n=16 segments and n=64 segments were compared, corresponding to a total number of averages of 31 (16 segments) and 127 (64 segments) for the intra-segment procedure, and 120 (16 segments) and 2016 (64 segments) for the inter-segment procedure. A 50% overlap was used for the intra-segment procedure, and no overlap was used for the inter-segment procedure, as recommended in Section 3.3. The sampling frequency for these signals was 80 MHz. The time duration of each segment was 0.62 msec, resulting in a total time duration of 9.92 msec with 16 segments, and of 39.68 msec with 64 segments.

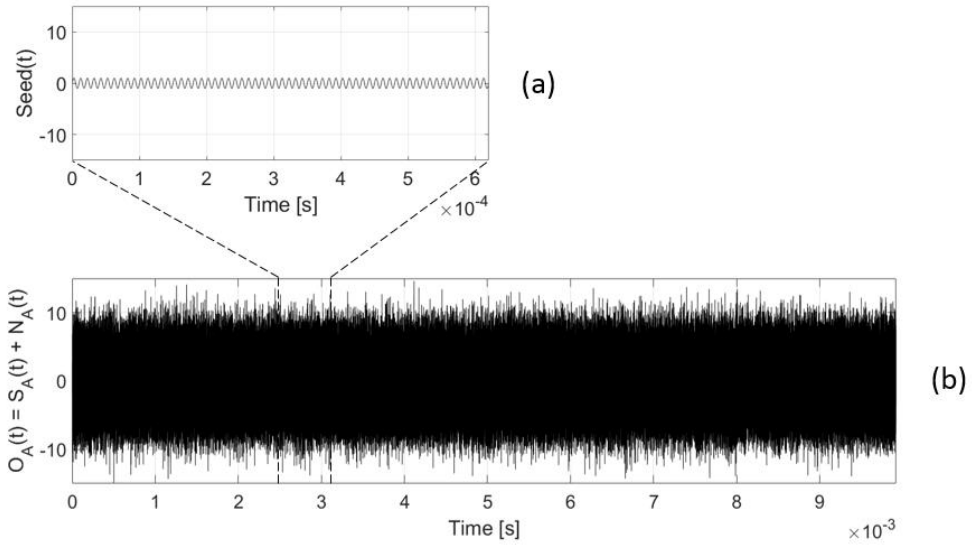

Figure 3.3: (a) Pure sinusoidal signal. (b) Sinusoidal signal with added white Gaussian noise (20 x power)

Fig. 3.4(a) shows the power spectra extracted from the total signal $O_A(t) = S_A(t) + N_A(t)$ of Fig. 3.3(b) using Options 1, 2, and 3 in (3.19), (3.20), and (3.21) when using 16 segments. In addition to the three options, an "ideal" case where the signal $S_A(f)$ is artificially correlated in phase among the different segments (hence no need for segment shifting) is shown for comparison. The metric of comparison for these results is the Signal-to-Noise Ratio (SNR) computed as the mean decibel value of the noise in the spectra provided (values around the 100 kHz peak). Fig. 3.4(a) clearly shows that Option 1 (intra-segment averaging) has the worst SNR, on the order of ~ 28.3 dB, as predicted by the theory. Option 1 also artificially broadens the signal peak at 100 kHz. This broadening is not caused by a specific window since all cases were Hamming windowed. Option 2 (inter-segment averaging with modulus) substantially sharpens the signal peak, but it brings only a slight improvement in SNR to ~ 30.7 dB, since it still contains a substantial amount of noise. The best result is obtained with Option 3 (inter-segment averaging with shifting) that maintains a sharp signal peak and achieves a SNR~ 39.2 dB. Furthermore, the performance of Option 3 is very close to that of the "ideal" case of perfect signal alignment, confirming that shifting by the maximum

cross-correlation lag effectively aligns the correlated portion of the signal and hence allows the averaging process to eliminate the noise components.

The results using 64 segments are shown in Fig. 3.4(b). This figure confirms Option 3 as

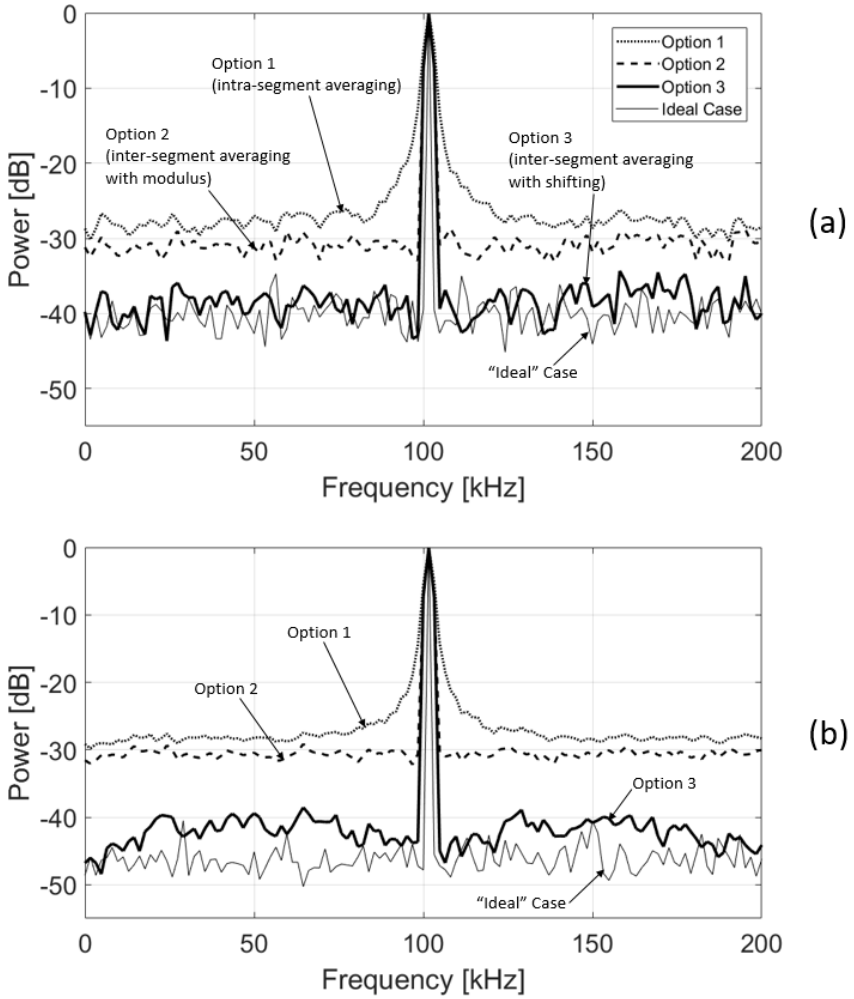

Figure 3.4: (a) Power spectra of sinusoidal signal with added noise extracted with intra-segment averaging (Option 1), inter-segment averaging with modulus (Option 2), inter-segment averaging with shifting (Option 3) and "ideal case" by using 16 segments. (b) Same as (a) by using 64 segments

the best option of the three. The figure also shows that only a marginal improvement in SNR is obtained by the increased number of averages (for Option 3, for example, SNR is ~ 44.8 dB with 64 segments against ~39.2 dB with 16 segments). While the specific improvement with increasing number of segments will obviously depend on the specific signals considered, the general encouraging conclusion is that a reasonable number of segments (e.g. 16) can be sufficient to

mitigate noise.

The second case study was that of a synthetic signal with a broad frequency range of 20 kHz – 50 kHz, with added white Gaussian noise (20x power) – Fig. 3.5. This signal was created by a chirped "seed" waveform, Fig. 3.5(a), corresponding to an individual time segment, that was then replicated with a randomized phase either 16 times or 64 times to create the entire signal $S_A(t)$. The total signal $O_A(t) = S_A(t) + N_A(t)$ for the 16-segment case is shown in Fig. 3.5(c). The sampling frequency for these signals was 80 MHz. The time duration of each segment was 0.62 msec, resulting in a total time duration of 9.92 msec with 16 segments, and of 39.68 msec with 64 segments.

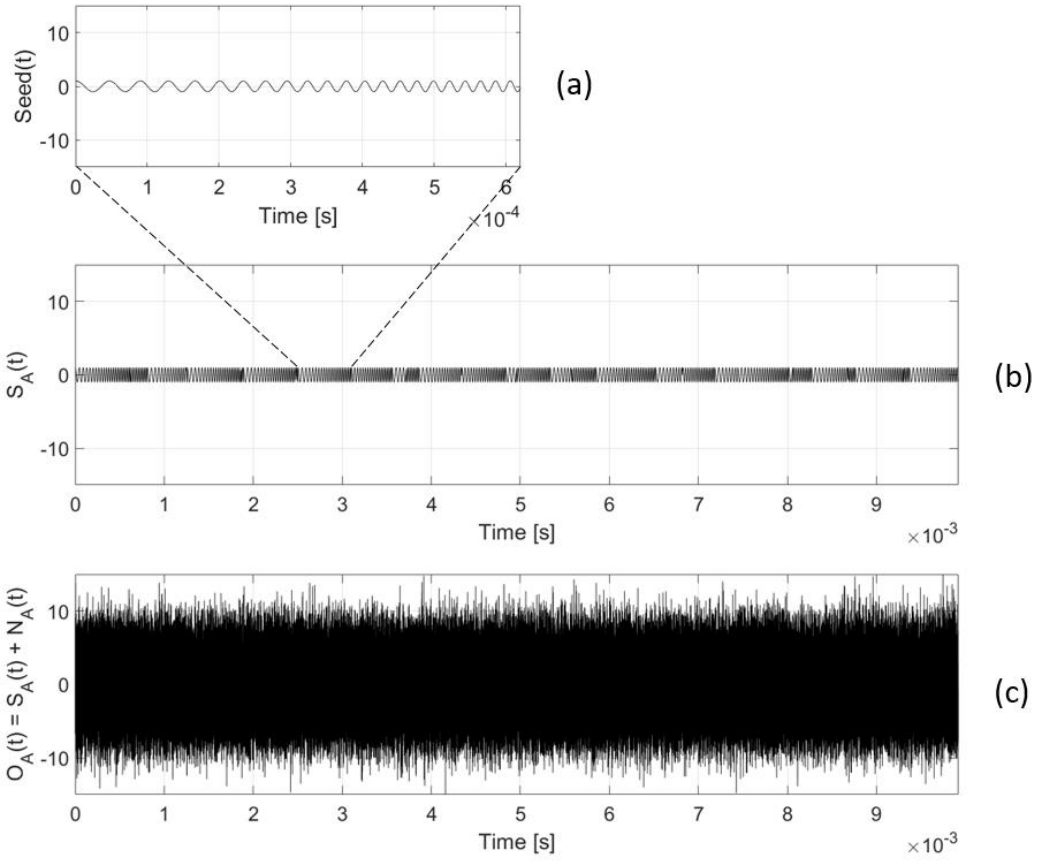

Figure 3.5: (a) "Seed" chirped signal. (b) Pure chirped signal. (c) Chirped signal with added white Gaussian noise (20x power)

Fig. 3.6 plots the signal spectra obtained with the three Options considered above, along with the "ideal" case of signal artificially correlated in phase among the different segments. The results for 16 segments are plotted in Fig. 3.6(a), that confirms Option 3 (inter-segment averaging with shifting) having the best performance with SNR ~ 29.3 compared to ~19.9 for Option 2 (inter-segment averaging with modulus) and ~19.2 for Option 1 (intra-segment averaging). Also, the Option 3 spectrum is virtually equivalent to the "ideal" spectrum. The 64-segment case, Fig. 3.6(b) confirms a slight improvement in SNR for Option 3 (~34.8 compared to ~29.3) in line with what found for the previous sinusoidal signal case.

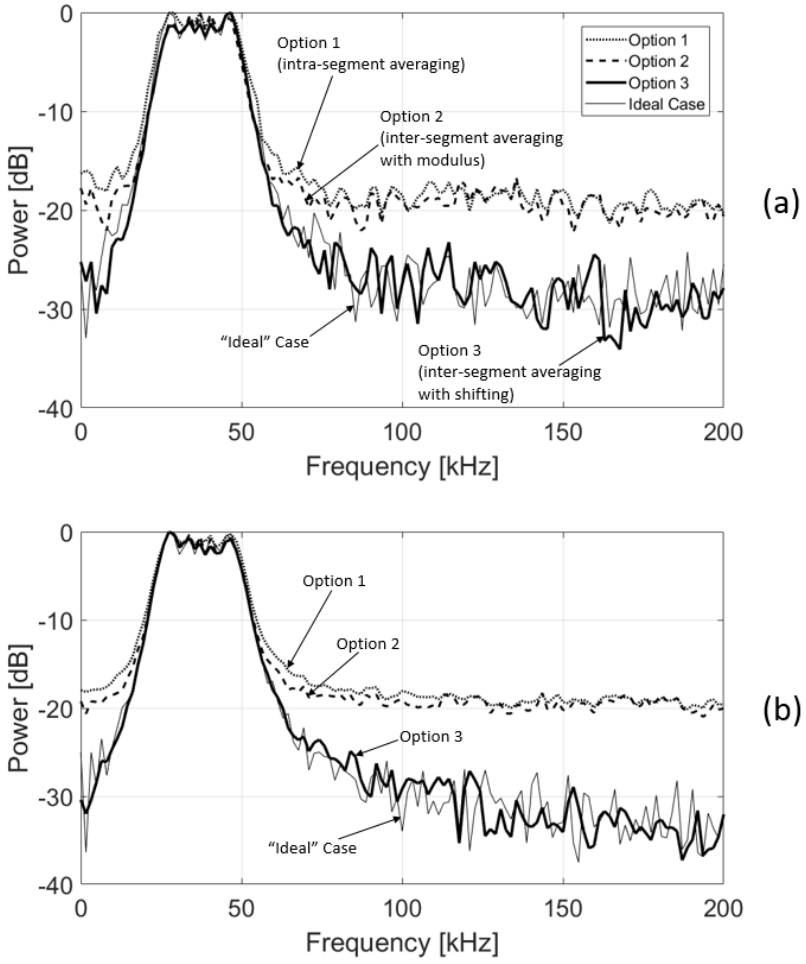

Figure 3.6: (a) Power spectra of chirped signal with added noise extracted with intra-segment averaging (Option 1), inter-segment averaging with modulus (Option 2), inter-segment averaging with shifting (Option 3) and "ideal case" by using 16 segments. (b) Same as (a) by using 64 segments

3.4.2 Experimental Signals

Additional studies were conducted on experimental signals consisting of ultrasonic waves propagating in steel rail tracks. In the first experimental study, a piezoelectric (PZT) stack actuator was used to excite an 80 kHz sinusoidal wave in an 8 ft long rail section in the laboratory – Fig. 3.7. This frequency was within the range of frequencies known to be effective for the detection of internal flaws in rails by guided-wave ultrasonic testing [30]. A capacitive air-coupled receiver was utilized to detect the waves from the rail section at a distance of ~ 2 ft from the PZT stack excitation. This was one of the sensors used by the UCSD prototype for passive high-speed rail inspection, shown in Fig. 3.7 [10].

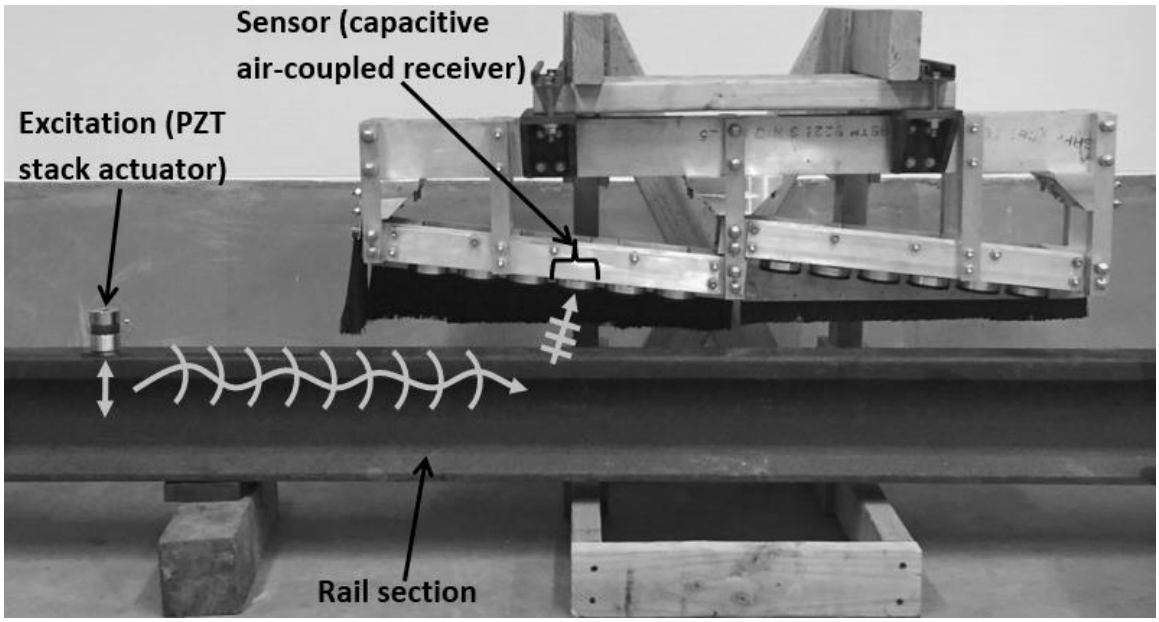

Figure 3.7: Setup for experimental validation using elastic waves in a rail track section

The sampling frequency of the acquisition was 80 MHz. Uncorrelated noise (white Gaussian, 20x power) was synthetically added to the measurements. The time duration of each segment was 0.625 msec, resulting in a total duration of 10 msec with 16 segments and of 40 msec with 64 segments.

Fig. 3.8 shows the power spectra obtained from the signal using the three options.

The experimental results confirm the conclusions of the synthetic results, i.e. that Option 3 (inter-segment averaging with shifting) from (3.21) is the best operation to isolate the signal power from

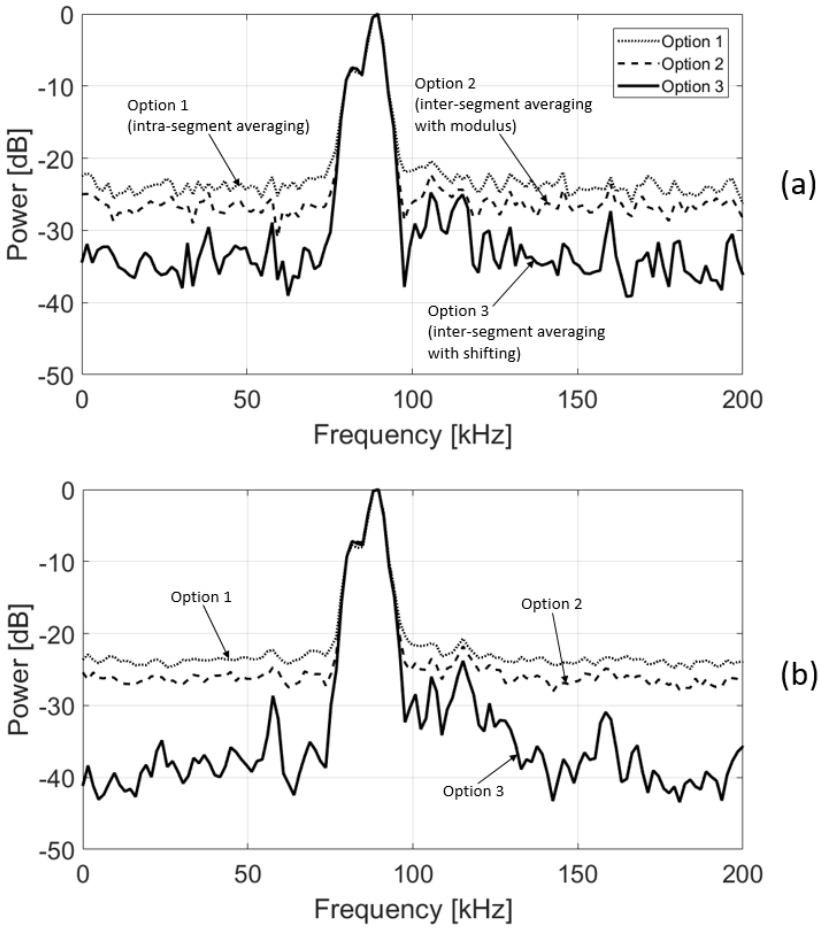

Figure 3.8: (a) Power spectra of experimental signal in rail section extracted with intra-segment averaging (Option 1), inter-segment averaging with modulus (Option 2), and inter-segment averaging with shifting (Option 3) by using 16 segments. (b) Same as (a) by using 64 segments

the noise, with Option 1 (intra-segment averaging) and Option 2 (inter-segment averaging with modulus) retaining noise components. For the 16 segments in Fig. 3.8(a), Option 3 yields a SNR as high as 36 dB, against SNRs of 24 dB for Option 1 and 27 dB for Option 2. Using 64 segments, Fig. 3.8(b), increases the SNR of Option 3 to ~ 41 dB, confirming the improvement already discussed for the synthetic signals. As discussed earlier, this improvement is not dramatic, suggesting that a small number of segments can actually be sufficient for a robust signal

reconstruction.

The last case study was performed to further validate the proper normalization option for the estimation of the complete transfer function H_{AB} in a realistic test scenario aimed at high-speed ultrasonic inspections of rail tracks. In the fall of 2016, a series of field tests were conducted at the Transportation Technology Center (TTC) in Pueblo, CO, where two arrays of air-coupled receivers were mounted underneath the FRA DOTX-216 test car (Fig. 3.9) [10]. The distance *A*-*B* between two sensors in each pair was 18.75 in (~ 47 cm). Several test runs were made on the of TTC, between markers R25 and R42 at speeds ranging from 20 mph to 80 mph (the maximum allowable speed in the track). The sampling frequency of the acquisition was 1 MHz.

The transfer function of the rail between the sensor positions, $H_{AB}(f)$, was extracted in the

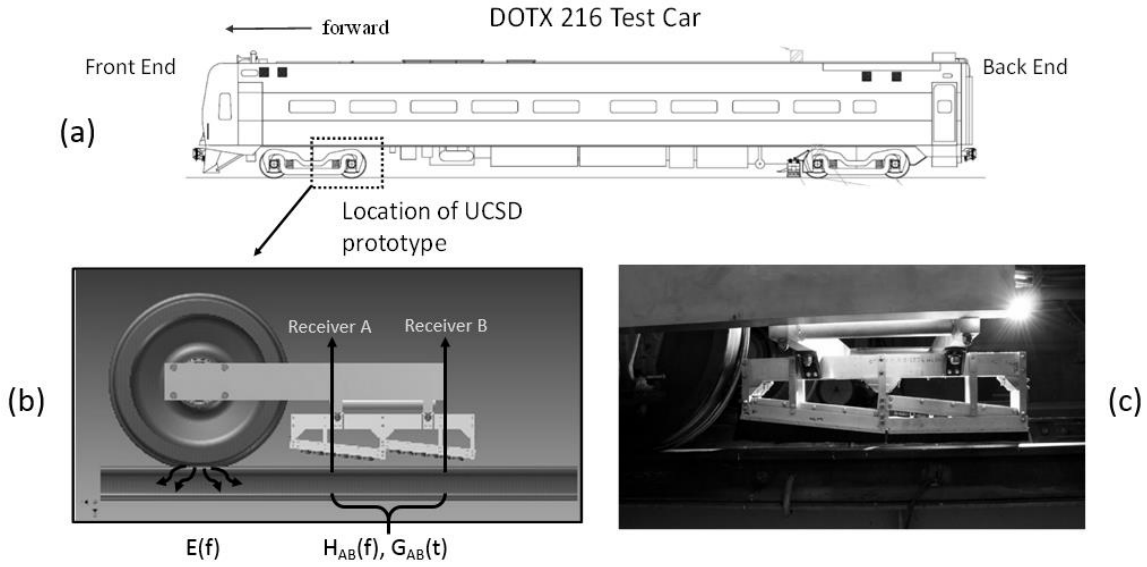

Figure 3.9: The FRA DOTX-216 test car used for the field tests of the passive rail inspection system at the Transportation Technology Center (TTC) in Pueblo, CO. (b) Schematic of the passive reconstruction of the rail transfer function between A and B using pairs of air-coupled receivers and the train wheel dynamic excitation. (c) Photo of the inspection prototype mounted underneath the DOTX-216 test car

frequency domain by using the normalized averaged cross-power spectrum procedures discussed in Section 3.3. The result was then transformed to the time domain. The presence of a structural discontinuity in the rail (whether a flaw, a joint or a weld) induces signal scattering which will

change the local transfer function (e.g. decrease its amplitude [30-33]). In the present paper, we compare the three different normalization options of (3.19), (3.20) and (3.21) in a short representative distance of 30 ft on the RTT at a test speed of 60 mph. The comparison is done in terms of sensitivity to a joint discontinuity, whose exact location in the track was well known. Also, 16 segments were used for these results (50% overlap for the intra-segment procedure, no overlap for the inter-segment procedure), corresponding to 31 intra-segment averages and 120 inter-segment averages. The total signal duration for the 16 segments was 7.62 msec, and each segment was 0.48 msec. Fig. 3.10 plots the "normalized signal loss" computed as the inverse of the passively-reconstructed transfer function strength for the three normalization options. This metric effectively represents a "Discontinuity Index" for the rail [30-33]. More specifically, this Index was calculated by plotting the inverse of the peak amplitude extracted from the time-domain reconstructed transfer function. Large values of this Index mean large loss of transmitted signal, as we would expect in the presence of a discontinuity or damage in the rail (e.g. a joint or a defect scattering the waves). The joint discontinuity is present at position ~ 14 feet in the *x*-axis of the graph. The best result is clearly obtained with normalization Option 3 (inter-segment averaging with shifting), i.e. using the $H_{AB}(f)$ estimation of (3.18), yielding a sensitivity to the joint as high as 6.7 (max peak/mean noise level). Option 1 and Option 2, instead, both result in a much smaller sensitivity (~ 2), because of their ineffectiveness to eliminate the added noise generated by the harsh experimental conditions of this test. Hence the conclusions from the previous case studies and from the theoretical derivations were confirmed.

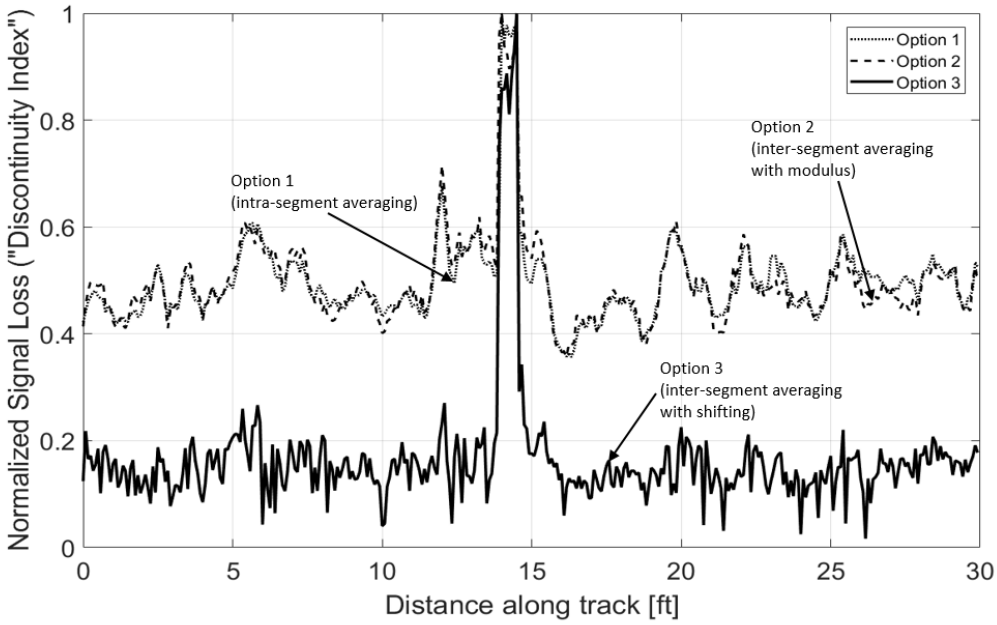

Figure 3.10: Normalized loss of passively-reconstructed transfer function of the rail from the TTC field tests at 60 mph on a section of the Railroad Test Track (RTT) with a joint by using intra-segment averaging (Option 1), inter-segment averaging with modulus (Option 2), and inter-segment averaging with shifting (Option 3)

3.5 Discussion and Conclusions

This paper has dealt with the estimation of the dynamic transfer function between two outputs of a linear system subjected to an uncontrolled, and generally unknown excitation, and accounting for possible uncorrelated noise present at both outputs. Several applications of this case exist in the non-destructive evaluation and structural health monitoring fields, among others, where ambient excitations can be exploited as an acoustic/ultrasonic source. In those cases, an opportunity exists for passive-only systems that can track changes in the transfer function (or Green's function) between two points and relate those to the presence of a structural discontinuity such as a flaw. It is important to highlight that a sufficient condition for structural inspection is not to reconstruct the "ideal" Green's function of the object, rather to reconstruct a *stable* transfer function, i.e. one that is invariant to changes in the excitation and/or the noise levels. A key

requirement for this task is to eliminate the effect of the (uncontrolled) source from the transfer function estimation.

In analogy with single-input-single-output linear systems, it was discussed how an averaged normalized cross-power spectrum between the two outputs should be considered as a first step for the dual-output transfer function estimation. However, the paper suggests that particular care must be used when choosing the normalization factor for the cross-power spectrum. Specifically, it is shown that the classical "intra-segment" averaging does not prevent the noise at one of the outputs to contaminate the transfer function estimation. Instead, an "inter-segment" averaging method is proposed to properly eliminate noise that is uncorrelated in time. This mode of averaging must also include a proper time-shifting at each segment for the normalization factor to obtain the dual result of (1) eliminating the excitation spectrum and (2) eliminating the uncorrelated noise from the transfer function estimation.

Results validating these conclusions were presented for the cases of a synthetic narrowband signal, a synthetic chirped signal, a signal experimentally measured from a rail section in the laboratory, and signals collected by air-coupled sensors from train wheel excitations running at 60 mph on a real rail track. The latter result is part of a broader project aimed at developing a high-speed inspection capability for rail tracks using passive-only ultrasonic monitoring.

Since noise elimination is based on an averaging process, increasing the number of average segments should improve signal-to-noise ratios. A quantitative study on the effect of the number of averages on the dual-output transfer function estimation goes beyond the present paper, and it could be a topic of a follow-on study. The validation results presented in Section 3.4 showed that as few as 16 segments provide enough noise suppression, and little additional gain was obtained when using 64 segments. Part of the reason for this promising result is that the number of averages

is greatly increased in an "inter-segment" approach (n!/2*(n-2)! averages for n segments) compared to the "intra-segment" approach (2n-1 averages for n segments with a 50% overlap).

An important hypothesis of this study, besides linearity, is that the source excitation is piecewise-stationary, meaning that its statistics do not change during the observation time window of the outputs. This condition is easily satisfied in the rail high-speed inspection case where the observation window can only be a few milliseconds to ensure localization along the rail of the transfer function estimation.

The rail tests shown in Fig. 3.10 were conducted on a moving platform. Therefore, the reconstructed transfer function is a spatial average across a finite "gage length" of the rail. For the 16-segment set shown in the figure, this gage length was 8 inches. A detailed discussion on the finite gage length, as it pertains to the passive transfer function estimation of the rail from a moving vehicle, is given in a previous work by the author of this dissertation [10].

The paper is focused on the case of an unknown source, such as that of the acoustic wheel excitation of the rail or other ambient excitation cases. Clearly, any information available of the input signal would benefit the impulse response reconstruction process in other cases.

The study also assumes that noise is uncorrelated, i.e. uncorrelated with itself over time and uncorrelated with the excitation. The case of correlated noise, e.g. output components coming from a secondary source, is not examined here.

Acknowledgements

Team members at UCSD Albert Liang, Margherita Capriotti, and Xuan "Peter" Zhu collaborated with this research. This project was primarily funded by the U.S. Federal Railroad Administration under grant FR-RRD-0027-11-01, with former Program Manager Mr. Mahmood Fateh and current Program Manager Dr. Robert Wilson. The authors also thank FRA Office of

Research, Development and Technology Division Chief Mr. Gary Carr for technical advice throughout this project. Additional funding was provided by the U.S. National Science Foundation grant CMMI-1362144 with Program Managers Irina Dolinskaya and Jordan Berg.

Chapter 3 is, in full, a reprint of material published in F. Lanza di Scalea, S. Sternini, A. Y. Liang, "Robust passive reconstruction of dynamic transfer function in dual-output systems," *Journal of the Acoustical Society of America*, vol. 143, no. 2, pp. 1019-1028, 2018. The dissertation author was the primary investigator and author of this paper.

References

[1] Roth, P. R., 1971, "Effective measurements using digital signal analysis," IEEE Spectrum, 8(4), pp. 62–70.

[2] Carter, G. C., Knapp, C. H., and Nuttall, A. H., 1973, "Estimation of the Magnitude-Squared Coherence Function Via Overlapped Fast Fourier Transform Processing," IEEE Trans. Audio Electroacoust., 21(4), pp. 337–344.

[3] Carter, G. C., 1987, "Coherence and time delay estimation," Proc. IEEE, 75(2), pp. 236–255.

[4] Welch, P. D., 1967, "The Use of Fast Fourier Transform for the Estimation of Power Spectra: A Method Based on Time Averaging Over Short, Modified Periodograms," IEEE Trans. Audio Electroacoust., AU-15(2), pp. 70–73.

[5] Farrar, C. R., and James, G. H., 1997, "System Identification From Ambient Vibration Measurements on a Bridge," J. Sound Vib., 205(1), pp. 1–18.

[6] Salvermoser, J., Hadziioannou, C., and Stähler, S. C., 2015, "Structural monitoring of a highway bridge using passive noise recordings from street traffic," J. Acoust. Soc. Am., 138(6), pp. 3864–3872.

[7] Snieder, R., and Şafak, E., 2006, "Extracting the building response using seismic interferometry: Theory and application to the Millikan Library in Pasadena, California," Bull. Seismol. Soc. Am., 96(2), pp. 586–598.

[8] Sabra, K. G., Winkel, E. S., Bourgoyne, D. A., Elbing, B. R., Ceccio, S. L., Perlin, M., and Dowling, D. R., 2007, "Using cross correlations of turbulent flow-induced ambient vibrations to estimate the structural impulse response. Application to structural health monitoring," J. Acoust. Soc. Am., 121(4), pp. 1987–1995.

[9] Tippmann, J. D., Zhu, X., and Lanza di Scalea, F., 2015, "Application of damage detection methods using passive reconstruction of impulse response functions," Phil. Trans. R. Soc. A.,

373(2035), pp. 1–17.

[10] Lanza di Scalea, F., Zhu, X., Capriotti, M., Liang, A. Y., Mariani, S., and Sternini, S., 2018, "Passive Extraction of Dynamic Transfer Function From Arbitrary Ambient Excitations: Application to High-Speed Rail Inspection From Wheel-Generated Waves," J. Nondestruct. Eval. Diagnostics Progn. Eng. Syst., 1(1), pp. 0110051–01100512.

[11] Sabra, K. G., Roux, P., and Kuperman, W. A., 2005, "Emergence rate of the time-domain Green's function from the ambient noise cross-correlation function," J. Acoust. Soc. Am., 118(6), pp. 3524–3531.

[12] Roux, P., Kuperman, W. A., and the NPAL Group, 2004, "Extracting coherent wave fronts from acoustic ambient noise in the ocean," J. Acoust. Soc. Am., 116(4), pp. 1995–2003.

[13] Sabra, K. G., Roux, P., and Kuperman, W. A., 2005, "Arrival-time structure of the time-averaged ambient noise cross-correlation function in an oceanic waveguide," J. Acoust. Soc. Am., 117(1), pp. 164–174.

[14] Campillo, M., and Paul, A., 2003, "Long-Range Correlations in the Diffuse Seismic Coda," Science, 299(5606), pp. 547–549.

[15] Roux, P., Sabra, K. G., Gerstoft, P., Kuperman, W. A., and Fehler, M. C., 2005, "P-waves from cross-correlation of seismic noise," Geophys. Res. Lett., 32(19), pp. 1–4.

[16] Shapiro, N. M., Campillo, M., Stehly, L., and Ritzwoller, M. H., 2005, "High-Resolution Surface-Wave Tomography from Ambient Seismic Noise," Science, 307(5715), pp. 1615–1618.

[17] Sabra, K. G., Gerstoft, P., Roux, P., Kuperman, W. A., and Fehler, M. C., 2005, "Extracting time-domain Green's function estimates from ambient seismic noise," Geophys. Res. Lett., 32(3), pp. 1–5.

[18] Sabra, K. G., Gerstoft, P., Roux, P., Kuperman, W. A., and Fehler, M. C., 2005, "Surface wave tomography from microseisms in Southern California," Geophys. Res. Lett., 32(14), pp. 1–4.

[19] Snieder, R., 2004, "Extracting the Green's function from the correlation of coda waves: A derivation based on stationary phase," Phys. Rev. Lett. E, 69, pp. 0466101–0466108.

[20] Lobkis, O. I., and Weaver, R. L., 2001, "On the emergence of the Green's function in the correlations of a diffuse field," J. Acoust. Soc. Am., 110(6), pp. 3011–3017.

[21] Michaels, J. E., and Michaels, T. E., 2005, "Detection of structural damage from the local temporal coherence of diffuse ultrasonic signals," IEEE Trans. Ultrason. Ferroelectr. Freq. Control, 52(10), pp. 1769–1782.

[22] Larose, E., Lobkis, O. I., and Weaver, R. L., 2006, "Passive correlation imaging of a buried scatterer," J. Acoust. Soc. Am., 119(6), pp. 3549–3552.

[23] van Wijk, K., 2006, "On estimating the impulse response between receivers in a controlled

ultrasonic experiment," Geophysics, 71(4), pp. SI79-SI84.

[24] Sabra, K. G., Srivastava, A., Lanza di Scalea, F., Bartoli, I., Rizzo, P., and Conti, S., 2008, "Structural health monitoring by extraction of coherent guided waves from diffuse fields," J. Acoust. Soc. Am., 123(1), pp. EL8-L13.

[25] Tippmann, J. D., and Lanza di Scalea, F., 2016, "Passive-Only Defect Detection and Imaging in Composites Using Diffuse Fields," Society for Experimental Mechanics, Mechanics of Composite and Multi-functional Materials, **7**, pp. 67–72.

[26] Tippmann, J. D., and Lanza di Scalea, F., 2015, "Passive-only damage detection by reciprocity of Green's functions reconstructed from diffuse acoustic fields with application to wind turbine blades," J. Intell. Mater. Syst. Struct., 26(10), pp. 1251–1258.

[27] Duroux, A., Sabra, K. G., Ayers, J., and Ruzzene, M., 2010, "Extracting guided waves from cross-correlations of elastic diffuse fields: applications to remote structural health monitoring," J. Acoust. Soc. Am., 127(1), pp. 204–215.

[28] Chehami, L., De Rosny, J., Prada, C., Moulin, E., and Assaad, J., 2015, "Experimental study of passive defect localization in plates using ambient noise," IEEE Trans. Ultrason. Ferroelectr. Freq. Control, 62(8), pp. 1544–1553.

[29] Lanza di Scalea, F., "Ultrasonic Testing Applications in the Railroad Industry," in *Non-destructive Testing Handbook*, 3rd edition, edited by P. O. Moore (American Society for Nondestructive Testing, Columbus, OH, 2007), pp. 535–552.

[30] Coccia, S., Bartoli, I., Marzani, A., Lanza di Scalea, F., Salamone, S., and Fateh, M., 2011, "Numerical and experimental study of guided waves for detection of defects in the rail head," NDT E Int., 44(1), pp. 93–100.

[31] Mariani, S., Nguyen, T., Phillips, R. R., Kijanka, P., Lanza di Scalea, F., Staszewski, W. J., Fateh, M., and Carr, G., 2013, "Noncontact ultrasonic guided wave inspection of rails," Struct. Heal. Monit. An Int. J., Spec. Issue Noncontact Meas. Technol., 12(5-6), pp. 539–548.

[32] Mariani, S., and Lanza di Scalea, F., 2017, "Predictions of defect detection performance of air-coupled ultrasonic rail inspection system," Struct. Heal. Monit. An Int. J., 17(3), pp. 684-705.

[33] Mariani, S., Nguyen, T., Zhu, X., and Lanza di Scalea, F., 2016, "Field Test Performance of Noncontact Ultrasonic Rail Inspection System," ASCE J. Transp. Eng., 143(5), pp. 040170071–0401700714.

Chapter 4

Rail Flaw Imaging by Improved Ultrasonic Synthetic Aperture Focus Techniques

Abstract

This paper presents a prototype system for the ultrasonic imaging of rail flaws that uses an improved version of the Synthetic Aperture Focus Technique (SAFT). A rail flaw imaging system is needed to quantitatively assess the size and the shape of a flaw in a manner that goes beyond the operator's judgement inevitably affecting current rail flaw verifications based on A-scans. Improvements in rail maintenance practice on several levels can be expected if the rail flaw verification step is truly quantitative. The SAFT was chosen over a traditional phased array imaging system due to the reduced hardware complexity, improved focus and speed. The system being developed implements various steps to further improve the performance of the SAFT including: (a) compounding various wave propagation modes to reduce artifacts and increase array gain, (b) include a wedge in the beamforming algorithm for optimum detection of transverse defects, (c) utilizing the parallel processing structure of the Graphical Processing Unit (GPU) architecture for increased imaging rates, and (d) stitching 2D slices to reconstruct 3D volumetric

images. Results are shown on rail sections with simulated and natural Transverse Defects borrowed from the Federal Railroad Administration (FRA) Rail Defect Library. While the focus of the current research is on manual hand-held flaw imaging, several of the proposed algorithmic steps can be useful for in-motion rail inspections.

4.1 Introduction

Identification of defects in railroad tracks is critical for rail safety and risk management. The cost of rail failure can be catastrophic, and substantial effort is required to reduce the risk. Proper allocation of resources for rail defect management requires not only detection, but also precise localization and characterization. Current techniques are limited to detection and have difficulty identifying the size and locate the orientation of the railhead defects due to operator's judgement. Transverse Defects (TDs) and detail fractures are some of the most widespread types of defects. TDs can originate as manufacturing defects such as hydrogen flakes and brittle sub-surface inclusions [1]. Improved manufacturing techniques over the years have reduced defects arising from manufacturing; however, TDs and detail fractures initiated from surface defects as a result of rolling contact fatigue (RCF) are widespread and continue to grow [2].

Ultrasonic inspection is the most common technique used for rail flaw detection [3, 4]. Typical ultrasonic testing for rails uses A-scans that cannot directly provide information on the flaw size. For unbiased sizing, ultrasonic arrays are needed in a beamforming technique.

The most common beamforming method uses the Phased-Array (PA) technique. Early implementations of phased-arrays in ultrasonic wheels for rail inspections were studied in the 70's to better detect sub-surface and surface breaking defects [5]. More recent applications of PAs for rail flaw imaging were examined by researchers at the Transportation Technology Center in Pueblo, CO, for both manual verification [6] and in-motion inspection [7].

The objective of this project is to demonstrate the ability to image rail flaws using ultrasonic Synthetic Aperture Focus (SAF) imaging [8, 9], which is a variation of phased-array imaging where each transducer can be treated individually and the focusing is done synthetically rather than physically. These features bring some key advantages in terms of image quality, image speed and hardware simplification. Experimental tests were performed to validate the algorithm for various flaw environments. The ultrasonic imaging algorithm developed utilizes the following main components: coherent image compounding to increase array gain without adding to the physical aperture of the array, wedge imaging through ray tracing for optimal identification of near vertical flaws (e.g. TDs), and real-time imaging using a Graphical Processing Unit (GPU) based computation compared to a slower Central Processing Unit (CPU) architecture.

Imaging results (2D and 3D) are presented from 141RE rail sections with simulated flaws (flat bottom holes drilled in the rail head to simulate TDs) and from a 136RE rail sample with a naturally occurring TD.

4.2 Synthetic Aperture Focus Technique

Synthetic Aperture Focus (SAF) for ultrasonic imaging has been around since the late 1960s and has found numerous applications in the medical imaging and structural health monitoring fields [10, 11]. A typical SAF approach uses an array of piezoelectric transducers that can act as both transmitters and receivers of ultrasonic waves. The image is constructed by

extracting features from the received ultrasonic waveforms that are appropriately backpropagated in time to account for delay due to the spatial position of the transmitter, receiver and focus point. This approach of temporal back propagation is also commonly known as Delay-and-Sum (DAS) algorithm. Another key aspect of SAF beamforming is the selection of weights attributed to each collected waveform [12].

Basic SAF algorithms use unity weights, or no weights applied, to the backpropagated and summed waveforms. Static apodization weights such as the Hanning or Kaiser-Bessel windows are also widely utilized to decrease artificial ringing effects in the image, but at the expense of smearing the image results and decreasing spatial resolution. The Hanning or Kaiser-Bessel windows are considered static since they are applied independently of the focus point. In this work, unity weights have been selected as apodization weights in the SAFT algorithm, even though weights based on the physics of the propagating waves could be applied to further improve the imaging results [10].

4.2.1 Theoretical Framework

Consider an ultrasonic transducer array with *M* transmitters and *N* receivers. Let the spatial coordinates of each transmitter $i = 1, \dots, M$ be (x_i, y_i) and the spatial coordinates of each receiver $j = 1, \dots, N$ also be (x_j, y_j), as shown in Figure 4.1.

A standard Delay-and-Sum (DAS) algorithm constructs an image $I\,(x, y)$ by summing, at each pixel $P\,(x, y)$, the amplitudes of the received signals, A, appropriately backpropagated, for each combination of transmitter i and receiver j. In the time domain, the backpropagated DAS algorithm is written as

$$I^{DS}(x, y) = \sum_{i=1}^{M} \sum_{j=1}^{N} w_{ij,xy}\, A_{ij}\left(\tau_{ij,xy}\right) \tag{4.1}$$

where $w_{ij,xy}$ represents the apodization weights previously discussed. The backpropagation time, $\tau_{ij,xy}$, corresponds to the travel time of the wave from the transmitter i, to the focus point $P\ (x, y)$, and back to the receiver j, and is calculated as

$$\tau_{ij,xy} = \frac{\sqrt{(x_i - x)^2 + (y_i - y)^2}}{c_{L,S}} + \frac{\sqrt{(x_j - x)^2 + (y_j - y)^2}}{c_{L,S}} \tag{4.2}$$

where the denominators can be the longitudinal wave speed c_L or the shear wave speed c_s in the solid.

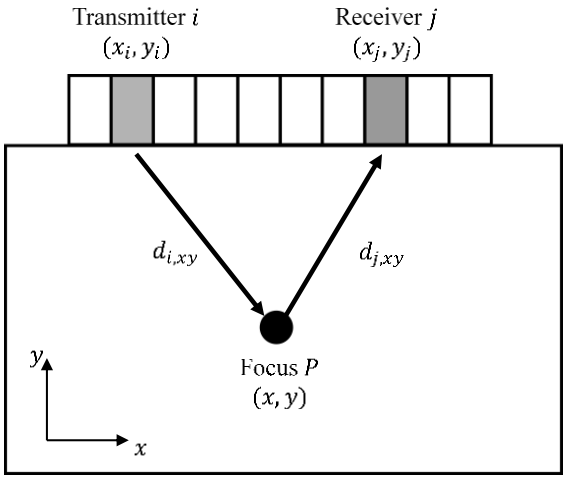

Figure 4.1: Schematic of the imaging setup

The received signal, A, in Equation 4.1, can be computed directly from the raw waveforms, from an enveloped version of the raw waveforms, or from the analytical signal representation of the raw waveforms. In the latter case, each waveform is decomposed into its in-phase and phase-quadrature components through the Hilbert transform. Equation 4.1 would then be applied to each of the Hilbert transformed components separately [13]. The final image would then be constructed by computing the modulus of the two contributions at each pixel (x, y). This method is utilized to generate the results shown in this work.

4.3 Compounding of Multiple Wave Modes

The possibility of combining different wave mode combinations comes from the realization that, in general, a defect in a solid can reflect one or both of a longitudinal L-wave and a shear S-wave, through either same mode reflection or mode conversion [10]. In the most general case, since the excitation from a transducer with a small footprint (width of 0.6mm for the sensors used in this work) can produce both L-wave and S-wave, thus acting as a point source, there can exist up to four combinations of wave modes available for imaging in a bulk solid: L-wave transmitted and reflected (LL), L-wave transmitted and S-wave reflected (LS), S-wave transmitted and reflected (SS), and S-wave transmitted and L-wave reflected (SL).

For the case where a transducer wedge is used, only the L-wave is considered inside the wedge and it can be refracted as both an L-wave and an S-wave in the test medium. Both wave modes can be reflected by the discontinuity within the test medium both as same-mode reflections and as mode-converted reflections and refract back to the L-mode in the wedge that is then finally received by the array. There can therefore exist up to four combinations of wave modes available for imaging a bulk solid using a transducer wedge: LLLL (L-wave transmitted in wedge, L-wave refracted in solid, L-wave reflected by reflector, L-wave refracted in wedge), LSLL (L-wave transmitted in wedge, S-wave refracted in solid, L-wave reflected by reflector, L-wave refracted in wedge), LLSL (L-wave transmitted in wedge, L-wave refracted in solid, S-wave reflected by reflector, L-wave refracted in wedge), and LSSL (L-wave transmitted in wedge, S-wave refracted in solid, S-wave reflected by reflector, L-wave refracted in wedge).

An opportunity arises to compound images obtained from different mode combinations to improve array gain. There are two main ways to compound images: incoherent and coherent compounding. Incoherent compounding is the simple summation of the image intensities.

Coherent compounding, instead, includes "cross-mode" terms because the summation is done before the squaring of the intensities. In this report, we focus on coherent compounding of wave modes. By coherently summing, this mode exploits the coherence across wave mode combinations (MC) as received by the array and can be expressed as

$$I_{TOT,\,coherent}(x,y) = \left(\sum_{MC} \left| \sqrt{I^{MC}(x,y)} \right| \right)^2 \tag{4.3}$$

4.4 Ultrasonic Imaging with Transducer Wedge

In some cases, it is useful to properly direct the ultrasonic beam to have maximum reflection from defects that lay at particular orientations. For example, naturally occurring TDs in rails are usually oriented at 20 degrees from the vertical. In this scenario, an ultrasonic transducer array oriented directly above the transverse defect is at a sub-optimal orientation, as shown in Figure 4.2(a). Using the same principles outlined in SAFT beamforming and using Snell's Law, ray-tracing can be applied to angle the ultrasonic waves and direct them in such a way that an optimal reflection from the defect can be obtained. From Figure 4.2(b), the wedge increases the available surface area for the reflection of the ultrasonic wave from the transverse defect to the sensor, improving the identification characteristics.

As mentioned above, the goal of the ray tracing approach is to find the rays that connect a given focus point to the various transducer elements in the array. As stated in the previous section, due to wave refraction, these rays do not have straight paths since they bend at the wedge/medium interface. The point at the interface where a ray connecting the focus point to a transducer element bends is the "virtual" position of that transducer. The "virtual" array can then be created by finding all the rays connecting a specific focus point to the physical array. Conceptually, the "virtual" array

can be thought of as the positions that the transducer elements need to have on the medium surface, without a wedge, in order to create the same image obtained with the transducer wedge connected to the physical array.

The ray tracing algorithm is dependent on the position of the focus point $P(x, y)$, the position of the transducer on the wedge surface, and the specific wave mode considered. Following Snell's law, propagating modes with different wave speeds will have different refraction angles at the interface of two materials having acoustic impedance mismatch. Therefore, different wave modes will have different ray paths connecting the same focus point to the physical array. The mode-dependent nature of ray tracing allows the wave modes to be exploited independently as well as in combinations, to enhance the image gain by means of wave mode compounding.

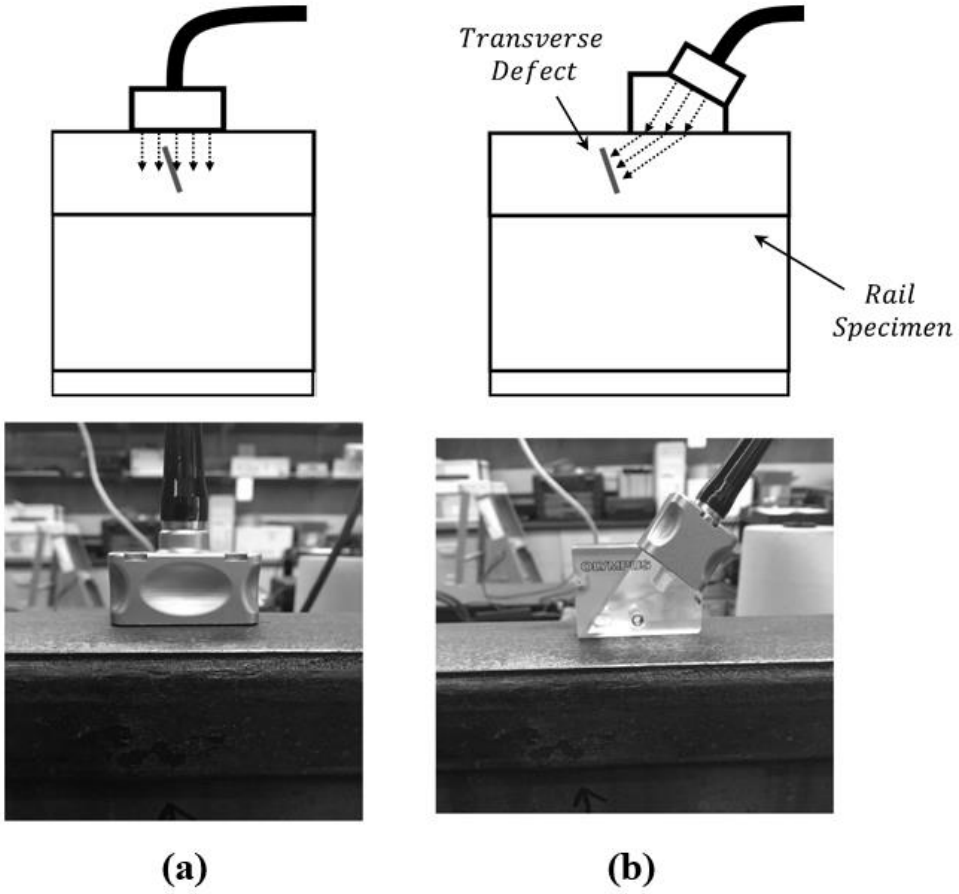

Figure 4.2: Ultrasonic array for TD imaging in rails (a) without a wedge and (b) with a wedge

4.5 Real-Time Imaging with GPU Processing

General-purpose computing on Graphics Processing Units (GPU) were first marketed by Nvidia to take advantage of a GPU's unique architecture. A traditional CPU in a standard PC usually has 4 to 6 cores whereas, in comparison, a GPU is composed of sets of multiprocessors, with each multiprocessor consisting of a set of scalar processors and can consist of thousands of mini-cores [14]. This architecture makes GPUs advantageous for performing large amounts of simple computations quickly, as in the case of a SAFT beamforming algorithm. Real-time imaging of structural components requires parallelization that is not achievable on the CPU despite vectorization. In order to fully take advantage of the GPU's speed, there should be minimal data transfer between the PC's RAM and the GPU's RAM. As such, data acquired from the linear array is directly fed into the GPU where it remains for the remainder of the algorithm. A speed improvement of 10 to 14 times is achieved in refresh rate through parallel processing on the GPU, yielding to a maximum image refresh rate of 5 – 8 Hz depending on the complexity of the algorithm.

4.6 Experimental Results

Four rail specimens from the Federal Railroad Administration (FRA) Defect Library were used for the experiments:

1. Section #20 141RE rail specimen with a drilled centered FBH inclined at 20° from the horizontal covering 20% of the head area (HA);
2. Section #12 141RE rail specimen with a drilled centered FBH inclined at 20° from the horizontal covering 10% of the HA;

3. Section #14 141RE rail specimen with a drilled FBH in the head corner inclined at 20° from the horizontal covering 10% of the HA;
4. Section #36-168-I 136RE rail specimen with a natural TD covering approximately 6% of HA.

The probes used were a 32-element linear array (Olympus NDT P/N 2/25L32-192X10-A11-P-2.5-OM), with central frequency at 2.25 MHz, and a 64-element linear array (Olympus NDT 5L64-38.4X10-A12-P-2.5-OM), with central frequency at 5 MHz. Both the 32-element array and the 64-element array were attached to a 55-degree wedge (Olympus NDT SA11-N55S and Olympus NDT SA12-N55S, respectively). The array was controlled by a full matrix capture (FMC) controller (Advanced OEM Solutions, Cincinnati, OH, USA) that generates pulsed excitations and allows access to raw waveforms in reception (Figure 4.3). The arrays were coupled to the railhead using conventional ultrasonic gel couplant. The first specimen used for the tests was a 15-inch long 141RE rail segment with an FBH centered in the rail head and covering 20% of the HA, which was drilled at a 20-degree orientation from the horizontal starting from 15 mm below the rail top surface. An FBH is commonly used to simulate a TD. The second specimen contains a smaller FBH, at 10% of HA. The third specimen has an FBH drilled into the head corner, at 10% of HA. Lastly, the fourth specimen was a 136RE rail section with a naturally occurring TD in the head field side extending for 6% of the HA.

The experiments were conducted in either a 64 x 64 or a 32 x 32 Full-Matrix Capture (FMC) scheme depending on the array used, with each of the elements firing sequentially, and all elements receiving at each firing, corresponding to 4096 or 1024 sets of raw waveforms, respectively. The waveforms were then transmitted via Ethernet to a CUDA enabled Alienware R13 Laptop with a NVIDIA GeForce GTX 1070 GPU (Figure 4.3). Each of these waveforms was

Hilbert transformed and then beamformed. The final image was obtained as the modulus of the Hilbert transformed images and plotted in dB scale. The purpose of these tests was to verify, experimentally, the effectiveness of ultrasonic imaging for defect identification in railroad tracks.

4.6.1 Results with No Transducer Wedge

The experimental SAFT-DAS images obtained with no transducer wedge are from section #20 141RE rail specimen with a head centered FBH covering 20% of the HA. The LL-mode reception of Figure 4.4(a) has the highest signal-to-noise (SNR) ratio with later artifacts arising from shear wave interference. The LS and SL modes of Figures 4.4(b) and 4.4(d) are similar, with both modes producing numerous artifacts.

The artifacts are a result of the slower shear wave speed that produces a slower backpropagated time delay which, considering the longitudinal wave arrival packet, places the defect in a region closer to the sensor array. Since shear waves possess lower energy than longitudinal waves in this array configuration, the SS-mode in Figure 4.4(c) shows significant artifacts and poor results.

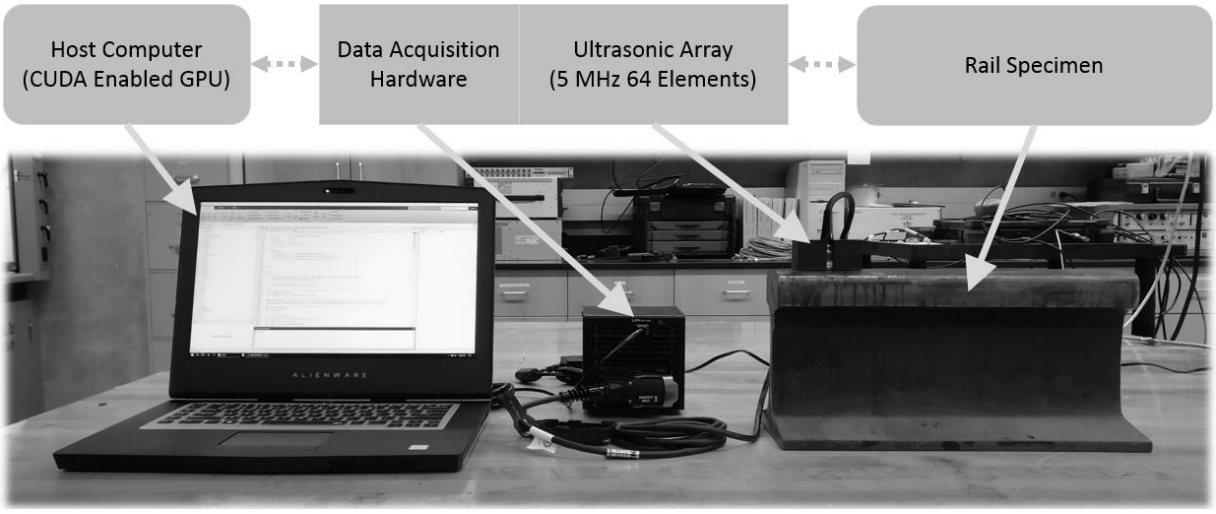

Figure 4.3: Experimental setup for ultrasonic imaging of rail specimens

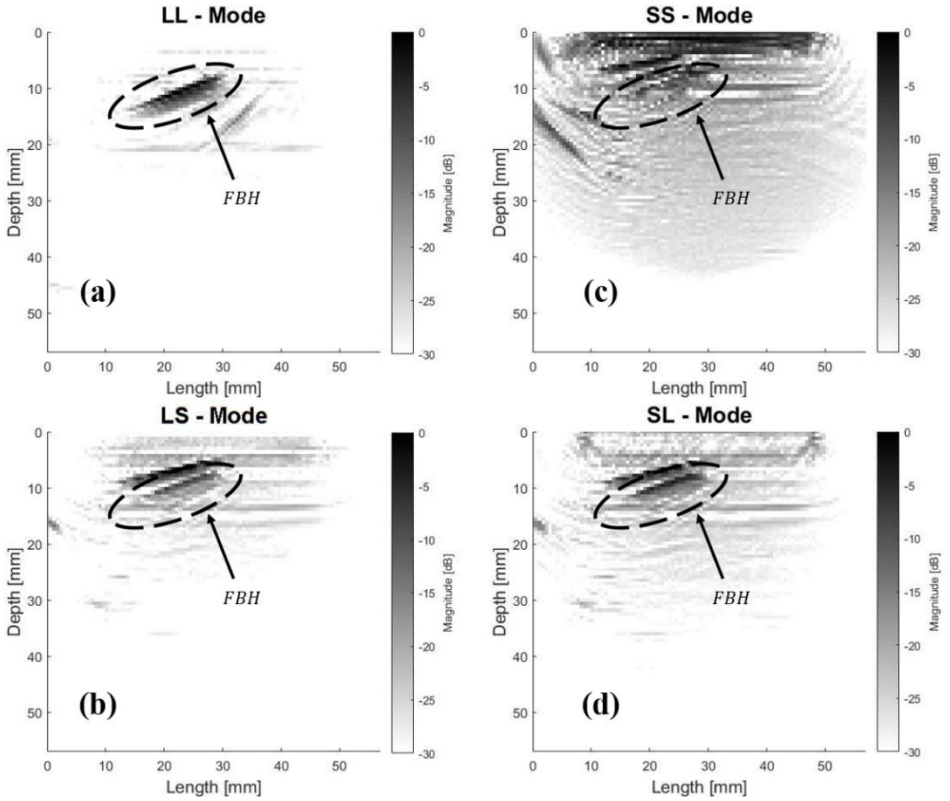

Figure 4.4: Images obtained from experimental testing of section #20 141RE rail specimen with a drilled FBH for (a) LL combination, (b) LS combination, (c) SS combination, and (d) SL combination

4.6.2 Results with Transducer Wedge

The experimental results for the section #36-168-I 136RE rail specimen with a natural TD are shown in Figure 4.5(a) and 4.5(b) and have resolutions of 96 by 96 and 175 by 150 pixels, respectively. The images were captured using a 32-element linear array with and without a 55-degree wedge. An illustration of the sensor orientation was shown earlier in Figure 4.2. Figure 4.5 demonstrates the importance of the array orientation when defects are nearly perpendicular to the array surface. Figure 4.5(a) was obtained by inspecting the rail specimen in the cross-sectional plane of the railroad track. Conversely, Figure 4.5(b) was computed after scanning the specimen along the rail longitudinal axis. As shown in Figure 4.5(a), only the top and bottom of the TD are

reflected to the array when no wedge is used. By using a wedge, the actual shape and orientation of the TD are properly imaged (Figure 4.5(b)).

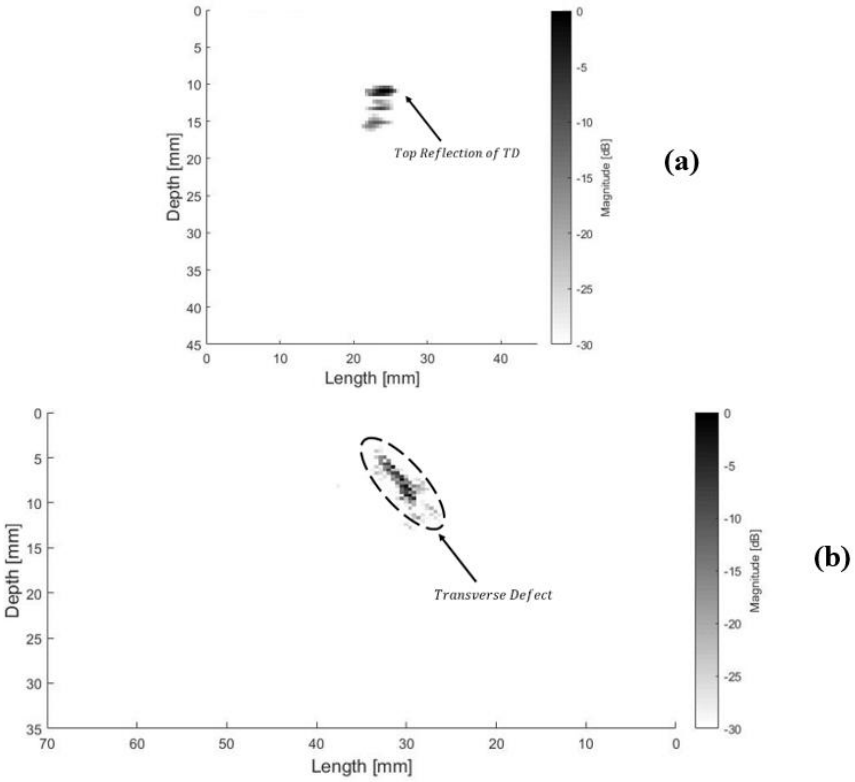

Figure 4.5: Image of a section #36-168-I 136RE rail specimen with a natural TD obtained using a 32-element linear array (a) without a wedge (cross-sectional image), and (b) with a 55-degree wedge (longitudinal section)

4.6.3 Wave Mode Compounding Results

Utilizing wave mode compounding, Figure 4.6 demonstrates a dramatic improvement in array performance. Only the LL and LS combinations were used in the case of no transducer wedge (Figure 4.6(a)). When the wedge was applied (Figure 4.6(b)), the LSSL and the LSLL combinations were considered in the image compounding. In both cases, image compounding brings a dramatic improvement in terms of dynamic range and spatial resolution, as well as a considerable reduction of artifacts and noise. The two images of Figure 4.6 show that using the ultrasonic array with and without the wedge allows reconstructing the overall profile of the FBH (e.g. top profile without wedge and lateral profile with wedge).

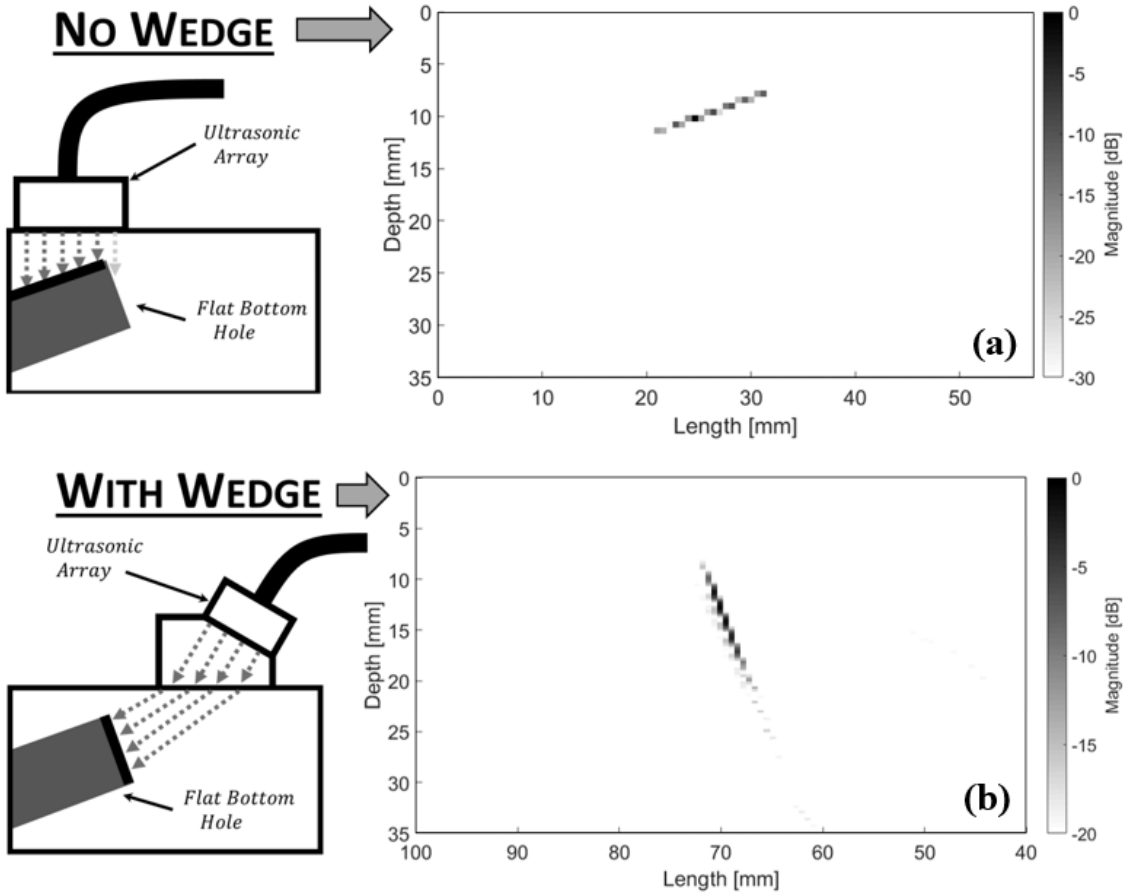

Figure 4.6: Images obtained from experimental testing of a section #20 141RE rail specimen with a drilled FBH: comparison of wave mode compounding with (a) no wedge using LL + LS combinations, and (b) with wedge using LSSL + LSLL combinations

4.6.4 Defect Sizing Comparison

A comparison between an ultrasonic A-scan (5 MHz single transducer) and the ultrasonic imaging system proposed in this paper was performed. Figure 4.7 is a representative comparison for an operator using an ultrasonic A-scan system on the left, and an ultrasonic imaging system on the right. The illustration demonstrates the ease of determining the defect size and orientation using the ultrasonic imaging system versus an ultrasonic A-scan system. In addition to improved qualitative defect location, the SAF ultrasonic imaging system improves the time it takes to return quantitative results. The defect size was estimated using an ultrasonic A-scan by marking the location were the reflected waveform amplitude was half of the maximum value. For the ultrasonic

imaging system, defect sizing was performed by taking the tail ends of the reconstructed images and calculating the resulting distance. The ultrasonic images used for the defect sizing comparison are shown in Figure 4.8. The quantification procedure was performed on all four rail sections from the FRA/TTC Rail Defect Library.

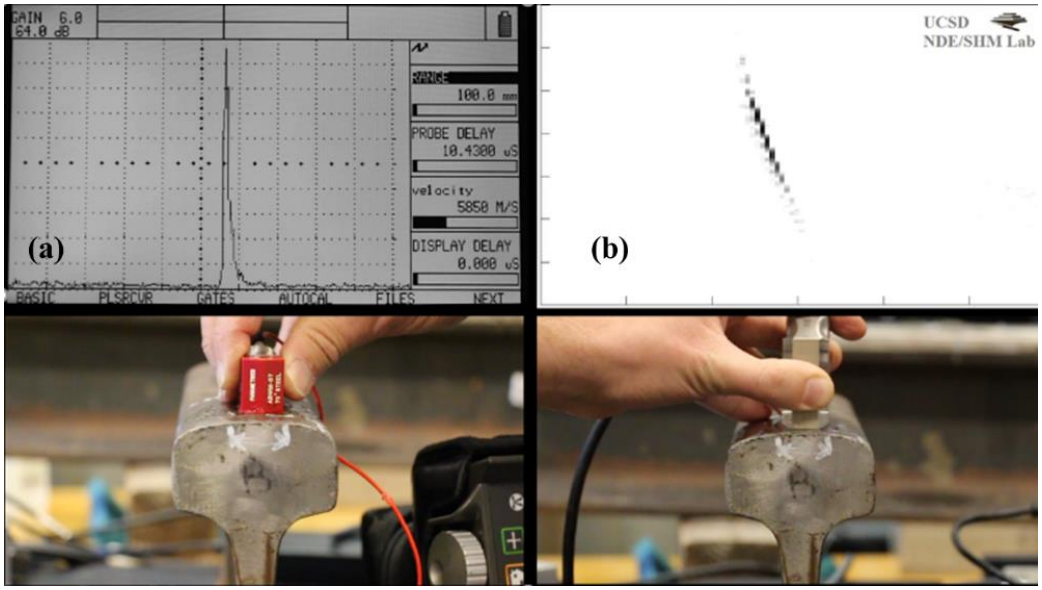

Figure 4.7: Comparison between (a) ultrasonic A-scan and (b) the proposed ultrasonic SAFT imaging system

The calculated sizes for the A-scan and imaging system are listed in Table 4.1. For the Specification Sheet Estimate, the rail HA was estimated to be 22.45 cm² (3.28 in²). The defect is assumed round, and an approximate diameter was subsequently calculated from the rail HA listed. The values estimated from the Specification Sheet, A-Scan, and Imaging System for Rail sections #20, #12, and #14 are in good agreement, although the Specification Sheet consistently estimates a larger value than the A-Scan and Imaging System result. For the rail section #36-168-I with a TD at approximately 6% of HA, the large variability from the A-Scan versus the Specification Sheet and Imaging System demonstrate the difficulties in estimating natural defect size using an A-Scan. The results tabulated in Table 4.1 highlight the potential for the ultrasonic imaging system for accurate and fast defect detection and characterization.

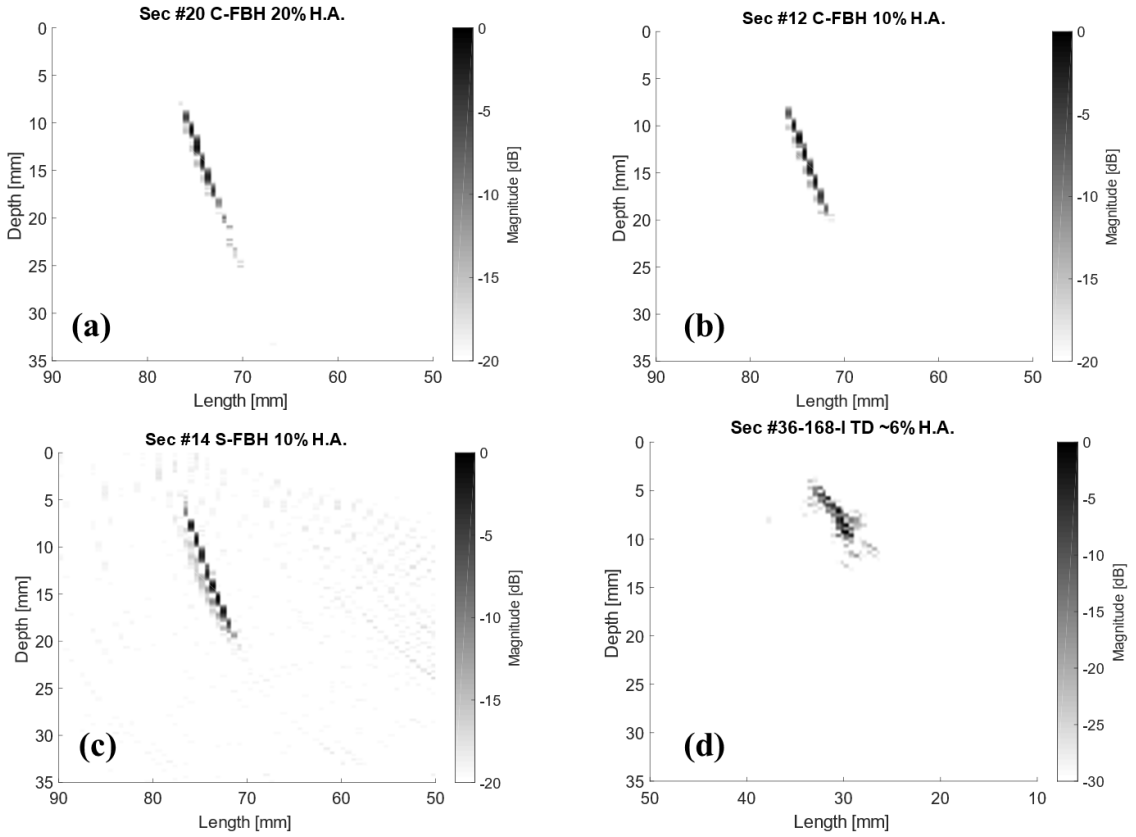

Figure 4.8: Ultrasonic images for (a) section #20 with centered FBH at 20% HA, (b) section #12 with centered FBH at 10% HA, (c) section #14 with head corner FBH at 10% HA, and (d) section #36-168-I with TD at approximately 6% of HA

Table 4.1: Defect Size Comparison

Rail Section	Description	Spec Sheet Estimate	A-Scan Estimate	Imaging System Estimate
#20	Centered FBH at 20% HA	~ 20 mm	16 – 20 mm	17 mm
#12	Centered FBH at 10% HA	~ 17 mm	9 – 12 mm	12 mm
#14	Head Corner FBH at 10% HA	~ 17 mm	13 – 14 mm	14 mm
#36-168-I	TD at ~6% HA	~ 12 mm	18 – 25 mm	10 mm

4.6.5 3D Reconstruction of Rail Flaws

The final step for the characterization of rail flaws is the reconstruction of their 3D shape from the 2D "slice" images. For this purpose, the rail is scanned along a transverse direction

perpendicular to the longitudinal axis. At each scanning point, a 2D image is generated using the SAF algorithm presented in the previous sections. Once all the scanning locations have been inspected, the images are then stitched together to create a single volumetric image of the flaw.

Figure 4.9(a) shows the scanning planes considered for the rail. As indicated by the black arrow, the 2D slice direction follows the transverse plane (scanning direction), whereas each 2D image represents the vertical plane at different scanning locations. Figure 4.9(b) illustrates the final result after all the 2D images have been combined. This image was obtained after inspecting section #20 141RE, which presents an FBH extending for 20% of the HA. From this volumetric image, accurate sizing can be performed in order to estimate the extent of the defect, thus allowing a more quantitative evaluation of the damage state of the rail specimen. From the 3D results of Figure 4.9(b), it can be inferred that the rail flaw has a pseudo-circular shape and its transverse dimension is about 22mm. These estimations were previously not possible by only inspecting 2D images, therefore this 3D representation is an important step to be performed in order to obtain a comprehensive image of the flaw.

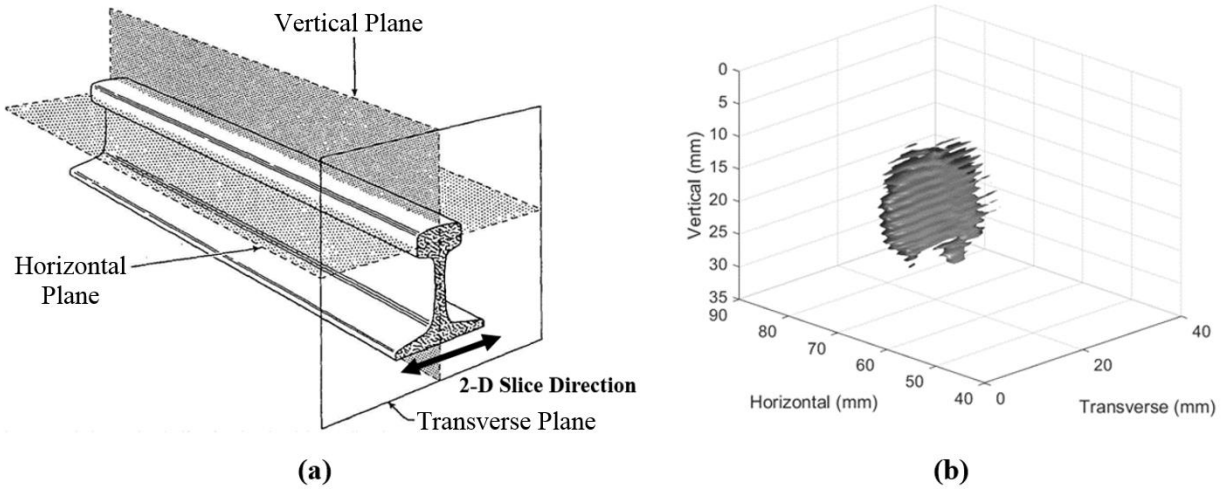

Figure 4.9: (a) Scanning planes in a rail specimen. (b) Reconstructed 3D image of a rail flaw obtained by combining multiple 2D images

4.7 Conclusions

Ultrasonic imaging has the potential for fast and precise damage detection and classification, resulting in reduced maintenance costs through more informed decision making. This paper has investigated improvements to the traditional SAF imaging technique to better identify rail flaws. Wedge imaging was explored for accurate identification of transverse defects, which are usually difficult to image without a wedge due to their orientation. Wave mode compounding was introduced by combining different images obtained with multiple wave mode combinations, in order to increase the array gain without increasing the array physical aperture. GPU-based image processing demonstrated capabilities for real-time identification of rail defects for improved operator feedback. Finally, 3D image reconstruction of rail flaws was performed using multiple 2D images obtained by scanning the rail specimen along its transverse plane, providing a robust identification of defects and, in general, a more reliable imaging system.

While the primary goal of the present research is to augment current hand verification techniques for rail flaws, the algorithmic steps introduced here can be also useful in an in-motion version of rail inspection.

Acknowledgements

Team member at UCSD Albert Liang collaborated with this research. This work was funded by the U.S. Federal Railroad Administration under contract no. DTFR5316C00024 (Mr. Mahmood Fateh, former Program Manager and Dr. Robert Wilson, current Program Manager). The authors acknowledge the technical feedback provided by Mr. Fateh, Dr. Wilson and Mr. Carr (Head, Track Research Division, FRA) throughout this project. The authors also acknowledge the

support of the Transportation Technology Center in Pueblo, CO, especially Drs. A. Poudel and D. Li for providing the rail specimens used in the experimental tests.

Chapter 4 is, in full, a reprint of S. Sternini, A. Y. Liang, F. Lanza di Scalea, "Rail Flaw Imaging by Improved Synthetic Aperture Focus Techniques," submitted to *Materials Evaluation*. The dissertation author was the primary investigator and author of this paper.

References

[1] Jeong, D. Y., 2003, "Correlations between rail defect growth data and engineering analyses, Part I: Laboratory tests," UIC/WEC joint research project on rail defect management, US Department of Transportation.

[2] Cannon, D. F., Edel, K.-O., Grassie, S. L., and Sawley, K., 2003, "Rail defects: an overview," Fatigue & Fracture of Engineering Materials & Structures, 26(10), pp. 865-886.

[3] Anon, F., 1990, "Rail-flaw detection. A science that works," Railway Track and Structures, 86(5), pp. 30-32.

[4] Lanza di Scalea, F., 2007, "Ultrasonic Testing Applications in the Railroad Industry," Chapter 15: Special Applications of Ultrasonic Testing, in Non-destructive Testing Handbook, 3rd edition, P.O. Moore, ed., American Society for Nondestructive Testing, pp. 535-552.

[5] Pagano, D. A., 1979, "Two-wheel ultrasonic rail testing system and method," U.S. Patent 4,174,636, issued November 20.

[6] Garcia, G., and Zhang, J., 2006, "Application of ultrasonic phased arrays for rail flaw inspection," Report DOT/FRA/ORD-06, July.

[7] Witte, M., and Poudel, A., 2016, "High-speed rail flaw detection using phased-array ultrasonics," Technology Digest TD-16-030, Transportation Technology Center, July.

[8] Flaherty, J. J., Erikson, K. R., and Lund, V. M., 1967, "Synthetic Aperture Ultrasonic Imaging Systems," U.S. Patent 3,548,642.

[9] Schmerr, L. W. Jr., 2016, "An Ultrasonic System," In Fundamentals of Ultrasonic Nondestructive Evaluation, Springer International Publishing, pp. 1-13.

[10] Lanza di Scalea, F., Sternini, S., and Nguyen, T. V., 2017, "Ultrasonic Imaging in Solids Using Wave Mode Beamforming." IEEE Transactions on Ultrasonics, Ferroelectrics, and Frequency Control, 64(3), pp. 602-616.

[11] Sternini, S., Quattrocchi, A., Montanini, R., Pau, A., and Lanza di Scalea, F., 2017, "A match coefficient approach for damage imaging in structural components by ultrasonic synthetic aperture focus," Procedia Engineering, 199, pp. 1544-1549.

[12] Hall, J. S., and Michaels, J. E., 2010, "Minimum variance ultrasonic imaging applied to an in

situ sparse guided wave array," IEEE Transactions on Ultrasonics, Ferroelectrics, and Frequency Control, 57(10), pp. 2311-2323.

[13] Frazier, C. H., and O'Brien, W. D., 1998, "Synthetic aperture techniques with a virtual source element," IEEE Transactions on Ultrasonics, Ferroelectrics, and Frequency Control, 45(1), pp. 196-207.

[14] Martin-Arguedas, C. J., Romero-Laorden, D., Martinez-Graullera, O., Perez-Lopez, M., and Gomez-Ullate, L., 2012, "An ultrasonic imaging system based on a new SAFT approach and a GPU beamformer," IEEE Transactions on Ultrasonics, Ferroelectrics, and Frequency Control, 59(7), pp. 1402-1412.

Chapter 5

Ultrasonic Synthetic Aperture Imaging with Interposed Transducer-Medium Coupling Path

Abstract

An interposed coupling material between an ultrasonic transducer and the test medium can be present in various non-destructive inspections and structural health monitoring imaging applications. One example is the wedge medium often used to direct ultrasonic beams into the test material for optimal interaction with internal defects. Another example is the ultrasonic imaging of multilayered structures. This paper discusses ways to perform Synthetic Aperture Focus (SAF) ultrasonic imaging in these cases where signal losses and complicated refractions at the coupling material/medium interface take place. Three main steps are proposed to maximize image quality. The first step is the Delay-Multiply-and-Sum (DMAS) algorithm that increases the number of independent terms in the beamforming equation compared to the Delay-and-Sum (DAS) algorithm. The second step is the utilization of a ray tracing algorithm to properly account for the refraction of the waves in both transmission and reflection paths, and accounting for both L-waves

and S-waves that can potentially propagate. The compounding of multiple wave mode combinations is the third step proposed to significantly improve image quality. Validating experiments are presented for a transducer array on a wedge to image two closely-spaced holes in an aluminum block. The DMAS algorithm and wave mode compounding algorithm are also in principle applicable to other structural health monitoring imaging approaches that use, for example, sparse transducer arrays and guided-wave probing.

5.1 Introduction

Ultrasonic imaging in both Non-Destructive Evaluation (NDE) and Structural Health Monitoring (SHM) often presents the need to detect reflectors (defects) that are not easily accessible from surface probing. In certain cases, the reflection of the ultrasonic waves from the discontinuity may not be directed in a favorable orientation for array detection due, for example, to the particular location, orientation and/or geometry of the reflector. In other cases, the structure to be imaged has a multilayered geometry that requires accessing an internal layer from transducers placed on the outer layer. The use of a transducer wedge is a classic case of interposed medium (Figure 5.1(a)). The wedge is connected to the ultrasonic array and allows to direct the ultrasonic wave energy along a preferred direction to maximize the detection of reflections. This kind of transducer wedges are widely employed in industrial applications of ultrasonic imaging, such as pipeline inspections and weld examinations [1-3]. Another typical application of transducer wedges for ultrasonic imaging is ultrasonic inspection of railroad tracks, and specifically the detection of “Transverse Defects” (TDs) that usually grow at a 20° orientation from the vertical direction [4]. In cases of non-contact imaging techniques, an interposed air or liquid layer is also present between the transducer and the test medium [5].

Ultrasonic imaging through an interposed layer is applicable to either portable transducer systems operated in a manual or in a scanning mode, or to transducers rigidly connected to the test part for continuous monitoring. One example of the latter case is the monitoring of dry storage casks that house spent nuclear fuel [6] (Figure 5.1(b)). These structures are made of a steel-concrete multilayer that is highly inaccessible by routine inspections because of the harsh environment and their often underground placement. In these cases, ultrasonic arrays have to be permanently fixed rather than periodically placed by an operator.

In various applications of ultrasonic imaging, phased arrays are used to inspect different portions of the medium by dynamic beam focusing and beam steering [7-12]. This is achieved by well-known focus laws that require multiple simultaneous active channels to the array transmitters, that also need to be controlled individually, in order to physically focus the transmitted beam. Hence the transmission hardware of phased-array probes can be fairly complex.

Synthetic Aperture Focus (SAF) techniques can be more practical especially for ultrasonic imaging applications that require a large transducer array and/or fast image rate. SAF techniques have been used for decades in applications spanning from medical diagnostic imaging [13-24] to non-destructive testing of solids [3, 5, 14, 25-32]. The SAF approach does not require multiple and individual control of the transmission channels. It instead allows a much simpler hardware architecture because the beamforming focusing is done synthetically (rather than physically) in both transmission and reflection.

Common imaging techniques such as the Total Focusing Method (TFM), which uses the Delay-and-Sum (DAS) beamformer, create the images by intersecting various elliptical focus lines based on transmitter-receiver pairs. An improved beamforming algorithm that builds on DAS is the Delay-Multiply-and-Sum (DMAS) beamformer [33, 34], initially introduced by Lim *et al.* [35]

in a study of RADAR imaging for breast cancer applications. Matrone *et al.* [33, 34] developed an improved version of the DMAS algorithm for B-mode medical imaging. Most of these previous works on DMAS were not implemented using the SAF technique, besides a work by Matrone *et al.* [34] where the DMAS algorithm was implemented using a modified version of SAF, called Synthetic Transmit Aperture (STA).

Another strategy used in SAF imaging to increase array gain without increasing the physical array aperture is compounding images obtained with multiple independent information. Compounding exploits the consistency of the true reflectors and the randomness of the spatial noise through the different images. This idea is used, for example, in underwater acoustics and matched field processing [37] (where images obtained from different frequencies are compounded) and in ultrafast biomedical imaging (where different transmission modes are compounded, e.g. plane-wave modes [22] or diverging-wave modes [23]). The author of this dissertation recently worked on a project proposing to compound longitudinal and shear waves to significantly enhance SAF images of solid media [32].

Another technique commonly used in underwater acoustics and tomography is ray tracing [12, 38-40]. Ray tracing allows computing the only physically possible wave propagation paths and allows to track changes along these paths. The rays are computed following Fermat's principle [12], which allows to identify the paths of least travel time between two points. This technique represents a simplification of the actual wavefield and propagation behavior, which can be complex to model. Imaging of the test medium can be performed by computing the rays that propagate between transmitter-receiver pairs (so-called eigenrays) and then tracking the medium changes (e.g. wave speed changes or scatterers) along the ray paths.

An extension of ray tracing to ultrasonic imaging through an interposed layer is presented in this paper, along with an application of the mode compounding and the DMAS improved algorithm. Specifically, the aim of this work is to enhance the imaging of discontinuities whose orientation, geometry and/or location are such that an interposed coupling path is required between the transducer and the test medium for optimum detection via ultrasonic transmissions and reflections.

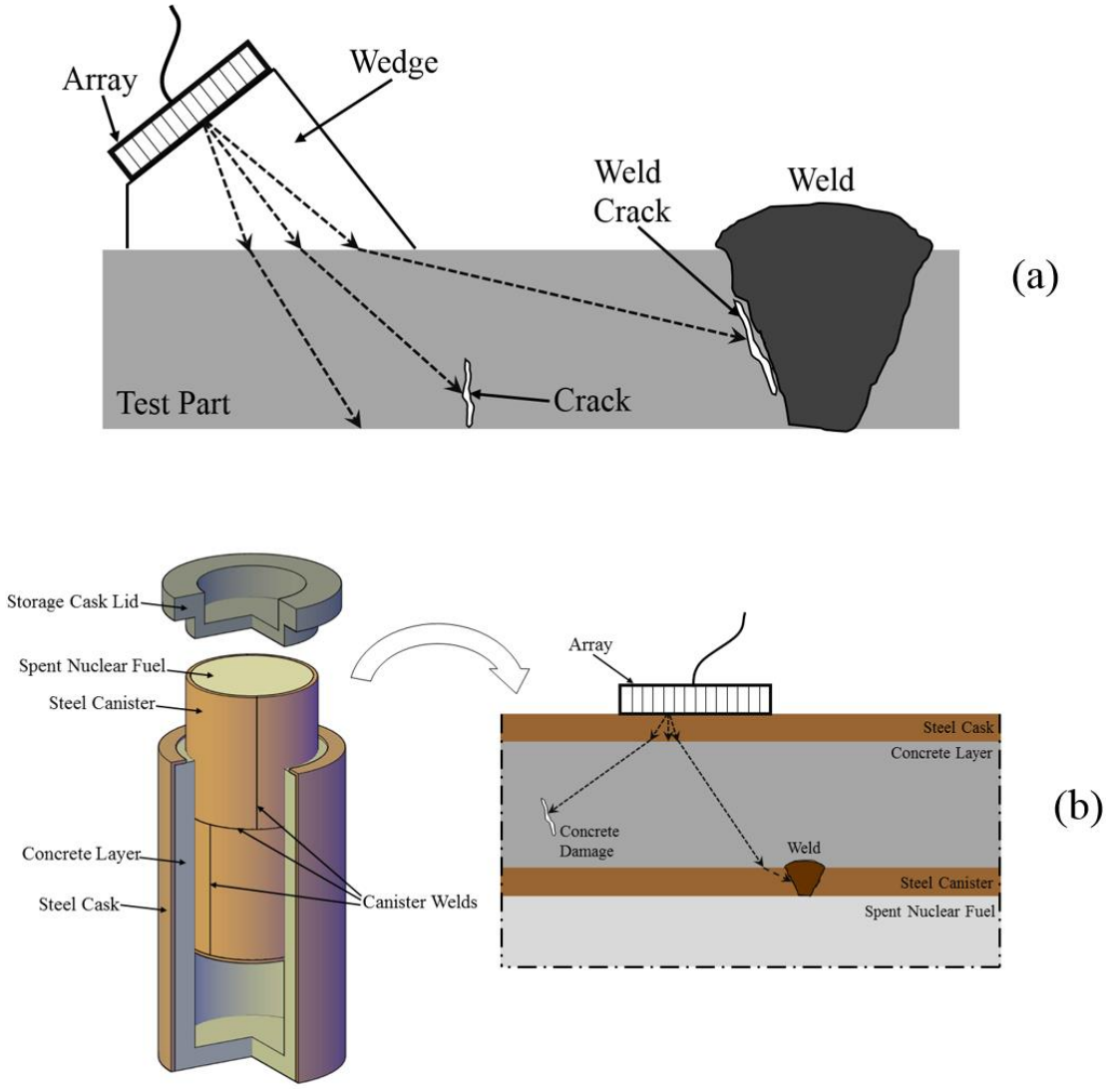

Figure 5.1: Ultrasonic imaging through interposed layer. (a) Transducer wedge. (b) Monitoring of multilayered structures (e.g. dry storage cask for spent nuclear fuel)

5.2 SAF Imaging Algorithm with Interposed Coupling Path

This section presents the various steps that are being proposed for an effective ultrasonic imaging that requires an interposed coupling path between the SAF transducer array and the test medium. These steps include: DMAS beamforming, ray tracing algorithm, and wave mode compounding. While the formulation discussion refers to the case of the wedge, the algorithms proposed are equally applicable to arrays monitoring multilayered structures (e.g. the case shown in Figure 5.1(b)).

5.2.1 Delay-Multiply-and-Sum Beamformer

A diagram of the DMAS algorithm is shown in Figure 5.2. Consider an ultrasonic transducer array consisting of *M* transmitters and *N* receivers. Let the spatial coordinates of transmitters $i = 1 \ldots M$ and receivers $j = 1 \ldots N$ be (x_i, y_i) and (x_j, y_j), respectively. The SAF-DMAS algorithm computes an image $I(x, y)$ by summing, at each pixel $P(x, y)$, the amplitudes A extracted from the received signals, after appropriate backpropagation and combinatorial multiplication. Analytically:

$$I^{DMAS}(x,y) = \sum_{k=1}^{L-1} \sum_{l=k+1}^{L} sign(A_k(\tau_{k,xy}) \cdot A_l(\tau_{l,xy})) \cdot \sqrt{\left| A_k(\tau_{k,xy}) \cdot A_l(\tau_{l,xy}) \right|} \qquad (5.1)$$

where $\tau_{k,xy}$ and $\tau_{l,xy}$ are the backpropagation times corresponding to the *k-th* and *l-th* transmitter-receiver pairs, respectively, and focus point $P(x, y)$. Each *l-th* combination, or similarly *k-th*, is formed by a different transmitter-receiver pair *i,j*. This explains why in equation (5.1) the indices *i* and *j* do not appear, but instead the combination indices *k* and *l* are used.

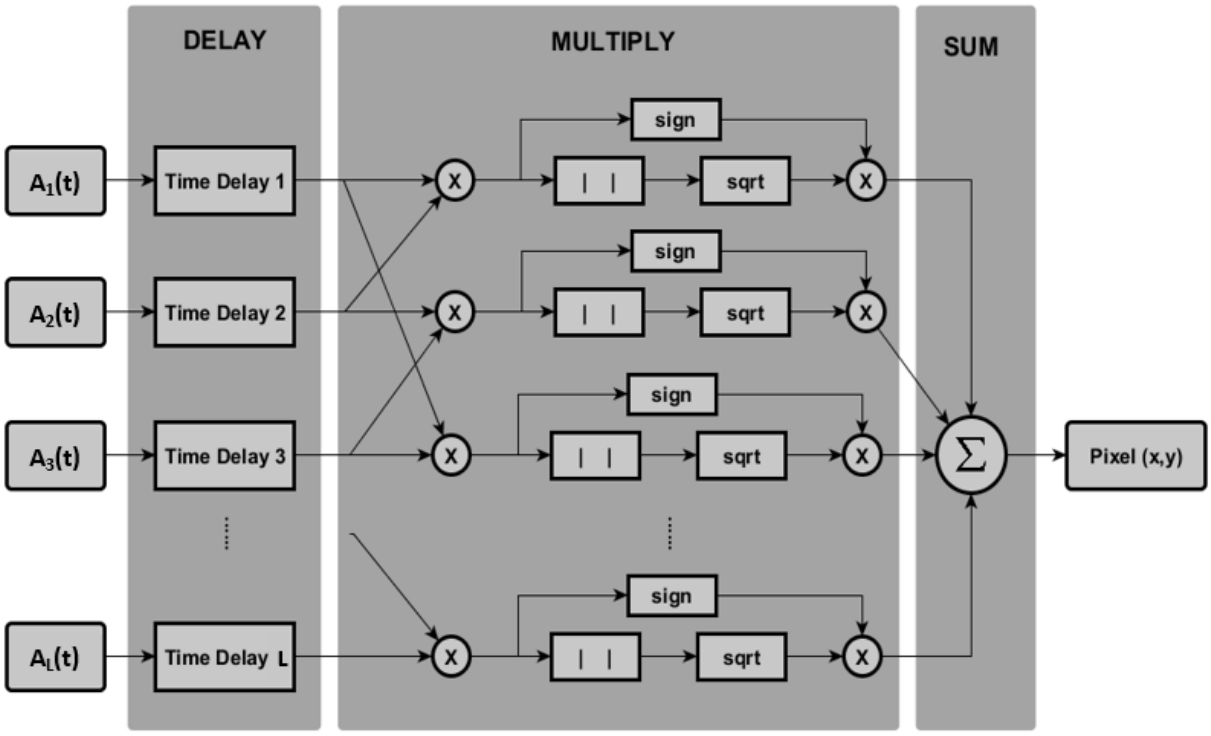

Figure 5.2: Schematic of the DMAS algorithm

$L = M \cdot N$ represents the total number of recorded waveforms obtained using the SAF technique. Equation (5.1) shows that the amplitudes A, after being backpropagated, are combinatorially multiplied following all the possible signal pair combinations. In this way, it is possible to exploit the correlation between signals belonging to the same transmission cycle, as well as the correlation between signals recorded during different sensor firings, thus increasing the overall array gain compared to a traditional DAS beamforming. As equation (5.1) shows, the "signed" square root is applied to the absolute value of the amplitudes obtained from combinatorial multiplication, in order to recover the correct units (Volts) of the partially rectified non-zero mean signals. The recovery of the sign after the square root is crucial in order to ensure the proper destructive interference of the noise in the signals. The difference between the procedure showed in equation (5.1) and the work by Matrone *et al.* [34] lies in the way the transmission cycles are combined. In fact, Matrone [34] takes the waveforms recorded by the receivers from different

transmissions and sums them up (summation over transmissions) to obtain the final set of signals to be used in the DMAS algorithm. In the present paper, the waveforms from different transmissions are treated independently during the combinatorial multiplication, in order to increase the total number of combinations in the imaging process.

Where DAS builds the image at each point from only L summation terms, the number of terms utilized by DMAS is as large as:

$$\binom{L}{2} = \frac{L^2 - L}{2} \tag{5.2}$$

In equation (5.2), the auto-products (signals multiplied with themselves) and the double multiplications ($A_k \cdot A_l$ and $A_l \cdot A_k$ terms) are excluded from the count. Since after multiplication the signal is dimensionally squared and partially rectified, the "signed" square root is applied to the absolute value of each pair of multiplied amplitudes.

As in classical DAS, the backpropagation time $\tau_{k,xy}$ depends on the location of the elements of the *k-th* transmitter-receiver pair and that of the focus point $P(x,y)$. The wave propagation paths to focus point P for a transmitter-receiver pair i,j are shown in Figure 5.3(a). Of importance here is the refraction of both transmitted wave and reflected wave at the wedge/medium interface. We will also consider a longitudinal (L-) wave propagation in the wedge material, while allowing both a longitudinal (L-) wave and a shear (S-) wave propagation in the test medium. This assumption reflects the fact that typical ultrasonic transducer arrays with a conventional gel coupling layer generate and detect mostly L-waves. The S-wave mode can then be generated through refractions at the wedge/medium interface and/or from mode-conversions at the reflector. In this general situation, the backpropagation time for the i,j pair can be expressed as:

$$\tau_{k,xy} = \tau_{ij,xy} = \frac{d_{i,xy}^{(1)}}{c_{LW}} + \frac{d_{i,xy}^{(2)}}{c_{L,S}} + \frac{d_{j,xy}^{(3)}}{c_{L,S}} + \frac{d_{j,xy}^{(4)}}{c_{LW}} \tag{5.3}$$

In equation (5.3), c_{LW} is the L-wave velocity in the wedge material, and $c_{L,S}$ are the L-wave and S-wave velocities in the test medium, respectively. The terms at the numerators represent the paths traveled by the wave from the *i-th* transmitter, to focus point $P(x, y)$, and back to the *j-th* receiver. Since refraction at the wedge/medium interface deflects the wave paths through Snell's law, transmitters (or similarly receivers) will not be connected to the focus point by straight paths. Hence the total wave path must be divided into four portions, namely the transmitter to wedge/medium interface distance, $d_{i,xy}^{(1)}$, the wedge/medium interface to focus point distance, $d_{i,xy}^{(2)}$, the focus point to wedge/medium interface distance, $d_{j,xy}^{(3)}$, and the wedge/medium interface to receiver distance, $d_{j,xy}^{(4)}$. In order to best express these distances, the array element locations are projected to "virtual" locations at the wedge/medium interface, as shown in Figure 5.3(a). The "virtual" locations satisfy the physics of the refracted wave for a given focus point and wave mode. In this case, the four wave distances of equation (5.3) can be calculated by:

$$d_{i,xy}^{(1)} = \sqrt{(x_i - x_{VIRT,i})^2 + (y_i - y_{VIRT,i})^2} \tag{5.4}$$

$$d_{i,xy}^{(2)} = \sqrt{(x_{VIRT,i} - x)^2 + (y_{VIRT,i} - y)^2} \tag{5.5}$$

$$d_{j,xy}^{(3)} = \sqrt{(x_{VIRT,j} - x)^2 + (y_{VIRT,j} - y)^2} \tag{5.6}$$

$$d_{j,xy}^{(4)} = \sqrt{(x_j - x_{VIRT,j})^2 + (y_j - y_{VIRT,j})^2} \tag{5.7}$$

where (x_i, y_i) and (x_j, y_j) are the coordinates of the *i-th* transmitter and *j-th* receiver respectively, (x, y) are the coordinates of the focus point, and $(x_{VIRT,i}, y_{VIRT,i})$, $(x_{VIRT,j}, y_{VIRT,j})$ are the coordinates of the *i-th* "virtual" transmitter and the *j-th* "virtual" receiver, respectively. The following section will utilize a ray tracing approach to derive the "virtual" array coordinates.

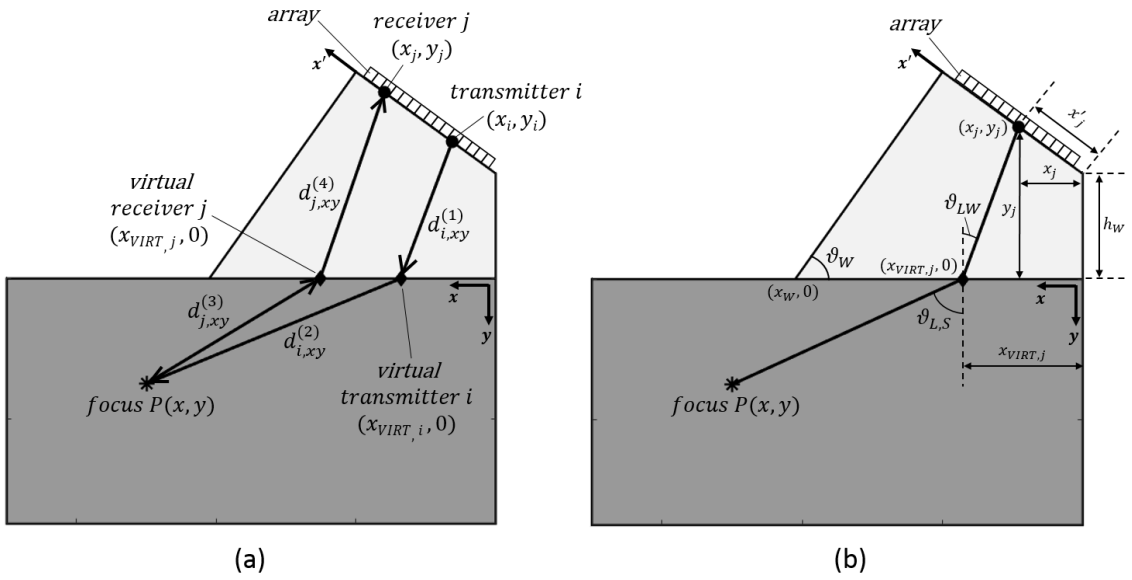

Figure 5.3: Transducer wedge imaging setup. (a) Wave propagation paths for focus point P(x,y) and a transmitter-receiver pair. (b) Ray tracing scheme for one focus point and one sensor

5.2.2 Ray Tracing

The goal of the ray tracing approach is to find the rays that connect a given focus point to the various transducer elements in the array. As stated in the previous section, due to wave refraction, these rays do not have straight paths since they bend at the wedge/medium interface, thus following the paths of least travel time described by Fermat's principle [12]. The point at the interface where a ray connecting the focus point to a transducer element bends is the "virtual" position of that transducer. The "virtual" array can then be created by finding all the rays connecting a specific focus point to the physical array. Conceptually, the "virtual" array can be thought of as the positions that the transducer elements need to have on the medium surface,

without a wedge, in order to create the same image obtained with the transducer wedge connected to the physical array.

The ray tracing algorithm is dependent on the position of the focus point $P(x, y)$, the position of the transducer on the wedge surface, and the specific wave mode considered. Following Snell's law, propagating modes with different wave speeds will have different refraction angles at the interface of two materials having acoustic impedance mismatch. Therefore, different wave modes will have different ray paths connecting the same focus point to the physical array. The mode-dependent nature of ray tracing allows the wave modes to be exploited independently as well as in combinations, to enhance the image gain, as discussed in the next section.

Let us consider the usual focus point $P(x, y)$ and a transducer element of coordinates (x_j, y_j) on the $x - y$ reference system and coordinate x'_j along the x' axis - Figure 5.3(b). Let x_b be the x-coordinate of the points at the wedge/medium interface, i.e. $0 \leq x_b < x_W$. The angle between the vertical direction and the path connecting the focus point to the points on the interface can be calculated as

$$\vartheta_{L,S}(x, y, x_b) = \arctan\left(\frac{|x - x_b|}{y}\right) \tag{5.8}$$

where $\vartheta_{L,S}$ is the angle associated to the longitudinal wave mode or to the shear wave mode, respectively. For each point $(x_b, 0)$ on the interface, there is an angle $\vartheta_{L,S}$. However, only one position (therefore only one angle) will allow the ray to reach the transducer element considered. Each ray forming an angle $\vartheta_{L,S}$ at the interface will be refracted into an angle ϑ_{LW} in the wedge, that can be calculated from Snell's law considerations as

$$\vartheta_{LW}(x, y, x_b) = \arcsin\left(\frac{c_{LW}}{c_{L,S}}\sin(\vartheta_{L,S}(x, y, x_b))\right) \tag{5.9}$$

where c_{LW} is the wave speed in the transducer wedge, $c_{L,S}$ is the longitudinal or shear wave velocity in the test medium, and $\vartheta_{L,S}$ is calculated from equation (5.8). Equation (5.9) shows that also the propagation angle in the wedge ϑ_{LW} depends on the position along the wedge/medium interface. The coordinates of the *j-th* transducer can be rotated from the x' axis to the $x - y$ reference system with the following transformations

$$x_j = x'_j \cdot \cos\left(\frac{\pi}{2} - \vartheta_W\right) \tag{5.10}$$

$$y_j = -\left(h_W + x'_j \cdot \sin\left(\frac{\pi}{2} - \vartheta_W\right)\right) \tag{5.11}$$

where ϑ_W and h_W are the wedge angle and height, respectively, also shown in Figure 5.3(b). The minus sign outside the bracket in equation (5.11) is justified by the fact that the *y* axis points down in the figure.

Considering one focus point and one transducer element, for every point on the wedge/medium interface it is possible to calculate a height h_j that represents the projection of the ray propagating in the wedge onto the vertical direction passing through the *j-th* element. On the wedge interface, at the correct "virtual" position of the element considered, the height h_j will match with the vertical coordinate y_j of the element, whereas in other locations along the interface the resulting height will be either larger or smaller than the element vertical coordinate. The height h_j can be calculated as follows

$$h_j(x, y, x_b) = (x_b - x_j) \cdot \tan\left(\frac{\pi}{2} - \vartheta_{LW}(x, y, x_b)\right) \tag{5.12}$$

where ϑ_{LW} and x_j are obtained from equation (5.9) and equation (5.10), respectively. As previously mentioned, the position x_b for which the height h_j is closest to the vertical coordinate of the *j-th* transducer element will represent the "virtual" position of that element along the wedge/medium interface. This concept can be formalized in the following expression:

$$x_{VIRT,j} = \arg\min_{x_b} \left| h_j(x, y, x_b) + y_j \right| \tag{5.13}$$

where the value of x_b that minimizes the absolute value on the right-hand side of equation (5.13) is taken as the "virtual" coordinate of the *j-th* transducer element. Notice that the summation sign inside the absolute value, instead of a minus sign, is used in equation (5.13) since the term y_j will always be negative in the $x - y$ reference system, which has the *y* axis pointing down according to Figure 5.3(b).

By repeating the ray tracing procedure presented above for each focus point in the imaging medium and each transducer element in the array, it is possible to locate the "virtual" array on the wedge/medium interface for any possible wave path. Furthermore, by changing the wave speed $c_{L,S}$ in equation (5.9), different "virtual" arrays can be derived for different wave modes. In this way, each wave mode will have unique paths connecting the various focus points to the physical array. This fact creates an opportunity for combining or "compounding" independent information from different wave modes. The following section will elaborate on this step.

5.2.3 Wave Mode Compounding

The multimodal nature of wave propagation can be successfully exploited to improve the array gain and image contrast without increasing its physical aperture. This aspect was recently considered by the authors of the present paper by exploiting both L-waves and S-waves propagating in a solid when the array is directly attached to the medium. This section extends the wave mode compounding to the case of imaging through an interposed medium.

For the case of the wedge, in general, the L-wave transmitted can be refracted as both an L-wave and an S-wave in the test medium – Figure 5.4. Both wave modes can be reflected by the discontinuity within the test medium both as same-mode reflections and as mode-converted reflections, and refract back to the L-mode in the wedge that is then finally received by the array. There can therefore exist up to four combinations of wave modes available for imaging a bulk solid using a transducer wedge: LLLL (L-wave transmitted in wedge, L-wave refracted in solid, L-wave reflected by reflector, L-wave refracted in wedge), LSLL (L-wave transmitted in wedge, S-wave refracted in solid, L-wave reflected by reflector, L-wave refracted in wedge), LLSL (L-wave transmitted in wedge, L-wave refracted in solid, S-wave reflected by reflector, L-wave refracted in wedge), and LSSL (L-wave transmitted in wedge, S-wave refracted in solid, S-wave reflected by reflector, L-wave refracted in wedge).

Figure 5.4 illustrates how different wave modes propagate along different paths when refracted at the wedge interface. Figures 5.4(a) and 5.4(b) show the propagation of the reflected S-wave and how the ray paths change for a reflection from a point $P(x_1, y_1)$ located in the near field and one from a point $P(x_2, y_2)$ located in the far field, respectively. Similarly, Figures 5.4(c) and 5.4(d) refer to the L-wave reflected in the near field and in the far field, respectively. It is important to notice how the refraction angles inside the wedge change for the different wave modes.

Consequently, the location of the "virtual" array at the wedge/medium interface changes when the wave mode combination changes, as well as when the focus point changes. The "virtual" array position is therefore adaptive to both the imaging volume and to the specific wave mode combination considered. This observation further highlights the importance of the ray tracing technique for an accurate computation of wave paths to be used in equation (5.3).

In general, compounding can be performed either incoherently [37, 41-43] or coherently [43-45]. Incoherent compounding is the simple incoherent summation of the image intensities obtained through the various wave mode combinations, and it is performed as follows

$$I_{TOT,incoherent}(x,y) = \sum_{MC=LLLL,LSLL,LLSL,LSSL} I^{MC}(x,y) \tag{5.14}$$

where the image $I^{MC}(x,y)$ (in decibels) for a given wave mode combination is calculated from equation (5.1) using the SAF-DMAS algorithm. This approach takes advantage of the consistency of the true reflector throughout the images versus the random spatial noise.

Coherent compounding differs from its incoherent version because it also includes "cross-mode" terms coming from the squaring of the final image after summation. In this way, coherence between wave mode combinations is exploited and further array gain is achieved. Hence

$$I_{TOT,coherent}(x,y) = \left(\sum_{MC=LLLL,LSLL,LLSL,LSSL} \left| \sqrt{I^{MC}(x,y)} \right| \right)^2 \tag{5.15}$$

where, as in the incoherent case, the images $I^{MC}(x,y)$ (in decibels) are given by equation (5.1). While the coherent approach should theoretically bring additional gain compared to its incoherent counterpart, the relative performance depends on the noise structure of the particular wavefield, as

is known for frequency compounding in the matched-field processing imaging community [43, 44].

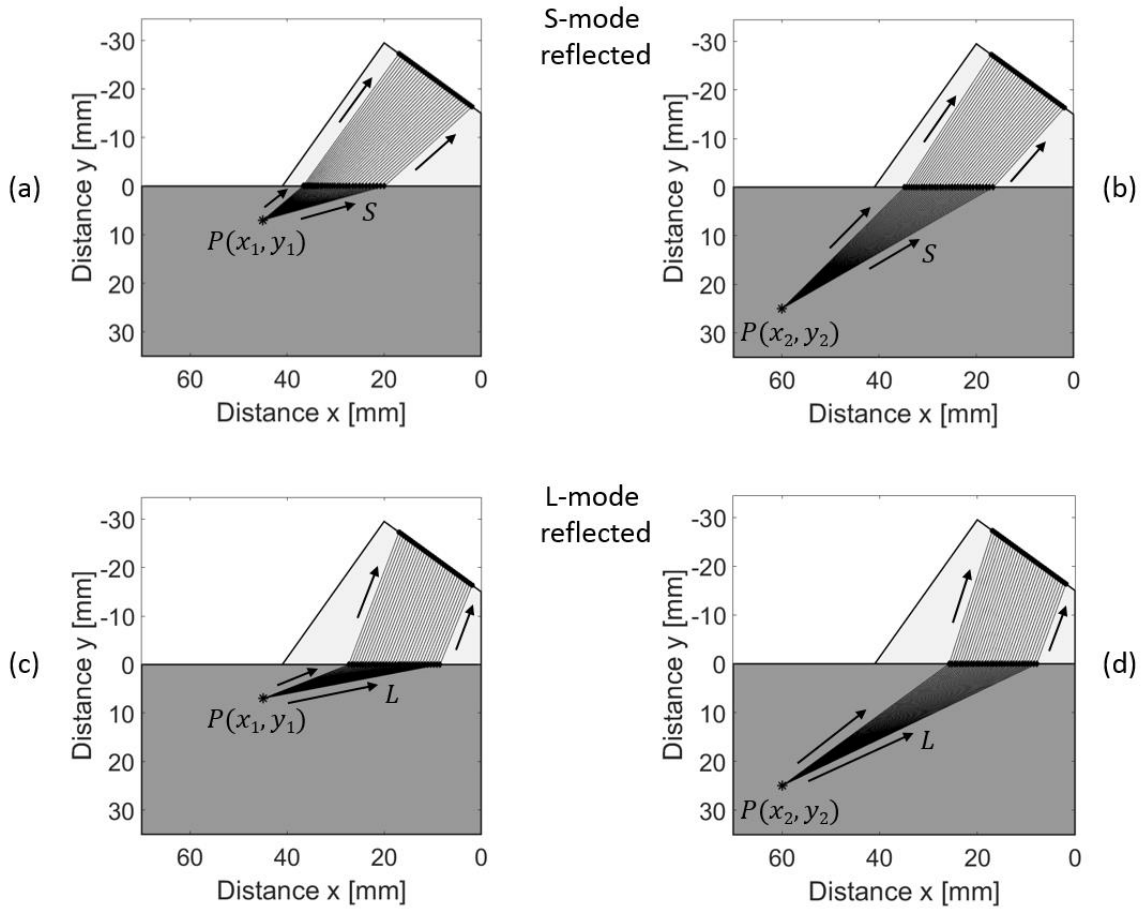

Figure 5.4: Ray paths for different propagating wave modes. (a) S-wave reflected in the near-field, (b) S-wave reflected in the far-field, (c) L-wave reflected in the near-field, and (d) L-wave reflected in the far-field

5.3 Experimental Results

An experimental test was carried out to test the SAF-DMAS algorithm using the transducer wedge implemented with the ray tracing technique and mode compounding. Figure 5.5 shows the experimental setup. The test piece used was an aluminum block with two 2.5 mm-diameter holes drilled at about 12 mm from the top surface. The distance between the two holes was 6 mm. The probe used was a 32-element linear array (Olympus NDT P/N 2.25L32-19.2X10-A11-P-2.5-HY),

with central frequency at 2.25 MHz, 19.2 x 10 mm total active aperture, and 0.6 mm element pitch. The wavelengths of the ultrasonic waves in aluminum were 2.8 mm and 1.4 mm for the L-wave and the S-wave, respectively. The transducer wedge connected to the probe was a Rexolite wedge (Olympus NDT SA11-N55S), 41.3 mm in length, 15 mm in height (h_W parameter in equation (5.11)), and 54° wedge angle (ϑ_W parameter in equations (5.10) and (5.11)).

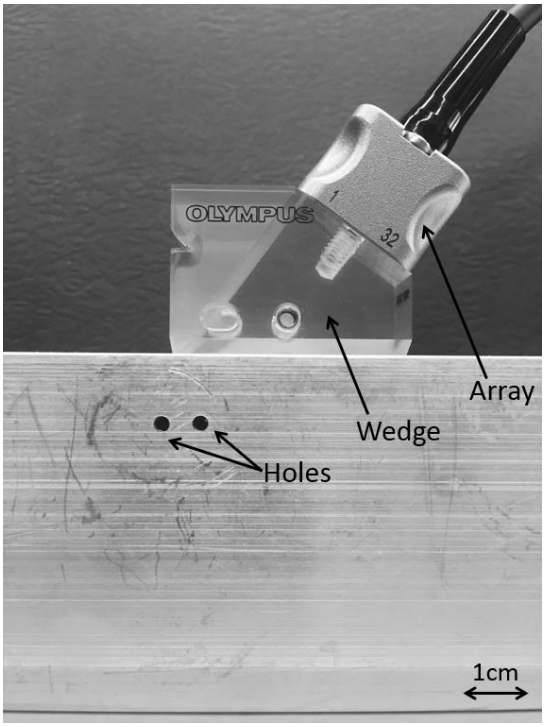

Figure 5.5: 32-element linear array with transducer wedge on the aluminum block with two closely-spaced reflector holes

The array was connected to a Full-Matrix Capture (FMC) controller (Advanced OEM Solutions, Cincinnati, OH, USA) generating pulsed excitations and allowing to access raw RF waveforms in reception. The array was connected to the transducer wedge by means of two screws in order to guarantee a rigid connection. Conventional ultrasonic gel-couplant was applied between the array and the wedge before connecting them, as well as at the wedge/aluminum interface to ensure proper transmission/reception of the ultrasonic waves. The experiments were conducted using a 32 x 32 FMC scheme, with each transducer in the array firing sequentially, and all

transducers receiving at each firing (giving a total of 1024 waveforms). Using the SAF-DMAS algorithm, each of the 1024 raw waveforms was combinatorially multiplied with the other waveforms in the set. According to equation (5.2), 1024 waveforms generated a total number of 523,776 combinations. As discussed previously, the large number of combinations, resulting in increased image contrast, is the advantage of the DMAS algorithm versus the traditional DAS algorithm.

5.3.1 Comparison DAS and DMAS. Validation of Ray Tracing Algorithm

The first test was performed to assess the performance of the SAF-DMAS algorithm compared to a conventional SAF-DAS algorithm, as well as to validate the ray tracing technique. The DAS formulation [20] uses the well-known double summation:

$$I^{DS}(x,y) = \sum_{i=1}^{M}\sum_{j=1}^{N} w_{ij,xy} A_{ij}(\tau_{ij,xy}) \tag{5.16}$$

where M is the number of transmitters, N is the number of receivers, A_{ij} is the amplitude extracted from the i,j transmitter-receiver pair, τ is the back-propagation time, and w is the apodization weight that helps improve the array focus. For the purpose of this comparison, the apodization weights were chosen as static unity weights. The back-propagation times in equation (5.16) were calculated using the conventional time of flight calculation (no transducer wedge and no ray tracing) used in TFM for the results shown in Figures 5.6(b), 5.6(c), and 5.6(d). For Figures 5.6(f), 5.6(g), and 5.6(h), since the transducer wedge was used, ray tracing was applied to compute the time delays in equation (5.16).The comparison was carried out using an ultrasonic array with and without the interposed wedge. Figure 5.6(a) shows the set-up for the first part of this test, where no transducer wedge was applied. Figures 5.6(b) and 5.6(c) show the imaging results obtained with

DAS and DMAS algorithms, respectively. Both images are displayed with a 50-dB dynamic range. For these results, the wave mode combination used was the LL combination (L-wave transmitted, L-wave reflected). From the images, it is clear that the DMAS algorithm significantly lowers the noise floor thereby increasing image contrast and spatial resolution compared to the DAS algorithm. As discussed above, the improvement is a result of the increased number of terms in the beamforming summation (523,776 terms for DMAS versus 1024 terms for DAS in the present experiment). To further highlight the algorithms' performance, the amplitude distributions computed at a depth of 12 mm (dashed line in Figures 5.6(b) and 5.6(c)) are plotted in Figure 5.6(d). This figure further highlights the improvements obtained by DMAS in terms of dynamic range and spatial resolution. Dynamic range (dB difference between the reflector peaks and the average noise floor) has an average improvement of ~25 dB compared to the DAS result. The spatial resolution (width of the reflector lobes) also improves as the two main lobes obtained with DMAS are sharper than those obtained with DAS. Specifically, the width of the main lobe at -6 dB with DMAS and DAS is 1.59 mm and 2.43 mm, respectively. Furthermore, DAS can only resolve the two closely-spaced reflectors up to a dynamic range of -25 dB, whereas DMAS resolves the two reflectors up to -65 dB.

The second part of the experimental test was aimed at validating the ray tracing algorithm in the case of the transducer wedge. Figure 5.6(e) illustrates the schematic of the test with the transducer wedge. Figures 5.6(f) and (g) show the imaging results obtained with DAS and DMAS algorithms, respectively, both implemented using the ray tracing technique and displayed in a 50-dB dynamic range. Here, the wave mode combination considered was the LSSL combination (illustrated in the wave mode compounding section). The ray tracing technique correctly locates the two drilled holes in the test medium by taking into account the refraction of the waves at the

wedge/medium interface, and by considering the correct propagation paths in the medium and in the wedge. If the ray tracing algorithm represented incorrect wave paths, the locations of the reflectors in the image would be inaccurate (in some cases not reconstructed).

Furthermore, Figures 5.6(f) and 5.6(g) confirm the improvements of the DMAS algorithm versus the DAS algorithm in the transducer wedge case, with the evident decrease in noise floor and increase in image contrast. Figure 5.6(h) illustrates the amplitude distributions obtained with the transducer wedge, showing an average improvement in dynamic range of ~ 30dB from the DMAS compared to the DAS. Similar improvements from DMAS are seen in spatial resolution, with a -6 dB lobe width of 0.5 mm compared to 0.61 mm of DAS, and an increased ability to resolve the two reflectors up to a dynamic range of -70dB, compared to -40 dB of DAS.

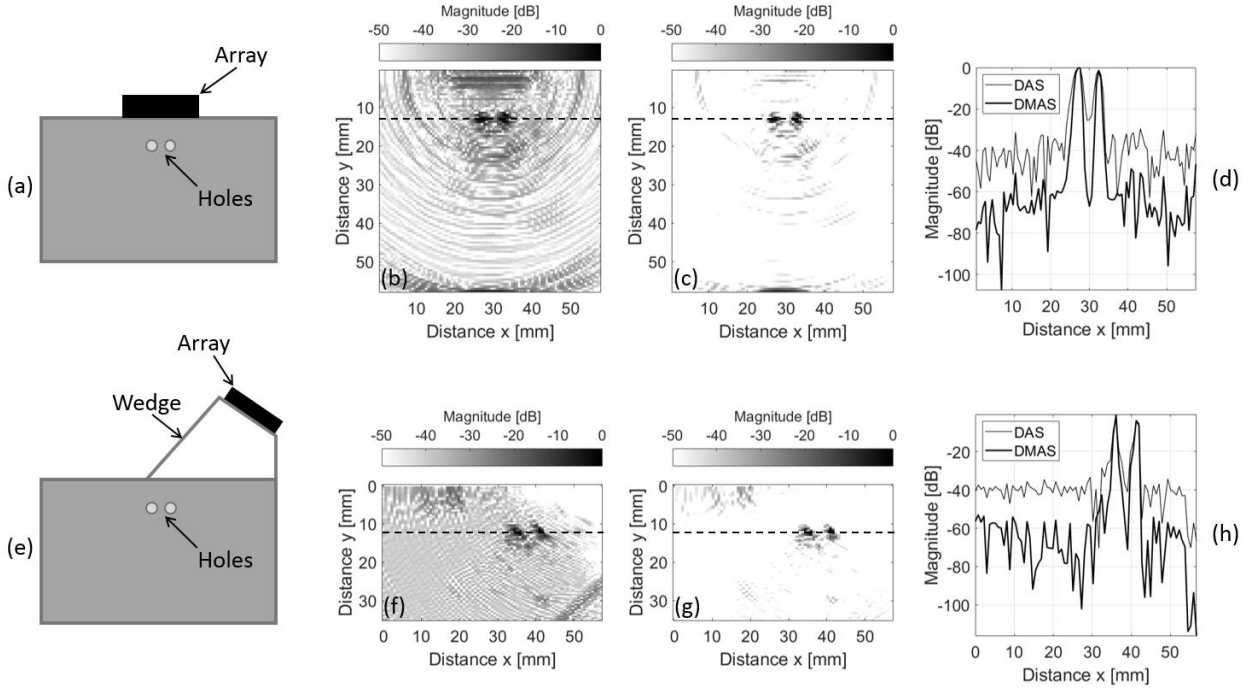

Figure 5.6: Experimental comparison of DAS and DMAS algorithms with and without transducer wedge. (a) Schematic of the imaging setup without wedge. (b) and (c) DAS and DMAS imaging results without wedge, respectively. (d) Amplitude distributions of DAS and DMAS from images (b) and (c). (e) Schematic of the imaging setup with transducer wedge. (f) and (g) DAS and DMAS results with wedge, respectively. (h) Amplitude distributions of DAS and DMAS from images (f) and (g). The LL and the LSSL wave mode combinations were used to obtain the images without wedge and with wedge, respectively

5.3.2 Demonstration of Wave Mode Compounding

The second objective of the experimental tests was to demonstrate the power of wave mode compounding in the transducer wedge case. The four aforementioned mode combinations (LLLL, LSLL, LLSL, LSSL) were considered. The ray tracing algorithm was modified according to each combination in order to take into account different refraction behaviors for wave modes with different velocities.

Figure 5.7 shows the four images computed separately from each of the four wave mode combinations using the DMAS algorithm. All images are displayed with a 50-dB dynamic range. Figure 5.7(a) was obtained using the LSSL combination, i.e. by considering only the S-wave in the aluminum test medium. This image shows the best result among the four combinations in terms of dynamic range and spatial resolution. It is not surprising that the S-wave performs well in spatial resolution, since its wavelength is roughly half that of the L-wave. Figures 5.7(b) and (c) were generated using the LLSL and LSLL combinations, respectively. These two images appear very similar because the combinations of wave modes considered have similar backpropagation times, therefore the features extracted from the recorded waveforms carry similar information. Furthermore, the two combinations do not perform greatly in terms of dynamic range, mainly due to the low energy carried by these wave modes. This low energy content may be explained by a poor mode conversion at the reflectors, from L-wave to S-wave and vice versa. Finally, Figure 5.7(d) shows the image obtained using the LLLL combination, therefore when only the L-wave is considered in the aluminum medium. The image shows a good performance in terms of dynamic range, due to the high energy carried by the L-wave, but a poor spatial resolution due to the larger wavelength of the L-mode. The fact that all four images locate correctly the general position of the reflector indicates that the ray tracing algorithm performed as expected in each case.

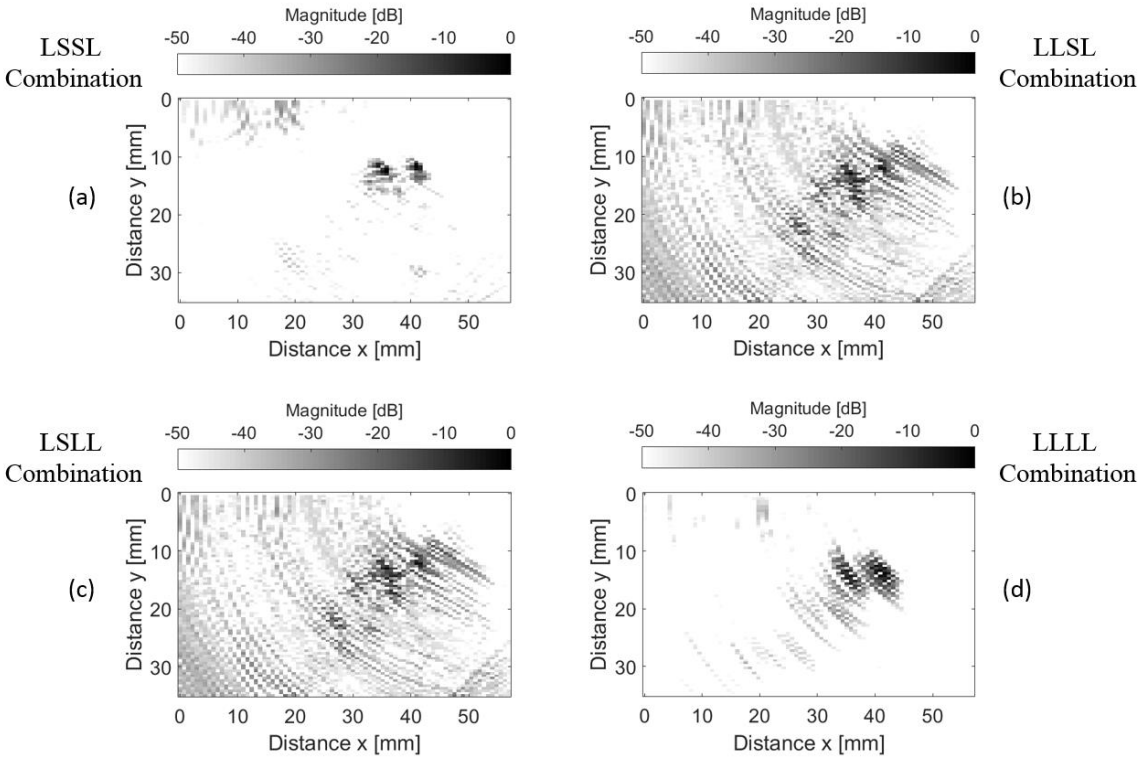

Figure 5.7: Images obtained from the experimental test of the aluminum block with two reflectors using the SAF-DMAS beamforming considering four different wave mode combination: (a) LSSL, (b) LLSL, (c) LSLL, and (d) LLLL

Once all the images from the different mode combinations were obtained, the final step was wave mode compounding. Both incoherent and coherent compounding were performed. The incoherent compounding, computed from equation (5.14), is shown in Figure 5.8(a), and the coherent compounding from equation (5.15) is shown in Figure 5.8(c). Both compounding methods dramatically improve image contrast and focus compared to the individual mode combination images of Figure 5.7, as a result of the significant increase in array gain. Specifically, incoherent and coherent compounding show an average noise floor of ~ -210dB and ~ -850dB, respectively, compared to the much higher average noise floors obtained with the individual wave mode combinations of Figure 5.7 (-67dB for the LSSL combination, -47dB for the LLSL and LSLL combinations, and -65dB for the LLLL combination). The improvement in terms of average dynamic range is therefore about 140 to 160dB with the incoherent compounding, and about 780

to 800dB with the coherent compounding. The dynamic range in Figures 5.8(a) and (c) is extremely large, with incoherent and coherent compounding displayed in an 80-dB and 220-dB range, respectively. Furthermore, these images are also well focused on the two reflectors, with the best focus obtained from the coherent compounding due to the added cross-mode terms.

Figures 5.8(b) and (d) show the amplitude distributions for incoherent and coherent compounding, respectively, and their comparison with the LLLL and LSSL combinations. The LLSL and LSLL combinations have been omitted for ease of visualization. The amplitude distributions were extracted from Figures 5.8(a) and (c) at the reflectors' location (y = 12mm). Figure 5.8(b) shows that incoherent compounding increases dynamic range and spatial resolution, when compared to the individual wave mode combinations, by lowering the noise floor and narrowing the main lobes. Specifically, the spatial resolution achieved by incoherent compounding is ~ 0.3mm (width of main lobe at -6dB), whereas the LLLL and the LSSL combinations can only achieve values of ~ 1.2mm and ~ 0.9mm, respectively. Similarly, Figure 5.8(d) illustrates the dramatic improvements deriving from coherent compounding in terms of increased dynamic range and spatial resolution (the dynamic range was plotted until -350dB for ease of comparison with the individual mode combinations). In particular, the spatial resolution obtained in the coherent case is ~ 0.04mm. The amplitude distributions also show that coherent compounding performs better than the incoherent version, since the added cross-mode terms bring additional improvements to dynamic range and spatial resolution.

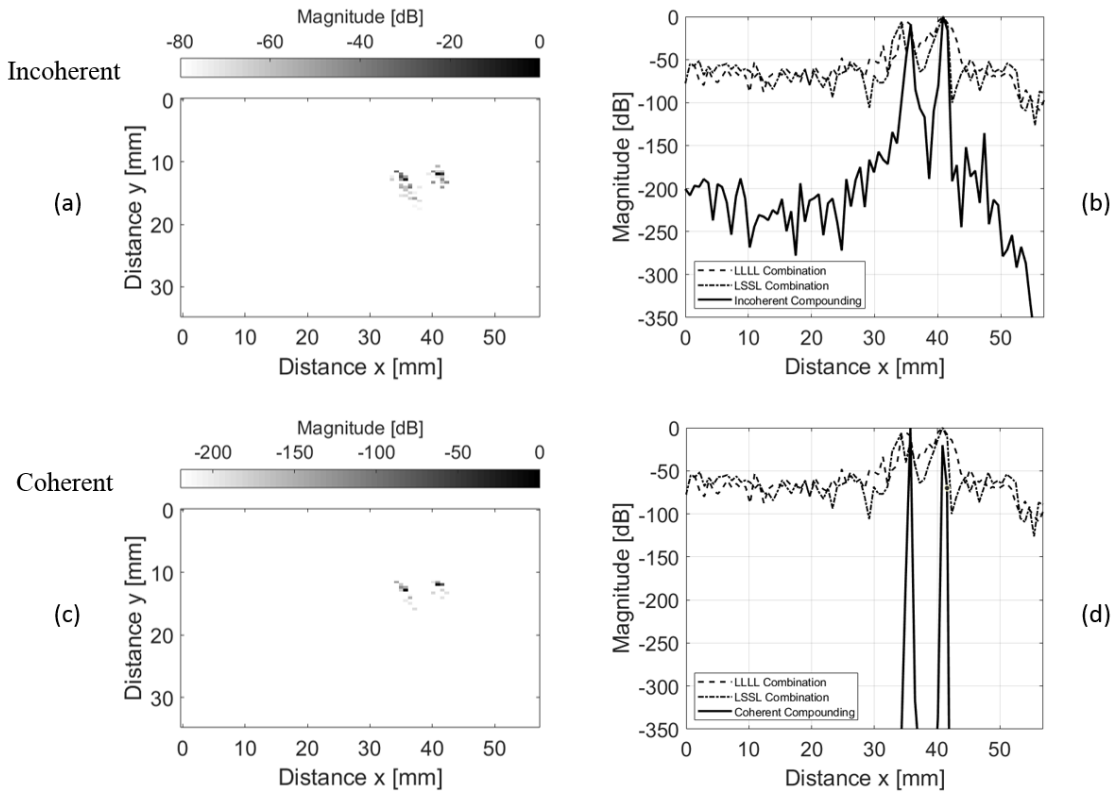

Figure 5.8: (a) and (c) Images obtained from the experimental test of the aluminum block with two reflectors by compounding the LSSL, LLSL, LSLL, and LLLL wave mode combinations in SAF-DMAS beamforming incoherently and coherently, respectively. (b) and (d) Amplitude distributions from incoherent and coherent compounding, respectively, compared with the distributions from the LLLL and LSSL combinations

5.4 Discussion and Conclusions

This paper has investigated ways to improve the performance of SAF ultrasonic imaging of internal discontinuities in cases where an interposed medium is present between the ultrasonic transducers and the test region. This is the case, for example, of a transducer wedge used to properly direct the ultrasonic beams for optimum interaction with the defects, or the case of monitoring multilayered structures with defects present in internal layers and only the outer layer being accessible for transducer installation. These cases can exist in both routine-type NDI inspections and in continuous SHM monitoring systems. Other examples where an interposed layer is present between the ultrasonic transducer and the test medium are non-contact imaging techniques through air or liquid couplants. While the primary focus of the paper is the imaging of

solid media, all considerations (with the exception of the S-wave propagation) also apply to the imaging of biological materials using ultrasonic arrays and interposed coupling paths.

The paper examines these problems in a Synthetic Aperture Focus (SAF) framework rather than in a Phased-Array (PA) framework. Clearly, the presence of an intermediate path complicates the imaging effort by adding unavoidable losses in signal amplitude and mode-dependent beam bending through refractions at the added interfaces. These factors affect both transmitted waves and reflected waves. Therefore, a particularly careful choice of the algorithmic steps is required to obtain satisfactory imaging performance in these cases.

The first step proposed in this paper is the use of the DMAS beamformer that substantially increases the number of summation terms compared to the traditional DAS beamformer. Consequently, the DMAS beamformer achieves increased dynamic range and spatial resolution of the image. This beamformer is applicable to both compact transducer arrays and to sparse transducers such as those used for guided-wave SHM imaging.

The second step proposes a ray tracing algorithm to properly account for the complicated wave refractions at the wedge-medium interface. The algorithm considers that both L-waves and S-waves can propagate in the bulk of the test medium, and it computes the individual propagation paths (from each transmitting array element to each focus point and back to each receiving array element) for each possible wave mode combination. The ray tracing algorithm identifies a "virtual" position of the array elements projected at the wedge/medium interface. Such "virtual" array is adaptive to both the specific wave modes and the specific focus point in the imaging medium.

Considering both L-mode and S-mode propagating in the medium is consistent with the SAF framework of ultrasonic imaging and generalizes the typical and limitative assumption of ultrasonic wedge transducers that only S-waves can be used for reflector detection. This limitation

is only correct in cases where all the array elements are fired simultaneously to create a "global" wavefront within the wedge that propagates at the wedge angle and is then refracted at the interface with the test medium. According to Snell's law, in this case, if the wedge angle is below the critical angle for the L-mode in the test medium, that mode will be "rejected" and only the S-mode will propagate to the reflector. In the case of SAF with ray tracing, there is no global wavefront propagating in the wedge, but rather only one spherical wavefront for each element firing. The spherical wavefront is incident to the wedge/medium interface at multiple angles, some of which are above the critical angle of the wave mode that would be otherwise reflected out in presence of a global wavefront. Since each element fires separately, both L-mode and S-mode can be refracted inside the test medium. Since each focus point corresponds to a unique set of ray paths for a given wave mode, the SAF-DMAS imaging algorithm with ray tracing is capable of simultaneously inspecting multiple locations inside the test medium without the need to change any focal law in transmission or the angle of the transducer wedge.

The fact that both L-waves and S-waves in the test medium are utilized brings the opportunity to increase the array gain without increasing its physical aperture by wave mode compounding. This is the third step proposed in this paper. Compounding can be performed incoherently and coherently, analogously to the combination of multiple frequencies or multiple excitations, and brings additional significant improvements to dynamic range and spatial resolution of the images. While compounding has been discussed here in the context of bulk wave (L and S) in three-dimensional solids, the idea could be also applied to the case of plate-like structures supporting guided waves which are, by their very nature, multimode. The authors are currently working on this extension.

Experimental validation tests were performed using a 32-element linear array, operated in FMC mode, on an aluminum block with two closely-spaced simulated reflectors (drilled holes). The first validation was conducted for the SAF-DMAS algorithm both with and without the wedge. The second validation was conducted for the ray tracing algorithm when using the wedge. Finally, wave mode compounding was demonstrated by combining the images from four different wave mode combinations (LLLL, LSSL, LSLL, and LLSL) resulting in an excellent image of the two reflectors despite the wedge interposition.

Acknowledgements

Team member at UCSD Albert Liang collaborated with this research. This work was supported by the U.S. Federal Railroad Administration under contract no. DTFR5316C00024 (Dr. Robert Wilson, Program Manager) and in part by the U.S. National Science Foundation under grant CMMI-1362144.

Chapter 5 is, in full, a reprint of material published in S. Sternini, A. Y. Liang, F. Lanza di Scalea, "Ultrasonic Synthetic Aperture Imaging with Interposed Transducer-Medium Coupling Path," *Structural Health Monitoring,* 2018, https://doi.org/10.1177/1475921718805514. The dissertation author was the primary investigator and author of this paper.

References

[1] Kono, N., Baba, A., and Ehara, K., 2010, "Ultrasonic multiple beam technique using single phased array probe for detection and sizing of stress corrosion cracking in austenitic welds," Mater. Eval., 68(10), pp. 1163–1170.

[2] Park, C., Park, J. K., Choi, W., Cho, S., Moon, E. S., and Huh, M. J., 2016, "Ultrasound phased array imaging on curved surface for weld inspection of elbow pipe as a replacement for radiographic inspection," In 19th World Conference on Non-Destructive Testing 2016.

[3] Drinkwater, B. W., and Wilcox, P. D., 2006, "Ultrasonic arrays for non-destructive evaluation: A review," NDT E Int., 39(7), pp. 525–541.

[4] Lanza di Scalea, F., 2007, "Ultrasonic testing applications in the railroad industry," In Non-destructive Testing Handbook, 3rd edition, P. O. Moore, Ed. American Society for Nondestructive Testing, Columbus, OH, USA, pp. 535–552.

[5] Holmes, C., Drinkwater, B. W., and Wilcox, P. D., 2008, "Advanced post-processing for scanned ultrasonic arrays: Application to defect detection and classification in non-destructive evaluation," Ultrasonics, 48(6-7), pp. 636-642.

[6] Choi, S., Cho, H., and Lissenden, C. J., 2018, "Nondestructive inspection of spent nuclear fuel storage canisters using shear horizontal guided waves," Nuclear Engineering and Technology, 50(6), pp. 890-898.

[7] Poguet, J., Garcia, A., Vazquez, J., Marguet, J., and Pichonnat, F., 2002, "Phased array technology. Concepts, probes and applications," In 8th European Congress on Non Destructive Testing.

[8] Azar, L., Shi, Y., and Wooh, S. C., 2000, "Beam focusing behavior of linear phased arrays," NDT E Int., 33(3), pp. 189-198.

[9] Wooh, S.-C., and Shi, Y., 1999, "Optimum beam steering of linear phased arrays," Wave Motion, 29(3), pp. 245–265.

[10] Wooh, S.-C., and Shi, Y., 1998, "Influence of phased array element size on beam steering behavior," Ultrasonics, 36(6), pp. 737-749.

[11] Satyanarayan, L., Sridhar, C., Krishnamurthy, C. V., and Balasubramaniam, K., 2007, "Simulation of ultrasonic phased array technique for imaging and sizing of defects using longitudinal waves," Int. J. Press. Vessel. Pip., 84(12), pp. 716-729.

[12] Brath, A. J., and Simonetti, F., 2017, "Phased array imaging of complex-geometry composite components," IEEE Trans. Ultrason. Ferroelectr. Freq. Control, 64(10), pp. 1573-1582.

[13] Huang, L., Labyed, Y., Simonetti, F., Williamson, M., Rosenberg, R., Heintz, P., and Sandoval, D., 2011, "High-resolution imaging with a real-time synthetic aperture ultrasound system: a phantom study," In Proc. SPIE Medical Imaging: Ultrasonic Imaging, Tomography, and Therapy, 7968, pp. 79681I–1–79681I–10.

[14] Simonetti, F., and Huang, L., 2009, "Synthetic aperture diffraction tomography for three-dimensional imaging," Proc. R. Soc. A Math. Phys. Eng. Sci., 465(2109), pp. 2877–2895.

[15] Flaherty, J. J., Erikson, K. R., and Lund, V. M., 1967, "Synthetic aperture ultrasound imaging systems," U.S. Patent 3 548 642.

[16] Burckhardt, C. B., Grandchamp, P. A., and Hoffmann, H., 1974, "An experimental 2 MHz synthetic aperture sonar system intended for medical use," IEEE Trans. Sonics Ultrason., 21(1), pp. 1-6.

[17] Karaman, M., and O'Donnell, M., 1995, "Synthetic aperture imaging for small scale systems," IEEE Trans. Ultrason. Ferroelectr. Freq. Control, 42(3), pp. 429-442.

[18] Frazier, C. H., and O'Brien, W. D., 1998, "Synthetic aperture techniques with a virtual source element," IEEE Trans. Ultrason. Ferroelectr. Freq. Control, 45(1), pp. 196-207.

[19] Lockwood, G. R., Talman, J. R., and Brunke, S. S., 1998, "Real-time 3-D ultrasound imaging using sparse synthetic aperture beamforming," IEEE Trans. Ultrason. Ferroelectr. Freq. Control, 45(4), pp. 980-988.

[20] Jensen, J. A., Nikolov, S. I., Gammelmark, K. L., and Pedersen, M. H., 2006, "Synthetic aperture ultrasound imaging," Ultrasonics, 44(SUPPL), pp. e5-e15.

[21] Oddershede, N., and Jensen, J. A., 2007, "Effects influencing focusing in synthetic aperture vector flow imaging," IEEE Trans. Ultrason. Ferroelectr. Freq. Control, 54(9), pp. 1811-1825.

[22] Montaldo, G., Tanter, M., Bercoff, J., Benech, N., and Fink, M., 2009, "Coherent plane wave compounding for very high frame rate ultrasonography and transient elastography," IEEE Trans. Ultrason. Ferroelectr. Freq. Control, 56(3), pp. 489-506.

[23] Papadacci, C., Pernot, M., Couade, M., Fink, M., and Tanter, M., 2014, "High-contrast ultrafast imaging of the heart," IEEE Trans. Ultrason. Ferroelectr. Freq. Control, 61(2), pp. 288-301.

[24] Tanter, M., and Fink, M., 2014, "Ultrafast imaging in biomedical ultrasound," IEEE Trans. Ultrason. Ferroelectr. Freq. Control, 61(1), pp. 102-119.

[25] Holmes, C., Drinkwater, B. W., and Wilcox, P. D., 2005, "Post-processing of the full matrix of ultrasonic transmit-receive array data for non-destructive evaluation," NDT E Int., 38(8), pp. 701-711.

[26] Michaels, J. E., Croxford, A. J., and Wilcox, P. D., 2008, "Imaging algorithms for locating damage via in situ ultrasonic sensors," In Proc. of IEEE Sensors Applications Sym., 3, pp. 63–67.

[27] Engholm, M., and Stepinski, T., 2010, "Adaptive beamforming for array imaging of plate structures using lamb waves," IEEE Trans. Ultrason. Ferroelectr. Freq. Control, 57(12), pp. 2712-2724.

[28] Hall, J. S., Fromme, P., and Michaels, J. E., 2014, "Guided wave damage characterization via minimum variance imaging with a distributed array of ultrasonic sensors," J. Nondestruct. Eval., 33(3), pp. 299-308.

[29] Hall, J. S., and Michaels, J. E., 2010, "Minimum variance ultrasonic imaging applied to an in situ sparse guided wave array," IEEE Trans. Ultrason. Ferroelectr. Freq. Control, 57(10), pp. 2311-2323.

[30] Wilcox, P. D., 2003, "Omni-directional guided wave transducer arrays for the rapid inspection of large areas of plate structures," IEEE Trans. Ultrason. Ferroelectr. Freq. Control, 50(6), pp. 699-709.

[31] Yu, L., and Giurgiutiu, V., 2008, "In situ 2-D piezoelectric wafer active sensors arrays for guided wave damage detection," Ultrasonics, 48(2), pp. 117-134.

[32] Lanza Di Scalea, F., Sternini, S., and Nguyen, T. V., 2017, "Ultrasonic imaging in solids using wave mode beamforming," IEEE Trans. Ultrason. Ferroelectr. Freq. Control, 64(3), pp. 602-616.

[33] Matrone, G., Savoia, A. S., Caliano, G., and Magenes, G., 2015, "The delay multiply and sum beamforming algorithm in ultrasound B-mode medical imaging," IEEE Trans. Med. Imaging, 34(4), pp. 940-949.

[34] Matrone, G., Savoia, A. S., Caliano, G., and Magenes, G., 2017, "Depth-of-field enhancement in filtered-delay multiply and sum beamformed images using synthetic aperture focusing," Ultrasonics, 75, pp. 216-225.

[35] Lim, H. B., Nhung, N. T. T., Li, E.-P., and Thang, N. D., 2008, "Confocal microwave imaging for breast cancer detection: delay-multiply-and-sum image reconstruction algorithm," IEEE Trans. Biomed. Eng., 55(6), pp. 1697-1704.

[36] Park, J., Jeon, S., Meng, J., Song, L., Lee, J. S., and Kim, C., 2016, "Delay-multiply-and-sum-based synthetic aperture focusing in photoacoustic microscopy," J. Biomed. Opt., 21(3), pp. 36010-1-36010–10.

[37] Baggeroer, A. B., Kuperman, W. A., and Schmidt, H., 1988, "Matched field processing: source localization in correlated noise as an optimum parameter esimation problem," J. Acoust. Soc. Am., 83(2), pp. 571-587.

[38] Peterson, J. C., and Porter, M. B., 2013, "Ray/beam tracing for modeling the effects of ocean and platform dynamics," IEEE J. Ocean. Eng., 38(4), pp. 655-665.

[39] Iturbe, I., Roux, P., Nicolas, B., Virieux, J., and Mars, J. I., 2009, "Shallow-water acoustic tomography performed from a double-beamforming algorithm: simulation results," IEEE J. Ocean. Eng., 34(2), pp. 140-149.

[40] Munk, W., Worcester, P., and Wunsch, C., 1995, "Ocean Acoustic Tomography," Cambridge, NY, USA: Cambridge University Press.

[41] Makris, N. C., 1995, "A foundation for logarithmic measures of fluctuating intensity in pattern recognition," Opt. Lett., 20(19), pp. 2012-2014.

[42] Baggeroer, A. B., Kuperman, W. A., and Mikhalevsky, P. N., 1993, "An overview of matched field methods in ocean acoustics," IEEE J. Ocean. Eng., 18(4), pp. 401-424.

[43] Michalopoulou, Z. H., and Porter, M. B., 1996, "Matched-field processing for broad-band source localization," IEEE J. Ocean. Eng., 21(4), pp. 384-391.

[44] Debever, C., and Kuperman, W. A., 2007, "Robust matched-field processing using a coherent broadband white noise constraint processor," J. Acoust. Soc. Am., 122(4), pp. 1979-1986.

[45] Orris, G. J., Nicholas, M., and Perkins, J. S., 2000, "The matched-phase coherent multi-frequency matched-field processor," J. Acoust. Soc. Am., 107(5), pp. 2563-2575.

Chapter 6

Ultrasonic Imaging in Solids Using Wave Mode Beamforming

Abstract

This paper discusses some improvements to ultrasonic synthetic imaging in solids with primary applications to non-destructive testing of materials and structures. Specifically, the study proposes new weights applied to the beamforming array that are based on the physics of the propagating waves, specifically the displacement structure of the propagating longitudinal (L) mode and shear (S) mode that are naturally co-existing in a solid. The wave mode structures can be combined with the wave geometrical spreading to better filter the array (in a matched filter approach) and improve its focusing ability compared to static array weights. The paper also proposes compounding, or summing, images obtained from the different wave modes to further improve the array gain without increasing its physical aperture. The wave mode compounding can be performed either incoherently or coherently, in analogy with compounding multiple frequencies or multiple excitations. Numerical simulations and experimental testing demonstrate the potential improvements obtainable by the wave structure weights compared to either static weights in

conventional delay-and-sum focusing, or adaptive weights based on geometrical spreading alone in minimum-variance distortionless response focusing.

6.1 Introduction

Synthetic Aperture Focus (SAF) for ultrasonic imaging has been around since the late 60's [1, 2]. This technique has found numerous applications, ranging from the medical imaging field, including blood flow imaging [3-9] and, more recently, ultrafast cardiac imaging [10-13], to the Structural Health Monitoring (SHM) and Non-Destructive Testing (NDT) fields, including defect imaging in waveguide structures [14-26].

The typical SAF approach uses an array of transducers that can act as both transmitters and receivers of ultrasonic waves in the imaging medium. The image is built by extracting specific features of the received ultrasonic signals, that are appropriately back-propagated in time depending on geometrical considerations involving the spatial position of the transmitter(s), receiver(s) and focus point(s) ("Delay-and-Sum"). Two typical SAF beamforming schemes are the elliptical method, where the images are constructed based on transmitter-receiver pairs creating elliptical focus lines, and the hyperbola method, where the images are constructed based on receiver-receiver pairs creating hyperbola focus lines.

Regardless of the mode of operation of the array, one common key aspect of SAF beamforming is the selection of the weights attributed to each collected waveforms. The most basic algorithm uses unity weights, and it simply relies on the back-propagated and summed waveform amplitudes. Static apodization weights (e.g. Hanning or Kaiser window) are also widely utilized to decrease the sidelobes of the array pattern, but at the expense of the broadening of the main peak, i.e. a degradation of the spatial resolution. This conventional weighting is performed statically, i.e. with weights independent of the focus point.

An improved solution is to utilize adaptive weights that can provide an effective "filter" on which the acquired set of waveforms ("data vector" in Matched Field Processing [27, 28] terminology) can be projected for an increased gain of the array. This is different, for example, from "compensation" strategies that can be applied to the array, such as time-gain compensation used in biomedical imaging. One such adaptive filtering technique, for example, accounts for geometrical beam spreading of the propagating waves, that involve an amplitude decay of 1/sqrt(d) in 2-D and 1/d in 3-D, where d is the wave propagation distance [20, 21, 25]. Another, more sophisticated approach, is to use the actual directional beam scattering profiles from the reflectors (defects in SHM and NDT) [25, 26]. However, the defect scattering approach is quite challenging since it requires precise knowledge of the scattering profile that is – of course- dependent on the specific morphology of the reflector, as well as on the transmitted wave type, direction and frequency.

A popular implementation of adaptive weights in SAF beamforming is the Minimum Variance Distortionless Response (MVDR) method, that has been around since the 60s and is also known as the Capon's Maximum Likelihood Method [29]. The MVDR has been applied to several imaging fields, spanning from underwater acoustics to active damage detection in structures [20, 21, 26]. The MVDR adaptive weights minimize the output of the array, except in the "look direction" of scanning. The MVDR is known to decrease the width of the main lobe in the beamformer pattern, while suppressing the sidelobes. However, the MVDR is derived under the idealized assumption of stationary noise and interference environment, and it can be detrimental when the wave models are not accurate and/or in cases of low Signal-to-Noise ratio (SNR) [27, 30].

Another strategy often used to increase the array gain without increasing its physical

aperture is compounding, or adding, images obtained with several independent parameters. This is the case, for example, of compounding images obtained from different frequencies in Matched Field Acoustics [31], or compounding images obtained from different excitations in a plane-wave mode [10] or a diverging-wave mode [11] in ultrafast biomedical imaging. The compounding can be done either incoherently [e.g. 27, 30-32] or coherently [e.g. 30, 33-35]. The incoherent compounding is a straight-forward manner to reinforce the common main peaks from the true reflectors, and suppress the sidelobes that are generally located at different positions of the individual images. The coherent compounding is a more sophisticated way to exploit the full complexity of the received signals in terms of their coherence, by adding cross-terms to the signal summation. However, the potential enhancement in performance comes at the expense of a greater sensitivity to mismatch between the expected received signal and the real received signal, which is a well-known issue, for example, of frequency compounding [33]. While, in general, the choice between incoherent and coherent compounding should depend on the noise structure expected from the imaging medium [30, 33], in ideal scenarios the coherent approach is expected to bring additional array gains through the cross-terms that result from the coherent summation.

This paper discusses improvements to ultrasonic synthetic imaging. The specific target application is in the non-destructive testing of materials and structures, although some aspects are also applicable to biomedical imaging. Specifically, the study proposes new weights applied to the beamforming array that are based on the physics of the propagating waves, specifically the displacement structure of the propagating longitudinal (L) mode and shear (S) mode that are naturally co-existing in a solid. In a matched filter approach, the wave mode structures can be combined with the wave geometrical spreading to better filter the array and improve its focusing ability compared to static array weights. The paper also proposes compounding, or summing,

images obtained from different wave modes to further increase the array gain without increasing its physical aperture. The wave mode compounding can be performed either incoherently or coherently, in analogy with the multiple frequency compounding or the multiple excitation compounding used in several applications. Numerical simulations and experimental tests demonstrate the potential improvements obtainable by the wave structure weights compared to either static weights in conventional delay-and-sum focusing or to adaptive weights based on geometrical spreading alone in minimum-variance distortionless response focusing.

6.2 Synthetic Aperture Focus: Background

Consider an ultrasonic transducer array consisting of M transmitters and N receivers. Referring to Fig. 6.1, let the spatial coordinates of each transmitter $i = 1..M$ be (x_i, y_i) and the spatial coordinates of each receiver $j = 1..N$ be (x_j, y_j).

The conventional SAF Delay-And-Sum (DAS) algorithm builds an image $I(x,y)$ by summing, at each pixel P(x,y), the amplitudes of the received signals, A, appropriately back-propagated, for each combination of transmitter i and receiver j. In the time domain, the back-propagation DAS algorithm can be written as [8]:

$$I^{DS}(x,y) = \sum_{i=1}^{M} \sum_{j=1}^{N} w_{ij,xy} A_{ij}(\tau_{ij,xy}) \tag{6.1}$$

where $w_{ij,xy}$ are weights (more on these later), and the back-propagation times, $\tau_{ij,xy}$, correspond to the travel time of the wave from the transmitter i, to the focus point P(x,y), and back to the receiver j :

$$\tau_{ij,xy} = \underbrace{\frac{\sqrt{(x_i - x)^2 + (y_i - y)^2}}{c_{L,S}}}_{\text{Transmitter to Focus Point}} + \underbrace{\frac{\sqrt{(x_j - x)^2 + (y_j - y)^2}}{c_{L,S}}}_{\text{Focus Point to Receiver}} \tag{6.2}$$

where the denominators can be either the longitudinal speed, $c_{L,}$ or the shear speed, c_S in the imaging medium. It should be noted that, where common SAF formulation assumes the same wave mode in transmission and reception (i.e. the same wave speed, generally c_L, is normally used in Eq. (6.2)), the transmission path and the reflection path are explicitly separated in the proposed equation. Making the wave velocities of the transmission path and the reflection path independent of one another allows to consider different wave mode combinations to enhance the focusing ability of the array, as discussed later in Section 6.5.

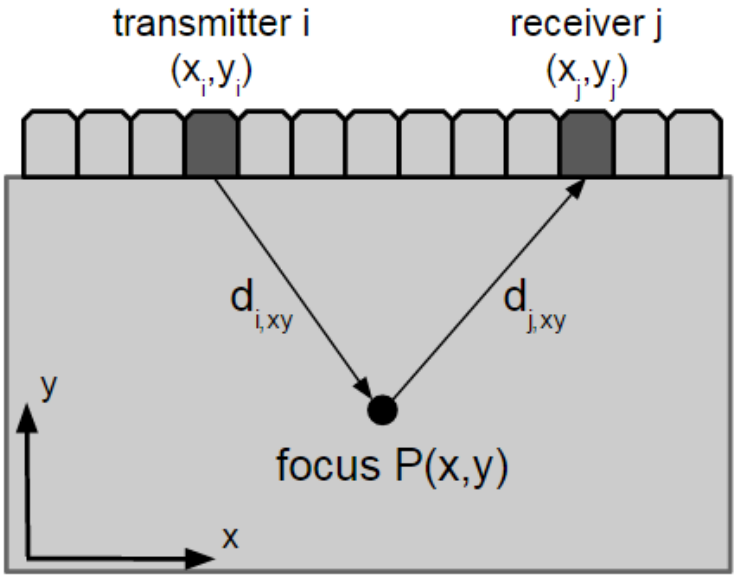

Figure 6.1: Basic concept of synthetic aperture focus

Another way of interpreting Eq. (6.1) is in a Matched Field Acoustics framework, as an inner product (or cross-correlation at zero time lag or a matched filter) between the vector of backpropagated signal amplitudes and the vector of "expected" amplitudes based on some physics of the problem. The wave structure weights proposed in Section 6.3 should be viewed in this

Matched Field processing framework.

The received signal, *A*, in Eq. (6.1) can be computed from the raw RF waveforms, from an enveloped versions of the RF waveforms, or from the analytical signal representation of the RF waveforms. In the latter case, each waveform is decomposed into its in-phase (*I*) and quadrature phase (*Q*) through the Hilbert Transform. Eq. (6.1) is then applied to each of the *I* and *Q* components separately, and the final image envelope is constructed by computing the modulus of the two contributions at each pixel (*x*,*y*) [4, 13, 36]. This is the method utilized to generate the results shown in the present paper.

It was discussed in Section 6.1 how the weights $w_{ij,xy}$ can be assumed unitary (i.e. no weights) or following an apodization window (e.g. Hanning or Kaiser) that is statically applied to the array. In a Matched Field Processing approach, instead, the weights change with focus point position (*x*,*y*) based on some physics of the wave propagation problem. If geometrical spreading is accounted for, the expression for the weights in 2D (circularly-crested waves) at each focus location (*x*,*y*), becomes [20, 21]:

$$w_{ij,xy} \propto \frac{1}{\sqrt[4]{\left[\left(x_i - x\right)^2 + \left(y_i - y\right)^2\right]\left[\left(x_j - x\right)^2 + \left(y_j - y\right)^2\right]}} = \frac{1}{\sqrt{d_{i,xy}\, d_{j,xy}}} \tag{6.3}$$

where ~ is the proportionality symbol, $d_{i,xy}$ is the transmitter-to-focus distance, and $d_{j,xy}$ is the focus-to-receiver distance.

In the MVDR implementation [20, 21, 26, 29], which is part of a Matched Field Processing approach, the matrix notation is best used. In this formulation, one can define the acquired (back-propagated) data vector $\overline{A_{xy}} = [A_{11}\ \ A_{12}..\ A_{1N}.....\ A_{M1}\ \ A_{M2}..\ A_{MN}]^T$, the set of weights ("look direction") $\overline{w_{xy}} = [w_{11}\ \ w_{12}..\ w_{1N}.....\ w_{M1}\ \ w_{M2}..\ w_{MN}]^T$, and an autocorrelation matrix defined as

$\overline{\overline{K_{xy}}} = \overline{A_{xy}} \times \overline{A_{xy}}^{T}$ where × is the outer product. The adaptive weight vector for the MVDR framework is calculated as [27, 28]:

$$\overline{w_{xy}}^{MV} = \frac{\overline{\overline{K_{xy}}}^{-1}\,\overline{w}}{\overline{w}^{T}\,\overline{\overline{K_{xy}}}^{-1}\,\overline{w}} \tag{6.4}$$

Various techniques exist for the regularization of the $\overline{\overline{K_{xy}}}$ matrix to enable a full rank and hence the computation of its inverse [27], diagonal loading being a common option [37]. The weights in Eq. (6.4) lead to an imaging algorithm for the MVDR technique that can be expressed as a quadratic version of the Delay-and-Sum formulation:

$$I^{MV}(x,y) = \left(\sum_{i=1}^{M} \sum_{j=1}^{N} w_{ij,xy}^{MV}\, A_{ij}(\tau_{ij,xy}) \right)^{2} \tag{6.5}$$

6.3 Weights Based on Wave Mode Structure

The possibility of using weights based on wave mode structure comes from the realization that, in general, a defect in a solid can reflect one or both of a longitudinal L-wave and a shear S-wave, through either same mode reflection or mode conversion. In the most general case, therefore, since the excitation can use both L-wave and S-wave, there can exist up to four combinations of wave modes available for imaging in a bulk solid: LL (L-wave transmitted, L-wave reflected), LS (L-wave transmitted, S-wave reflected), SL (S-wave transmitted, L-wave reflected), and SS (S-wave transmitted, S-wave reflected). An additional opportunity therefore exists to compound images obtained from the different mode combinations so as to improve the array gain. The compounding will be discussed later in the paper.

Irrespective of the excitation, the signal strength received by the array will be modulated

by the particular reflected mode structure (L- or S- wave reflected) and the reflector position $P(x,y)$.

Referring to Fig. 6.2, for the case of an L-wave reflected by $P(x,y)$ and impinging on receiver j, the particle motion will be confined to the wave propagation direction (vector $\overline{u_{j,xy}}^{L}$ in Fig. 6.2). Let us assume a typical ultrasonic transducer array that uses gel couplant and is sensitive to the out-of-plate motion of the surface (direction y in Fig. 6.2). The distribution of out-of-plane displacements across the array due to a L-wave reflected by $P(x,y)$ and impinging on the array can be simply calculated by projecting the wave vector $\overline{u_{j,xy}}^{L}$ on the out-of-plane direction, y. Hence, the corresponding weights are:

$$w_{j,xy}^{LL \text{ or } SL} = \left|\overline{u_{j,xy}}^{L}\right| \cos\theta_{j,xy} = \left|\overline{u_{j,xy}}^{L}\right| \frac{\left|y_j - y\right|}{\sqrt{\left(x_j - x\right)^2 + \left(y_j - y\right)^2}} \tag{6.6}$$

L-mode reflected

or:

$$w_{j,xy}^{LL \text{ or } SL} \propto \frac{\left|y_j - y\right|}{\sqrt{\left(x_j - x\right)^2 + \left(y_j - y\right)^2}} \tag{6.7}$$

L-mode reflected

If the reflector is located on-axis at the center of the array footprint (Fig. 6.2(a)), this equation leads to a measured amplitude distribution that is simply a cosine function. The distribution will be appropriately skewed if the reflector is located off-axis to the array (Fig. 6.2(b)).

The geometrical spreading effect from Eq. (6.3), that also depend on the transmitter i, can be added to the wave structure weights, giving:

$$w_{ij,xy}^{LL\ \text{or}\ SL} \propto \frac{1}{\sqrt{d_{i,xy}\ d_{j,xy}}} \cdot \frac{\left|y_j - y\right|}{\sqrt{\left(x_j - x\right)^2 + \left(y_j - y\right)^2}} \tag{6.8}$$

L-mode reflected

Eq. (6.8) is therefore the final expression for the new weights, based on the mode structure of a reflected L-wave and including geometrical spreading, that depend on the location of each transmitter *i*, each receiver *j*, and each position of the "focus" reflector (*x*, *y*). Moreover, Eq. (6.8) applies to either an L-wave or an S-wave used in transmission.

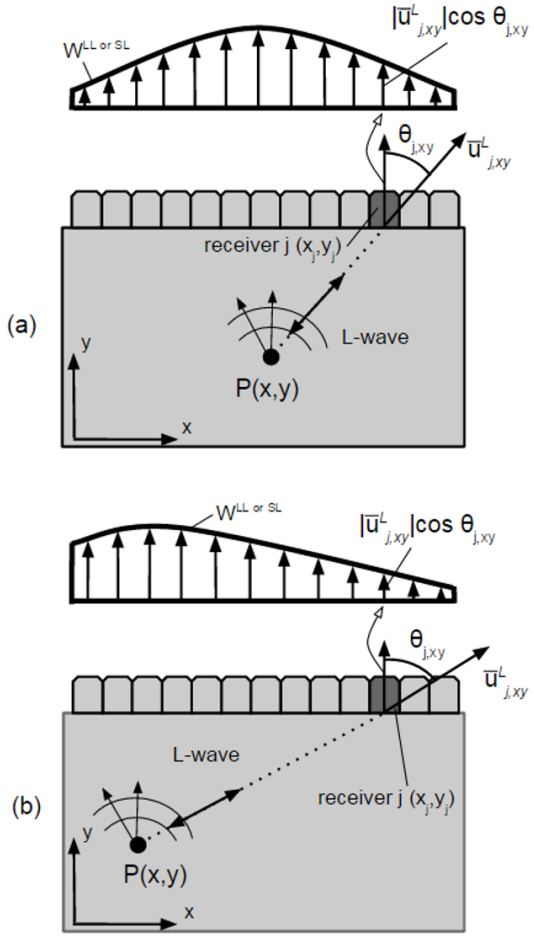

Figure 6.2: Weights based on wave mode structure measured by the array for an L-wave reflection. (a) Reflector located on-axis at the center of the array footprint. (b) Reflector located off-axis

The case of an S-wave reflected by the focus point onto the array can be derived

analogously (Fig. 6.3). For a shear wave (polarized in the *x,y* plane) , the particle motion $\overline{u_{j,xy}}^{S}$ is perpendicular to the direction of wave propagation. The amplitude distribution measured by a typical transducer array will be, again, the out-of-plane component of the wave displacement at the array surface. In the case of an S- wave reflection, the mode structure weights will therefore be:

$$w_{j,xy}^{LS \text{ or } SS} = \left|\overline{u_{j,xy}}^{S}\right| \cos(90 - \theta_{j,xy}) = \left|\overline{u_{j,xy}}^{S}\right| \frac{\left|x_j - x\right|}{\sqrt{\left(x_j - x\right)^2 + \left(y_j - y\right)^2}} \tag{6.9}$$

S-mode reflected

Fig. 6.3(a) shows the distribution of the S-mode weights for a reflector located on-axis to the array (following a sine function), and Fig. 6.3(b) shows the skewed distribution obtained from a reflector located off-axis. By adding the 2D geometrical spreading effect, Eq. (6.9) becomes:

$$w_{ij,xy}^{LS \text{ or } SS} \propto \frac{1}{\sqrt{d_{i,xy}\, d_{j,xy}}} \cdot \frac{\left|x_j - x\right|}{\sqrt{\left(x_j - x\right)^2 + \left(y_j - y\right)^2}} \tag{6.10}$$

S-mode reflected

Eq. (6.10) is the final expression for the new wave mode weights applied to an S-wave reflection (for either an L-wave or an S-wave transmission).

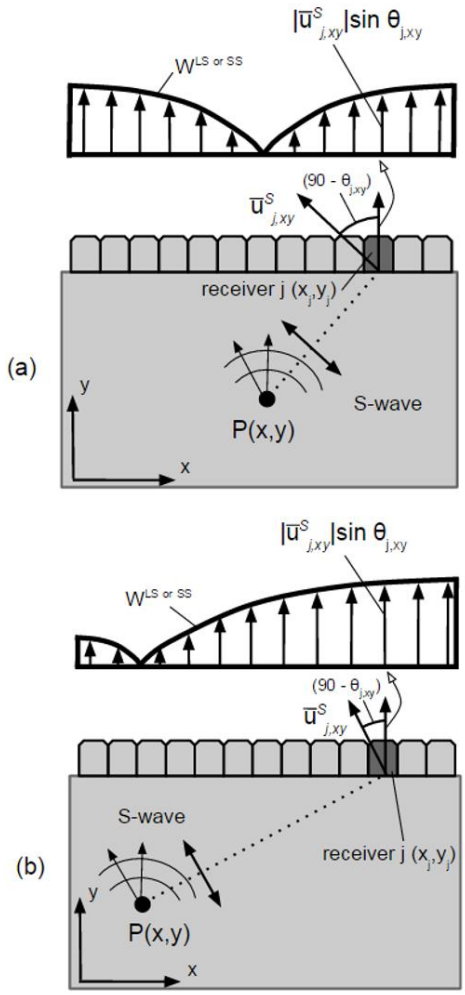

Figure 6.3: Weights based on wave mode structure measured by the array for an S-wave reflection. (a) Reflector located on-axis at the center of the array footprint. (b) Reflector located off-axis

6.4 Implementation of the Wave Structure Weights in SAF Beamforming

The weights proposed in the previous section can be applied to SAF beamforming, on either the basic Delay-and-Sum algorithm, or the MVDR algorithm. The application to the Delay-and-Sum algorithm for the case of the L-wave reflection becomes:

$$I^{DS,LL\ or\ SL}(x,y) = \sum_{i=1}^{M}\sum_{j=1}^{N} w_{ij,xy}^{LL\ \text{or}\ SL} A_{ij}(\tau_{ij,xy}) \tag{6.11}$$

L-mode reflected

where the L-mode weights $w_{ij,xy}^{LL\text{ or }SL}$ are given in Eq. (6.8) and the back-propagation time delays $\tau_{ij,xy}$ are given by Eq. (6.2) with the appropriate wave velocities at the denominators (c_L or c_S).

For the case of the S-wave reflection, the DAS beamforming with the new weights becomes:

$$I^{DS,\ LS\ or\ SS}(x,y) = \sum_{i=1}^{M}\sum_{j=1}^{N} w_{ij,xy}^{LS\ or\ SS} A_{ij}(\tau_{ij,xy}) \tag{6.12}$$

S-mode reflected

where the S-mode weights $w_{ij,xy}^{LS\text{ or }SS}$ are given in Eq. (6.10), and the back-propagation time delays $\tau_{ij,xy}$ are given by Eq. (6.2) with the appropriate wave velocities at the denominators (c_L or c_S).

The new weights can also be applied to the MVDR algorithm. In this case, for the L-mode reflection, the MVDR beamforming with the wave-structure weights becomes:

$$I^{MV,\ LL\ or\ SL}(x,y) = \left(\sum_{i=1}^{M}\sum_{j=1}^{N} w_{ij,xy}^{MV,\ LL\text{ or }SL} A_{ij}(\tau_{ij,xy}) \right)^2 \tag{6.13}$$

L-mode reflected

where the weights $w_{ij,xy}^{MV,\ LL\text{ or }SL}$ are calculated from the MVDR Eq. (6.4) with the substitution of the wave-structure weights $\bar{w} = \left\{ w_{ij,xy}^{LL\text{ or }SL} \right\}$ given, in turn, in Eq. (6.8).

In an analogous manner, the MVDR beamforming with wave structure weights applied to the S-wave reflection can be formulated as:

$$I^{MV,\ LS\ or\ SS}(x,y) = \left(\sum_{i=1}^{M}\sum_{j=1}^{N} w_{ij,xy}^{MV,\ LS\text{ or }SS} A_{ij}(\tau_{ij,xy}) \right)^2 \tag{6.14}$$

S-mode reflected

where the weights are calculated in the same manner as described above for the L-reflection, but

using the S-reflection expressions of Eq. (6.10) instead of Eq. (6.8).

6.5 Image Compounding from Multiple Wave Modes

Incoherent compounding is simply the incoherent summation of the image intensities obtained by the various wave mode combinations. Hence:

$$I_{TOT,incoherent}(x,y) = \sum_{MC=LL,LS,SL,SS} I^{MC}(x,y) \tag{6.15}$$

where the image $I^{MC}(x,y)$ (in decibels) for a given mode combination can be either the Delay-and-Sum beamforming from Eqs. (6.11, 6.12) (appropriately chosen for either an L-wave reflection or an S-wave reflection), or the MVDR beamforming of Eqs. (6.13, 6.14). This approach simply relies on the consistency of the true reflector versus the randomness of the noise in each image.

Coherent compounding, instead, includes "cross-mode" terms because the summation is done before the squaring. Therefore, this mode exploits the coherence across wave modes as received by the array. This is in analogy with the "cross-frequency" terms appearing from coherent frequency summation in Matched Field Processing. In the coherent case, therefore:

$$I_{TOT,coherent}(x,y) = \left(\sum_{MC=LL,LS,SL,SS} \sqrt{I^{MC}(x,y)} \right)^2 \tag{6.16}$$

where, again, the images $I^{MC}(x,y)$ are given in Eqs. (6.11, 6.12) for DAS and in Eqs. (6.13, 6.14) for MVDR (in decibels).

6.6 Numerical Results: Wave Mode Structure Weights

A proof-of-principle numerical evaluation of the wave structure weights was carried out in

the SAF-DAS implementation and in the SAF-MVDR implementation. The numerical simulation was performed with the k-wave module of Matlab© in a 2D (plane strain) scenario. Synthetic focusing was performed in reception, which was adequate for comparing the performance of the various weights. The simulation modeled a 57.15 mm × 57.15 mm (2.25 in × 2.25 in) aluminum square with a simulated ultrasonic array consisting of 32 receiving points spaced at 0.6 mm (corresponding to half wavelength of an S-wave in aluminum at 2.5 MHz to avoid grating lobes). Hence each array element was simplified to a point, which was considered quite adequate to compare the different beamforming algorithms.

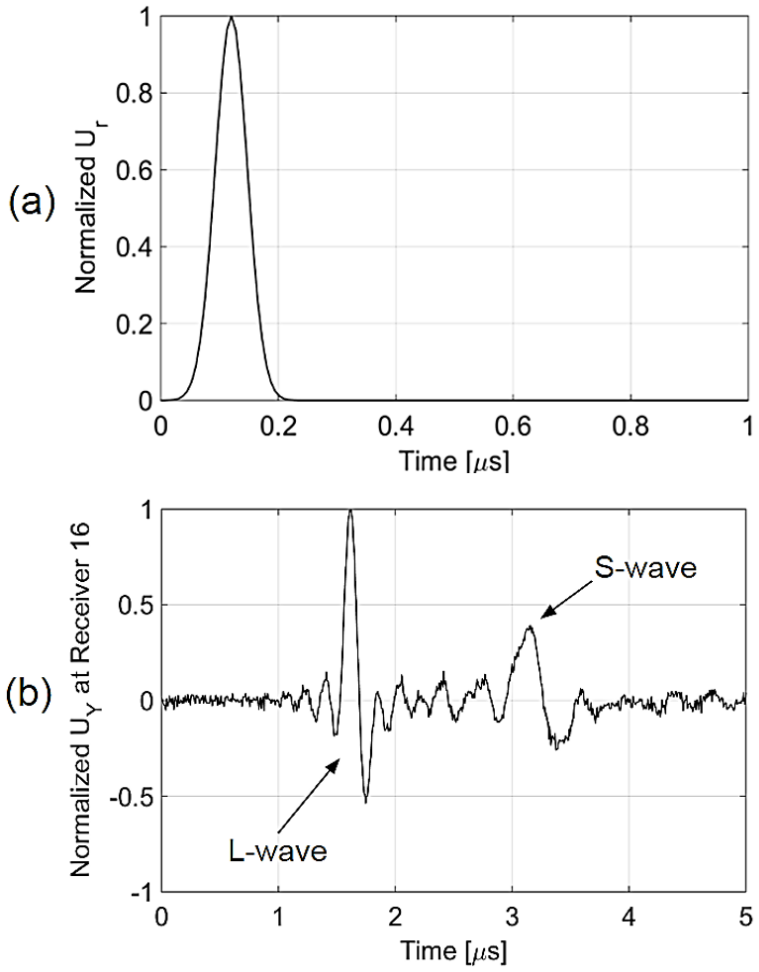

Figure 6.4: (a) Impulse used to simulate the wave source in the numerical model. (b) Typical RF waveform recorded by receiver element no. 16 of the simulated array, with digitally added random noise, when the source is central to the array and at a depth of 9 mm into the aluminum medium

The Line Spread Function (LSF) of the array was computed by simulating an impulsive omni-directional displacement excitation at the specific focus point [13, 38], recording the corresponding out-of-plane displacements at each of the simulated receiver positions (assuming gel-coupling), and then applying the beamforming algorithm for DAS and MVDR, respectively. Fig. 6.4(a) shows the impulse used as the wave source at the focus points. Random noise was numerically added to the RF waveforms, corresponding to 30% of the clean signal's Root Mean Square (RMS). Fig. 6.4(b) shows a typical RF waveform (with added noise) for receiver element no. 16 of the simulated array when the source was centrally located relative to the array and at a depth of 9 mm from the array surface. Notice in the waveform the arrival of both the L-wave and the S-wave.

The array imaging performance was examined as a function of both lateral position and depth position in the imaging space. Accordingly, the LSF was initially computed for nine different focus points, consisting of three points located in the center of the array footprint at different depths (points P1, P2 and P3 in Fig. 6.5), three points slightly offset from the center of the array (points P4, P5 and P6 in Fig. 6.5), and three points located at the edge of the array footprint at the same three different depths (points P7, P8 and P9 in Fig. 6.5). For the DAS framework, the results were computed for three sets of beamforming weights, $w_{ij,xy}$, applied in reception, namely: (1) unity weights (i.e. no weights), (2) Hanning window (static) apodization weights, and (3) the new wave mode structure weights. For the MVDR algorithm, the comparison was done between a classical "look direction" that uses only the geometrical spreading weights, and the new weights that also incorporate the mode structure. The wave mode weights were then applied, separately, to the L-wave reception focus and to the S-wave reception focus.

The performance metrics of interest include: the Dynamic Range or Contrast (defined as

the difference between the LSF dB maximum and minimum across the 57.15 mm imaging width), the Side Lobe level (defined as the LSF dB level of the first sidelobe), and the Spatial Resolution (defined as the -6 dB full width of the LSF main peak).

6.6.1 Results from Delay-and-Sum

The LSF results of the simulation using the DAS algorithm with the different weights are plotted in Fig. 6.5 for the L-wave reception case. For this figure, the wave mode weights were therefore $w_{ij,xy}^{LL\text{ or }SL}$ computed from Eq. (6.8). The plots show that the LSF performance of the wave structure weights is either equivalent or improved compared to that of the unity weights or the static Hanning weights. In terms of Dynamic Range or Contrast, the wave structure weights perform better than the unity weights and similarly to the static Hanning weights for on-axis focus points (P1, P2 and P3), and better than either unity or Hanning weights for off-axis focus points (P4 through P9). The improvement in Dynamic Range is as high as ~20 dB (points P4 and P7). Since the L-wave mode structure for on-axis reflectors is similar in shape to the static Hanning window, see Fig. 6.2(a), the performance is also similar in these regions. The clear improvement from the wave structure weights is seen for the off-axis points where the static Hanning window remains, instead, unchanged. The contrast increase is more evident at focus points close to the array (e.g. P4 and P7 in the near-field), due to the increased curvature of the displacement structure of the reflected wave at these locations that can be exploited best by considering the mode weights. Accordingly, decreased Side Lobe levels with the wave mode weights are seen for points P1 through P8, with the improvement tapering off at the largest depths (P3, P6 and P9). The Side Lobe level reductions with the wave mode weights are as high as ~10 dB (point P8).

In terms of Spatial Resolution (here defined as the -6 dB full width of the LSF main peak), the wave mode weights overall maintain the resolution of the unity static weights.

Fig. 6.6 plots the LSF results in the S-wave reception case for the same nine focus points. The wave mode weights were therefore $w_{ij,xy}^{LS\ or\ SS}$ computed from Eq. (6.10). For the S-wave reception, the wave structure weights show Spatial Resolution equivalent to the unity weights and

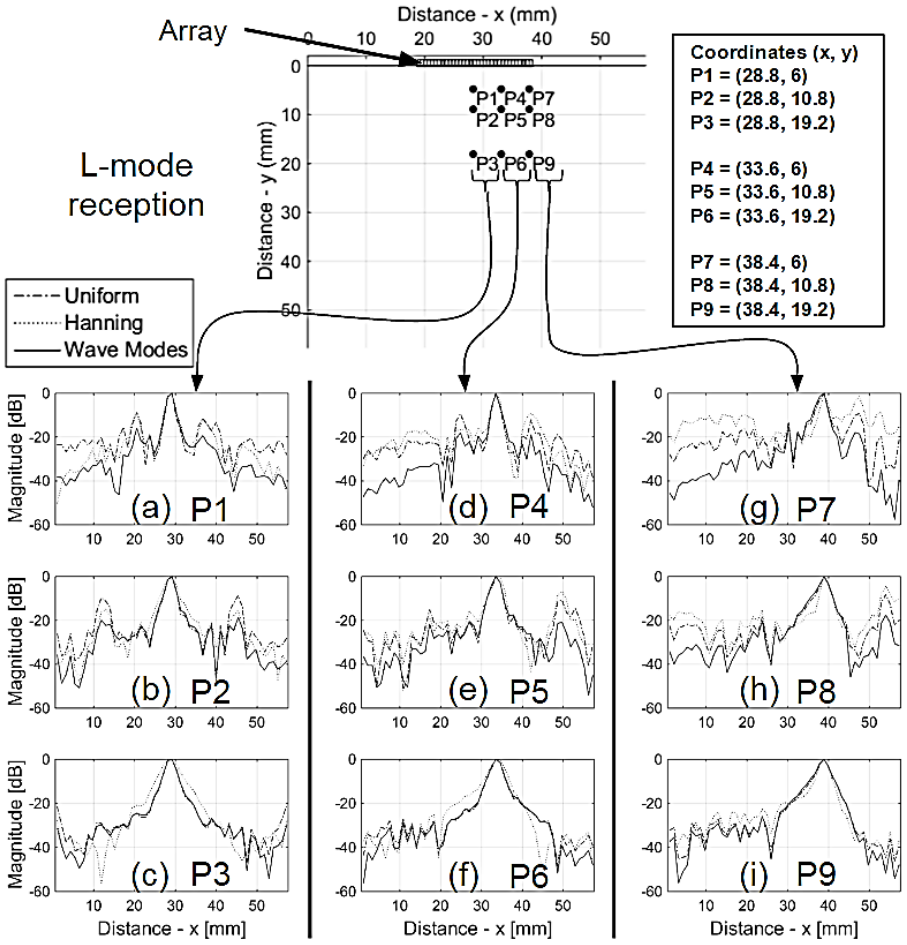

Figure 6.5: Line Spread Functions of focusing the L-wave in reception from the SAF-DAS simulation for different focus points, and comparing the wave mode weights from the L-mode wave structure, uniform (unity) weights, and static Hanning apodization weights

improved compared to the static Hanning weights (e.g. P2, P3 and P6) without degradation of the Dynamic Range. The performance is maintained in the off-axis focus points (e.g. P9), since the out-of-plane displacement of an S-wave impinging on the array (hence the SNR of the RF waveforms) is substantial at large incident angles for this wave mode.

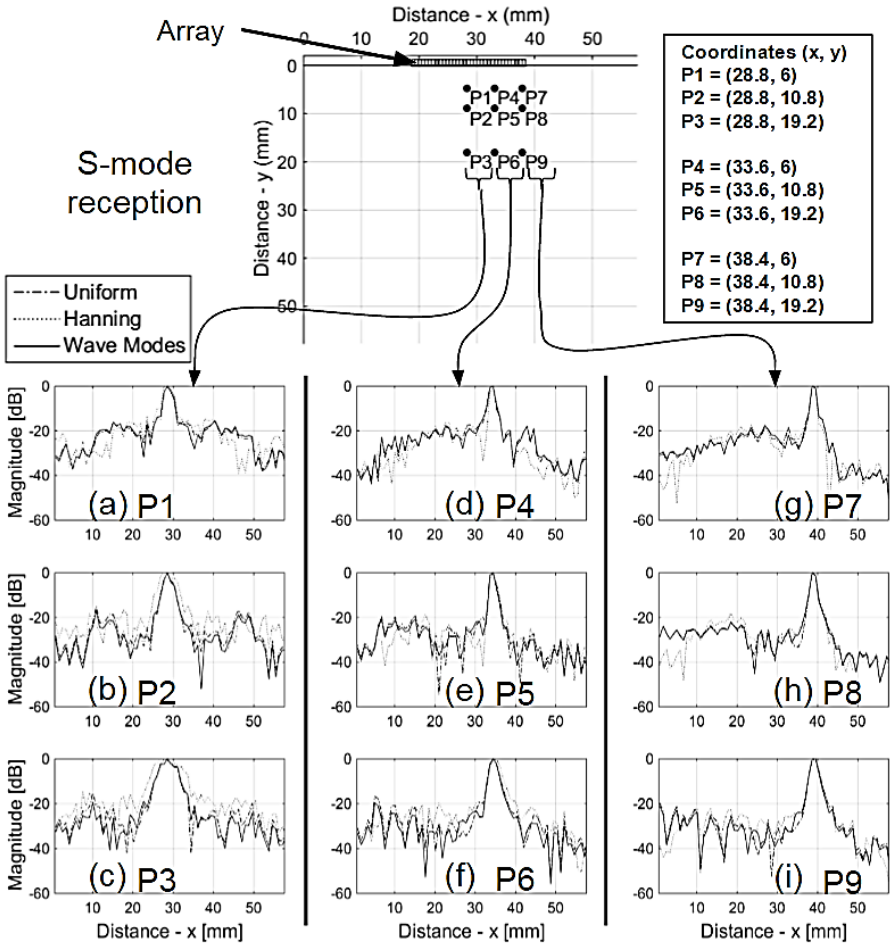

Figure 6.6: Line Spread Functions of focusing the S-wave in reception from the SAF-DAS simulation for different focus points, and comparing the wave mode weights from the S-mode wave structure, uniform (unity) weights, and static Hanning apodization weights

As a further evaluation of contrast performance, the simulation was carried out for a first "strong" source (point P1) co-existent with a second "weaker" source (point P7) located in the side-lobe region of the first source. The strength of the weaker emitter was set as 70% that of the strong emitter. All other parameters were the same as discussed when first presenting the simulation, except for the addition of the weaker source. The LSF results of this analysis are shown in Fig. 6.7 for the L-mode reception case, where the wave structure weights are compared to the unity and Hanning static weights. The wave structure focusing clearly shows a ~ 20 dB increase in Dynamic Range compared to the other two cases, primarily due to the superior contrast

performance for the off-axis "weak" source as discussed for Fig. 6.5. More importantly, the wave structure (or wave mode) weights also detect the second source at P7 as a second peak to the right of the main peak at P1. This second peak is not present when only the source at P1 exists (see Fig. 6.5(a)). The unity and Hanning weights, instead, show only a marginal increase in the right-hand side lobe level compared to the left-hand side lobe level, resulting in a more challenging detection of the second source.

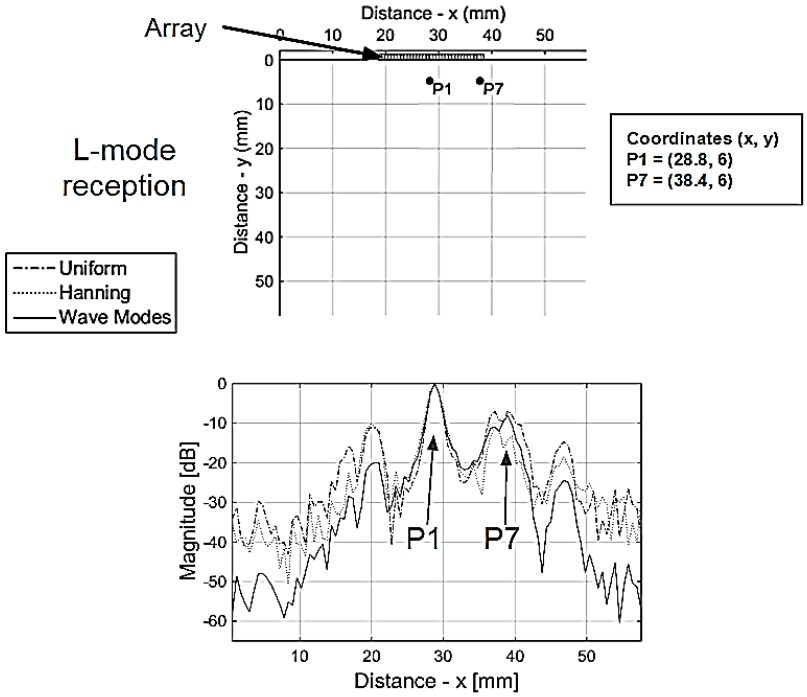

Figure 6.7: Line Spread Functions of focusing the L-wave in reception from the SAF-DAS simulation for two co-existing focus points, namely a strong emitter (100% strength) at P1 and a weaker emitter (70% strength) at P7, comparing the wave mode weights from the L-mode wave structure, uniform (unity) weights, and static Hanning apodization weights

A more global picture of the array performance with wave structure weights on a larger imaging space is provided in the contour plots of Figs. 6.8 and 6.9 that depict the entire imaging space. To obtain these figures, the Matlab simulation and SAF-DAS algorithm was run for a grid of wave source (focus) points across half of the entire 57.15 mm × 57.15 mm space. At each of the focus points, the LSF was calculated and the Dynamic Range and Spatial Resolution metrics were extracted. The two metrics are plotted, respectively, in Figs. 6.8 and 6.9.

Seen in Fig. 6.8(a), the Dynamic Range for the L-mode reception maintains a high value across most of the imaging space, with largest Dynamic Range obtained in regions close to the array and along its central region. The large contrast from these regions is due to the combination of large amplitude and large curvature of the out-of-plane component of the L-wave impinging on the array. Nevertheless, it is encouraging that a good Dynamic Range is maintained also at quite extreme off-axis position.

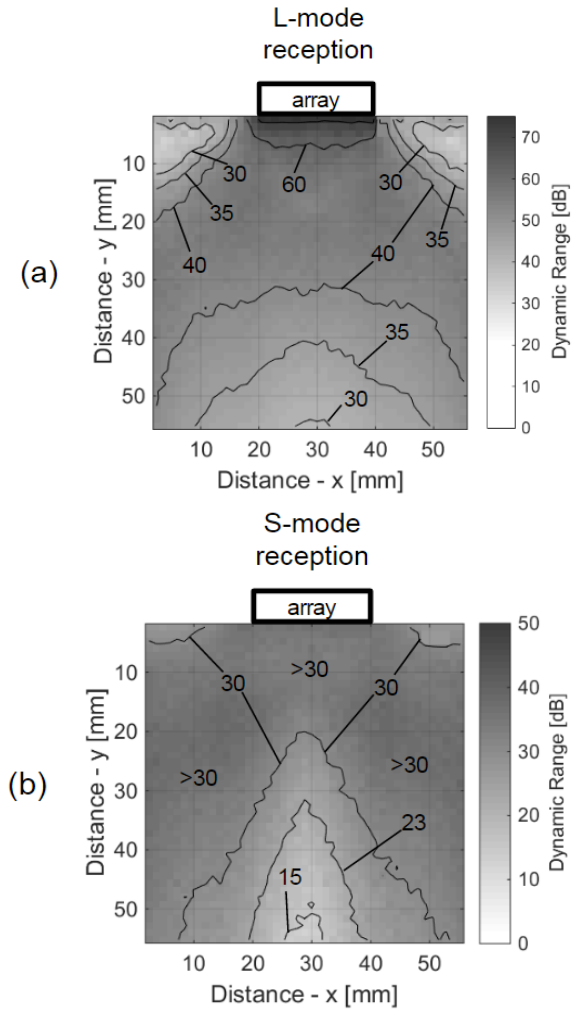

Figure 6.8: Contour plots of Dynamic Range (difference between the LSF dB maximum and minimum across the imaging width) from the numerical simulations of SAF-DAS focusing with wave structure weights for (a) the L-mode reception and (b) the S-mode reception

Fig. 6.8(b) shows the same results using, instead, the S-wave reception weights. In this case, the largest Dynamic Range is obtained in the off-axis regions, as a result, as discussed above,

of the larger out-of-plane component of the S-wave impinging on the array at oblique angles. It is also encouraging that a high Dynamic Range is maintained across the different depths.

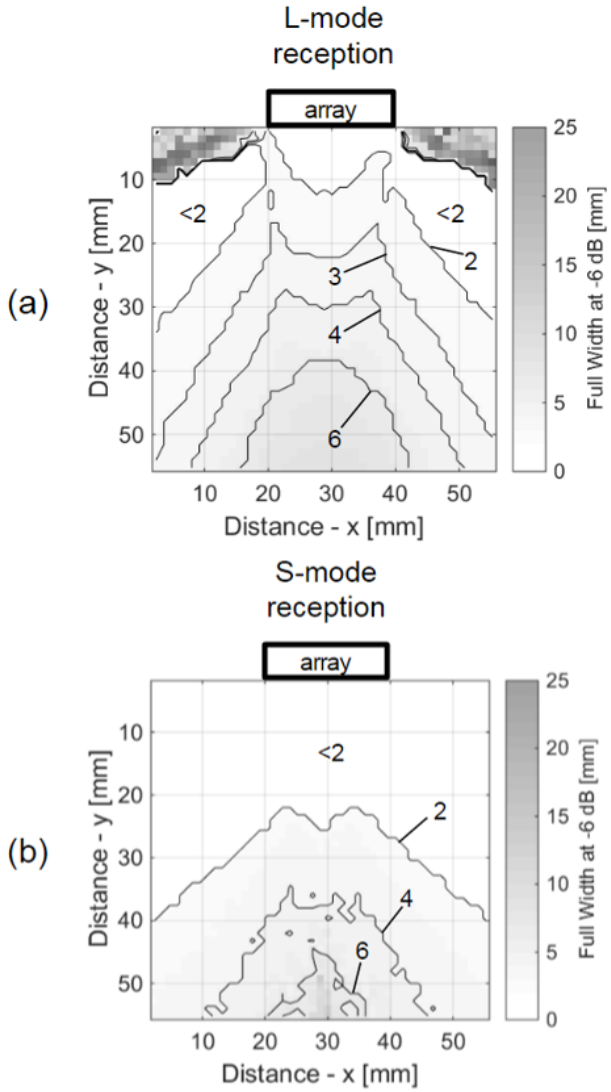

Figure 6.9: Contour plots of Spatial Resolution (-6 dB full width of the LSF main peak) from the numerical simulations of SAF-DAS focusing with wave structure weights for the L-mode reception for (a) the L-mode reception and (b) the S-mode reception

Fig. 6.9(a) shows the Spatial Resolution contour plots for the L-mode reception. It can be seen that the best resolution is obtained in the near field, with resolution increasing with increasing depth, following the known behavior of static apodization weights where main lobe widths increase with depth. The good behavior at shallow positions (near-field) is a result, again, of the increased curvature of the displacement structure across the array at these focus locations. The

black area at extreme angles seen in the L-wave plot is likely due to the very poor SNR of the out-of-plane component received by the array from L-waves incoming at these extremely oblique angles.

A similar overall trend of Spatial Resolution with focus depth is seen for the S-wave reception, Fig. 6.9(b) showing, again, best performance close to the array. In addition, the large out-of-plane displacements of the S-wave at large incoming angles result in a small resolution maintained at off-axis oblique focus locations. The results of Dynamic Range and Spatial Resolution shown here are, of course, limited to the specific numerical analysis performed. Nevertheless, they provide a convincing argument for the effectiveness of the wave structure weights in DAS beamforming.

6.6.2 Results from Minimum Variance Distortionless Response

For the MVDR algorithm, the comparison was done between a classical "look direction" for the array that used only the geometrical spreading weights of Eq. (6.3), and the new weights that also incorporate the L-wave or S-wave mode structure.

For the MVDR results, diagonal loading of the autocorrelation matrix $\overline{\overline{K_{xy}}}$, with factor equal to 10^5 times the largest eigenvalue, was used to ensure the numerical stability of the solutions.

Fig. 6.10 presents the LSF simulation results using MVDR for the L-mode reception case. Eq. (6.13) with the $w_{ij,xy}^{MV,\,LL\,\text{or}\,SL}$ wave structure weights was therefore used to generate the results. As seen previously in the DAS framework, also for MVDR the new weights clearly improve the imaging performance, with increased Dynamic Range, decreased Side Lobe level, and no degradation in Spatial Resolution. Also consistently with the DAS results, the largest Dynamic Range increase in the MVDR framework, on the order of 5 dB, is seen at shallow focus points

(e.g. P1, P4 and P7), as a result of the large amplitude and curvature of the L-wave out-of-plane displacement distribution across the array. The improvements taper off at the larger focus depths (points P3, P6 and P9), where the curvature of the displacement structure across the array decreases and the wave structure performance becomes equivalent to the geometrical spreading performance. The Side Lobe levels are appreciably smaller with the wave structure weights across the focus grid, with side lobe reductions as large as 3 dB (e.g. pointP8). At the same time, the Spatial Resolution (-6dB main peak width) does not degrade.

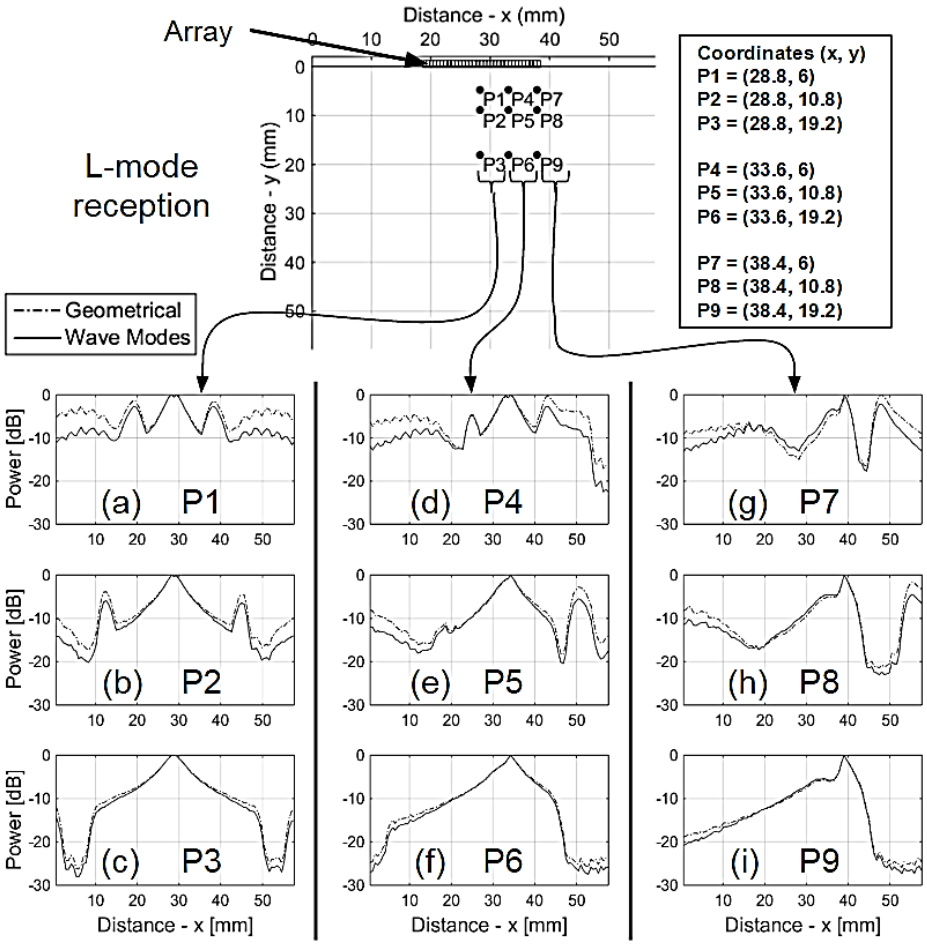

Figure 6.10: Line Spread Functions of focusing the L-wave in reception from the SAF-MVDR simulation for different focus points, and comparing a look vector that only accounts for geometrical spreading to the wave mode weights that also account for the L-wave structure

The MVDR LSF results for the S-mode reception case are shown in Fig. 6.11. Again, the

wave structure look vector performs better than the geometrical spreading look vector alone across the focus grid points. Compared to the conventional geometrical spreading weights, the new wave structure weights show an increase in Dynamic Range as high as ~ 8 dB for focus points at shallow depths (P1, P4 and P7), and a comparable Spatial Resolution across the focusing grid points. At larger depths (points P3, P6 and P9), the improvement from the wave structure weights is more marginal, as the two performances tend to become essentially equivalent.

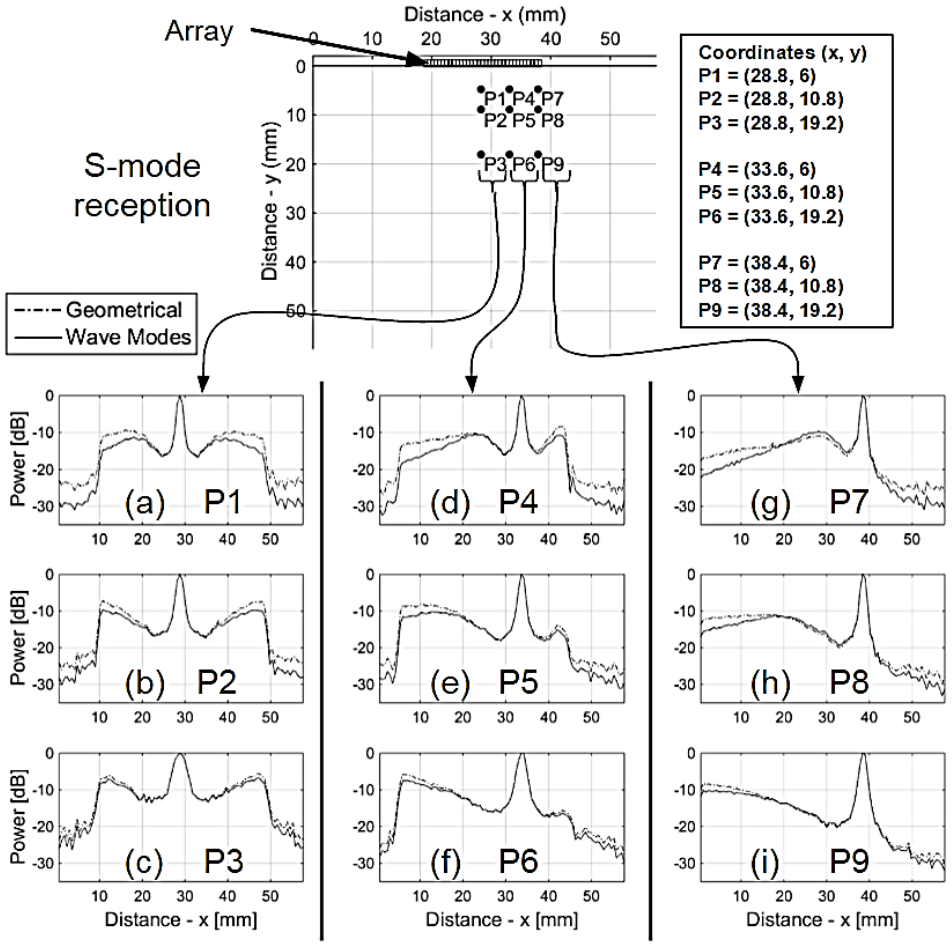

Figure 6.11: Line Spread Functions of focusing the S-wave in reception from the SAF-MVDR simulation for different focus points, and comparing a look vector that only accounts for geometrical spreading to the wave mode weights that also account for the S-wave structure

The more complete pictures of the Dynamic Range and Spatial Resolution across the entire imaging space obtained with the wave structure weights in the MVDR algorithm are shown in Fig.

6.12 and 6.13, respectively. To obtain these figures, the Matlab simulation and MVDR algorithm was run for a grid of wave source (focus) points across half of the entire 57.15 mm × 57.15 mm space. At each of the focus points, the LSF was calculated and the Dynamic Range and Spatial Resolution metrics were extracted.

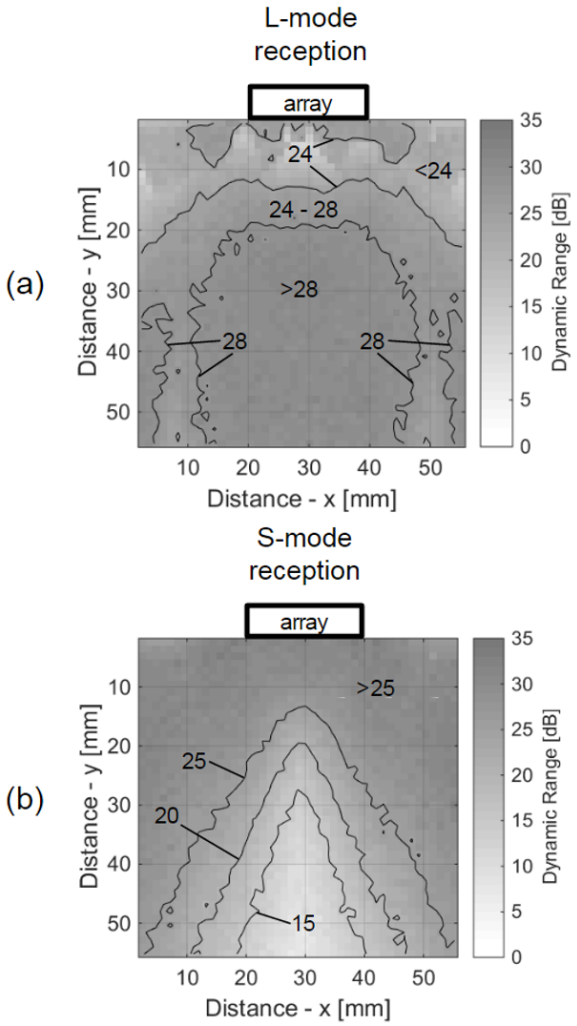

Figure 6.12: Contour plots of Dynamic Range (difference between the LSF dB maximum and minimum across the imaging width) from the numerical simulations of SAF-MVDR focusing with wave structure weights for (a) the L-mode reception and (b) the S-mode reception

For the L-wave reception case, Fig. 6.12(a), the Dynamic Range behaves quite uniformly across the imaging space, with slight improvements in the central region at shallow depths. This is consistent with the DAS results of Fig. 6.8(a). In the S-wave reception, Fig. 6.12(b), the highest

Dynamic Range is obtained in the off-axis regions, again due to the increased out-of-plane displacements of S-waves impinging on the array at oblique angles. This behavior is also consistent with the DAS results for the S-wave shown in Fig. 6.8(b).

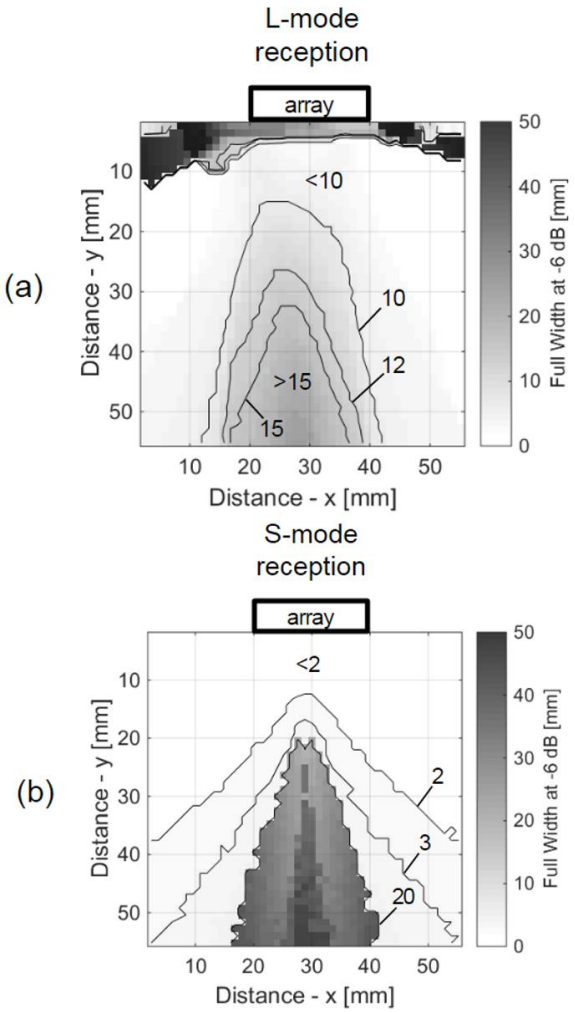

Figure 6.13: Contour plots of Spatial Resolution (-6 dB full width of the LSF main peak) from the numerical simulations of SAF-MVDR focusing with wave structure weights for (a) the L-mode reception and (b) the S-mode reception

The distribution of the Spatial Resolution is shown in Fig. 6.13(a) for the L-wave reception and in Fig. 6.13(b) for the S-wave reception. Both cases show the expected degradation in resolution with increasing depth, with the S-wave reception doing particularly well at the oblique angles. As commented for the analogous DAS result of Fig. 6.9(a), the black area at extreme angles seen in the L-wave plot is likely due to the very poor SNR of the out-of-plane component of the

L-mode waveforms in the simulations. Similarly, the dark area in the on-axis deep region seen in the S-wave plot is likely due to the small out-of-plane component of the shear wave incoming on –axis to the array. The common observation from Fig. 6.13 is that both wave modes maintain a particularly good resolution in the near-field region, as expected due to the increased curvature of the wave mode amplitude distribution across the array that helps "filtering" the response according to the wave mode structure specific to the true focus points.

In summary, as already suggested by the DAS beamforming results in the previous section, these analyses confirm the appropriateness of the wave structure weights also for MVDR beamforming.

6.7 Numerical Results: Multi-Wave Mode Compounding

As discussed in Section 6.5, an opportunity exists to further improve the imaging contrast by compounding (coherently or incoherently) images generated from wave mode weights relative to different wave modes. A proof-of-principle analysis of this approach was carried out by combining the numerical results discussed in the previous section for the L-mode reception and the S-mode reception.

The Dynamic Range results after combining the L-mode and the S-mode in reception for the DAS algorithm are shown in Fig. 6.14(a) for the incoherent compounding and Fig. 6.14(b) for the coherent compounding. These results were obtained, as in the previous plots, by numerically computing the LSF for source points located all across the imaging space, and then calculating the max-min of the LSF for each of these points. The results were obtained by using Eq. (6.15) for the incoherent case, and Eq. (6.16) for the coherent case. As expected, both incoherent and coherent summations produce Dynamic Ranges substantially larger than those obtained by the L-mode

alone in Fig. 6.8(a) or the S-mode alone in Fig. 6.8(b). Also, the compounded Dynamic Range maintains a high value throughout the imaging space. Interestingly, a slight increase in contrast is visible in the off-axis regions compared to the on-axis regions, likely owing to the beneficial contribution of the S-mode incoming at oblique angles. It can be also seen that the coherent compounding of Fig. 6.14(b) produces higher gains than its incoherent counterpart of Fig. 6.14(a).

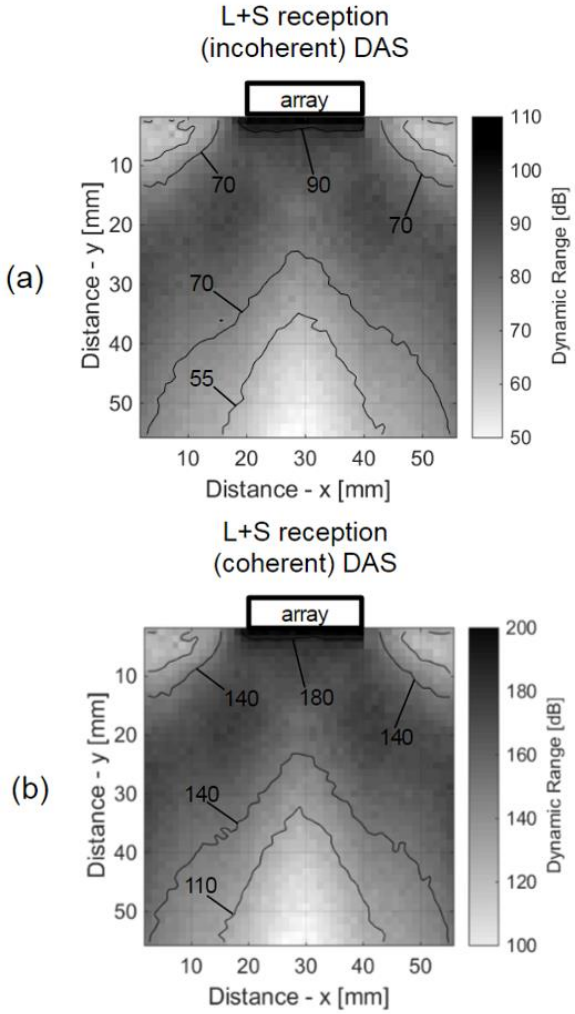

Figure 6.14: Contour plots of Dynamic Range (difference between the LSF dB maximum and minimum across the imaging width) from the numerical simulations of SAF-DAS focusing with wave structure weights by compounding the L-mode reception and the S-mode reception (a) incoherently and (b) coherently

While, as discussed in Section 6.5, the relative performance of coherent vs. incoherent summation depends on the level of SNR of the case at hand, the simulation considered here evidently

benefitted from the additional “cross-mode” terms provided by the coherent compounding.

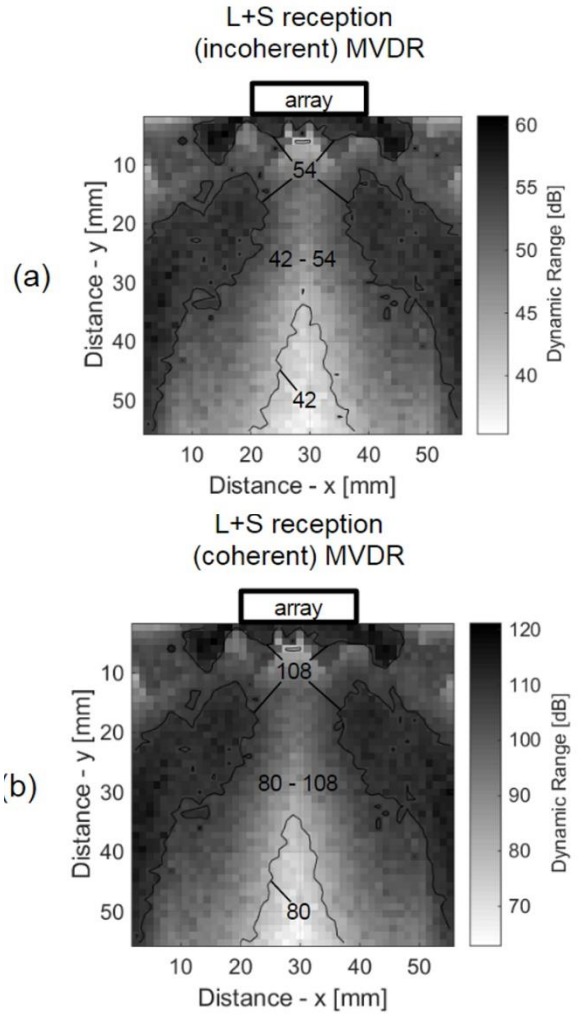

Figure 6.15: Contour plots of Dynamic Range (difference between the LSF dB maximum and minimum across the imaging width) from the numerical simulations of SAF-MVDR focusing with wave structure weights by compounding the L-mode reception and the S-mode reception (a) incoherently and (b) coherently

The effectiveness of the L+S compounding can also be seen for the MVDR algorithm, shown in Fig. 6.15(a) for the incoherent case and in Fig. 6.15(b) for the coherent case. As suggested by the DAS results, the compounding increases greatly the MVDR Dynamic Range compared to the L-mode alone of Fig. 6.12(a) or the S-mode alone of Fig. 6.12(b). Furthermore, as for the DAS results, the coherent MVDR compounding leads to larger contrast gains compared to its incoherent counterpart. This can be, again, attributed to the additional contribution of the “cross-mode” terms,

that is beneficial for the particular SNR of this simulation. Also, the further increase in gain seen in the off-axis positions of the plots in Fig. 6.15 is likely due to the favorable mode structure of the S-mode incoming onto the array at oblique angles.

In summary, in both the DAS algorithm and the MVDR algorithm, the wave mode compounding, implemented with mode-specific weights, seems to indeed generate substantial array gains without increasing the array physical size. Again, this behavior is conceptually analogous to compounding multiple reception frequencies or multiple excitations as routinely done in other imaging applications.

6.8 Experimental Results: Wave Mode Structure Weights and Multi-Mode Compounding

Proof-of-principle experimental results were obtained by imaging a drilled hole in an aluminum block. The probe used was a 32-element linear array (Olympus NDT P/N 2.25L32-19.2X10-A11-P-2.5-HY), with central frequency at 2.25 MHz, 19.2 × 10 mm total active aperture, 0.6 mm pitch, and 10 mm elevation.

The array was controlled by a full matrix capture controller (Advanced OEM Solutions, Cincinnati, OH) that generated pulsed excitations and allowed access to the raw RF waveforms in reception. The array was coupled to the aluminum using conventional ultrasonic gel-couplant. The 2mm-diameter hole was drilled at about 22 mm from the array, and it was imaged at two different lateral positions: at the center of the array footprint, Fig. 6.16(a), and at the edge of the array footprint, Fig. 6.16(b). The experiments were conducted in a 32×32 full-matrix capture scheme, with each of the 32 elements firing sequentially, and all elements receiving at each firing (for a total of 1024 set of RF waveforms). Each of these waveforms was Hilbert transformed and beamformed to obtain the *I* and *Q* image versions, and the final image was obtained as the modulus

of the *I* and *Q* value plotted in a typical dB scale. The purpose of these tests was to verify, experimentally, the effectiveness of the wave structure weights as well as the increased gain from

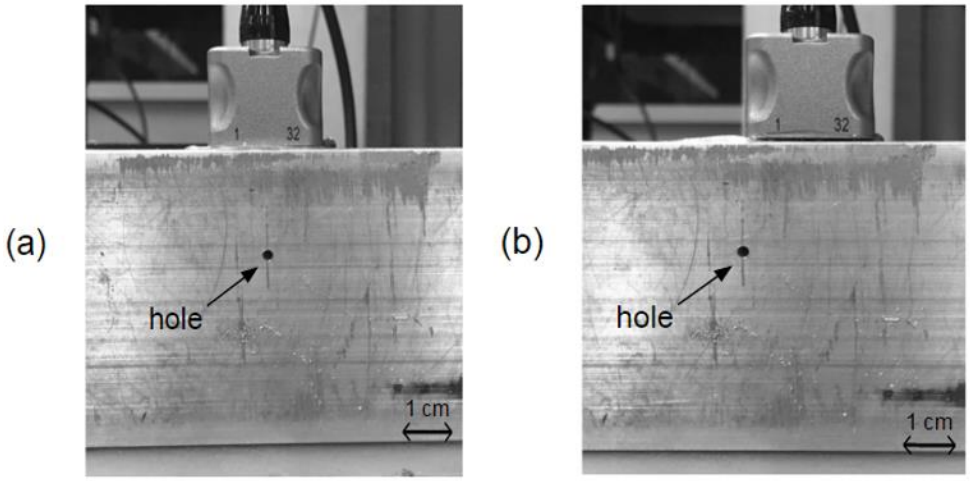

Figure 6.16: The linear array on the aluminum block with the hole reflector (a) in the center of the array footprint, and (b) at the edge of the array footprint

wave mode compounding in both SAF-DAS beamforming and SAF-MVDR beamforming. Since the hole was drilled deep into the block, the experimental test configuration was close to a plane strain case as far as the (linear) array was concerned. In any case, any 3D effects will not affect the comparison of the results for the different weights considered.

6.8.1 Results from Delay-and-Sum

The experimental SAF-DAS images obtained with the wave structure weights for the L-mode reception are compared in Fig. 6.17 with uniform (unity) weights and static Hanning apodization weights, as done in the simulation discussed previously. In this figure, the left-hand plots compare the results for the central hole position, and the right-hand plots compare the results for the off-axis hole position. The images in this figure were obtained by using the DAS beamforming of Eq. (6.11), with the L-wave weights $w_{ij,xy}^{LL\text{ or }SL}$ from Eq. (6.8). The images are displayed in a 50 dB range. The display ranges used in this figure and in the subsequent images of this section were chosen to clearly highlight the differences between the wave mode weights and

the static weights. For both on-axis reflector and off-axis reflector, the wave mode weights of Figs. 6.17(c) and 6.17(f) perform clearly better than the static weights (unity and Hanning), with a significant improvement in focusing and reduction in side lobes.

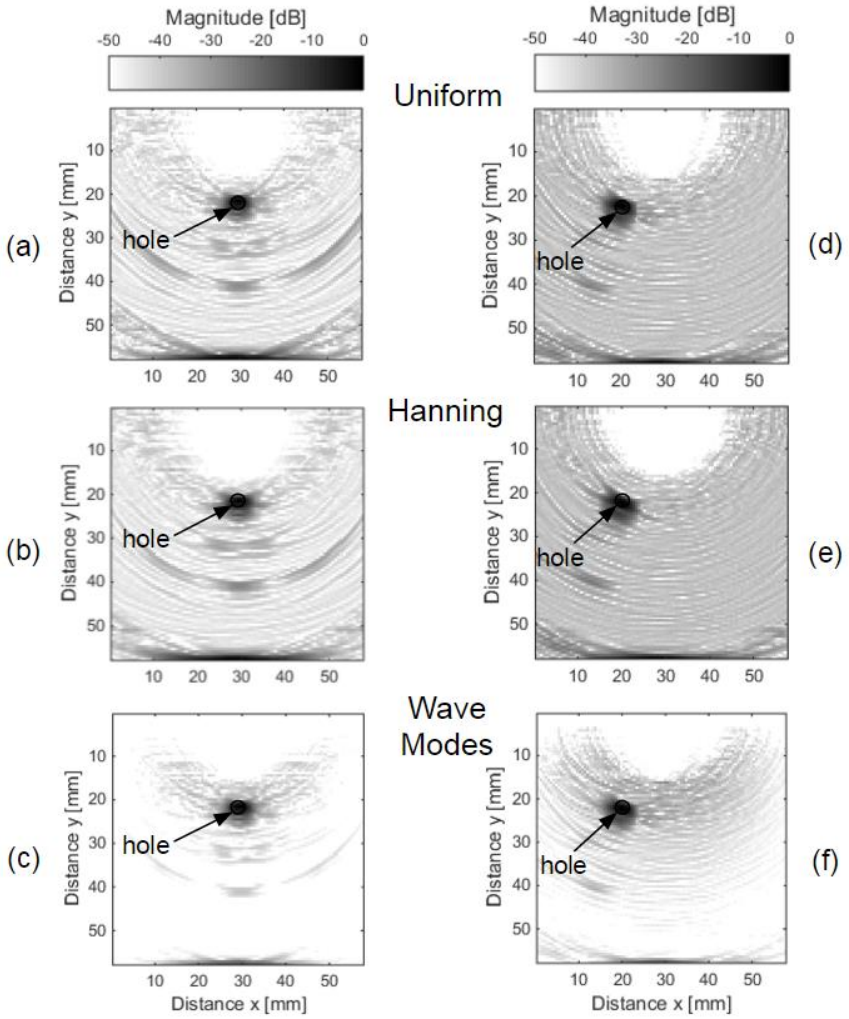

Figure 6.17: Images obtained from the experimental testing of the aluminum block with the hole by focusing the L-wave in reception in SAF-DAS beamforming, and comparing: (a), (d) uniform unity weights; (b), (e) static Hanning apodization weights; (c), (f) the new wave mode weights from the L-mode wave structure

The results for the S-mode reception (hence using Eq. (6.12) with the S-mode weights), displayed in a 25 dB range, are shown in Fig. 6.18. It can be seen that, also in the S-mode case, the wave structure weights of Figs. 6.18(c) and 6.18(f) improve the image focus, for both the on-axis hole and the off-axis hole, compared to the static weights.

These results are consistent with the conclusions from the numerical simulations discussed in section 6.6.

Fig. 6.19 shows the effects of compounding the L-mode images with the S-mode images for the two hole positions. The incoherent compounding is shown in Figs. 6.19(a) and 6.19(c), and the coherent compounding in Figs. 6.19(b) and 6.19(d).

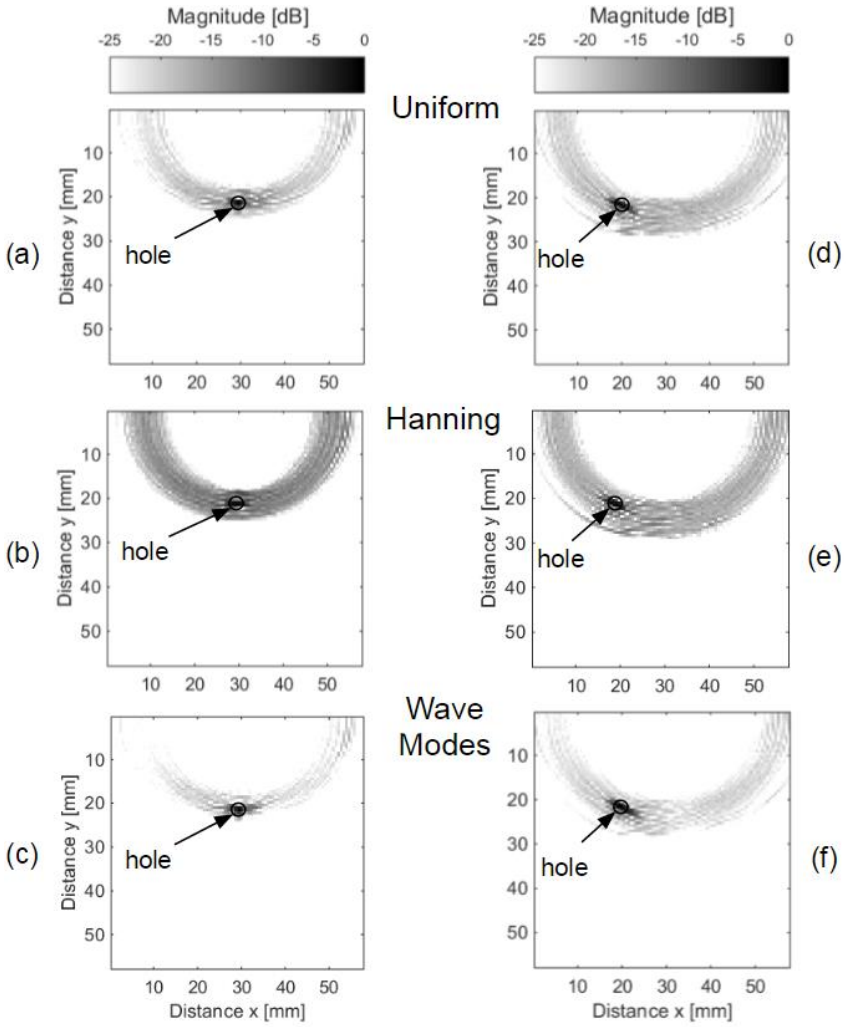

Figure 6.18: Images obtained from the experimental testing of the aluminum block with the hole by focusing the S-wave in reception in SAF-DAS beamforming, and comparing: (a), (d) uniform unity weights; (b), (e) static Hanning apodization weights; (c), (f) the new wave mode weights from the S-mode wave structure

Comparing the images of Fig. 6.19 with the individual mode images of Figs. 6.17 and 6.18, it is clear that the image compounding brings a further, quite dramatic improvement to the focusing abilities of the beamformer. Fig. 6.19 also shows that the coherent compounding leads to a better

focus than the incoherent compounding (due to the added cross-mode terms), while either case, again, substantially improves the L-mode or S-mode images taken individually. These results are consistent with the conclusions from the numerical simulations discussed in section 6.7.

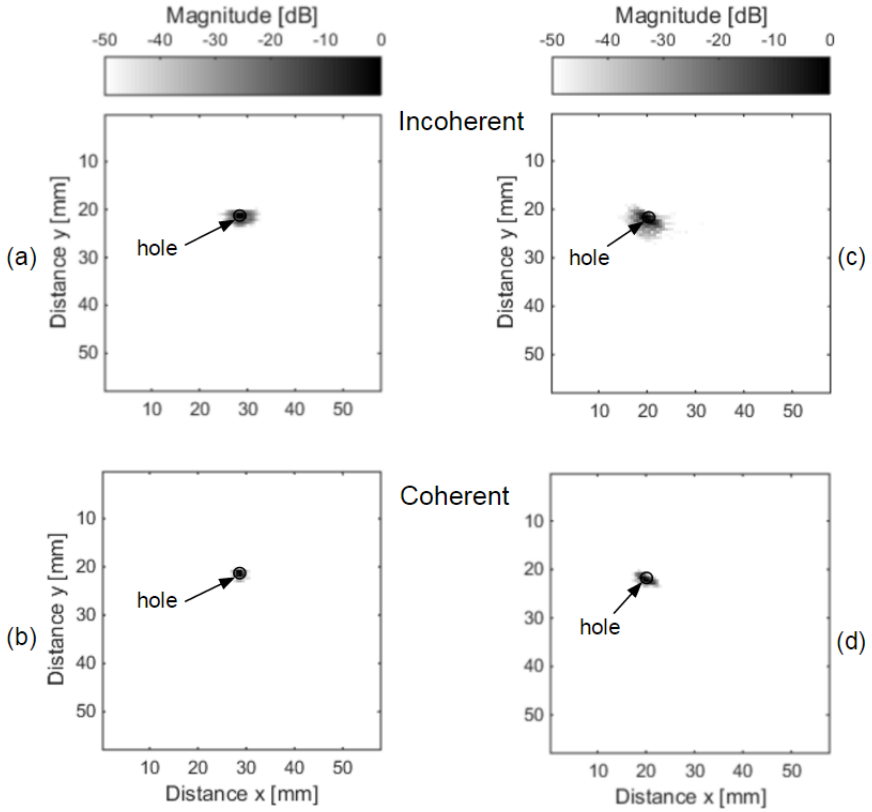

Figure 6.19: Images obtained from the experimental testing of the aluminum block with the hole by compounding the L-mode reception and the S-mode reception in SAF-DAS beamforming: (a), (c) incoherently; (b), (d) coherently

6.8.2 Results from Minimum Variance Distortionless Response

The experimental results of the hole imaging using the MVDR framework are shown in Fig. 6.20 for the L-mode reception. As done in the simulation study discussed previously, the results compare a MVDR algorithm that uses the geometrical beam spreading alone as the "look vector" [20, 26], Figs. 6.20(a) and 6.20(c), with one that adds the contribution of the new wave structure weights, Figs. 6.20(b) and 6.20(d). The results were obtained using Eq. (6.13), with the appropriate $w_{ij,xy}^{MV,\ LL\ \text{or}\ SL}$ weight vector. The images are plotted in the same dB range for each of the

two hole positions (central and off-axis), to allow for comparison between the two sets of weights. Once more, the images obtained with the wave structure weights are improved compared to those with geometrical spreading alone, with increased focus. The elimination of the back-wall reflections is due to the increased gain provided to the image in regions close to the array, where the wave structure weights can best exploit the large curvature of the displacement distribution across the array.

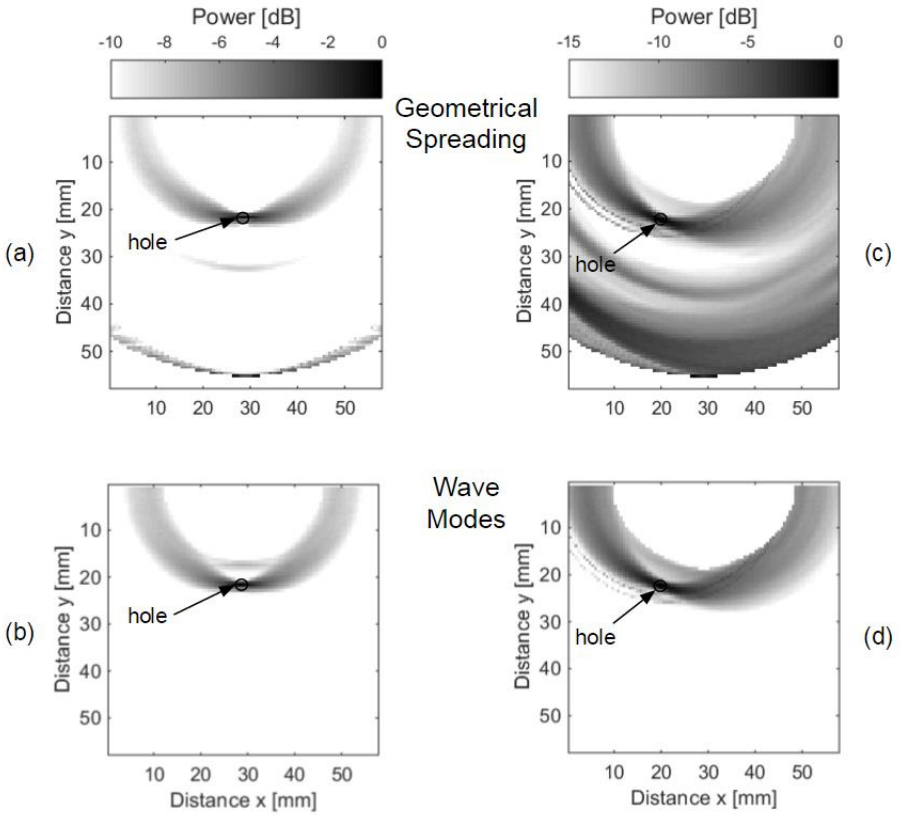

Figure 6.20: Images obtained from the experimental testing of the aluminum block with the hole by SAF-MVDR beamforming, and comparing: (a), (c) a look vector that only accounts for geometrical spreading; (b), (d) the wave mode weights that also account for the L-wave structure

The MVDR results for the S-mode reception case show similar improvements, and are not shown here for the sake of brevity.

Finally, Fig. 6.21 shows the dramatic improvement that can be obtained by compounding the L-reception with the S-reception in the MVDR framework, for both the incoherent formulation,

Figs. 6.21(a) and 6.21(c), and the coherent formulation, Figs. 6.21(b) and 6.21(d). As previously seen in the DAS results, both the incoherent and coherent MVDR compounding substantially improve the focusing compared to the L-mode alone or S-mode alone. Furthermore, the coherent compounding is confirmed to provide a better focus compared to its incoherent counterpart for these experimental results.

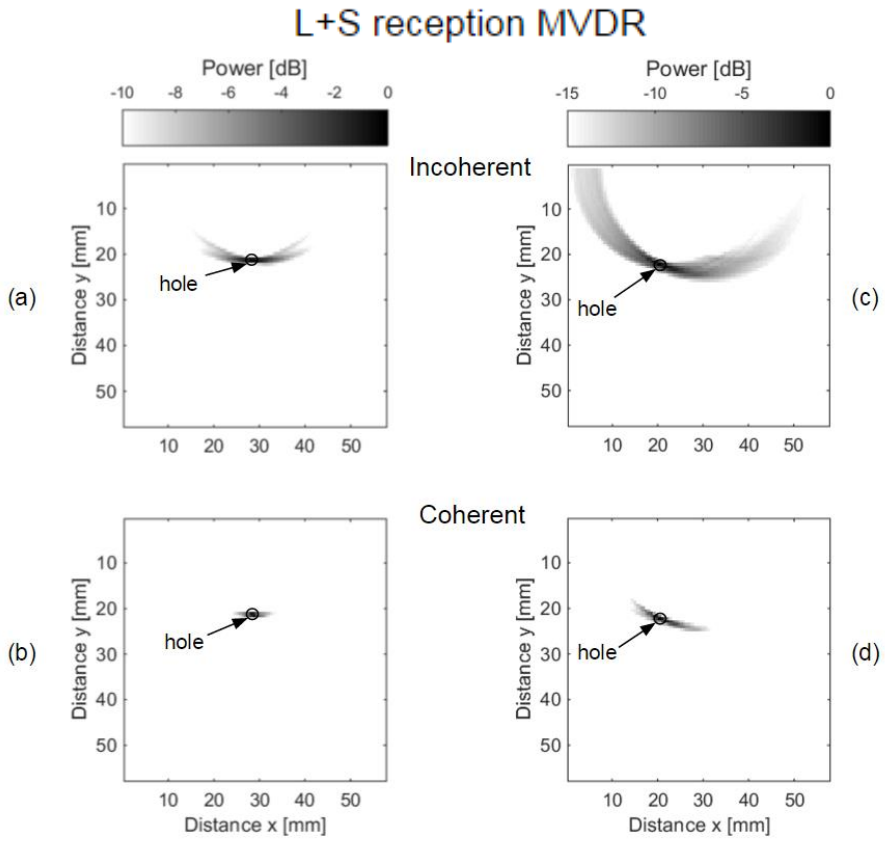

Figure 6.21: Images obtained from the experimental testing of the aluminum block with the hole by compounding the L-mode reception and the S-mode reception in SAF-MVDR beamforming: (a), (c) incoherently; (b), (d) coherently

6.9 Discussion and Conclusions

This paper has investigated the use of new weights in SAF beamforming that are based on the displacement structure of the wave modes received across the transducer array. The primary envisioned application is the field of non-destructive testing of materials and structures, although

some aspects are also applicable to biomedical imaging. For bulk solids, expressions for these weights were derived for the case of a Longitudinal (L) wave and a Shear (S) wave, also including geometrical spreading to better capture the actual distribution of the received wavefronts across the array. The application of the proposed weights follows a matched field processing approach. In this framework, the goal is to match (adaptively, at each location of the imaging space) the measured waveform amplitude distribution across the array with the expected amplitude distribution from a "true" focus point on the basis of the physics of the propagating wave (specifically the expected distribution of out-of-plane displacements across the array). The effectiveness of these wave structure weights for improved array focusing best applies to circularly-crested received wavefronts, or, equivalently, to reflectors located close to the array (e.g. in the near-field). For far-field sources generating planar wavefronts on the array, the mode structures would result in uniform weighting across the array, and thus no additional focusing compared to what obtainable using, for example, typical apodization weights.

The paper also explores the opportunity to compound images obtained from different wave mode combinations to improve the array gain without increasing its physical size. The compounding can be done either incoherently or coherently, in analogy with combining multiple frequencies or multiple excitation events.

A proof-of-principle numerical simulation was carried out in a 2D case considering both DAS and MVDR frameworks and focusing in reception only. A comparison of Line Spread Functions shows an improved focusing when the mode structure weights are used, in terms of increased Dynamic Range and decreased Side Lobe level, when compared to either unity or static Hanning apodization weights for DAS and to geometrical spreading look vectors for MVDR. At the same time, the wave structure weights maintain the Spatial Resolution performance of the other

weights. The simulations also showed the further substantial improvements in array gain that can be obtained by compounding the L-mode reception with the S-mode reception. The coherent compounding proved the most effective option, likely due to the beneficial contribution of the "cross-mode" terms in the coherent beamforming summation.

Experimental tests were also performed by using a 32-element linear ultrasonic array, operated in a full matrix capture mode, on an aluminum block containing a hole reflector. Two locations of the hole were tested, one central to the array ("on-axis"), and the other one at the edge of the array footprint ("off-axis"). SAF images were obtained for both DAS algorithm and MVDR algorithm. The experimental results essentially confirmed the numerical simulations. In both DAS and MVDR frameworks, the measurements demonstrated the improved focusing obtained by the wave structure weights when compared to the other weights (static apodization in DAS and geometrical spreading alone in MVDR), as well as the further substantial gains obtained by L+S mode compounding, with the coherent compounding, again, performing better than its incoherent counterpart.

The paper has considered a typical ultrasonic array coupled with ultrasonic gel, and hence primarily sensitive to the out-of-plane components of the wave displacement received at the array surface.

The opportunity to exploit all four wave mode combinations theoretically available in a bulk solid for compounding will depend on the ability of the array to generate a shear wave in transmission, as well as on the ability of the reflector (e.g. a defect) to mode convert in reflection. It is, in theory, quite possible for an ultrasonic array to generate both longitudinal waves and shear waves (e.g. with the use of a viscous shear couplant, shear transducers, wedges, etc..).

Finally, the framework proposed in the paper could be applied to both "active" imaging

and “passive” imaging of wave sources in solids (e.g. acoustic emission source location). The main idea behind wave structure weights and compounding could be also extended to imaging waveguides by exploiting the multimode propagation of ultrasonic guided waves, as shown in Chapter 7.

Acknowledgements

Team member at UCSD Thompson Nguyen collaborated with this research. This work was supported by grant FR-RRD-0027-11-01 (Mr. Mahmood Fateh, Program Manager) and contract DTFR-5316C00024 (Dr. Robert Wilson, Program Manager) from the US Federal Railroad Administration, and by grant CMMI-1362144 from the US National Science Foundation (Drs. Atul Kelkar and Irina Dolinskaya, Program Managers).

Chapter 6 is, in full, a reprint of material published in F. Lanza di Scalea, S. Sternini, T. V. Nguyen, “Ultrasonic Imaging in Solids Using Wave Mode Beamforming,” *IEEE Transactions on Ultrasonics, Ferroelectrics, and Frequency Control*, vol. 64, no. 3, pp. 602-616, 2017. The dissertation author was the primary investigator and author of this paper.

References

[1] Flaherty, J. J., Erikson, K. R., and Lund, V. M., 1967, “Synthetic Aperture Ultrasound Imaging systems,” United States Patent, US 3,548,642.

[2] Burckhardt, C. B., Grandchamp, P.-A., and Hoffmann, H., 1974, “An experimental 2 MHz synthetic aperture sonar system intended for medical use,” IEEE Trans. Son. Ultrason., 21(1), pp. 1-6.

[3] Karaman, M., Li, P. C., and O’Donnell, M., 1995, “Synthetic aperture imaging for small scale systems,” IEEE Trans. Ultrason. Ferroelectr. Freq. Control, 42(3), pp. 429-442.

[4] Frazier, C. H., and D. O’Brien, W., 1988, “Synthetic aperture techniques with a virtual source element,” IEEE Trans. Ultrason. Ferroelectr. Freq. Control, 45(1), pp. 196-207.

[5] Lockwood, G. R., Talman, J. R., and Brunke, S. S., 1998, "Real-time 3D ultrasound imaging using sparse synthetic aperture beamforming," IEEE Trans. Ultrason. Ferroelectr. Freq. Control, 45(4), pp. 980-988.

[6] Hazard, C. R., and Lockwood, G. R., 1999, "Theoretical assessment of a synthetic aperture beamformer for rail-time 3-D imaging," IEEE Trans. Ultrason. Ferroelectr. Freq. Control, 46(4), pp. 972-980.

[7] Nikolov, S. I., and Jensen, J. A., 2003, "In-vivo synthetic aperture flow imaging in medical ultrasound," IEEE Trans. Ultrason. Ferroelectr. Freq. Control, 50(7), pp. 848-856.

[8] Jensen, J. A., Nikolov, S. I., Gammelmark, K. L., and Pedersen, M. H., 2006, "Synthetic aperture ultrasound imaging," Ultrasonics, 44(1), pp. e5-e15.

[9] Oddershede, N., and Jensen, J. A., 2007, "Effects influencing focusing in synthetic aperture vector flow imaging," IEEE Trans. Ultrason. Ferroelectr. Freq. Control, 54(7), pp. 1811-1825.

[10] Montaldo, G., Tanter, M., Bercoff, J., Benech, N., and Fink, M., 2009, "Coherent plane-wave compuding for very high frame rate ultrasonography and transient elastography," IEEE Trans. Ultrason. Ferroelectr. Freq. Control, 56(3), pp. 489-506.

[11] Papadacci, C., Pernot, M., Couade, M., Fink, M., and Tanter, M., 2014, "High-contrast ultrafast imaging of the heart," IEEE Trans. Ultrason. Ferroelectr. Freq. Control, 61(2), pp. 288-301.

[12] Tanter, M., and Fink, M., 2014, "Ultrafast imaging in biomedical ultrasound," IEEE Trans. Ultrason. Ferroelectr. Freq. Control, 61(1), pp. 102-119.

[13] Rasmussen, M. F., and Jensen, J. A., 2014, "Comparison of 3-D synthetic aperture phased-array ultrasound imaging and parallel beamforming," IEEE Trans. Ultrason. Ferroelectr. Freq. Control, 61(10), pp. 1638-1650.

[14] Wilcox, P. D., 2003, "Omni-directional guided wave transducer arrays for the rapid inspection of large areas of plate structures," IEEE Trans. Ultrason. Ferroelectr. Freq. Control, 50(6), pp. 699-709.

[15] Wang, C. H., Rose, J. T., and Chang, F.-K., 2004, "A synthetic time-reversal imaging method for structural health monitoring," Smart Mater. Struct., 13(2), pp. 415-423.

[16] Purekar, A. S., Pines, D. J., Sundararaman, S., and Adams, D. E., 2004, "Directional piezoelectric phased array filters for detecting damage in isotropic plates," Smart Mater. Struct., 13(4), pp. 838–850.

[17] Yu, L., and Giurgiutiu, V., 2008, "In situ 2-D piezoelectric wafer active sensors array for guided wave damage detection," Ultrasonics, 48(2), pp. 117–134.

[18] Ambrozinski, L., 2013, "Beamforming of guided waves," Chapter 7 of Advanced Structural Damage Detection: From Theory to Engineering Applications, Stepinski, T., Uhl, T., and Staszewski, W., eds., pp. 177-211, John Wiley and Sons, Ltd.

[19] Clarke, T., Cawley, P., Wilcox, P. D., and Croxford, A. J., 2009, "Evaluation of the damage detection capability of a sparse-array guided-wave SHM system applied to a complex structure under varying thermal conditions," IEEE Trans. Ultrason. Ferroelectr. Freq. Control, 56(12), pp. 2666–2678.

[20] Hall, J. S., and Michaels, J. E., 2010, "Minimum variance ultrasonic imaging applied to an in situ sparse guided wave array," IEEE Trans. Ultrason. Ferroelectr. Freq. Control, 57(10), pp. 2311–2323.

[21] Hall, J. S., and Michaels, J. E., 2015, "Multipath ultrasonic guided wave imaging in complex structures," Struct. Health Monit., 14(4), pp. 345-358.

[22] Flynn, E. B., Todd, M. D., Wilcox, P. D., Drinkwater, B. W., and Croxford, A. J., 2011, "Maximum-likelihood estimation of damage location in guided-wave structural health monitoring," Proc. Roy. Soc. A: Math. Phy., 471(2181), pp. 2575–2596.

[23] Harley, J. B., and Moura, J. M. F., 2014, "Data-driven matched field processing for Lamb wave structural health monitoring," J. Acoust. Soc. Am., 135(3), pp. 1231–1244.

[24] Engholm, M., and Stepinski, T., 2010, "Adaptive beamforming for array imaging of plate structures using Lamb waves," IEEE Trans. Ultrason. Ferroelectr. Freq. Control, 57(12), pp. 2712–2724.

[25] Zhang, J., Drinkwater, B. W., and Wilcox, P. D., 2008, "Defect characterization using an ultrasonic array to measure the scattering coefficient matrix," IEEE Trans. Ultrason. Ferroelectr. Freq. Control, 55(10), pp. 2254-2265.

[26] Hall, J. S., Fromme, P., and Michaels, J. E., 2014, "Guided wave damage characterization via minimum variance imaging with a distributed array of ultrasonic sensors," J. Nondestr. Eval., 33(3), pp. 299-308.

[27] Baggeroer, A. B., Kuperman, W. A., and Mikhalevsky, P. N., 1993, "An overview of matched field methods in ocean acoustics," IEEE Ocean. Eng., 18(4), pp. 401-424.

[28] Kuperman, W. A., and Turek, G., 1997, "Matched field acoustics," Mech. Syst. Sig. Proc., 11(1), pp. 141-148.

[29] Capon, J., 1969, "High resolution frequency wavenumber spectrum analysis," Proc. IEEE, 57, pp. 1408-1418.

[30] Michalopoulou, Z.-H., and Porter, M. B., 1996, "Matched-field processing for broad-band source localization," IEEE Ocean. Eng., 21(4), pp. 384-392.

[31] Baggeroer, A. B., Kuperman, W. A., and Schmidt, H., 1988, "Matched-field processing: source localization in correlated noise as an optimum parameter estimation process," J. Acoust. Soc. Am., 83(2), pp. 571-587.

[32] Makris, N. C., 1995, "A foundation for logarithmic measures of fluctuating intensity in pattern recognition," Opt. Lett., 20(19), pp. 2012-2014.

[33] Debever, C., and Kuperman, W. A., 2007, "Robust matched-field processing using a coherent broadband white noise constraint processor," J. Acoust. Soc. Am., 122(4), pp. 1979-1986.

[34] Tolstoy, A., 1993, Matched Field Processing, World Scientific, New York.

[35] Orris, G. J., Nicholas, M., and Perkins, J. S., 2000, "The matched-phase coherent multi-frequency matched-field processor," J. Acoust. Soc. Am., 107(5), pp. 2563-2575.

[36] Martin-Arguedas, C. J., Romero-Laorden, D., Martinez-Graullera, O., Perez-Lopez, M., and Gomez-Ullate, L., 2012, "An ultrasonic imaging system based on a new SAFT approach and a GPU beamformer," IEEE Trans. Ultrason. Ferroelectr. Freq. Control, 59(7), pp. 1402-1412.

[37] Carlson, B. D., 1988, "Covariance matrix estimation errors and diagonal loading in adaptive arrays," IEEE Trans. Aero. Elect. Sys., 24(4), pp. 397-401.

[38] Rao, N. A., Mehra, S., Bridges, J., and Venkatraman, S., 1995, "Experimental point spread function of FM pulse imaging scheme," Ultras. Imaging, 17(2), pp. 114-141.

Chapter 7

Minimum Variance Imaging in Plates Using Guided Wave Mode Beamforming

Abstract

This paper presents improvements to ultrasonic imaging of solid plate-like structures using the minimum variance distortionless response (MVDR) beamforming processor. The primary application of this work is the nondestructive testing of plate-like components that are widely used in aerospace, marine, and civil structures. The study proposes a new set of weights, or MVDR replica vectors, that are based on the physics of the propagating Lamb modes, including the symmetric mode S0, the antisymmetric mode A0, and the shear horizontal mode SH0. Numerical results show that these wave mode weights, combined with geometrical spreading, improve the focus of the array by increasing dynamic range and spatial resolution of the image. Additionally, quite dramatic improvements in image quality are achieved by combining, or compounding, the multiple Lamb modes naturally present in the plate in both transmission and reflection. As shown in recent work applied to bulk waves in 3D solids, the compounding of Lamb modes in plates increases the array gain without increasing its physical aperture.

7.1 Introduction

Ultrasonic imaging is utilized in a wide range of applications from the medical field to the inspection of structural components. Continued research in this area has allowed ultrafast cardiac imaging [1-4] and blood flow imaging [5-11], as well as effective nondestructive testing (NDT) of structures for damage detection and characterization [12-26].

Most of the ultrasonic imaging beamformers involve the use of weighting functions, often called apodization weights, attributed to the collected waveforms to suppress the sidelobes in the final image. Usually, these apodization weights are static (e.g. Hanning window), therefore they do not change with respect to different focus points in the imaging medium. A different application of these weights can be found in a Matched Field Processing framework [27, 28], where they serve as a filtering tool to locate the reflector using the recorded signals. In this implementation, weights are often referred to as "replica vectors" since they "replicate" the expected response of the array for a specific recorded feature. The overall concept is to find the best match between the replica vectors, calculated for each discretized point in the imaging medium, and the "data vector" measured by the transducer array. The points showing the best match are the true locations of the reflectors. A common set of weights (replicas) accounts for the geometrical spreading of the waves travelling through the material, which involves an amplitude decay proportional to *1/sqrt(d)* for the 2D case and *1/d* for the 3D case, where *d* is the propagation distance [18, 19], [23]. Other types of weights, instead, account for the scattering patterns of the wave reflected by a given structural feature [23, 24].

A known beamforming algorithm found in matched field processing is the minimum variance distortionless response (MVDR) method. MVDR, also known as Capon's Maximum Likelihood Method (MLM), has been around since the 1960s [29] and has found numerous

applications in underwater acoustics, structural damage detection [18], [19], [24] and, more recently, medical imaging [30-33]. The MVDR beamformer is an adaptive processor, which means that the weights depend both on the replica field (expected response) and on the actual measured data. This processor is able to suppress the sidelobe level while narrowing the main lobe in the beamformer pattern. The concept behind MVDR is to minimize the output of the array except in the "look direction", so as to reject any signal (or noise) coming from a direction different from the direction of scanning. The MVDR beamformer is strongly affected by the model used to describe the imaging medium, therefore an accurate representation of the wave propagation characteristics is a crucial part needed to create a reliable replica field.

A strategy used to increase the array gain without increasing its physical aperture is compounding. The idea is to combine images obtained with different independent parameters in order to increase the image contrast and spatial resolution. Examples of compounding can be found in matched field acoustics, where images from multiple frequencies are combined [34], or in medical imaging, in the form of plane wave compounding [1]. There are two main ways of compounding images (or features): incoherently [27], [34-36], or coherently [35], [37-39]. While in theory the coherent version should bring additional gain due to the added cross terms, the relative performance generally depends on the noise structure in the imaging medium [35], [37]. The authors have recently demonstrated the benefits of compounding for the case of bulk waves in 3D solids [25], by combining images from longitudinal and shear waves naturally coexisting in the imaging medium.

This paper extends some of these ultrasonic imaging strategies based on matched field processing (MVDR) to the case of guided (Lamb) waves in plate-like solid components that are widely used in aerospace, marine, and civil structures. Because of this widespread use, guided-

wave ultrasonic testing has arguably become in recent years the most popular technique for structural health monitoring (SHM). In particular, the paper proposes new weight vectors (replica vectors) based on the physics of the propagating Lamb modes to increase the focus of the array on the reflector (e.g. damage) locations. The paper also exploits the compounding of multiple Lamb modes to improve the imaging results compared to the traditional use of a single Lamb mode. The improvements are shown in a proof-of-principle numerical test of an aluminum plate with a blind-hole reflector located either on-axis or off-axis relative to the transducer array.

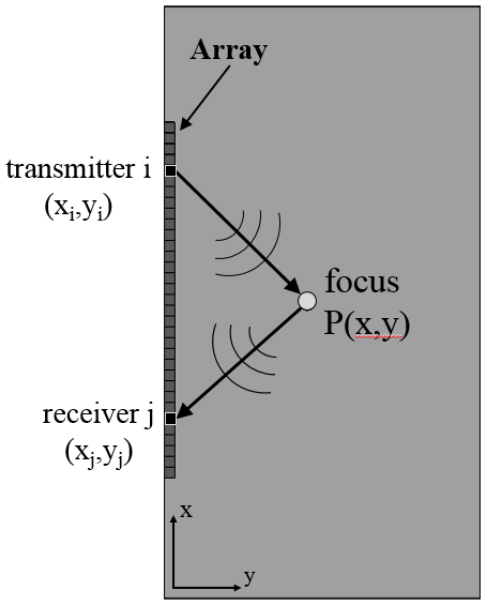

Figure 7.1: Schematic of ultrasonic imaging on a plate

7.2 Minimum Variance Distortionless Response Processor

Considering an array of *M* transmitters and *N* receivers (Fig. 7.1), let the spatial coordinates of each transmitter $i = 1..M$ be (x_i, y_i) and the spatial coordinates of each receiver $j = 1..N$ be (x_j, y_j). From the recorded waveforms, it is possible to extract amplitudes *A* from the time domain signals based on the travel time of a specific guided wave mode from transmitter *i* to focus point

P(x,y), and back to receiver *j*. For each focus point *P(x,y)* and each transmitter *i*, a vector of amplitudes (data vector) can be constructed as follows

$$\overline{A_{i,xy}} = [A_{i1} \quad A_{i2} \quad \dots \quad A_{iN}]^T \tag{7.1}$$

where the superscript *T* denotes transpose and A_{ij} is the amplitude related to each transmitter-receiver pair *i-j*. The data vectors are then compared with the replica field, formed by the vectors of expected responses of the array, by means of the MVDR processor. Each focus point in the discretized imaging domain represents a "scanning" location where the data vector is compared with a replica vector. Hence the coordinates *(x,y)* of the focus points are used as parameters for which each replica field is constructed. Through this comparison, an ambiguity function is obtained, representing a map of similarity between data and replica vectors, which can be used to identify the reflectors (e.g. damage) anywhere in the plate. A high level of match, or similarity, between data and replicas will result in large intensity values in the ambiguity function, hence a "true" reflector.

The MVDR beamformer tries to optimize the match to a signal from a specific "look direction" while rejecting signals and correlated noise coming from different scanning locations. This procedure can be carried out by computing a replica vector $\overline{w_{IJ,xy}^{MVDR}}$ that minimizes the output of the beamformer except in the "look direction" of scanning. The MVDR replica vector is chosen to minimize the following functional

$$F = \overline{w_{ij,xy}^{MVDR}}^T \overline{\overline{K_{xy}}}\, \overline{w_{ij,xy}^{MVDR}} + \gamma\left(\overline{w_{ij,xy}^{MVDR}}^T \overline{e_{ij,xy}} - 1\right) \tag{7.2}$$

where γ is a Lagrange multiplier, and $\overline{e_{J,xy}}$ represents the normalized weighting functions (normalized replica vectors) on which the data vectors, forming the autocorrelation matrix $\overline{\overline{K_{xy}}}$, are projected. The matrix $\overline{\overline{K_{xy}}}$ is calculated as follows

$$\overline{\overline{K_{xy}}} = \frac{1}{M}\sum_{i=1}^{M} \overline{A_{i,xy}}\,\overline{A_{i,xy}}^{T} \tag{7.3}$$

where it is shown that the autocorrelation matrix for the focus point of coordinates *(x,y)* is calculated by the outer product of the data vectors computed in (7.1), averaged over *M* transmissions. Typically, the number of transmissions should be greater than or equal to the number of receivers for the autocorrelation matrix to have full rank. The normalized replica vectors are obtained as follows

$$\overline{e_{ij,xy}} = \frac{\overline{w_{ij,xy}}}{\left|\overline{w_{ij,xy}}\right|} \tag{7.4}$$

so that the replica vectors, normalized by their L_2 norm, all have unit length. Section 7.3 will show how these replica vectors, or weights, can be constructed based on the physics of the propagating wave modes.

Taking the gradient of (7.2) with respect to $\overline{w_{J,xy}^{MVDR}}$ and setting it equal to zero results in

$$\overline{w_{ij,xy}^{MVDR}} = -\frac{\gamma}{2}\left(\overline{\overline{K_{xy}}}^{-1}\overline{e_{ij,xy}}\right) \tag{7.5}$$

and using the constraint condition of unity

$$\overline{w_{ij,xy}^{MVDR}}^{T}\overline{e_{ij,xy}} = 1 \tag{7.6}$$

it is possible to obtain the following expression for γ

$$\gamma = -2\left(\overline{\overline{e_{ij,xy}}}^{T}\,\overline{\overline{K_{xy}}}^{-1}\,\overline{\overline{e_{ij,xy}}}\right)^{-1}. \tag{7.7}$$

By substituting (7.7) into (7.5), the MVDR replica vector is obtained as [27], [28], [40]

$$\overline{w_{ij,xy}^{MVDR}} = \frac{\overline{\overline{K_{xy}}}^{-1}\,\overline{\overline{e_{ij,xy}}}}{\overline{\overline{e_{ij,xy}}}^{T}\,\overline{\overline{K_{xy}}}^{-1}\,\overline{\overline{e_{ij,xy}}}} \tag{7.8}$$

which can be used in the MVDR beamformer as

$$B_{MVDR}(x,y) = \overline{\overline{w_{ij,xy}^{MVDR}}}^{T}\,\overline{\overline{K_{xy}}}\,\overline{\overline{w_{ij,xy}^{MVDR}}} \tag{7.9}$$

leading to the following final expression

$$B_{MVDR}(x,y) = \left[\overline{\overline{e_{ij,xy}}}^{T}\,\overline{\overline{K_{xy}}}^{-1}\,\overline{\overline{e_{ij,xy}}}\right]^{-1}. \tag{7.10}$$

Equation (7.8) shows that the weight vectors for the MVDR beamformer are constructed depending on the data itself. For this reason, MVDR is an *adaptive* beamforming technique and a nonlinear function of the received wave field. Equation (7.10) produces an ambiguity function, in the *(x,y)* location space, used for localizing the true reflectors.

Although MVDR has high resolution capabilities, modeling of the environment (replica field) should be carefully carried out. In fact, errors in the replica field deriving from geometrical or physical inaccuracies (e.g. transducer locations, wave mode velocities, etc.) can strongly affect the output of the MVDR beamformer and, in general, adaptive processes. Furthermore, as previously discussed, an insufficient number of transmissions could cause the autocorrelation

matrix to be rank deficient [27]. In this case, the inverse of the autocorrelation matrix in (7.10) would not exist and a pseudoinverse matrix is required. To address these problems, a regularization procedure is performed using diagonal loading [18] of the autocorrelation matrix $\overline{\overline{K_{xy}}}$. A fraction *f* of the largest eigenvalue λ_1 of $\overline{\overline{K_{xy}}}$ is used for diagonal loading

$$\overline{\overline{K_{xy}}}^{-1} = \left(\overline{\overline{K_{xy}}} + f\lambda_1 \overline{\overline{I}}\right)^{-1}. \tag{7.11}$$

For the MVDR results presented in this chapter, the regularization factor *f* was chosen to be equal to 10^{-2}.

7.3 Wave Mode Structure Weights

This work considers the three fundamental Lamb modes that can generally co-exist in a plate: symmetric (axial) mode S0, antisymmetric (flexural) mode A0, and shear horizontal mode SH0. The excitation frequency and thickness of the plate considered here were below the cutoff values for the higher-order modes, that were therefore ignored.

Each wave mode that is reflected by a particular focus point will result in a particular distribution of responses across the array that can be used as the replica vector for the MVDR beamformer. In other words, the displacement "structure" of each mode can be used to generate the replica field.

7.3.1 S0 and A0 Wave Modes

For the case of an S0 or A0 wave mode reflected by point *P(x,y)* and impinging on receiver *j*, as illustrated in Fig. 7.2, the component of displacement considered for the replica vectors calculation is the displacement parallel to the wave propagation direction. Assuming that the array

elements are only sensitive to the component of displacement along the normal to the surface (direction *y* in Fig. 7.1), it is possible to calculate the expected distribution of displacements across the array by simply projecting the wave vector $u_{j,xy}^{S0,A0}$ onto the *y* direction. This expected response of the array becomes the replica vector, or weight vector, for that particular reflector location *(x,y)*. By computing the expected array response for all possible reflector locations in the plate, a replica field can be constructed as follows

$$w_{j,xy}^{S0,A0} = \left|\overline{u_{j,xy}^{S0,A0}}\right| \cos\,\theta_{j,xy} = \left|\overline{u_{j,xy}^{S0,A0}}\right| \frac{\left|y_j - y\right|}{\sqrt{\left(x_j - x\right)^2 + \left(y_j - y\right)^2}} \tag{7.12}$$

or

$$w_{j,xy}^{S0,A0} \propto \frac{\left|y_j - y\right|}{\sqrt{\left(x_j - x\right)^2 + \left(y_j - y\right)^2}} \tag{7.13}$$

where the superscript *S0, A0* indicates a reflected S0 or A0 mode. Fig. 7.2(a) shows the response of the array for a reflector located on-axis at the center of the array. If the reflector is located off-axis, the distribution of amplitudes will be appropriately skewed, as shown in Fig. 7.2(b).

The geometrical spreading effect [18], [19], which also depends on the transmitter *i*, can be included in the calculation of the weights by modifying Eq. (7.13) as follows

$$w_{ij,xy}^{S0,A0} \propto \frac{1}{\sqrt{d_{i,xy} d_{j,xy}}} \cdot \frac{\left|y_j - y\right|}{\sqrt{\left(x_j - x\right)^2 + \left(y_j - y\right)^2}} \tag{7.14}$$

where $d_{i,xy}$ is the distance between transmitter *i* and focus point *P(x,y)*, and similarly $d_{j,xy}$ is the distance between receiver *j* and the same focus point at *(x,y)*. Notice that the 2D geometrical spreading has been considered (square root of propagation distance). Equation (7.14) is the final

relation for the calculation of wave mode weights for a reflected S0 or A0 mode (applicable to any wave mode used in transmission), and it depends on transmitter, receiver, and focus point location.

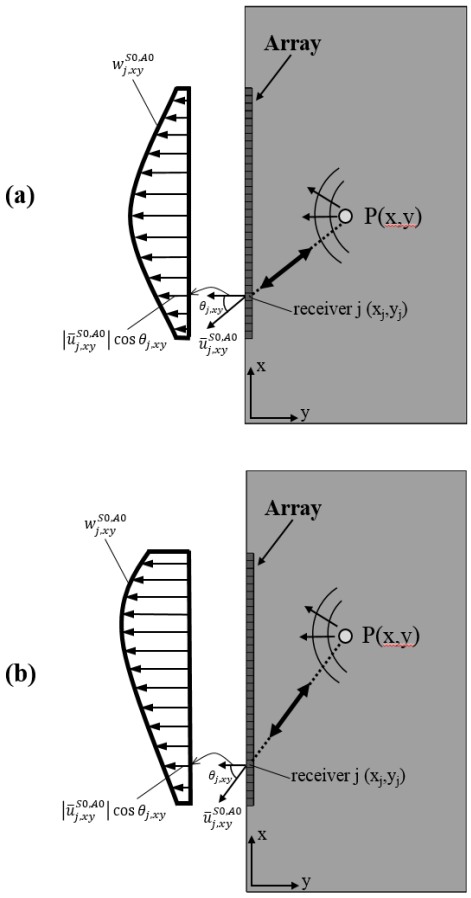

Figure 7.2: Weight vectors, or replica vectors, based on wave mode structure for an S0 or A0 mode reflection. (a) Reflector located on-axis at the center of the array. (b) Reflector located off-axis

7.3.2 SH0 Wave Mode

The case of a shear horizontal (SH0) wave reflected by a focus point in the plate can be derived analogously. Fig. 7.3 illustrates the array response to an SH0 wave mode. In this case, the point motion is perpendicular to the wave propagation direction, similarly to shear waves in bulk solids. Since the array is still only sensitive to the displacement component along the normal to the surface (*y* direction), the SH0 displacement can be projected as in (7.12), thus giving the relation for SH0 wave mode weights as follows

$$w_{j,xy}^{SH0} = \left|\overline{u_{j,xy}^{SH0}}\right| \cos(90° - \theta_{j,xy}) = \left|\overline{u_{j,xy}^{SH0}}\right| \frac{|x_j - x|}{\sqrt{(x_j - x)^2 + (y_j - y)^2}} \tag{7.15}$$

Fig. 7.3(a) shows the array response for a reflector located on-axis to the array, and Fig. 7.3(b) shows the skewed response for a reflector located off-axis. By including 2D geometrical spreading, (7.15) becomes

$$w_{ij,xy}^{SH0} \propto \frac{1}{\sqrt{d_{i,xy} d_{j,xy}}} \cdot \frac{|x_j - x|}{\sqrt{(x_j - x)^2 + (y_j - y)^2}} \tag{7.16}$$

Equation (7.16) is the final expression for wave mode weights applied to an SH0 wave reflection (applicable to any mode used in transmission).

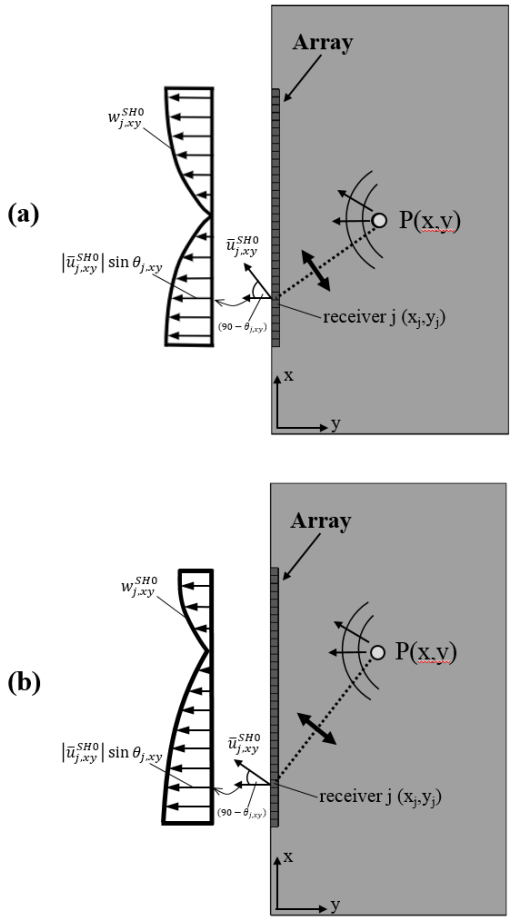

Figure 7.3: Weight vectors, or replica vectors, based on wave mode structure for an SH0 mode reflection. (a) Reflector located on-axis at the center of the array. (b) Reflector located off-axis

7.4 Guided Wave Mode Compounding

The multi-modal nature of Lamb waves (and guided waves in general) allows exploiting the different propagating modes to create multiple replica fields. If the information from the different modes can be combined, or compounded, very significant improvements in array gain can be obtained without increasing the array's physical aperture.

More specifically, in analogy to the case of bulk wave propagation in 3D solids examined recently by the authors [25], a reflector in a plate-like structure that is illuminated by a given incident Lamb mode can generate both same-mode reflections and mode-converted reflections. The results shown here consider both S0 transmissions and SH0 transmissions that can be generated simultaneously by a point-source acting in the mid-plane of the plate (see Fig. 7.4). The incident S0 mode can be reflected as a same-mode S0 ("S0-S0 combination") and a converted mode A0 ("S0-A0 combination"), if the reflector is generally not symmetric with respect to the mid-plane of the plate [41]. Also, the incident S0 can be generally mode-converted into a reflected SH0 mode ("S0-SH0 combination").

The test case considered in the paper consist of a blind hole in the plate as the reflector (simulating corrosion) and allowing the following four mode combinations: S0-S0, S0-A0, S0-SH0, and SH0-SH0. Fig. 7.4 illustrates how the different transmitted modes (S0 and SH0) are reflected through either same-mode reflection or mode conversion. The dashed lines in Fig. 7.4 represent the main directivity lobes of the transmitted modes, whereas the solid lines indicate the directivity lobes of the reflected modes.

Wave mode compounding can be performed either incoherently or coherently. Incoherent compounding is the simple summation of the image intensities obtained by the different wave mode combinations. It is implemented as follows

$$B_{TOT,incoherent}(x,y) = \sum_{MC} B_{MVDR}^{MC}(x,y) \tag{7.17}$$

where *MC = S0-S0, S0-A0, S0-SH0, SH0-SH0* indicates the various wave mode combinations, and $B_{MVDR}^{MC}(x,y)$ (in decibels) is the image obtained using the MVDR algorithm for a specific mode combination. This incoherent approach exploits the consistency of the true reflector throughout the different mode combinations, while reducing the random spatial noise in each individual image.

Coherent compounding, instead, considers "cross-mode" terms that represent the spatial cross-correlation between the various images. The coherent way of combining different images comes from the "cross-frequency" terms used in matched field processing, which exploit the phase coherence of waves at different frequencies. In the coherent case, the final image intensity is

$$B_{TOT,coherent}(x,y) = \left(\sum_{MC} \left| \sqrt{B_{MVDR}^{MC}(x,y)} \right| \right)^2 \tag{7.18}$$

where, as in the incoherent case, the images $B_{MVDR}^{MC}(x,y)$ (in decibels) are given by (7.10) for the different wave mode combinations *MC*.

7.5 Numerical Results

A finite element model was created to simulate the propagation of guided Lamb waves in an aluminum plate with a blind hole as the reflector (simulating a corrosion defect). An on-axis hole and an off-axis hole were considered.

The transmission and reception of the guided waves was performed using a simulated 33-element linear array. The excitation considered to obtain the incident S0 and SH0 modes was a

force parallel to the plane of the plate, applied as a point source (Fig. 7.4). The following section presents the details of the model.

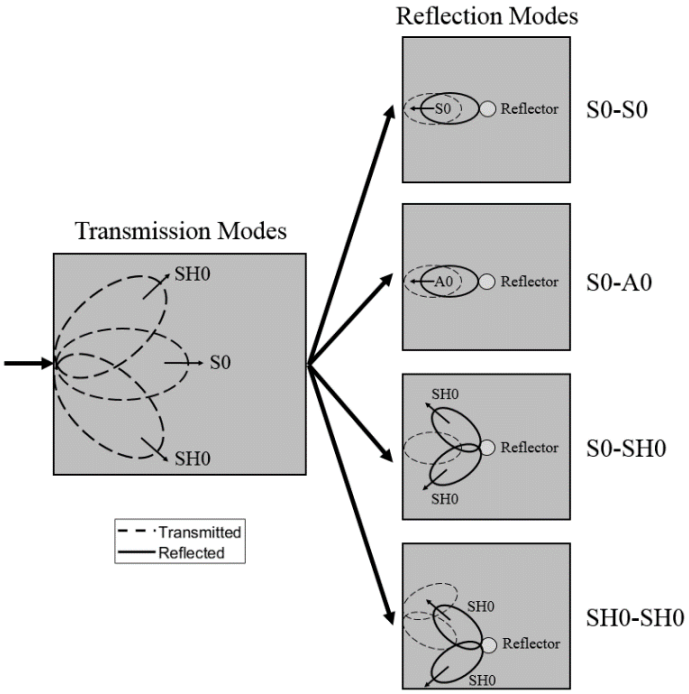

Figure 7.4: Schematic of transmitted and reflected wave modes in a plate subjected to a point source parallel to the plane of the plate. The reflector is an antisymmetric defect (blind hole)

7.5.1 Finite Element Model

The Finite Element model describes a plate 0.45m x 0.76m in size and 9 mm in thickness. The material is aluminum with density 2810 kg/m^3, Young's modulus 7*10^{10} N/m^2, and Poisson's ratio 0.32. The model was realized with the software Ansys using SHELL 181 elements. This is a 3D shell element with four nodes and six degrees-of-freedom per node, that are translations of the plane of the plate according to the three Cartesian axes and rotations about them. The plane of the plate is in the *x-y* plane, and the *z* axis is orthogonal to the plane. This element supports layered composites, and this property can be exploited to model the off-axis discontinuity. This is defined as an area made of two layers, occupying respectively the volume under and above the symmetry

plane. One of the two layers has the same material properties as the rest of the plate, the second one has zero density and stiffness to simulate the blind hole.

The plate is clamped on one side and has free boundaries on the other three edges. Waves are generated using an in-plane point force whose time history is a sine enveloped by a Gaussian curve (toneburst), with center frequency of ~ 90 kHz. This results into a value for the product of excitation frequency and plate thickness of ~ 0.8 MHz*mm, where only the fundamental zero-order modes S0, SH0, and A0 can exist [42]. Time and space discretizations are appropriately scaled accounting for the wave physics. The time step is $5.5*10^{-7}$ s, which is 1/20 of the period of the travelling waves, and the largest size of the elements in the mesh is 1 mm, which is around 1/25 of the smallest wavelength involved, associated to the A0 mode.

The components of displacements for modes S0 and SH0 are directly obtained from the in-plane displacements in the plane of the plate, that are assumed to be constant through the plate thickness, and therefore coincide with those at the surface of the plate. On the contrary, the components of displacement for mode A0 at the surface of the plate are indirectly obtained from the rotations about the *x* and *y* axes, by assuming a linear distribution of displacements through the plate thickness (low frequency approximation).

7.5.2 Results: Wave Mode Structure Weights

The results compare the MVDR algorithm that uses geometrical spreading alone as the "look direction" (replica vectors) [18], [24], with one that uses replica vectors obtained from the proposed guided wave mode weights in (7.14) and (7.16) of Section 7.3, which combine geometrical spreading with the wave mode structure.

Fig. 7.5 shows the results obtained for the on-axis reflector. The aluminum plate dimensions were 0.45m in the *x* direction and 0.76m in the *y* direction. The blind hole was located

at x = 0.19m and y = 0.38m. The results plot the power (in dB) of the beamformed acoustic feature recorded by the array, since the MVDR relation used to obtain the images, Eq. (7.10), is a quadratic form. All images are plotted in the same dB scale (0 to -25dB) for a better comparison of the different sets of weights. Figs. 7.5(a)-7.5(d) are obtained using only geometrical spreading weights for the S0-S0, S0-A0, S0-SH0, and SH0-SH0 combinations, respectively. Figs. 7.5(e)-7.5(h) are obtained using the proposed wave mode structure weights for the same four combinations. Comparing Fig. 7.5(a) to Fig. 7.5(e), it is clear that the wave mode weights for the S0-S0 combinations considerably improve the imaging result. Specifically, the wave mode weights increase the dynamic range (lower noise floor) and suppress the sidelobes, compared to using only geometrical spreading weights. Similarly, for the S0-A0 combination (Figs. 7.5(b) and 7.5(f)), the dynamic range improves. Moreover, the S0-A0 combination achieves a higher spatial resolution compared to S0-S0 case, due to the smaller wavelength of the reflected A0 mode compared to the reflected S0 mode.

The third combination involves the mode conversion of S0 into SH0. Fig. 7.5(c) shows the result with the geometrical spreading weights. In this case, around the reflector location there are other high intensity areas which are likely artifacts deriving from other wave mode combinations. The reflection from the boundary on the right side of the plate also appears in the image. Fig. 7.5(g) illustrates the image obtained using the same S0-SH0 combination, with the application of the wave mode weights. In this case, the improvement from Fig. 7.5(c) is evident, as the artifacts and the reflection from the boundary are eliminated, and the energy is correctly focused on the true reflector. A slight improvement in dynamic range is also visible.

Finally, the last combination, SH0-SH0, is shown in Figs. 7.5(d) and 7.5(h). Similarly to the S0-SH0 combination, the geometrical spreading weights generate artifacts from other wave

move combinations and boundary reflections on the right edge of the plate. The application of the wave mode weights considerably reduces both artifacts and reflections, and increases the dynamic range by lowering the noise floor of the image.

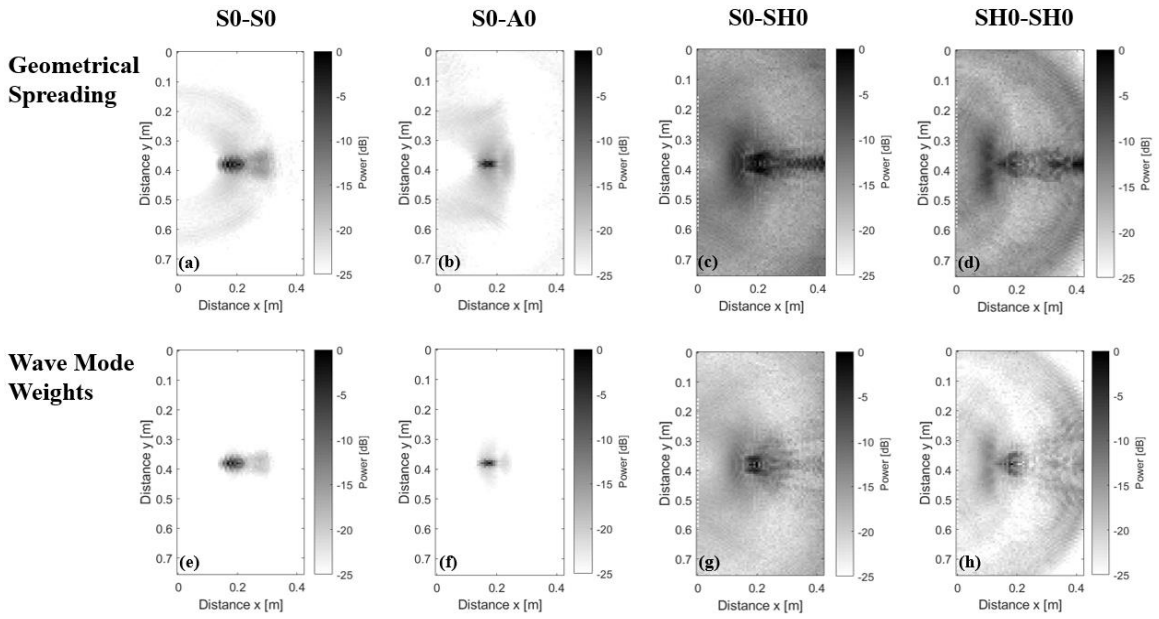

Figure 7.5: Numerical results for the on-axis blind hole reflector obtained using MVDR with geometrical spreading only and with wave mode weights. (a)-(d) Results obtained with geometrical spreading for the S0-S0, S0-A0, S0-SH0, and SH0-SH0 combinations, respectively. (e)-(h) Results obtained using wave mode weights for the S0-S0, S0-A0, S0-SH0, and SH0-SH0 combinations, respectively

In general, the S0-S0 and S0-A0 combinations carry more energy than the S0-SH0 and SH0-SH0 combinations, as seen from the images of Fig. 7.5, thus resulting in a lower noise floor. This is partly due to the fact that more energy is transferred from the incident S0 mode into a reflected S0 mode, or into a mode converted A0 mode. Furthermore, given the normal point excitation force used in the simulations, the transmitted SH0 mode carries less energy than the transmitted S0 mode.

Fig. 7.6 shows the Line Spread Functions (LSFs) obtained from the images of Fig. 7.5 by plotting the intensity distribution along the *y* direction at x = 0.19m (reflector location). All four plots show an improvement in dynamic range when the wave mode weights are applied. Fig. 7.6(a)

shows that the wave mode weights for the S0-S0 combination increase the dynamic range by about 5dB compared to the geometrical spreading only. Similarly, the S0-A0 combination (Fig. 7.6(b)) shows an average improvement of 3dB. The S0-SH0 case in Fig. 7.6(c) shows a similar increase in dynamic range, around 5dB, as in Fig. 7.6(a). The last combination, SH0-SH0, in Fig. 7.6(d) has the best of dynamic range improvement, lowering the noise floor by 10dB relative to the geometrical spreading case.

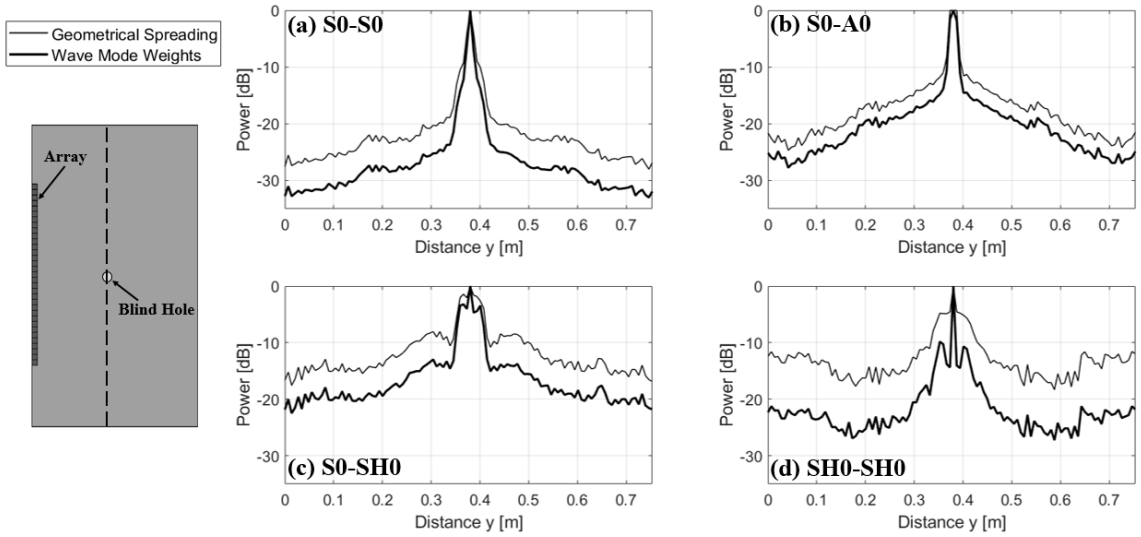

Figure 7.6: Line Spread Functions (LSFs) along the *y* direction for the on-axis blind hole reflector for geometrical spreading only (thin solid line) and for the wave mode weights (thick solid line). (a) S0-S0 combination. (b) S0-A0 combination. (c) S0-SH0 combination. (d) SH0-SH0 combination

In terms of spatial resolution, the two sets of weights behave in a similar manner, with the largest improvements brought by the wave mode weights in the S0-SH0 and SH0-SH0 combinations. The metric used to compare the spatial resolution performance is the full width of the main lobe of the LSF at -6dB. For the S0-S0 combination, the width of the main lobe obtained with wave mode weights shows a decrease of about 6.80mm compared to the geometrical spreading case, thus showing an increase in spatial resolution. For the other wave modes, the width of the main lobe at -6dB decreased by 3.38mm, 8.54mm, and 57.05mm for the S0-A0, S0-SH0, and SH0-SH0 combinations, respectively, when the wave mode weights are applied.

These improvements in dynamic range and spatial resolution are expected since the wave mode weights applied to the MVDR algorithm force the array to look for the best match between expected and recorded guided wave structures across the array. This requirement constitutes a much stronger constraint than the one imposed by the geometrical spreading weights alone.

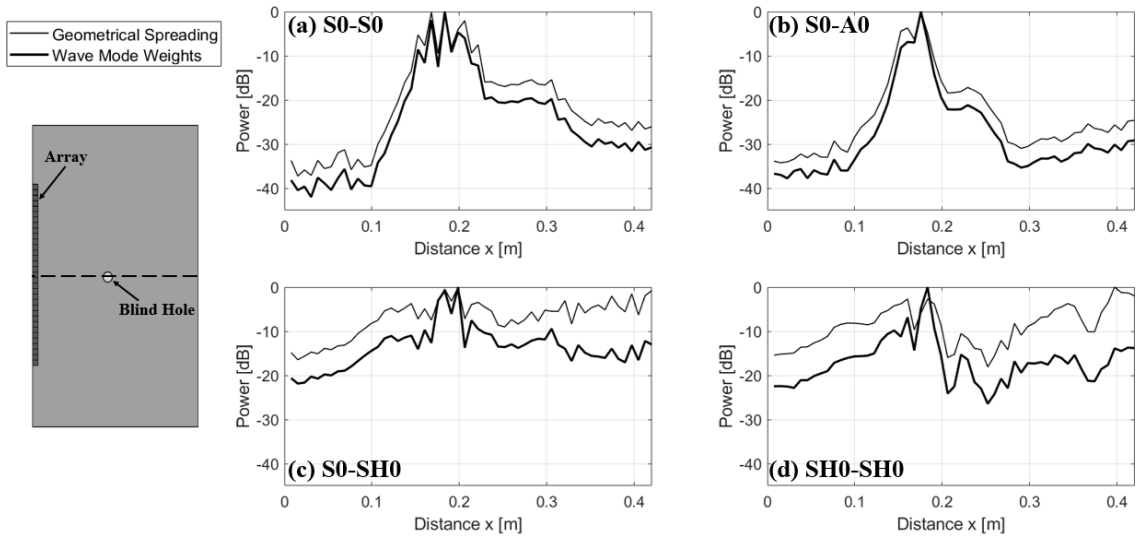

Figure 7.7: Line Spread Functions (LSFs) along the *x* direction for the on-axis blind hole reflector for geometrical spreading only (thin solid line) and wave mode weights (thick solid line). (a) S0-S0 combination. (b) S0-A0 combination. (c) S0-SH0 combination. (d) SH0-SH0 combination

Fig. 7.7 presents the LSFs results along the *x* direction, plotted at y = 0.38m (reflector location). This set of axial LSFs confirms how artifacts and boundary reflections can be suppressed using the wave mode weights. Overall, all four mode combinations show an increase in dynamic range when the wave mode weights are applied, compared to the geometrical spreading weights. Specifically, the S0-S0 and the S0-A0 combinations show an average increase in dynamic range of 4dB. The S0-SH0 combination has an increase in dynamic range of about 5dB, with local increases of up to 12dB close to the boundary. Similarly, the SH0-SH0 mode combination shows an average 8dB increase, reaching 13dB at the boundary. The axial resolution does not show a noticeable improvement, since this parameter is mainly influenced by the excitation frequency (or pulse width) of the transmitted signal, which is constant for both sets of weights.

It is worth noticing how the wave mode weights help limit artifacts. Due to the different wave speeds of the three guided wave modes considered, "ghost" images of the reflector can be generated by a simple time backpropagation algorithm. Since the wave mode weights rely on the match between expected and measured wave structure across the array (which is different for every point in the imaging domain), there will be only a good match with the wave mode combination corresponding to a specific set of weights, while the other combinations will be "rejected" (poor match). For example, the values around x = 0.1m in Fig. 7.7(d) correspond to a "faster" combination than SH0-SH0 and using the wave mode weights it is possible to suppress it by ~ 8dB, so as to allow the correct identification of the true reflector. Furthermore, the S0-SH0 and the SH0-SH0 combinations show high intensity values close to the right boundary of the plate (for SH0-SH0 the boundary reflection has even a larger value of intensity compared to the reflector) when geometrical spreading weights are used. Applying the wave mode weights allows reducing the boundary reflection and focusing on the real location of the damage (Figs. 7.7(c) and 7.7(d)).

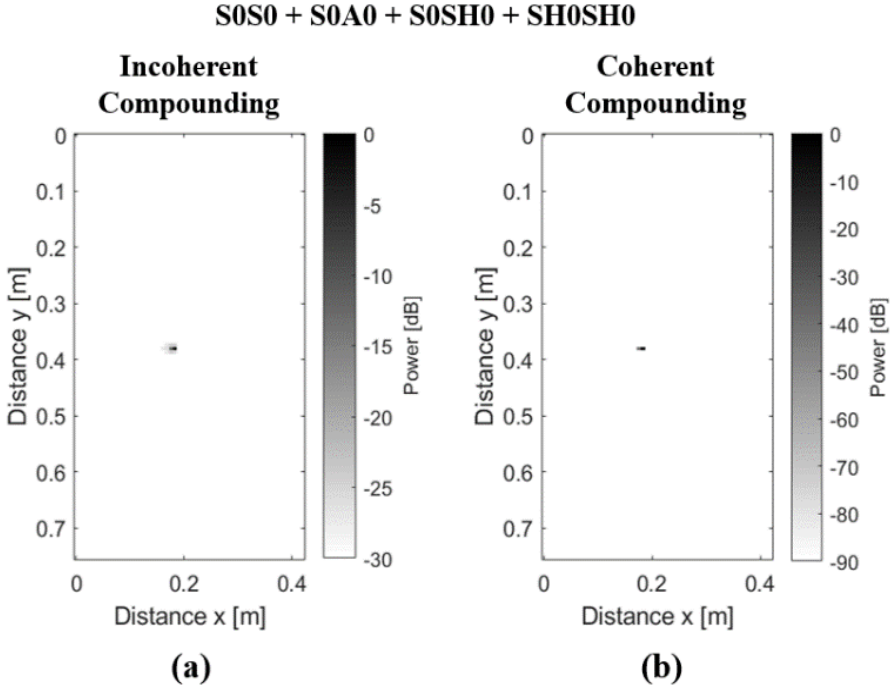

Figure 7.8: Results obtained for the on-axis blind hole reflector after compounding the S0-S0, S0-A0, S0-SH0, and SH0-SH0 wave mode combinations (a) incoherently and (b) coherently

7.5.3 Results: Wave Mode Compounding

Fig. 7.8 shows the effect of compounding the four wave mode combinations for the on-axis reflector. The incoherent compounding is shown in Fig. 7.8(a) and the coherent compounding in Fig. 7.8(b). Comparing the images in Fig. 7.8 with the individual combinations in Fig. 7.8, it is clear that compounding brings a quite dramatic improvement to the image focus and gain. Fig. 7.8 also shows that the added cross-mode terms of the coherent compounding bring some additional improvements in image focus compared to the incoherent compounding.

7.5.4 Results: Off-axis Reflector

The second proof-of-principle test was performed considering an off-axis blind hole reflector located at x = 0.19m and y = 0.30m. Fig. 7.9 shows the results with the wave mode weights compared to the geometrical spreading only for the four wave mode combinations. Analogously to Fig. 7.5, the wave mode weights show improvements with respect to the geometrical spreading weights in terms of dynamic range and spatial resolution. All images are plotted from 0dB to -25dB for ease of comparison with the on-axis case. In the S0-S0 combination in Figs. 7.9(a) and 7.9(e), the noise floor is lowered, and the sidelobes are suppressed when wave mode weights are applied. Similarly, in the S0-A0 combination, Figs. 7.9(b) and 7.9(f), a considerable increase in dynamic range is seen. Figs. 7.9(c) and 7.9(g) show the S0-SH0 case where, besides a slight increase in dynamic range, reflections from the boundaries and artifacts from other wave modes are reduced when wave mode weights are used. The SH0-SH0 combination shown in Figs. 7.9(d) and 7.9(h) shows similar improvements in reducing undesired artifacts and edge reflections.

The improvements in spatial resolution can be better appreciated by looking at the LSFs for the off-axis case. Fig. 7.10 shows the lateral LSFs plotted across the *y* direction at x = 0.19m

(reflector location). The application of the wave mode weights reduces the main lobe of the LSFs, compared to geometrical spreading only, by 2.25mm, 5.65mm, 42.80mm, and 55.74mm for S0-S0, S0-A0, S0-SH0, and SH0-SH0, respectively. Furthermore, the dynamic range shows an average increase of 5dB in the S0-S0, S0-SH0, and SH0-SH0 cases, and 3dB in the S0-A0 case.

The axial LSFs, plotted across the *x* direction and at y = 0.30m (reflector location), are shown in Fig. 7.11. Similarly to the on-axis case, all four combinations show that the two sets of weights present similar axial resolution performances. The dynamic range, instead, increases 4dB for S0-S0, 3dB for S0-A0, and from 5dB to 10dB for S0-SH0 and SH0-SH0, when wave mode weights are used. Figs. 7.11(c) and 7.11(d) show the reduction of artifacts and boundary reflections that can be achieved with the proposed set of wave mode weights. For instance, the values around 0.1m in Fig. 7.11(d), which are artifacts related to a faster wave mode combination than SH0-SH0, are decreased by 5dB.

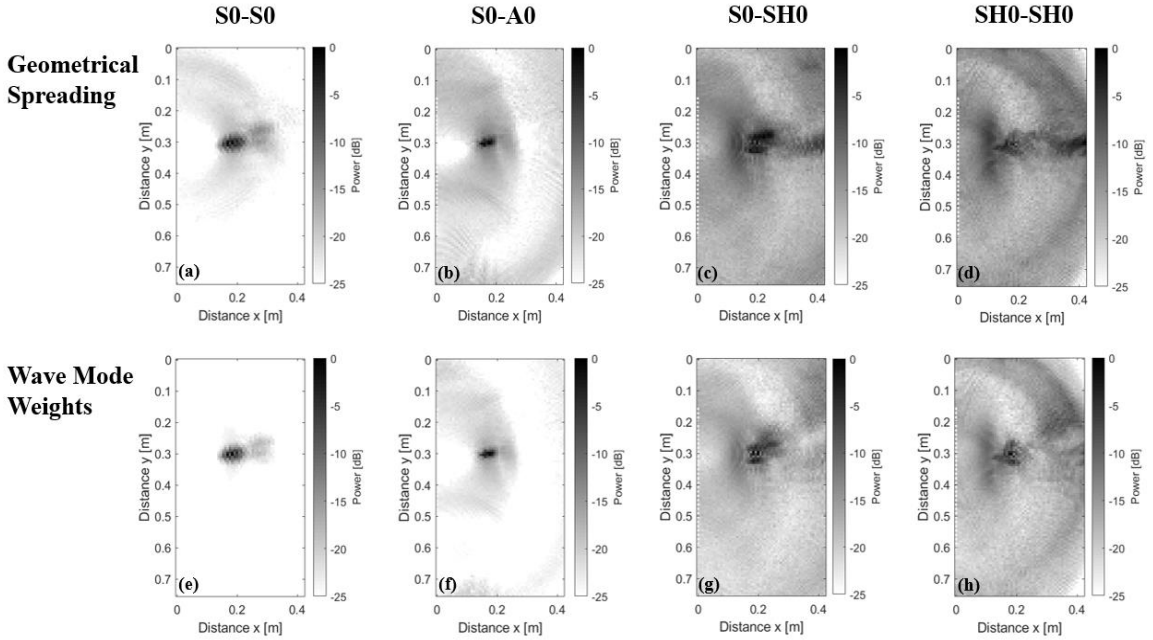

Figure 7.9: Numerical results for the off-axis damage obtained using MVDR with geometrical spreading only and wave mode weights. (a)-(d) Results obtained with geometrical spreading for the S0-S0, S0-A0, S0-SH0, and SH0-SH0 combinations, respectively. (e)-(h) Results obtained using wave mode weights for the S0-S0, S0-A0, S0-SH0, and SH0-SH0 combinations, respectively

The compounding of the different wave mode combinations for the off-axis case is shown in Fig. 7.12. Incoherent and coherent compounding show, again, a very significant improvement compared to any of the individual mode combinations, with increased dynamic range and spatial resolution.

In summary, the location of the reflector in the plate (on-axis or off-axis) does not seem to alter the general improvements obtained in the MVDR images by the wave structure weights and the wave mode compounding.

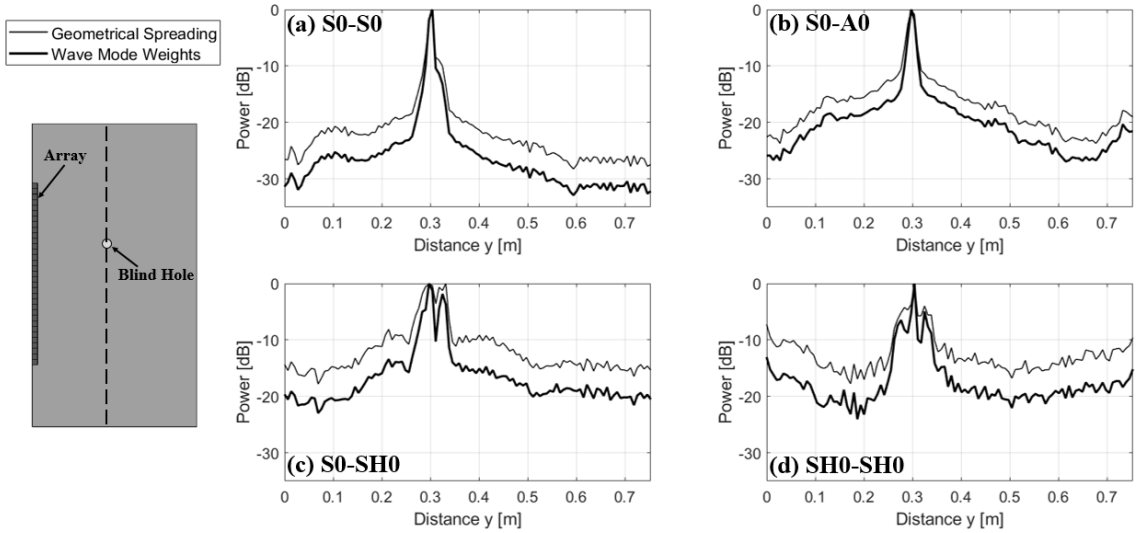

Figure 7.10: Line Spread Functions (LSFs) along the *y* direction for the off-axis blind hole reflector for geometrical spreading only (thin solid line) and wave mode weights (thick solid line). (a) S0-S0 combination. (b) S0-A0 combination. (c) S0-SH0 combination. (d) SH0-SH0 combination

7.6 Discussion and Conclusions

This paper has investigated improvements to the MVDR beamforming imaging algorithm applied to ultrasonic guided waves in plates (Lamb modes). The improvements consist of (a) the use of weights, or MVDR replica vectors, based on the distribution of displacements (mode structure) as received by the transducer array, and (b) the combination, or compounding, of multiple Lamb modes to create an improved image of reflectors (e.g. damage) in the plate.

Closed-form expression for the mode structure weights were derived for reflected symmetric modes S0, antisymmetric modes A0, and shear horizontal modes SH0. Geometrical spreading of the waves in transmission and reception was also included in the analytical formulation of the weights. The application of the weights for the different wave modes was performed in a matched field processing approach. The goal is to match, for every point in the imaging domain, the measured amplitude distribution across the array with the expected amplitude distribution based on the physics of the propagating guided wave modes. The effectiveness of these weights is fully exploited in the case of circular wavefronts, or reflectors close to the array (near field). In the far field of the array, these wavefronts will tend to a planar wavefront and thus a constant displacement distribution over the array, for every point in the medium, which does not improve the focus on the damage location.

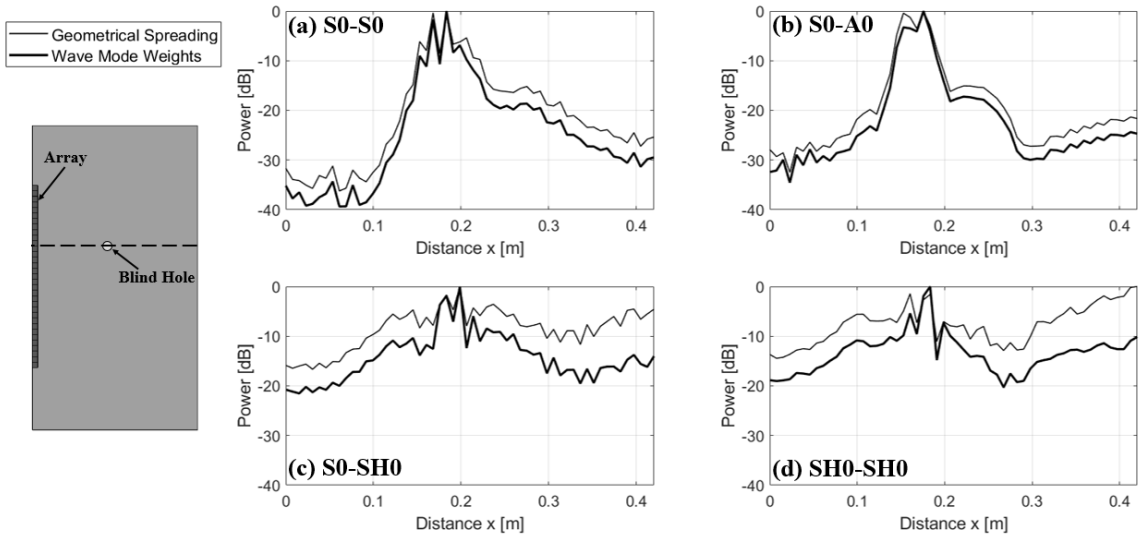

Figure 7.11: Line Spread Functions (LSFs) along the *x* direction for the off-axis blind hole reflector for geometrical spreading only (thin solid line) and wave mode weights (thick solid line). (a) S0-S0 combination. (b) S0-A0 combination. (c) S0-SH0 combination. (d) SH0-SH0 combination

The paper also exploits the opportunity of compounding different wave mode combinations obtained from multiple guided wave modes naturally existing in the plate, in order to increase the array gain without increasing its physical aperture. The compounding can be performed either

coherently or incoherently, in analogy with the combination of multiple excitation events or frequencies.

A proof-of-principle study demonstrating these improvements was performed using an FEM model of an aluminum plate with an antisymmetric reflector (blind hole) located either on-axis or off-axis with respect to the transducer array. Four different wave mode combinations were considered, namely S0-S0, S0-A0, S0-SH0, and SH0-SH0. For both on-axis and off-axis reflector locations, the wave mode weights as well as the wave mode compounding showed substantial increases in dynamic range, decrease in sidelobe levels, and improved spatial resolution as compared to a classical MVDR framework utilizing simple geometrical wave spreading as the replica vectors. The compounding resulted in the most dramatic improvements in image quality compared to the use of individual modes.

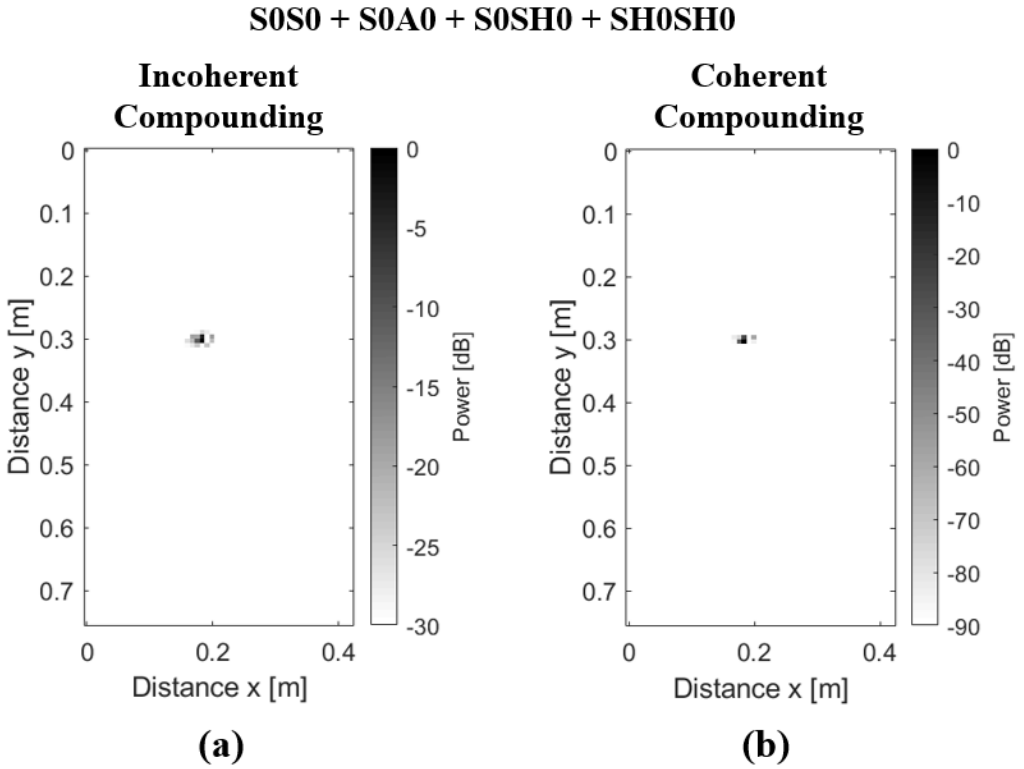

Figure 7.12: Results obtained for the off-axis reflector location after compounding the S0-S0, S0-A0, S0-SH0, and SH0-SH0 wave mode combinations (a) incoherently and (b) coherently

These concepts can be extended to more general cases of guided wave propagation than the specific cases examined in the numerical study. For example, results were only shown for the S0 mode and the SH0 mode in transmission. These can be easily extended to the A0 mode in transmission, which would bring additional opportunities for wave mode compounding. In a practical experiment, the choice of the type and the position of the transducer array will largely dictate the specific Lamb modes that can be utilized for imaging. Similarly, the specific mode frequency and plate thickness combination will dictate whether higher-order guided modes can exist and can be used for further image improvements.

This study has also considered a small reflector compared to the incident ultrasonic wavelength. The possibility of including specific scattering patterns from reflectors of general size and orientation in the proposed MVDR wave structure weights will be the focus of a future study.

Acknowledgements

Prof. Annamaria Pau from La Sapienza University in Rome collaborated with this research. This work was supported by US Federal Railroad Administration contract no. DTFR5316C00024, by US National Science Foundation grant no. CMMI-1362144, and by Ateneo Sapienza and PRIN 2015.

Chapter 7 is, in full, a reprint of S. Sternini, A. Pau, F. Lanza di Scalea, "Minimum Variance Imaging in Plates Using Guided Wave Mode Beamforming," submitted to *IEEE Transactions on Ultrasonics, Ferroelectrics, and Frequency Control*. The dissertation author was the primary investigator and author of this paper.

References

[1] Montaldo, G., Tanter, M., Bercoff, J., Benech, N., and Fink, M., 2009, "Coherent plane-wave compounding for very high frame rate ultrasonography and transient elastography," IEEE Trans. Ultrason. Ferroelectr. Freq. Control, 56(3), pp. 489-506.

[2] Papadacci, C., Pernot, M., Couade, M., Fink, M., and Tanter, M., 2014, "High-contrast ultrafast imaging of the heart," IEEE Trans. Ultrason. Ferroelectr. Freq. Control, 61(2), pp. 288-301.

[3] Tanter, M., and Fink, M., 2014, "Ultrafast imaging in biomedical ultrasound," IEEE Trans. Ultrason. Ferroelectr. Freq. Control, 61(1), pp. 102-119.

[4] Rasmussen, M. F., and Jensen, J. A., 2014, "Comparison of 3-D synthetic aperture phased-array ultrasound imaging and parallel beamforming," IEEE Trans. Ultrason. Ferroelectr. Freq. Control, 61(10), pp. 1638-1650.

[5] Karaman, M., Li, P. C., and O'Donnell, M., 1995, "Synthetic aperture imaging for small scale systems," IEEE Trans. Ultrason. Ferroelectr. Freq. Control, 42(3), pp. 429-442.

[6] Frazier, C. H., and O'Brien, W. D., 1998, "Synthetic aperture techniques with a virtual source element," IEEE Trans. Ultrason. Ferroelectr. Freq. Control, 45(1), pp. 196-207.

[7] Lockwood, G. R., Talman, J. R., and Brunke, S. S., 1998, "Real-time 3D ultrasound imaging using sparse synthetic aperture beamforming," IEEE Trans. Ultrason. Ferroelectr. Freq. Control, 45(4), pp. 980-988.

[8] Hazard, C. R., and Lockwood, G. R., 1999, "Theoretical assessment of a synthetic aperture beamformer for rail-time 3-D imaging," IEEE Trans. Ultrason. Ferroelectr. Freq. Control, 46(4), pp. 972-980.

[9] Nikolov, S. I., and Jensen, J. A., 2003, "In-vivo synthetic aperture flow imaging in medical ultrasound," IEEE Trans. Ultrason. Ferroelectr. Freq. Control, 50(7), pp. 848-856.

[10] Jensen, J. A., Nikolov, S. I., Gammelmark, K. L., and Pedersen, M. H., 2006, "Synthetic aperture ultrasound imaging," Ultrasonics, 44(1), pp. e5-e15.

[11] Oddershede, N., and Jensen, J. A., 2007, "Effects influencing focusing in synthetic aperture vector flow imaging," IEEE Trans. Ultrason. Ferroelectr. Freq. Control, 54(7), pp. 1811-1825.

[12] Wilcox, P. D., 2003, "Omni-directional guided wave transducer arrays for the rapid inspection of large areas of plate structures," IEEE Trans. Ultrason. Ferroelectr. Freq. Control, 50(6), pp. 699-709.

[13] Wang, C. H., Rose, J. T., and Chang, F.-K., 2004, "A synthetic time-reversal imaging method for structural health monitoring," Smart Mater. Struct., 13(2), pp. 415-423.

[14] Purekar, A. S., Pines, D. J., Sundararaman, S., and Adams, D. E., 2004, "Directional piezoelectric phased array filters for detecting damage in isotropic plates," Smart Mater. Struct., 13(4), pp. 838–850.

[15] Yu, L., and Giurgiutiu, V., 2008, “In situ 2-D piezoelectric wafer active sensors array for guided wave damage detection,” Ultrasonics, 48(2), pp. 117–134.

[16] Ambrozinski, L., 2013, Beamforming of guided waves. Chapter 7 of Advanced Structural Damage Detection: From Theory to Engineering Applications, Stepinski, T., Uhl, T., and Staszewski, W., eds., pp. 177-211, John Wiley and Sons, Ltd.

[17] Clarke, T., Cawley, P., Wilcox, P. D., and Croxford, A. J., 2009, “Evaluation of the damage detection capability of a sparse-array guided-wave SHM system applied to a complex structure under varying thermal conditions,” IEEE Trans. Ultrason. Ferroelectr. Freq. Control, 56(12), pp. 2666–2678.

[18] Hall, J. S., and Michaels, J. E., 2010, “Minimum variance ultrasonic imaging applied to an in situ sparse guided wave array,” IEEE Trans. Ultrason. Ferroelectr. Freq. Control, 57(10), pp. 2311–2323.

[19] Hall, J. S., and Michaels, J. E., 2015, “Multipath ultrasonic guided wave imaging in complex structures,” Struct. Health Monit., 14(4), pp. 345-358.

[20] Flynn, E. B., Todd, M. D., Wilcox, P. D., Drinkwater, B. W., and Croxford, A. J., 2011, “Maximum-likelihood estimation of damage location in guided-wave structural health monitoring,” Proc. Roy. Soc. A: Math. Phy., 471(2181), pp. 2575–2596.

[21] Harley, J. B., and Moura, J. M. F., 2014, “Data-driven matched field processing for Lamb wave structural health monitoring,” J. Acoust. Soc. Am., 135(3), pp. 1231–1244.

[22] Engholm, M., and Stepinski, T., 2010, “Adaptive beamforming for array imaging of plate structures using Lamb waves,” IEEE Trans. Ultrason. Ferroelectr. Freq. Control, 57(12), pp. 2712–2724.

[23] Zhang, J., Drinkwater, B. W., and Wilcox, P. D., 2008, “Defect characterization using an ultrasonic array to measure the scattering coefficient matrix,” IEEE Trans. Ultrason. Ferroelectr. Freq. Control, 55(10), pp. 2254-2265.

[24] Hall, J. S., Fromme, P., and Michaels, J. E., 2014, “Guided wave damage characterization via minimum variance imaging with a distributed array of ultrasonic sensors,” J. Nondestr. Eval., 33(3), pp. 299-308.

[25] Lanza Di Scalea, F., Sternini, S., and Nguyen, T. V., 2017, “Ultrasonic imaging in solids using wave mode beamforming,” IEEE Trans. Ultrason. Ferroelectr. Freq. Control, 64(3), pp. 602–616.

[26] Sternini, S., Quattrocchi, A., Montanini, R., Pau, A., and Lanza di Scalea, F., 2017, “A match coefficient approach for damage imaging in structural components by ultrasonic synthetic aperture focus,” Proc. Eng., 199, pp. 1544-1549.

[27] Baggeroer, A.B., Kuperman, W. A., and Mikhalevsky, P. N., 1993, “An overview of matched field methods in ocean acoustics,” IEEE Ocean. Eng., 18(4), pp. 401-424.

[28] Kuperman, W. A., and Turek, G., 1997, "Matched field acoustics," Mech. Syst. Sig. Proc., 11(1), pp. 141-148.

[29] Capon, J., 1969, "High resolution frequency wavenumber spectrum analysis," Proc. IEEE, 57, pp. 1408-1418.

[30] Arabshahi, F., Monajemi, S., Sheikhzadeh, H., Raahemifar, K., and Faraji-Dana, R., 2013, "A frequency domain MVDR beamformer for UWB microwave breast cancer imaging in dispersive mediums," IEEE International Symposium on Signal Processing and Information Technology, Athens, pp. 000362-000367.

[31] Synnevag, J. F., Austeng, A., and Holm, S., 2007, "Adaptive beamforming applied to medical ultrasound imaging," *IEEE* Trans. Ultrason. Ferroelectr. Freq. Control, 54(8), pp. 1606-1613.

[32] Deylami, A. M., Jensen, J. A., and Asl, B. M., 2016, "An improved minimum variance beamforming applied to plane-wave imaging in medical ultrasound," 2016 IEEE International Ultrasonics Symposium (IUS), Tours, pp. 1-4.

[33] Diamantis, K., Greenaway, A., Anderson, T., Jensen, J. A., and Sboros, V., 2017, "Experimental performance assessment of the sub-band minimum variance beamformer for ultrasound imaging," Ultrasonics, 79, pp. 87-95.

[34] Baggeroer, A.B., Kuperman, W. A., and Schmidt, H., 1988, "Matched-field processing: source localization in correlated noise as an optimum parameter estimation process," J. Acoust. Soc. Am., 83(2), pp. 571-587.

[35] Michalopoulou, Z.-H., and Porter, M. B., 1996, "Matched-field processing for broad-band source localization," IEEE Ocean. Eng., 21(4), pp. 384-392.

[36] Makris, N.C., 1995, "A foundation for logarithmic measures of fluctuating intensity in pattern recognition," Opt. Lett., 20(19), pp. 2012-2014.

[37] Debever, C., and Kuperman, W. A., 2007, "Robust matched-field processing using a coherent broadband white noise constraint processor," J. Acoust. Soc. Am., 122(4), pp. 1979-1986.

[38] Tolstoy, A., 1993, Matched Field Processing, World Scientific, New York.

[39] Orris, G. J., Nicholas, M., and Perkins, J. S., 2000, "The matched-phase coherent multi-frequency matched-field processor," J. Acoust. Soc. Am., 107(5), pp. 2563-2575.

[40] Jensen, F. B., Kuperman, W. A., Porter, M. B., and Schmidt, H., 2011, "Signals in noise," in Computational Ocean Acoustics, 2nd ed., Springer Publishing Company, Inc., pp. 705-772.

[41] Pau, A., and Achillopoulou, D. V., 2017, "Interaction of shear and Rayleigh-Lamb waves with notches and voids in plate waveguides," Materials, 10(7), 841.

[42] Rose, J. L., 2014, "Waves in plates," in Ultrasonic Guided Waves in Solid Media, Cambridge University Press, pp. 76-106.

Chapter 8

Conclusions

Passive data collection in the field of NDE and SHM have been previously applied to various scenarios where different types of structures were subjected to random acoustic excitations (noise fields). Chapter 2 extended these concepts to the inspection of railroad tracks using the random acoustic vibrations caused by the wheel/rail interaction. It has been shown that the normalized cross-correlation operator can successfully extract the acoustic transfer function of the system (the rail in the present case) in a robust manner, therefore removing the influence of the random excitation source and reconstructing a stable signal along the railroad track. A statistical outlier analysis, using some features obtained from the transfer functions, produced damage index traces giving indications about the location of discontinuities in the rail, namely joints, welds, and internal defects. These traces show the successful identification of several discontinuities at speeds ranging from 25mph to 80mph.

Chapter 3 introduced a robust technique to eliminate the effect of possible uncorrelated noise in the recorded signals during the transfer function reconstruction process. This technique, which was formulated for dual-output systems, was applied to the calculation of the auto-power spectrum of the recorded signals using inter-segment averaging in order to eliminate uncorrelated

noise that might affect the transfer function reconstruction. It was shown that the technique successfully increases the SNR of the reconstructed transfer function both for the case of synthetic signals and experimental signals.

Chapter 4 investigated the task of defect imaging and characterization in rail specimens using ultrasonic imaging techniques such as SAFT and DAS. This effort is relevant to enable rail maintenance engineers to make informed decisions based on the size of the defect following a flaw detection. A real-time imaging system was developed by implementing the imaging algorithm on a GPU framework. The system showed the potential for 2D and 3D imaging of both natural and simulated defects, such as TDs in the rail head. Compounding of multiple wave modes propagating in the material was introduced to improve the image reconstruction in terms of dynamic range and spatial resolution.

Chapter 5 applied the DMAS beamforming technique to the case of imaging with interposed coupling path between the ultrasonic array and the test medium. The interposed medium (usually a wedge) is often required to properly direct the ultrasonic beams for maximum reflections from defects oriented at specific directions. A ray tracing formulation was developed to account for the different propagation paths of the multiple wave modes that coexist in the material. Wave mode compounding was also applied to improve the imaging results. A proof-of-concept test on an aluminum specimen showed the potential of the algorithm to improve defect imaging when an interposed medium, such as a transducer wedge, is used.

Chapter 6 applied the DAS and the MVDR beamformers to the general imaging of internal defects in solids using a new set of weights, or replica vectors, based on the structure of the propagating wave modes, corresponding to longitudinal and shear wave modes in the bulk material. These new wave mode weights were compared to conventional static apodization

weights, and they showed their potential for improved defect imaging by increasing dynamic range and spatial resolution of the reconstructed images. Wave mode compounding was also explored to further improve the algorithm performance.

Finally, Chapter 7 extended the imaging framework introduced in Chapter 6 to the case of imaging in plates using ultrasonic guided (Lamb) waves. The MVDR beamformer was used in the image reconstruction process together with new weights based on the wave structure of the propagating guided modes considered (S0, A0, and SH0). Similarly to the results shown in Chapter 6, the new guided wave mode weights and wave mode compounding successfully improve the imaging performance when compared to conventional weights such as geometrical spreading.